Mathematical Modelling of Droplets Climbing an Oscillating Plane

Joel Bradshaw, MMaths and Phys.

Thesis submitted to The University of Nottingham
for the degree of Doctor of Philosophy

February 2016

Abstract

Recent experiments [P. Brunet, J. Eggers, and R. Deegan, Phys. Rev. Lett. 99, 114501 (2007)] have shown that a liquid droplet on an inclined plane can be made to move uphill by sufficiently strong, vertical oscillations. In order to investigate this counterintuitive phenomenon we will derive three different models that qualitatively reproduce the main features of the experiment.

For the first model the liquid's inertia and viscosity are assumed negligible, so that the motion of the droplet is dominated by the applied acceleration due to the oscillation of the plate, gravity and surface tension and that the droplet is thin. We explain how the leading order motion of the droplet can be separated into a spreading mode and a swaying mode. For a linear contact line law, the maximum rise velocity occurs when the frequencies of oscillation of the two modes are in phase. We show that, both with and without contact angle hysteresis, the droplet can climb uphill and also that, for certain contact line laws, the motion of the droplet can produce footprints similar to experimental results. We show that if the two modes are out of phase when there is no contact angle hysteresis, the inclusion of hysteresis can force them into phase. This in turn increases the rise velocity of the droplet and can, in some cases, cause a sliding droplet to climb.

For the second model we use a two-dimensional flow where the Reynolds number is assumed large enough for viscosity to be neglected. We show that the leading order motion of the droplet can be separated into the same two modes and the net motion of the droplet is an oscillatory function of the frequency. For increasingly non-wetting droplets we discover that the rise velocity begins to oscillate very rapidly as a function of the static contact angle. What we also discover is that the change in the free surface of the droplet is actually a wave travelling travelling across the droplet, and the amount of modes present coincide with the rapid change in the rise velocity. Using a cubic contact line law and contact angle hysteresis we observe a droplet that

can climb uphill for parameter values similar to that of the experiment. With the addition of a time dependent term within the contact line law we show that it is possible to obtain a multi-valued relationship between the velocity of the contact line and the respective contact angles, reproducing experimental observations seen for unsteady, moving contact lines.

For the third model we again assume that the liquid's viscosity is negligible, similar to model 2, only now for a three-dimensional, thin droplet. For very small amplitudes the motion of the droplet is a combination of a swaying mode and a spreading mode that interact causing a net motion of the droplet. This motion is found to be an oscillatory function of the driving frequency and the magnitude of the peak rise velocity is proportional to one over the frequency squared. By examining the velocity of the centre of the droplet and the displacement of the contact line we see that the absolute maximums of both of these, over one period of oscillation, contain natural frequencies, which are evenly spaced with respect to the square root of the frequency of the oscillation.

Acknowledgements

First and foremost I would like to thank Prof. John Billingham for all the support provided during my PhD study. You were always confident that I knew what I meant, and with your guidance other people could know what I meant as well. I would also like to thank Dr. Paul Matthews for helping steer my writing in the right direction, reminding me that a lot more explanation would be required for anyone other than me to follow my work.

The work described in chapter 2 has been published as J. Bradshaw and J. Billingham, Phys. Rev. E, 93, 013123 (2016) and from this I would like to thank most of my referees involved with my submission. The feedback they provided very much helped guide the focus of my results for this chapter.

Thank you to the EPSRC for providing the funding to allow me to do this research.

Thank you to Ben and Tom for all the help and friendly chats at the office over the past 3 years, all of the game nights which reminded me to relax every once in a while and some much needed Subways to keep me going. Thanks to my family for all the constant love and support they have always given me, to Ellie for always being ready with a cup of tea when I needed it and to Scamp for always being there for a well deserved cuddle.

Contents

1 Introduction **1**

1.1 Static contact lines 2
1.2 Steady, dynamic contact lines 3
1.3 Unsteady, dynamic contact lines 6
1.4 Recent droplet models 9
1.5 Overview 11

2 Model 1: The surface tension dominated, three-dimensional, shallow droplet **14**

2.1 The model 14
2.1.1 Three-dimensional Navier-Stokes equations 14
2.1.2 Dimensionless variables 16
2.1.3 Governing equations 18
2.2 Solution method 19
2.2.1 Redefined droplet height 19
2.2.2 Discretisation 21
2.2.3 Influence coefficients 22
2.2.4 Mass conservation 24
2.2.5 Evolution of the boundary 28
2.2.6 The Newton method 29
2.3 Results 29
2.3.1 Validation of the solution method 29
2.3.2 The effect of hysteresis 34
2.3.3 Alternative contact line law 40
2.3.4 Droplet footprints 42
2.4 Discussion 45

3 Model 2: The inviscid, two-dimensional droplet **47**
3.1 The model . . . 47
3.1.1 Two-dimensional Euler equations . . . 47
3.1.2 Moving reference frame . . . 49
3.1.3 Dimensionless variables . . . 50
3.1.4 Governing equations . . . 52
3.2 Small amplitude asymptotic solution . . . 52
3.2.1 Polar coordinates . . . 52
3.2.2 Asymptotic expansion . . . 54
3.2.3 First order terms . . . 57
3.2.4 Second order terms . . . 69
3.3 Numerical solution method . . . 74
3.3.1 The full problem . . . 74
3.3.2 First order asymptotic, time independent problem . . . 86
3.3.3 Second order asymptotic, time averaged problem . . . 89
3.3.4 Validation of solution methods . . . 90
3.3.5 Breaking the droplet . . . 94
3.4 Results . . . 98
3.4.1 Linear contact line law . . . 98
3.4.2 Non-linear contact line law . . . 119
3.4.3 Time dependent contact line law . . . 135
3.5 Discussion . . . 149

4 Model 3: The inviscid, three-dimensional, shallow droplet **152**
4.1 The Model . . . 152
4.1.1 Two-dimensional shallow water equations . . . 152
4.1.2 Moving reference frame . . . 154
4.1.3 Dimensionless equations . . . 155
4.1.4 Governing equations . . . 156
4.2 Small amplitude asymptotic solution . . . 157
4.2.1 Polar coordinates . . . 157
4.2.2 An unperturbed droplet . . . 157
4.2.3 Asymptotic expansion . . . 158
4.2.4 First order terms . . . 161
4.2.5 The spreading mode . . . 163
4.2.6 The swaying mode . . . 167

4.2.7 Second order terms . . . 170
4.2.8 Force Balance . . . 172
4.2.9 Comparison between model 2 and 3 . . . 176
4.3 High frequency, small amplitude limit - WKB . . . 177
4.3.1 High frequency spreading mode . . . 177
4.3.2 High frequency swaying mode . . . 180
4.3.3 The conditions for the upper boundary . . . 182
4.3.4 Boundary Layer . . . 183
4.4 Discussion . . . 188

5 Conclusion **189**
5.1 Future work . . . 193

A Force balance for alternative contact line laws **195**
A.1 A square root in the contact line law . . . 196
A.2 Time dependent contact line law . . . 196

B Balancing the inertia with the acceleration of the substrate for Models 2 and 3 **198**

Chapter 1

Introduction

The focus of this work is the mechanics of a droplet on an inclined substrate, and the surprising uphill motion that can be obtained when vertical oscillations are applied. The inspiration for this work is an experiment carried out in 2007 by Brunet, Eggers and Deegan [8] who found that they could always cause a droplet to climb uphill if the amplitude of the applied acceleration was large enough. The reason we will cover this work is that it is about an unsteady flow containing a contact line, an area of fluid dynamics with a lot of experimental research [8][9][27][30][34] and has been shown to produce some very counter-intuitive results.

Picture a droplet sliding down the side of a window. This everyday phenomenon may seem insignificant but the precise physics of the motion of the droplet is poorly understood. When an interface between two fluids comes in contact with a solid it forms what is known as a contact line. When such a line is present, the dynamics of a flow are altered greatly and, as we shall discover, can produce some unusual results. When a droplet is on a surface, a slope is formed between the fluid and the solid at the contact line. The gradient of this slope is known as the contact angle and it is believed there is a strong correlation between the size of this angle and the velocity of the contact line [7][23][33]. Returning to the droplet on a window, it may not necessarily be sliding down as it could be at rest on the surface. When talking about the relationship between the velocity of the contact line and the size of the contact angle, there will usually be a range of angles where the contact line remains stationary. This is known as contact angle hysteresis and is a very important mechanism we will need to examine.

The reason we will discuss moving contact lines is that flows containing

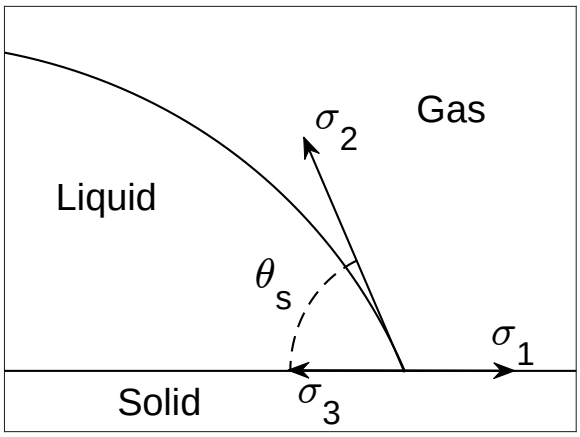


Figure 1.1: The balancing of the horizontal components of surface tensions at a contact line to form Youngs equation.

them are commonly found in modern day industry, including things such as coating processes [36], the application of pesticides, digital micro fluids [18], painting, cooling processes and even inkjet printers [12]. Considering the extent in which we encounter dynamic contact lines it would be assumed that they are better understood.

1.1 Static contact lines

Young [37] was the first person to derive an equation for calculating static contact angles (i.e. the contact angles for stationary droplets), known as Young's equation. Using the assumption that the solid/gas, gas/liquid and liquid/solid interfaces all possess a constant surface tension, Young deduced that the static contact angle can be found using

$$\sigma_2 \cos\theta_s = \sigma_1 - \sigma_3, \tag{1.1}$$

where σ_i represent the surface tension at the interfaces and θ_s is the static contact angle (see figure 1.1). Dussan V. [14] explained that Young's equation is hard to verify experimentally due to the inability to measure the surface tensions of the solid/gas and liquid/solid interfaces.

A direct measurement of the contact angle can also pose problems. Dettre and Johnson [13] showed this by placing fluid droplets on a horizontal surface,

which appeared flat on a length scale similar to that of the droplet but actually contained concentric axially symmetric scratches in the form of a sine wave. They used this experiment to show that the observed contact angle θ does not match the actual one θ_s, and most importantly two droplets sitting in different positions will have different observed contact angles but the actual contact angles are the same. This example of surface roughness is a cause of hysteresis. Zisman [38] showed that only by treating 'very smooth' surfaces could he achieve no contact angle hysteresis.

1.2 Steady, dynamic contact lines

When a viscous fluid is in contact with a rigid body it satisfies a 'no-slip' condition on the liquid/solid interface. The presence of a moving contact line seems to contradict this. Any classical approach to a problem such as this leaves a singularity in the shear stress along the contact line which is left unresolved [15][25][29].

Moffatt [29] examined the flow in a wedge where one of the surfaces was rigid and the other was either rigid or free; the latter of these two is similar to the way in which the fluid moves near a contact line. He modelled the flow using a creeping flow approximation and observed that very close to the corner of the wedge eddies formed within the flow. For the case of a rigid surface and a free one he still encountered a discontinuity in the velocity at the corner, where the free surface must be distorted both by surface tension and by pressure gradients. This analysis also requires the shape of the free surface to remain flat.

Using a combination of experiments/theory Dussan V. and Davis [15] showed that at the fluid/fluid interface in the vicinity of the contact line, the fluids undergo a 'rolling' motion. They did this by injecting dye into droplets, set up in different ways, in order to watch how the particles within the flow move. The theory still left the shear stress at the contact line as singular as well as leaving the velocity at the contact line undefined.

To deal with the stress singularity near the contact line, the problem has been examined at both a microscopic and a macroscopic level [11][19]. When looking at the problem at a microscopic level we are looking at the intermolecular forces and how they influence the flow [21][24]. The macroscopic approach looks at the problem on a length scale similar to that of the droplet. This usu-

ally involves dealing with the singularity using some sort of 'slip condition' close to the contact line.

In addition to a method for eliminating the stress singularity, we also need a way to calculate the velocity of the contact line. Experimentally it is commonly shown that there is a relationship between the velocity of the contact line and the contact angle [23][28][33], an approach we will consider in more detail.

Huh and Scriven [25] looked at a similar example to Moffatt [29] and solved it using the stream function for a two-dimensional, creeping flow approximation. Similarly they concluded that using a no-slip condition all the way up to the contact line results in a singularity in the stress. One solution they suggested to overcome the discontinuity is to replace the no-slip condition with a linear slip condition but they were unable to satisfy this new condition using any form of their stream function. Another method they examined is a lubrication flow model which concluded that long range interactions dominate the local force balance on the interface near the contact line and that increasingly free slip when approaching the contact line can cause the shear stress to remain finite. Unfortunately this lubrication flow model can only properly be applied to very small dynamic contact angles.

Hoffman [23] examined the motion of a contact line experimentally by measuring the velocity of an advancing meniscus and their apparent contact angles by driving fluids through a tube using a plunger. He found a strong correlation between the apparent contact angle and the capillary number, which is the balance between the viscous forces and the surface tension at the liquid/air interface, (plus a shifting factor) for the liquid/air interface in motion when viscous and interfacial forces are dominant. This gave good experimental data to examine the velocity at the contact line and was expanded by Hoffman [24] to also include the theory. He did this by looking at the capillary number as a function of the dynamic contact angle. He created a two part model where the mechanism of the effect depends on the size of the contact angle. For contact angles less than 120 degrees the motion of the contact line is dominated by liquid diffusion. For this, molecules of fluid on the surface have 'preferred absorption sites' where they tend to sit. When a flow is advancing the potential energy of the molecules is increased up to a point where the can jump to the next site. For contact angles approximately 180 degrees the velocity is dominated by a 'tank tread' motion. Here the molecules on the liquid/gas interface are consecutively pushed on the solid, once their potential energy is

large enough, causing the tread like movement. The energy required again is generated by the advancing fluid. For angles between these two the velocity is a combination of these two mechanisms. This model shows good agreement to results obtained by Hoffman [23] as well as others, although it takes no inertial or gravitational effects into account and only works for liquid/gas systems. When comparing experimental data to this model the molecular structures of the liquid and the solid are both very important.

Hocking [19] postulated that when one fluid displaces another on a solid boundary, the displaced fluid remains at a microscopic level within the irregularities of the surface causing the discontinuity to by replaced by a slip condition. This suggests that the velocity of the contact line is related to a slip coefficient between the two fluids.

Marsh, Garoff and Dussan V. [28] looked at the relationship between the size of the contact angle and the velocity of the moving contact line by submerging cylinders, inclined at various angles, into a bath of silicon oil. They found that the relationship could be written as

$$\theta = (296^\circ \pm 4^\circ)Ca^{0.347\pm0.002}, \tag{1.2}$$

where Ca is the Capillary number.

Hocking [21] later looked at droplets spreading over a surface with the inclusion of intermolecular forces. Instead of assuming the radius (contact line) evolves explicitly from the contact angle, instead the contact angle is a fixed term calculated in terms of the relative strengths of the fluid-fluid and fluid-solid attractions. Hocking deduced a term for the spreading of a thin droplet ('thin' meaning that the contact angle is small) over a surface under the effects of capillary, viscosity and intermolecular forces. He concluded that the radius of the drop is proportional to $t^{1/10}$, irrespective of the solid/liquid used. Although this model only works up to the point where the droplet has reached some equilibrium shape, Hocking extended this [22] to cover fully wetting droplets.

By examining the spread of silicone oil drops on horizontal surfaces, Tanner [33] used lubrication approximations to find a relationship between the speed of the contact line and the contact angle. Since the spreading of the oil matches a slow viscous flow, Tanner deduced that the movement is dominated by both the surface tension and the viscosity of the drop. By using an inflection point

near the edge of the drop, Tanner calculated that

$$\theta \propto Ca^{1/3}, \tag{1.3}$$

with good agreement to experiments; a result very similar to [28]. The lubrication approximation theory fails however for drop thicknesses below 2 to 9 $\times 10^{-8}$m (for increasing viscosity) where the inclusion of other effect may be important.

Further work relating to [33] was carried out by Eggers and Stone [17] where they produced two models, one which incorporates van der Waals forces and the other which allows slip at the contact line to attempt to give a more accurate relationship between the speed and the contact angle. Both models, although different, give that the contact angle cubed is proportional to the Capillary number multiplied by a logarithmic term, involving the Capillary number to the order of some power, where the power differs depending on the model. They also include experimental results in which both models show good comparison. Unfortunately both [33] and [17] make the assumption that the fluid is fully wetting and so no equilibrium contact angle, or hysteresis, is included.

Shikhmurzaev [32] produced a paper that contains a long and detailed explanation of the moving contact line problem as well as a review of many different approaches to solving this problem, including both intermolecular forces and slip conditions near the contact line to resolve the discontinuity. In addition to this Shikhmurzaev included a model to solve the problem that focuses on the process of interface formation (or disappearance) from first principles. The incompleteness of this model has been covered in great detail by Billingham [6].

1.3 Unsteady, dynamic contact lines

So far every example looked at has been of a steady flow however Ting and Perlin [34] examined dynamic contact lines from a different approach. By placing a vertical plate in a water bath and oscillating it vertically they examined how contact lines evolve in a non steady flow. This is interesting because instead of working with a droplet they have taken a two-dimensional problem in order to solely focus on how the velocity at the contact line relates to the contact angle.

When carrying out the experiment they varied the frequency and amplitude of the oscillations in order to produce results for Reynolds numbers varying between 1 and 1900. For amplitudes < 1 mm the flow at the contact line exhibited the no-slip condition, where the velocity matched that of the plate and was independent of the changing contact angle. For larger amplitudes the flow at the contact line acts either in a free-slip motion, which means that the contact angle remains constant but the velocity of the flow changes, or a partial-slip motion which is an intermediate between no-slip and slip. The frequency of the oscillations also caused the results to change although not by much when compared to changing the amplitude and so is neglected in the analysis. Similar to [15] and [19] they deduced that only near the contact line would the fluid not follow the no-slip boundary condition but they were unable to define the length of the slip region. Finally, a model for the boundary conditions on the plate is derived which consists of three parts. Away from the contact line the flow obeys the no-slip condition but in a region close to the contact line the flow is related to the vorticity of the fluid near the boundary region. At the contact line the flow is a function of the gradient of the slope between the fluid and the plate (i.e. the contact angle) but to calculate this function the 'capillary coefficient' (a non linear function which depends on time, the amplitude and the frequency) needs to be known. The model included for this coefficient is not ideal and further work needs to be done on the contact line acceleration in order to improve this.

Lyubimov, Lyubimova and Shklyaev [27] also examined moving contact lines for an unsteady flow using a hemispherical drop on a vertically oscillating, horizontal plane. Since they were looking at very large frequency oscillations they assumed the Reynolds number is large enough to ignore the effects of viscosity in the problem. For the boundary condition at the contact line they let the velocity of the contact line equal the change in the contact angle from its equilibrium angle times the 'phenomenological constant', a parameter related to the wettability of the fluid. They first examined the movement of the contact line for natural oscillations where they found that the contact line law used was responsible for oscillation damping. They also looked at forced and non-linear oscillations in which a resonant frequency would be obtained. They discovered that in the presence of dissipation on the contact line caused not only a damping on the amplitude of the resonant frequency but also a shift in the resonant frequency. Although contact angle hysteresis was mentioned in

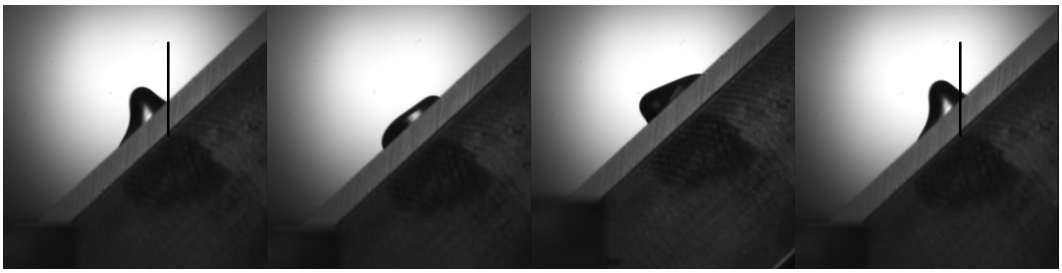


Figure 1.2: Frames taken of the droplet climbing the oscillating substrate. The time intervals are evenly space such that the last frame is exactly one period of oscillation after the first. The vertical black line present in the first and last frame is situated in the same place relative to the substrate in order to show the distance covered by the droplet over a single period.

their paper, it was not included in the model.

Brunet, Eggers and Deegan [8][9] focused on a liquid droplet placed on an inclined substrate, which is partially wetted by the drop. The droplets were a glycerol-water mixture, with a volume $\mathcal{V}$ ranging between 0.5 and 20 μl, placed on a Plexiglas substrate inclined at an angle α of up to 85° to the horizontal. When the plate was stationary the droplet would either slide down or remain pinned, depending on the size of the droplet and the angle of inclination, however when a vertical, sinusoidal oscillation was applied a third option was observed. Brunet et al discovered that by oscillating the substrate vertically at accelerations of up to 50 times the acceleration due to gravity, and frequencies between 30 to 200 Hz, they could cause the droplet to climb uphill (figure 1.2).

What Brunet et al found was that this unusual phenomenon is the result of an up and down symmetry breaking, due to the presence of the substrate, and has little to do with the presence of gravity. They deduced that, irrespective of the volume or viscosity of the liquid, the angle of inclination or the frequency of the oscillations, the droplet can always be made to climb uphill if the amplitude of the acceleration is large enough. This is limited however by the droplet 'breaking up' before the onset of climbing if the liquid's viscosity is too small.

In addition to oscillating an inclined substrate vertically, Brunet et al also took a horizontal substrate and oscillated at an angle; again to produce the same effect but without the acceleration due to gravity. They carried out this experiment with both sessile droplets (on top of the horizontal substrate) and pendant droplets (underneath the horizontal substrate). They found that for both cases when the vertical component of the substrates motion was towards

Parameter	Symbol	Typical Value	Units
Volume	$\mathcal{V}$	5×10^{-9}	m^3
Contact Angle	θ_0	1.08	rad
Density	ρ	1190	$\mathrm{kg\,m}^{-3}$
Viscosity	ν	3.1×10^{-5}	$\mathrm{m}^2\,\mathrm{s}^{-1}$
Surface Tension	σ	0.066	$\mathrm{kg\,s}^{-2}$
Acceleration	a_0	174	$\mathrm{m\,s}^{-2}$
Frequency	f	50.77	s^{-1}
Slope	α	$\pi/4$	rad

Table 1.1: Typical values for the parameters taken from [8].

the droplet (up for sessile and down for pendant), the horizontal component of the substrate motion would coincide with the direction that the droplet travels. This result shows that the first experiment would always produce a climbing droplet with the absence of gravity.

The typical parameter values used to produce most of the results published in [8] are shown in Table 1.1. This has been included as a set of values that will be used in order to compare the results from the experiment with that of the models outlined in the following sections.

Similar to [8], Noblin, Kofman and Celestini [30] placed a droplet on a horizontal surface and applied horizontal and vertical oscillations of different amplitudes and with a phase difference. They discovered that by changing the amplitudes and phase they could actually tune the droplets to move at a desired speed and direction. They also noted that by setting the phase to equal π they could directly relate this experiment to that by Brunet et al.

1.4 Recent droplet models

The motion described in [8] is the focus of work carried out by Benilov [1] in which he created a model of two-dimensional droplet. By examining the case where the frequency is small enough a model was derived in which the inertia and viscosity of the fluid are negligible compared to its surface tension; this is known as the quasistatic approximation. The main result obtain by Benilov was that the droplet can be made to climb uphill if the acceleration of the plate is a combination of deep, narrow troughs and low, wide peaks. He showed this result analytically for the case where the droplet is thin and numerically for the general case. These results require the acceleration of the substrate to be

asymmetric whereas in [8] it was in fact sinusoidal.

Benilov [2] looked at another model, this time for a three-dimensional, thin droplet, where the strength of the vibration induced inertial force is assumed small in comparison to the droplet's surface tension. Again using the quasistatic approximation he showed that the three-dimensional droplet could climb uphill for a sinusoidal oscillation, now similar to [8]. Benilov produced an asymptotic solution to the velocity of the droplet for small amplitude oscillations. The solution gives a droplet which can either climb up or slide down the substrate and also compares the difference between modelling the droplet in two-dimensions or three-dimensions, but due to the simplicity of the contact line law hysteresis could not be included.

This model has been extended by Benilov and Cummins [4] with the removal of the thin droplet approximation. They showed that again the quasistatic approximation resulted in a droplet that could either slide down or climb up hill in the small amplitude limit. The additional results showed that by increasing the magnitude of the contact angles the droplet would begin to climb uphill at lower amplitudes; however when the magnitude of the contact angles reached a certain size, with respect to the chosen contact line law, the frequencies where the droplet would climb became bounded by a critical value. Although the allowance for order one contact angles gives a more physically realistic model, the lack of contact angle hysteresis still restricts the comparison to [8].

Another model was produced by Benilov and Billingham [3], who used two-dimensional inviscid shallow water equations in order to match qualitatively the main features of [8]. They produced an asymptotic solution for the rise velocity for small amplitude oscillations (again lacking hysteresis) and also a numerical solution which examined larger amplitude oscillations and contained the effects of hysteresis. Since the droplet was assumed to be thin a quantitative comparison between their results and the actual experiment was unobtainable. All the models mentioned above have shown that the leading order motion of the droplet, for small amplitude oscillations, can be separated into two modes; one of which is even with respect to the centre of the droplet and one which is odd. They have all also either noted or shown the importance of hysteresis in this problem.

Walker [35] produced a two-dimensional model of a droplet with moving contact lines that includes both viscosity and inertia. The framework has been

designed to easily incorporate other physical effects (such as electric fields and thermal effects) and can also be extended to a full three-dimensional model (although not quite as easily). The proposed model has used a slip condition close to the contact line to avoid the discontinuity and a linear contact line model, although this can be modified to make it non-linear by altering the dissipation functional. Unfortunately the model has not been compared to any experimental results and so the accuracy cannot be commented upon.

1.5 Overview

Over the course of this thesis we will look at several models for the experiments described in [8] using different approximations. Before explaining each model separately we will first cover the general assumptions that are made throughout the whole of the work. First of all we shall assume in all of these models that the liquid's viscosity is negligible. This is a similar approach to [2][3][4] as opposed to [26] who examined Stokes flow for describing the problem. The advantage of this assumption is that an inviscid fluid does not require the 'no-slip' condition to be applied on the liquid/solid interface and so the discontinuity of the velocity at the contact line is negated.

The next general assumption we will make is how we will define the dynamics of the contact line. There currently is no definitive way in which we should model the velocity at a moving contact line, although many experiments [7][23][28][33] have found a strong correlation between the size of the dynamic contact angle and the velocity of the contact line. Therefore we will use a method similar to [2][3][4][20] in which we will assume that the velocity at the contact line $v = f(\theta)$ where

$$\left.\begin{array}{lll} f < 0 & \text{if} & \theta < \theta_R, \\ f = 0 & \text{if} & \theta_R \geq \theta \geq \theta_A, \\ f > 0 & \text{if} & \theta > \theta_A. \end{array}\right\} \tag{1.4}$$

This is known as the contact line law where θ_A is the advancing angle, θ_R is the receding angle and the difference between them will be known as the hysteresis interval. We will also look at the case where $\theta_A = \theta_R \equiv \theta_0$, i.e. no contact angle hysteresis, and in addition will later add a time dependent term to the left hand side of the law in order for the velocity to not be a single valued func-

tion of the angle. We can now use (1.4) to easily change the contact line law and see what effect this has on our results. These are the two main assumptions that we will use and so now let us outline each of the chapters separately.

Chapter 2: In this chapter we will cover our first model, which will be a three-dimensional, thin droplet where the fluid's inertia and viscosity are negligible meaning that the droplet's shape is determined by balancing surface tension with gravity and vibration-induced inertial force. This is done using the quasistatic approximation, similar to [2], only instead of finding the small amplitude asymptotic solution we will use a boundary integral method and solve the problem numerically. This will allow for large amplitude oscillations as well as the inclusion of hysteresis and altering of the contact line law. The main benefits of this model are that, if we assume that the oscillations are slow enough, the quasistatic approximation agree with some of the experiments in [8] and we are able to use this model to examine how the mechanics change when we introduce contact angle hysteresis. We begin this chapter by outlining the model in section 2.1, as well as the solution method in section 2.2. We then move onto examining the results in section 2.3, starting with a small amplitude comparison between this model and [2] and moving onto larger amplitudes, the inclusion of hysteresis and alternate contact line laws. We end this chapter with an overall discussion of the model in section 2.4.

Chapter 3: This is the largest of the chapters where we will look at a two-dimensional, inviscid droplet. This model is similar to [3] only we are able to vary the magnitude of the contact angles since we have not used the shallow water approximation. The main benefit of this model is the ability to change the magnitude of the contact angles allowing the droplets to be thick, whilst including the physical effects of inertial forces and a variable contact line law. We will derive the governing equations in section 3.1 and then examine the mechanics for small amplitude forcing in section 3.2. This is followed by an explanation of the solution method for larger amplitude forcing in section 3.3. In section 3.4 we will examine the results produced by the solution method, starting with some numerical verifications and examples of limitations of the model. We will then examine how varying the parameters affects the solution for a linear contact line law and move onto non-linear contact line laws, such as the inclusion of hysteresis. The final results we will look at will be for a time

dependent contact line law making some comparisons with [8] and discuss the model in full in section 3.5.

Chapter 4: This chapter contains the final model we will look at which is a three-dimensional, inviscid, thin droplet. This model is again similar to [3] but for a full 3-D problem, i.e. a droplet not a ridge. The main benefit of this model is that it includes the effects of inertia and although the droplet is assumed thin, shallow water models such as these often produce reasonable results. We will derive the governing equations in section 4.1 and then examine the mechanics for small amplitude forcing in section 4.2. This section includes separating the leading order motion into two modes, solving a boundary layer at the contact line and then comparing the small amplitude results to Model 2. We will then examine the high frequency asymptotic limit in section 4.3 and finally end with a discussion of the model in section 4.4.

Chapter 5: We will finalise this work with some conclusions made about each of the models, how they compare to each other and [8] and any further work that can be done to improve on this.

Chapter 2

Model 1: The surface tension dominated, three-dimensional, shallow droplet

In this chapter we will look at a thin, three-dimensional droplet where the fluid's inertia and viscosity are negligible meaning that the droplet's shape is determined by balancing surface tension with the applied forces from gravity and the oscillating plate. The benefits of this model are that the simplifications make it quite easy to solve and are justified for slow frequency oscillations. The simplifications reduce the problem to a linear equation for the height of the droplet, along with mass conservation and the boundary conditions at the contact line.

2.1 The model

2.1.1 Three-dimensional Navier-Stokes equations

Consider a droplet of liquid of density ρ, kinematic viscosity ν and surface tension σ on a plane, solid substrate that is inclined at an angle α to the horizontal and oscillating sinusoidally and vertically. We fix the frame of reference so that the substrate lies in the plane $z = 0$ and the positive $x-$axis is uphill. This means that gravity and the acceleration due to the substrate can be combined to make an effective gravity acting at an angle $\pi/2 - \alpha$ to the $x-$axis, given by $a(t) = g + a_0 \sin \omega t$, where g is the acceleration due to gravity and a_0 and ω are the maximum acceleration and frequency of the

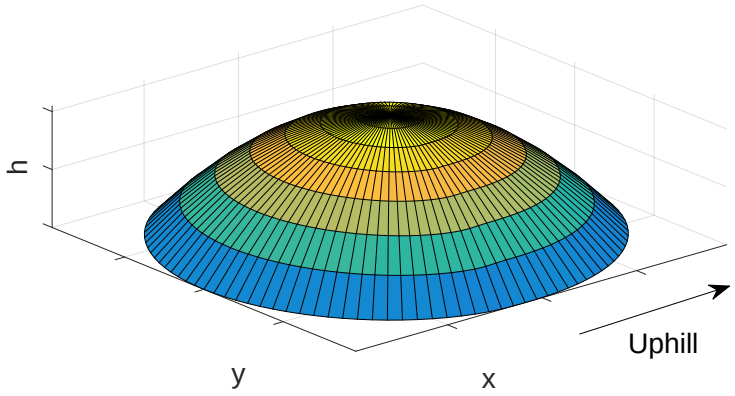


Figure 2.1: A droplet and the coordinate system.

oscillations of the substrate. The domain of solution for this problem is the droplet, $0 \leq z \leq h(x, y, t)$, where h is the height of the free surface above the plane $z = 0$ and x and y lie in the footprint of the droplet, $\mathcal{R}(t)$. The contact line is at $\partial\mathcal{R}(t)$, the boundary of $\mathcal{R}(t)$, as shown in figure 2.1. By writing the body forces per unit volume as the potential of the effective gravity, we can write the Navier-Stokes equations as

$$\rho\frac{d\mathbf{u}}{dt} = -\boldsymbol{\nabla}p + \rho\nu\nabla^2\mathbf{u} - \rho a\boldsymbol{\nabla}(x\sin\alpha + z\cos\alpha), \tag{2.1}$$

$$\boldsymbol{\nabla}\cdot\mathbf{u} = 0. \tag{2.2}$$

The traction boundary condition at the free surface is

$$\bar{\mathbf{n}}\cdot\mathbf{S}\bar{\mathbf{n}} = \sigma\kappa, \quad \bar{\mathbf{t}}\cdot\mathbf{S}\bar{\mathbf{n}} = 0 \quad \text{on } z = h(x, y, t),$$

where $\mathbf{S}$ is the stress tensor, $\bar{\mathbf{n}}$ is the outward unit normal on the surface, $\bar{\mathbf{t}}$ is the unit tangential vectors on the surface, σ is the surface tension and κ is the curvature of the surface. The stress tensor is $\mathbf{S} = -p\mathbf{I} + 2\rho\nu\mathbf{e}$ where $\mathbf{I}$ is the unit tensor and the components of $\mathbf{e}$ are $e_{ij} = \frac{1}{2}\left(\frac{\partial u_i}{\partial x_j} + \frac{\partial u_j}{\partial x_i}\right)$. By expressing the curvature as minus the divergence of the normal, the traction boundary condition perpendicular to the surface becomes

$$p - 2\rho\nu\mathbf{n}\cdot(\mathbf{e}\mathbf{n}) = \sigma\boldsymbol{\nabla}\cdot\mathbf{n}, \qquad \text{on } z = h(x, y, t). \tag{2.3}$$

We also have

$$h(\mathbf{x}, t) = 0, \qquad \text{for } x, y \in \partial\mathcal{R}(t), \tag{2.4}$$

in addition to a no-slip condition where the fluid is in contact with the substrate; however this has no been included since we will be assuming inviscid flow and will therefore neglect this equation. From the continuity equation we known that the conservation of mass is,

$$\rho \int \int_{\mathcal{R}(t)} h(x, y, t) \mathrm{d}x\mathrm{d}y = M, \tag{2.5}$$

where M is the initial mass of the droplet. We will assume that the velocity of the contact line is a function of the contact angle,

$$\mathbf{n} \cdot \frac{d\mathbf{x}}{dt} = v(\theta), \qquad \text{for } x, y \in \partial\mathcal{R}(t), \tag{2.6}$$

where $\mathbf{n}$, the normal along the contact line, points away from the droplet and $v(\theta)$ is the contact line law given by (1.4). In Benilov's small amplitude solutions [2] the forcing from the substrate is small enough to cause only small changes from the equilibrium contact angle, in which case the contact line velocity can be written as a Taylor expansion about θ_0,

$$v(\theta) = V'(\theta - \theta_0) + \frac{1}{2}V''(\theta - \theta_0)^2 + ..., \tag{2.7}$$

where V', V'' are the first and second derivatives of the contact line law at equilibrium.

2.1.2 Dimensionless variables

In order to simplify (2.1)-(2.7) we write the equations in dimensionless form, using scaled variables [2],

$$x = R_0\hat{x}, \quad y = R_0\hat{y}, \quad z = R_0\theta_0\hat{z}, \quad u = U\hat{u}, \quad v = U\hat{v}, \quad w = U\theta_0\hat{w},$$
$$\theta = \theta_0\hat{\theta}, \quad a = a_0\hat{a}, \quad t = T\hat{t}, \quad p = \frac{\sigma\theta_0}{R_0}\hat{p}, \quad \omega = \frac{1}{T}\hat{\omega}.$$

Here R_0 is the typical length scale, $U = R_0/T$ and $T = \sqrt{R_0/g}$. We have scaled the pressure using the capillary pressure scale and also, in order to make it easier compare our solution to Benilov's, we define R_0 such that $2\pi\rho\theta_0 R_0^3 = M$.

We will assume that the droplet is thin, $\theta_0 \ll 1$, and seek the leading order asymptotic solution. Henceforth the variables will be dimensionless, with hats omitted (unless stated otherwise). The dimensionless x momentum equation is

$$\delta_1 \frac{du}{dt} = -\frac{\partial}{\partial x}\left[p + \epsilon a\,(x+\gamma z)\right] + \delta_2\left[\frac{\partial^2 u}{\partial z^2} + O(\theta_0^2)\right], \tag{2.8}$$

where the effective gravity becomes

$$a(t) = \bar{a} + \sin(\omega t), \tag{2.9}$$

with $\bar{a} = g/a_0$, and similarly

$$\delta_1 \frac{dv}{dt} = -\frac{\partial}{\partial y}\left[p + \epsilon a\,(x+\gamma z)\right] + \delta_2\left[\frac{\partial^2 v}{\partial z^2} + O(\theta_0^2)\right]. \tag{2.10}$$

The dimensionless parameters

$$\epsilon = \frac{\rho a_0 R_0^2 \sin\alpha}{\sigma\theta_0}, \qquad \gamma = \frac{\theta_0}{\tan\alpha},$$

characterise the strength of the effective gravitational force relative to surface tension and the ratio of the slope of the droplet's surface to the slope of the substrate. The other dimensionless parameters are

$$\delta_1 = \frac{\rho R_0^2 g}{\sigma\theta_0}, \qquad \delta_2 = \frac{\rho\nu\sqrt{R_0 g}}{\sigma\theta_0^3},$$

which represent the balance between the inertial and viscous forces and the droplet's surface tension respectively. The z component of the momentum equation is

$$\theta_0^2\delta_1 \frac{dw}{dt} = -\frac{\partial}{\partial z}\left[p + \epsilon a(x+\gamma z)\right] + \theta_0^2\delta_2\left[\frac{\partial^2 w}{\partial z^2} + O(\theta_0^2)\right]. \tag{2.11}$$

Similarly, (2.3) becomes

$$p + 2\delta_2\theta_0^2\left[\boldsymbol{\nabla}(h-z)\cdot\frac{\partial \mathbf{u}}{\partial z}\right] = -\tilde{\nabla}^2 h + O(\theta_0)^2, \qquad \text{on } z = h(x,y,t), \tag{2.12}$$

where $\tilde{\nabla}^2 = \frac{\partial^2}{\partial x^2} + \frac{\partial^2}{\partial y^2}$. Our next step is to simplify (2.8)-(2.12) further by taking only the leading order terms when $\delta_1, \delta_2, \theta_0 \ll 1$. In order to evaluate how accurate these assumptions are we will use typical values of each parameter

from [8] (see Table 1.1) in order to estimate the sizes of the dimensionless parameters. In order to make some progress, we have assumed that $\theta_0 \ll 1$ so that we can use the small slope approximation. Although θ_0 is not small in the experiments, we can still expect to draw some sensible conclusions about the mechanisms that are relevant to this problem, and note that shallow water models like ours often produce reasonable results, even when the small slope approximation is not obviously relevant to the real physical problem. Inserting the typical values into the dimensionless parameters gives

$$\delta_1 \approx 0.13, \qquad \delta_2 \approx 0.042,$$

which shows that inertia is more important than viscous forces, and that we can reasonably neglect them both at leading order compared to surface tension and the applied acceleration. The other parameters are typically

$$\epsilon \approx 1.63 \qquad \gamma \approx 1.08, \qquad \omega \approx 3.06, \qquad \bar{a} \approx 0.056,$$

which shows that the small ϵ asymptotic solution is not likely to be a good approximation for the actual experiment. A similar comparison is carried out in section V. of [4] which agrees that the quasistatic approximation will hold for some of the experiments.

2.1.3 Governing equations

Now that we have covered how physically realistic our model is, the next step is to apply the assumptions we are using and obtain the governing equations. By keeping only the leading order terms in (2.8) - (2.11) we are left with

$$p(x, y, z, t) = -\epsilon a(t)(x + \gamma z) - F(t), \tag{2.13}$$

where the gradient operator has been integrated out producing an arbitrary function, $F(t)$. Next we will take the leading order form of (2.12) to give

$$p = -\tilde{\nabla}^2 h, \qquad \text{on } z = h(x, y, t), \tag{2.14}$$

and by combining (2.13) and (2.14) on the free surface, $z = h(x, y, t)$, reduce this three-dimensional problem to a two-dimensional one where the height of the droplet is an unknown variable. The new equation (with $\tilde{}$ above the ∇

omitted) is

$$\left[\nabla^2 - \epsilon\gamma a(t)\right] h(x,y,t) = \epsilon a(t)x + F(t), \tag{2.15}$$

whilst the boundary condition for the height of the droplet along the contact line remains

$$h(x,y,t) = 0 \qquad \text{for } x, y \in \partial\mathcal{R}(t). \tag{2.16}$$

Equation (2.5) becomes

$$\int\int_{\mathcal{R}(t)} h(x,y,t)\mathrm{d}x\mathrm{d}y = 2\pi, \tag{2.17}$$

and (2.6) becomes

$$\mathbf{n}\cdot\frac{\partial \mathbf{X}}{\partial t} = \theta - 1 + \frac{1}{2}v''(\theta-1)^2 + O(\theta-1)^3, \tag{2.18}$$

where $U = V'\theta, v'' = V''\theta_0^2/U$ and $\mathbf{X} = (x,y) \in \partial\mathcal{R}(t)$. Since we are dealing with small contact angles we know that

$$\theta = -\frac{\partial h}{\partial n}, \qquad \text{for } x, y \in \partial\mathcal{R}(t).$$

We will alter (2.18) in later sections to look at different contact line laws, including hysteresis. Note that $a(t)$ changes sign as a function of time, so that (2.15) can be the inhomogeneous Helmholtz equation, inhomogeneous, modified Helmholtz equation or Poisson's equation.

2.2 Solution method

2.2.1 Redefined droplet height

In order to solve (2.15)-(2.18) we will first redefine the height in order to absorb the right hand side of (2.15) leaving the remaining equation homogeneous. The redefined height, $H(\mathbf{x},t)$ [where $\mathbf{x} = (x,y)$], is defined to be

$$H(\mathbf{x},t) = h(\mathbf{x},t) + \begin{cases} -\epsilon a x^3/6 - Fx^2/2, & \gamma a = 0, \\ x/\gamma + F/\epsilon\gamma a, & \gamma a \neq 0, \end{cases} \tag{2.19}$$

where the two options exist since γ can equal zero for the theoretical case of a vertical substrate and a will often become zero as the substrate oscillates. At

no point can ϵ equal zero without γ or a technically becoming infinite, keeping $\epsilon\gamma a$ bounded. Inserting (2.19) onto (2.15) gives

$$\left(\nabla^2 - \epsilon\gamma a\right) H(\mathbf{x}, t) = 0. \tag{2.20}$$

Now that we have a new governing equation we will describe the solution method that we will use [31]. If we define a Green's function $G(\mathbf{x}; \mathbf{x_0})$ such that

$$\left(\nabla^2 - \epsilon\gamma a\right) G(\mathbf{x}; \mathbf{x_0}) = -\delta(\mathbf{x} - \mathbf{x_0}),$$

for all values of $\epsilon\gamma a$, where $\delta(\mathbf{x} - \mathbf{x_0})$ is the two-dimensional delta function, we can combine this equation with (2.20) to give

$$\int_{\mathcal{R}} \left[G(\mathbf{x}; \mathbf{x_0})\nabla^2 H(\mathbf{x}, t) - H(\mathbf{x}, t)\nabla^2 G(\mathbf{x}; \mathbf{x_0})\right] \mathrm{d}A = \int_{\mathcal{R}} H(\mathbf{x}, t)\delta(\mathbf{x} - \mathbf{x_0})\mathrm{d}A.$$

Now by using the divergence theorem on the left hand side of the equation, along with the integral properties of the delta function on the right hand side, we get

$$\left(\frac{1}{2}\right) H(\mathbf{x_0}, t) = \int_{\partial\mathcal{R}} G(\mathbf{x}; \mathbf{x_0}) \frac{\partial H}{\partial n}(\mathbf{x}, t)\mathrm{d}l - \int_{\partial\mathcal{R}}^{(PV)} \frac{\partial G}{\partial n}(\mathbf{x}; \mathbf{x_0}) H(\mathbf{x}, t)\mathrm{d}l, \tag{2.21}$$

where the principal value of the second integral has to be taken and the factor of $1/2$ in front of $H(\mathbf{x_0}, t)$ has to be included when $\mathbf{x_0} \in \partial\mathcal{R}$. This is the boundary integral equation [31] and it is ideal for solving our problem as it requires us just to solve on the contact line instead of the entire droplet. The Green's function $G(\mathbf{x}, \mathbf{x_0})$ for this problem is

$$G(\mathbf{x}; \mathbf{x_0}) = \begin{cases} -Y_0\left(k|\mathbf{x} - \mathbf{x_0}|\right)/4, & \gamma a < 0, \\ -\ln|\mathbf{x} - \mathbf{x_0}|/2\pi, & \gamma a = 0, \\ K_0\left(k|\mathbf{x} - \mathbf{x_0}|\right)/2\pi, & \gamma a > 0, \end{cases} \tag{2.22}$$

where Y_0 and K_0 are the regular and modified Bessel functions of the second kind respectively and $k^2 = |\epsilon\gamma a|$. Now inserting the redefined height into (2.16) gives

$$H(\mathbf{x}, t) = \begin{cases} -\epsilon a x^3/6 - F x^2/2, & \gamma a = 0, \\ x/\gamma + F/\epsilon\gamma a, & \gamma a \neq 0, \end{cases} \qquad \text{for } \mathbf{x} \in \partial\mathcal{R}(t), \tag{2.23}$$

whilst (2.17) becomes

$$\begin{aligned}\int\int_{\mathcal{R}(t)} H(\mathbf{x},t)\mathrm{d}A &= 2\pi - \int\int_{\mathcal{R}(t)} \left(\frac{1}{6}\epsilon a x^3 + \frac{1}{2}F(t)x^2\right)\mathrm{d}A, \\ &= 2\pi - \int_{\partial\mathcal{R}(t)} n_x \left(\frac{1}{24}\epsilon a x^4 + \frac{1}{6}F(t)x^3\right)\mathrm{d}l,\end{aligned} \tag{2.24}$$

for $\gamma a = 0$ and similarly

$$\int\int_{\mathcal{R}(t)} H(\mathbf{x},t)\mathrm{d}A = 2\pi + \int_{\partial\mathcal{R}(t)} n_x \left(\frac{1}{2\gamma}x^2 + \frac{1}{\epsilon\gamma a}F(t)x\right)\mathrm{d}l, \tag{2.25}$$

for $\gamma a \neq 0$, where n_x is the $x-$component of the outward normal to $\partial\mathcal{R}$. The contact angle is now given by

$$\theta = -\frac{\partial H}{\partial n} + \begin{cases} -n_x\left(\epsilon a x^2/2 - Fx\right), & \gamma a = 0, \\ n_x/\gamma, & \gamma a \neq 0, \end{cases} \qquad \text{for } \mathbf{x} \in \partial\mathcal{R}(t), \tag{2.26}$$

and we can now use (2.21) - (2.26), along with (2.18), to set up our numerical solution method (which will be implemented using Matlab).

2.2.2 Discretisation

We begin by discretising the boundary into N nodes that are connected using straight lines. These are the simplest elements to use since it only requires knowledge of the nodes to define the domain. The set of parameterised, one-dimensional elements can be written as

$$\mathbf{x}^{(i)}(\xi) = \bar{\mathbf{x}}_\mathbf{i} + \mathbf{\Delta x_i}\xi, \qquad -1 \leq \xi \leq 1,$$

where $i = 1, ..., N$, $\bar{x}_i = (x_{i+1} + x_i)/2$, $\Delta x_i = (x_{i+1} - x_i)/2$ (with similar for y) and $\mathbf{x}_{N+1} = \mathbf{x}_1$ since the boundary is closed. This means that the differential arc length for each element is given by

$$\mathrm{d}l^{(i)} = \sqrt{\mathrm{d}x^2 + \mathrm{d}y^2}^{(i)} = |\mathbf{\Delta x_i}|\mathrm{d}\xi.$$

The simplest approximation that we can use to solve the boundary integral equation is using uniform elements, i.e. the functions $H(\mathbf{x},t)$ and $\mathbf{n}\cdot\boldsymbol{\nabla}H(\mathbf{x},t)$ are constant over each boundary element and so can be replaced by f_i and q_i respectively. Applying this to (2.21), and assuming that x_0 lies on the

boundary, gives

$$\frac{1}{2}H(\mathbf{x_0}) = \sum_{i=1}^{N} \alpha_i(\mathbf{x_0})q_i - \sum_{i=1}^{N} \beta_i(\mathbf{x_0})f_i. \tag{2.27}$$

at each time step, where

$$\alpha_i(\mathbf{x_0}) \equiv \int_{E_i} G(\mathbf{x};\mathbf{x_0})\mathrm{d}l, \qquad \beta_i(\mathbf{x_0}) \equiv \int_{E_i} \mathbf{n}\cdot\boldsymbol{\nabla}G(\mathbf{x};\mathbf{x_0})\mathrm{d}l,$$

are known as the influence coefficients. Now if we knew f_i and q_i, we could use this equation to find the height at all points within the droplet (with the factor of 1/2 removed), however what we will use this equation for is to find q_i on each element with our prior knowledge of f_i. Since we are looking for $\mathbf{x_0}$ on the boundary we will evaluate it at the midpoint of each element giving

$$\mathbf{x_0}^{(j)} = \bar{\mathbf{x}}_\mathbf{j}, \qquad j = 1, ..., N.$$

We will use this in order to write (2.27) as

$$A_{ji}q_i = B_{ji}f_i, \tag{2.28}$$

for

$$A_{ji} = |\boldsymbol{\Delta}\mathbf{x_i}| \int_{-1}^{1} G(\mathbf{x}^{(i)};\bar{\mathbf{x}}_\mathbf{j})\mathrm{d}\xi, \quad B_{ji} = \frac{1}{2}\delta_{ji} + |\boldsymbol{\Delta}\mathbf{x_i}| \int_{-1}^{1} \mathbf{n}^{(i)}\cdot\boldsymbol{\nabla}G(\mathbf{x}^{(i)};\bar{\mathbf{x}}_\mathbf{j})\mathrm{d}\xi, \tag{2.29}$$

where δ_{ji} is the Kronecker delta.

2.2.3 Influence coefficients

Our next step is to evaluate the influence coefficients for the two situations i does or does not equal j. Since we already know that $G(\mathbf{x}, \mathbf{x_0})$ takes the form of either a logarithm or a regular or modified Bessel function of the second kind, we know that the integrals in (2.29) will not always have an analytical solution and therefore when $i \neq j$ we will solve these integrals using the Gauss-Legendre quadrature. Using this the integral of a non singular function $f(\xi)$ over the interval [-1,1] is approximated with a weighted sum of the values of

ξ_k	w_k
0	0.569
$\pm$0.538	0.479
$\pm$0.906	0.237

Table 2.1: Roots of the Legendre polynomial $P_5(\xi)$ with corresponding weights used to solve the Gauss-Legendre quadrature (to 3 significant figures).

the integrand at selected locations, in the form

$$\int_{-1}^{1} f(\xi)\mathrm{d}\xi \approx \sum_{k=1}^{Q} f(\xi_k)w_k, \tag{2.30}$$

where Q is a specified number of quadrature base points, ξ_k is the kth root of the Legendre polynomial $P_Q(\xi)$, taking values in the interval [-1,1], and w_k is a weight function given by

$$w_k = \frac{2(1-\xi_k)^2}{(Q+1)^2[P_{Q+1}(\xi_k)]^2}, \qquad \sum_{k=1}^{Q} w_k = 2.$$

We find that 5 quadrature points provides enough accuracy. The roots and corresponding weights for 5 quadrature points are given in Table 2.1. Now if we return to (2.29) we know that

$$A_{ji} = |\mathbf{\Delta x_i}| \sum_{k=1}^{5} G(\mathbf{\bar{x}_i} + \mathbf{\Delta x_i}\xi_k; \mathbf{\bar{x}_j})w_k, \qquad i \neq j, \tag{2.31}$$

$$B_{ji} = \frac{1}{2}\delta_{ji} + \sum_{k=1}^{5} \left(\Delta y_i \frac{\partial G}{\partial x} - \Delta x_i \frac{\partial G}{\partial y} \right) w_k, \qquad i \neq j, \tag{2.32}$$

since $\mathbf{n}^{(i)} = (\Delta y_i, -\Delta x_i)/|\mathbf{\Delta x_i}|$. The derivatives of the Green's functions, (2.22), with respect to x and y are

$$\frac{\partial G}{\partial x_p} = \begin{cases} k(x_p - x_{0p})Y_1\left(k|\mathbf{x}-\mathbf{x_0}|\right)/4|\mathbf{x}-\mathbf{x_0}|, & \gamma a < 0, \\ -(x_p - x_{0p})/2\pi|\mathbf{x}-\mathbf{x_0}|^2, & \gamma a = 0, \\ -k(x_p - x_{0p})K_1\left(k|\mathbf{x}-\mathbf{x_0}|\right)/2\pi|\mathbf{x}-\mathbf{x_0}|, & \gamma a > 0, \end{cases} \qquad p = 1, 2. \tag{2.33}$$

As well as solving each element numerically for $i \neq j$ we also need to use the analytical solution for when $i = j$; since each of our Green's functions (and their derivatives) are singular at $\mathbf{x} = \mathbf{x_0}$. By referring back to (2.27) we will

begin by evaluating the second of these two integrals as it is a lot simpler. Using (2.33) we know that the second integral for each Green's function takes the form

$$|\mathbf{\Delta x_i}| \int_{-1}^{1} \mathbf{n}^{(i)} \cdot (\mathbf{x}^{(i)} - \mathbf{x_0}) f(|\mathbf{x}^{(i)} - \mathbf{x_0}|) \mathrm{d}\xi,$$

so when $\mathbf{x_0}$ lies on element i we know that $\mathbf{n}$ is perpendicular to $\mathbf{x} - \mathbf{x}_0$ giving

$$B_{ii} = \frac{1}{2}. \tag{2.34}$$

Now for the first integral we will need to approximate our Bessel functions for when $|\mathbf{x} - \mathbf{x_0}| \ll 1$ giving

$$G(\mathbf{x}; \mathbf{x_0}) \approx -\frac{1}{2\pi} \ln |\mathbf{x} - \mathbf{x_0}| - \frac{1}{2\pi} \begin{cases} \ln(k/2) + \gamma_E, & \gamma a \neq 0, \\ 0, & \gamma a = 0, \end{cases} \tag{2.35}$$

where γ_E is Euler's constant (not to be confused with γ the ratio of the slope of the droplet's surface to the slope of the substrate). Now if we insert this approximation of the Green's functions into the first integral in (2.27) we get

$$A_{ii} = \frac{|\mathbf{\Delta x_i}|}{\pi} (1 - \ln |\mathbf{\Delta x_i}|) - \frac{|\mathbf{\Delta x_i}|}{\pi} \begin{cases} \ln(k/2) + \gamma_E, & \gamma a \neq 0, \\ 0, & \gamma a = 0. \end{cases} \tag{2.36}$$

We have now evaluated both of the influence coefficients and from (2.23) we know that $H(\mathbf{x}, t)$ on each element of the boundary takes the form $f_i = \hat{g}_i + F(t)\tilde{g}_i$, we can rewrite (2.28) as

$$A_{ji} q_i - B_{ji} \tilde{g}_i F(t) = B_{ji} \hat{g}_i. \tag{2.37}$$

2.2.4 Mass conservation

Although we have a linear system of equations that we can solve for q_i given f_i we still have an unknown we need to find, $F(t)$. In order to do this we need to evaluate the integral constraint given by (2.24) and (2.25), i.e. solve an equation of the form

$$\begin{aligned} \int \int_{\mathcal{R}(t)} H(\mathbf{x}, t) \mathrm{d}x \mathrm{d}y &= 2\pi + \int_{\partial \mathcal{R}(t)} n_x r(x) \mathrm{d}l \\ + F(t) \int_{\partial \mathcal{R}(t)} n_x s(x) \mathrm{d}l &= 2\pi + \hat{r} + F(t)\hat{s}, \end{aligned} \tag{2.38}$$

	c_r	n_r	c_s	n_s
$\gamma a = 0$	$-\frac{\epsilon a}{24}$	4	$-\frac{1}{6}$	3
$\gamma a \neq 0$	$\frac{1}{2\gamma}$	2	$\frac{1}{\epsilon\gamma a}$	1

Table 2.2: The known constants for $\hat{r}$ and $\hat{s}$.

where $H(\mathbf{x}, t)$ is given by (2.21) and $r(x), s(x)$ are known functions. The right hand side of (2.38) is the easiest of the two and so we will solve this first. Again from (2.24) and (2.25) we know that both $r(x)$ and $s(x)$ are of the form

$$r(x), s(x) = c_{(r,s)} x^{n_{(r,s)}},$$

where c and n are both constants, and so by discretising the boundary (with subscripts omitted) we get

$$\begin{aligned} \hat{r}, \hat{s} &= c \sum_{i=1}^{N} \Delta y_i \int_{-1}^{1} (\bar{x}_i + \Delta x_i \xi)^n \, \mathrm{d}\xi, \\ &= \frac{c}{n+1} \sum_{i=1}^{N} \frac{\Delta y_i}{\Delta x_i} \left[(\bar{x}_i + \Delta x_i)^{n+1} - (\bar{x}_i - \Delta x_i)^{n+1} \right], \end{aligned}$$

with constants given in Table 2.2. Next we will take the left hand side of (2.38) and insert (2.21) to give

$$\begin{aligned} \int\int_{\mathcal{R}(t)} H(\mathbf{x_0}, t) \mathrm{d}A(\mathbf{x_0}) = \int_{\partial\mathcal{R}(t)} \Bigg[\mathbf{n}(\mathbf{x}) \cdot \boldsymbol{\nabla} H(\mathbf{x}, t) \int\int_{\mathcal{R}(t)} G(\mathbf{x_0}; \mathbf{x}) \mathrm{d}A(\mathbf{x_0}) \\ - H(\mathbf{x}, t) \mathbf{n}(\mathbf{x}) \cdot \int\int_{\mathcal{R}(t)} \boldsymbol{\nabla} G(\mathbf{x_0}; \mathbf{x}) \mathrm{d}A(\mathbf{x_0}) \Bigg] \mathrm{d}l(\mathbf{x}). \end{aligned} \tag{2.39}$$

In order to make the next steps easier to follow we have written if each term in (2.39) is a function of either $\mathbf{x}$ or $\mathbf{x_0}$ (or both), and also swapped these around in the Green's function without changing the problem. In order to solve this triple integral we will alter it until it is a double integral around the boundary and use the same discretisation as before to solve. The integral involving $\boldsymbol{\nabla} G$ is the easiest of the two to simplify, by using the divergence theorem we get

$$\begin{aligned} \int\int_{\mathcal{R}(t)} \boldsymbol{\nabla} G(\mathbf{x_0}; \mathbf{x}) \mathrm{d}A(\mathbf{x_0}) &= - \int\int_{\mathcal{R}(t)} \boldsymbol{\nabla}_0 G(\mathbf{x_0}; \mathbf{x}) \mathrm{d}A(\mathbf{x_0}) \\ &\equiv - \int_{\partial\mathcal{R}(t)} \mathbf{n}(\mathbf{x_0}) G(\mathbf{x_0}; \mathbf{x}) \mathrm{d}l(\mathbf{x_0}), \end{aligned} \tag{2.40}$$

where $\boldsymbol{\nabla}_0$ is the gradient operator with respect to $\mathbf{x_0}$. In order to simplify the integral of G over the domain, we will first define a new function $\hat{G}(\mathbf{x_0};\mathbf{x})$ such that

$$G(\mathbf{x_0};\mathbf{x}) = \boldsymbol{\nabla}_0 \cdot \left[(\mathbf{x_0}-\mathbf{x})\hat{G}(\mathbf{x_0};\mathbf{x})\right]. \tag{2.41}$$

By returning to (2.22) we know that all our Green's functions have the form $G(\mathbf{x_0};\mathbf{x}) = f(|\mathbf{x_0}-\mathbf{x}|)$, and so by letting $\mathbf{r} = \mathbf{x_0}-\mathbf{x}$ we can rewrite (2.41) as

$$f(r) = \boldsymbol{\nabla}\cdot\left(\mathbf{r}\hat{f}(r)\right) = \frac{1}{r}\frac{\partial}{\partial r}\left[r^2\hat{f}(r)\right].$$

Now by rearranging this we get

$$\hat{f}(r) = \int_0^r \frac{s}{r^2} f(s)\mathrm{d}s,$$

which we can solve, and rewrite in its original form, to give our new function as

$$\hat{G}(\mathbf{x_0};\mathbf{x}) = -\frac{1}{2\pi}\begin{cases} \pi Y_1(\hat{k})/2\hat{k} + 1/\hat{k}^2, & \epsilon\gamma a < 0, \\ \ln|\mathbf{x_0}-\mathbf{x}|/2 - 1/4, & \epsilon\gamma a = 0, \\ K_1(\hat{k})/\hat{k} - 1/\hat{k}^2, & \epsilon\gamma a > 0, \end{cases} \tag{2.42}$$

where $\hat{k} = k|\mathbf{x_0}-\mathbf{x}|$. We can now use this to simplify the other integral in (2.39) giving

$$\begin{aligned}\int\int_{\mathcal{R}(t)} G(\mathbf{x_0};\mathbf{x})\mathrm{d}A(\mathbf{x_0}) &= \int\int_{\mathcal{R}(t)} \boldsymbol{\nabla}_0\cdot\left[(\mathbf{x_0}-\mathbf{x})\hat{G}(\mathbf{x_0};\mathbf{x})\right]\mathrm{d}A(\mathbf{x_0}), \\ &= \int_{\partial\mathcal{R}(t)} \mathbf{n}(\mathbf{x_0})\cdot(\mathbf{x_0}-\mathbf{x})\hat{G}(\mathbf{x_0};\mathbf{x})\mathrm{d}l(\mathbf{x_0}).\end{aligned} \tag{2.43}$$

Inserting both (2.40) and (2.43) into (2.39) gives

$$\begin{aligned}\int\int_{\mathcal{R}(t)} H(\mathbf{x_0},t)\mathrm{d}A(\mathbf{x_0}) = \int_{\partial\mathcal{R}(t)}\int_{\partial\mathcal{R}(t)} &[H(\mathbf{x},t)\mathbf{n}(\mathbf{x})\cdot\mathbf{n}(\mathbf{x_0})G(\mathbf{x_0};\mathbf{x}) \\ &+\mathbf{n}(\mathbf{x})\cdot\boldsymbol{\nabla}H(\mathbf{x},t)\mathbf{n}(\mathbf{x_0})\cdot(\mathbf{x_0}-\mathbf{x})\hat{G}(\mathbf{x_0};\mathbf{x})\Big]\mathrm{d}l(\mathbf{x})\mathrm{d}l(\mathbf{x_0}),\end{aligned} \tag{2.44}$$

which is now in a form that we can discretise as before. If we again discretise the boundary into straight elements and assume that the redefined height, and its derivative, are constant on each element we get

$$\int\int_{\mathcal{R}} H(\mathbf{x}_0)\mathrm{d}A(\mathbf{x}_0) = \sum_{i=1}^{N}\left(a_i q_i + b_i f_i\right), \tag{2.45}$$

at each time step, where

$$a_i = \sum_{j=1}^{N} \int_{E_i} \int_{E_j} \mathbf{n}(\hat{\mathbf{x}}) \cdot (\hat{\mathbf{x}} - \mathbf{x}) \hat{G}(\hat{\mathbf{x}}; \mathbf{x}) \mathrm{d}l(\hat{\mathbf{x}}) \mathrm{d}l(\mathbf{x}),$$

$$b_i = \sum_{j=1}^{N} \mathbf{n}(\mathbf{x}) \cdot \mathbf{n}(\hat{\mathbf{x}}) \int_{E_i} \int_{E_j} G(\hat{\mathbf{x}}; \mathbf{x}) \mathrm{d}l(\hat{\mathbf{x}}) \mathrm{d}(\mathbf{x}).$$

Similar to before we will now evaluate these integrals using the Gauss-Legendre quadrature when $i \neq j$ and analytically when $i = j$. Starting with the first integral we get

$$\begin{aligned} a_i = \sum_{j \neq i} |\boldsymbol{\Delta}\mathbf{x_i}| \sum_{k,l=1}^{5} \left[\Delta y_j \left(\bar{x}_j - \bar{x}_i - \Delta x_i \xi_k\right) - \Delta x_j \left(\bar{y}_j - \bar{y}_i - \Delta y_i \xi_k\right)\right] \\ \times \hat{G}(\bar{\mathbf{x}}_\mathbf{j} + \boldsymbol{\Delta}\mathbf{x_j}\xi_l; \bar{\mathbf{x}}_\mathbf{i} + \boldsymbol{\Delta}\mathbf{x_i}\xi_k) w_k w_l, \end{aligned} \tag{2.46}$$

where the analytical solution to the integral for $i = j$ is 0. The second integral is given by

$$\begin{aligned} b_i = \sum_{j \neq i} \left[\boldsymbol{\Delta}\mathbf{x_j} \cdot \boldsymbol{\Delta}\mathbf{x_i} \sum_{k,l=1}^{5} G(\bar{\mathbf{x}}_\mathbf{j} + \boldsymbol{\Delta}\mathbf{x_j}\xi_l; \bar{\mathbf{x}}_\mathbf{i} + \boldsymbol{\Delta}\mathbf{x_i}\xi_k) w_k w_l \right] \\ + \int_{E_i} \int_{E_i} G(\hat{\mathbf{x}}; \mathbf{x}) \mathrm{d}l(\hat{\mathbf{x}}) \mathrm{d}l(\mathbf{x}), \end{aligned} \tag{2.47}$$

where the analytical solution to the integral for $j = i$ can be evaluated fully when $\gamma a = 0$, or by using the asymptotic approximation for the Green's function otherwise. The solution to the remaining integral in (2.47) is

$$\begin{aligned} \int_{E_i} \int_{E_i} G(\hat{\mathbf{x}}; \mathbf{x}) \mathrm{d}l(\hat{\mathbf{x}}) \mathrm{d}l(\mathbf{x}) = \frac{2|\boldsymbol{\Delta}\mathbf{x_i}|^2}{\pi} \left[\ln(4|\boldsymbol{\Delta}\mathbf{x_i}|) - \frac{3}{2} \right] \\ - \frac{2|\boldsymbol{\Delta}\mathbf{x_i}|^2}{\pi} \begin{cases} \ln(k/2) + \gamma_E & \gamma a \neq 0, \\ 0 & \gamma a = 0. \end{cases} \end{aligned} \tag{2.48}$$

Now we have shown the numerical method for the integral constraint we will combine (2.38) with (2.45), and again let $f_i = \hat{g}_i + F(t)\tilde{g}_i$, to get

$$a_i q_i + (b_i \tilde{g}_i - \hat{s})\, F(t) = 2\pi + \hat{r} - b_i \hat{g}_i, \tag{2.49}$$

which we can now combine with (2.37) to give

$$\left(\begin{array}{c|c} A & -B\mathbf{h} \\ \hline \mathbf{a} & \mathbf{b}^T\tilde{\mathbf{g}} - \hat{s} \end{array}\right)\left(\begin{array}{c} \mathbf{q} \\ \hline F \end{array}\right) = \left(\begin{array}{c} B\hat{\mathbf{g}} \\ \hline 2\pi + \hat{r} - \mathbf{b}^T\hat{\mathbf{g}} \end{array}\right),$$

and finally we can solve to approximate $\partial H/\partial n$ on each element. With q_i we can find the contact angle on each element, by discretising (2.26), using

$$\theta_i = -q_i + \begin{cases} -\Delta y_i \left(\epsilon a \bar{x}_i^2/2 - F\bar{x}_i\right)/|\mathbf{\Delta x_i}|, & \gamma a = 0, \\ \Delta y_i/\gamma|\mathbf{\Delta x_i}|, & \gamma a \neq 0, \end{cases} \qquad i = 1, .., 2N, \tag{2.50}$$

which we will use to evolve the boundary.

2.2.5 Evolution of the boundary

The discretised boundary integral equation, along with the volume conservation equation provide enough information to solve for $\partial H/\partial n$ and $F(t)$ on the boundary. These can now be used to obtain the contact angle between the droplet and the plate at each of the grid points providing enough information to solve the equation

$$\frac{d\mathbf{X}_i}{dt} = V(\theta_i)\mathbf{n}_i + T_i\mathbf{s}_i. \tag{2.51}$$

This is a modified version of equation (2.18) in which the movement of the nodes which define the contact line have been decomposed into a movement in the normal and tangential direction. The normal component of the contact line's velocity is given by (2.18), and the contact angle, whilst the tangential component is

$$T_i = N^2\left[\sqrt{(x_{i+1} - x_i)^2 + (y_{i+1} - y_i)^2} - \sqrt{(x_i - x_{i-1})^2 + (y_i - y_{i-1})^2}\right]. \tag{2.52}$$

This function [5] is designed to keep the grid spacing ratios constant so that the nodes along the boundary remain evenly spaced as the droplet evolves. Now in order to evaluate (2.51) at each time time step we will use Crank-Nicolson time stepping [10] and we will solve using the Newton method. The reason we require the use of implicit time stepping is that if we use explicit time stepping the velocity of the contact line, as specified by the contact line law, will not

be the same as the velocity determined from solving the boundary integral equation equation meaning we could not conserve mass.

2.2.6 The Newton method

The Newton method (or Newton-Raphson method) is a very accurate way of solving systems of equations of the form

$$\frac{x_i - x_i^{t-\Delta t}}{\Delta t} = f_i(x_1, ..., x_N, x_1^{t-\Delta t}, ..., x_N^{t-\Delta t}), \quad \text{for } i = 1, ..., N, \tag{2.53}$$

where x_i are unknown and $x_i^{t-\Delta t}$ are known. This is an iterative method that works by taking a calculated guess to the exact solution to x_i and solving the equation

$$0 = r_i(x_1, ..., x_N) + \sum_{j=1}^{N} J_{ij}(x_1, ..., x_N)\Delta x_j, \quad \text{for } i = 1, ..., N, \tag{2.54}$$

where r_i is the residual of (2.53) for the guessed solution, Δx_j are the first order errors in the guess and J_{ij} is a numerical approximation of the Jacobian, given by

$$J_{ij} = \frac{r_i(x_1, ..., x_j + \delta, ..., x_N) - r_i(x_1, ..., x_j, ..., x_N)}{\delta},$$

for some prescribed δ. Once (2.54) has been solved the new 'guess' is given by $x_i^{new} = x_i + \Delta x_i$ and then the method is repeated. Assuming that the initial guess is close enough to the exact solution to avoid any local minimums, the Newton method will very efficiently close in on a solution for x_i that gives $\max |r_i(x_1, ..., x_N)| \leq Er$. As this is a numerical method we will not get the exact solution (unless f_i is a linear function of x_i) and so instead will find a solution accurate to $O(Er)$. As long as the time steps are small enough a good initial guess is the solution to the previous time step.

2.3 Results

2.3.1 Validation of the solution method

Now we have described our solution method, we shall compare it to some analytical solutions tp check its accuracy. We will begin by solving (2.20) along with the boundary conditions (2.23)-(2.26) for the special case where

the boundary is a fixed circle of radius R. We can solve this analytically for all values of $\epsilon\gamma a$ and so this will be an appropriate test for our boundary integral method. After this we will test the convergence rates for the grid spacing and time step sizes to ensure they are converging at the correct rate. Our final comparison will be between our full time dependant solution and the small amplitude asymptotic results [2] for the special case where $\epsilon \ll 1$. Once we have made comparisons in order to verify our method we will look at the results for larger amplitude oscillations, the inclusion of hysteresis and different contact line laws.

An example using a fixed boundary

We already know that in (2.20) a is the oscillatory term but for our first fixed boundary example we will set $\gamma = 0$. This allows us to keep a more general solution since setting $a = 0$ loses one of the terms in (2.23). For the other two examples we will set $\gamma > 0$ and then look at the solutions to the two different sign choices for a. The solution to (2.20), along with (2.23)-(2.24), in polar coordinates for the case where $\gamma = 0$ is

$$H(r,\phi) = \frac{4}{R^4}\left(R^2 - r^2 + 2r^2\cos^2\phi\right) - \frac{1}{8}\epsilon a r\cos\phi\left(R^2 - r^2 + \frac{4}{3}r^2\cos^2\phi\right). \tag{2.55}$$

Since the normal of the boundary is always pointing out radially for a disk, we can differentiate the redefined height with respect to r and insert this into (2.26) to give the contact angle as

$$\theta(\phi) = \frac{8}{R^3} - \frac{1}{4}\epsilon a R^2\cos\phi, \qquad \gamma = 0. \tag{2.56}$$

In order for our dimensionless contact angle to equal 1 when there are no external forces applied we will need to set $R = 2$, which is again due to the scale that we have used to non-dimensionalise the mass of the droplet. A similar method can be used when $\gamma a < 0$ to give the results

$$H(r,\phi) = \frac{2J_0(kr)}{R^2 J_2(kR)} + \frac{RJ_1(kr)}{\gamma J_1(kR)}\cos\phi, \tag{2.57}$$

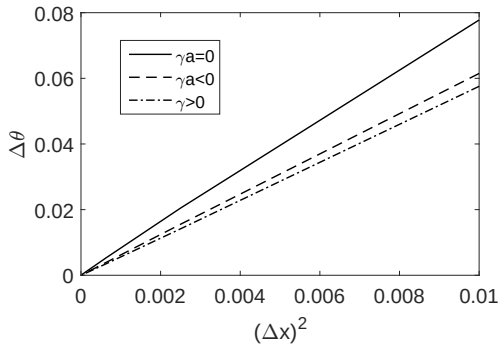


Figure 2.2: The difference between the numerical solution and the analytical solution for the contact angle in a fixed circular domain with $\epsilon = 1, \gamma a$ greater than, less than or equal to 0 and a linear contact line law with no hysteresis.

where J_n is the Bessel function of the first kind and (as a reminder) $k^2 = |\epsilon\gamma a|$. Using (2.26) gives the contact angle as

$$\theta(\phi) = \frac{2kJ_1(kR)}{R^2 J_2(kR)} + \frac{1}{\gamma}\left[1 - kR\frac{J_0(kR) - J_2(kR)}{2J_1(kR)}\right]\cos\phi, \qquad \gamma a < 0. \tag{2.58}$$

The solution for the final case, where $\gamma a > 0$, is

$$H(r,\phi) = -\frac{2I_0(kr)}{R^2 I_2(kR)} + \frac{RI_1(kr)}{\gamma I_1(kR)}\cos\phi, \tag{2.59}$$

where I_n is the modified Bessel function of the first kind. This gives the contact angle as

$$\theta(\phi) = \frac{2kI_1(kR)}{R^2 I_2(kR)} + \frac{1}{\gamma}\left[1 - kR\frac{I_0(kR) + I_2(kR)}{2I_1(kR)}\right]\cos\phi, \qquad \gamma a > 0. \tag{2.60}$$

If we examine the dimensionless contact angle for both (2.58) and (2.60) in the limit of $k \to 0$ we retrieve (2.56), meaning R still needs to equal 2.

Convergence tests

Now that we have an analytical result for the contact angle, for the simplified case of a fixed circular boundary, we can now compare them to the numerical result with the difference between the two contact angles shown in figure 2.2. We can see from this graph that not only is the size of the error small but it is also converging at the correct rate [$\Delta\theta \propto (\Delta x)^2$].

In addition to verifying the accuracy of the boundary integral formulations

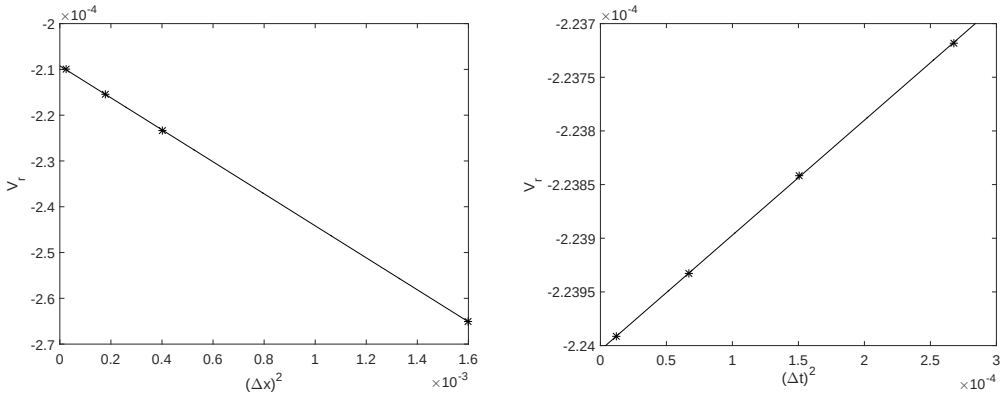


Figure 2.3: The convergence rate of the rise velocity for both space (left) and time (right) for $\epsilon = 0.01, \gamma = 25, \omega = 4, \bar{a} = 1/25, v'' = 0$ and no hysteresis.

for a time independent case, we will look at the rate in which our full solution converges with respect to its grid and time spacings. The discretisation we have used for the boundary, as well as using Crank-Nicolson time steps, means that the accuracy of the solution should converge quadratically in both space and time. In order to show this we have made a plot of the rise velocity against the grid spacing squared as well as the time steps squared (see figure 2.3). Both of these graphs are linear meaning that they are converging at the correct rate.

Comparison with small amplitude asymptotic solution

We will begin by comparing our numerical solution of (2.15)-(2.18) to Benilov's asymptotic solution for $\epsilon \ll 1$, [2]. The main result that Benilov obtained was the rise velocity of the droplet,

$$V_r^{(B)} = \epsilon^2 \left[\frac{\gamma[3 + 4\omega^2(1 - v'')]}{12(9 + 4\omega^2)} - \frac{\bar{a}}{\epsilon} \right] + o(\epsilon^2). \tag{2.61}$$

We can deduce from this that $V_r^{(B)}$ is monotone increasing with ω for $v'' < 2/3$, monotone decreasing for $v'' > 2/3$ and independent of ω for $v'' = 2/3$. Although Benilov included the quadratic term in the Taylor expansion of the contact line law in [2], for larger values of ϵ, for which the range of contact angles that are driven by the oscillation, is larger, this leads to an unphysical model, since the contact line velocity may be a decreasing function of contact angle. We therefore focus on the case $v'' = 0$ for our fully non-linear simulations, as well as an alternative, cubic law, in section 2.3.3. We also know that when $\bar{a} = O(\epsilon)$, $V_r^{(B)} = O(\epsilon^2)$. Rearranging (2.61) also gives us the condition

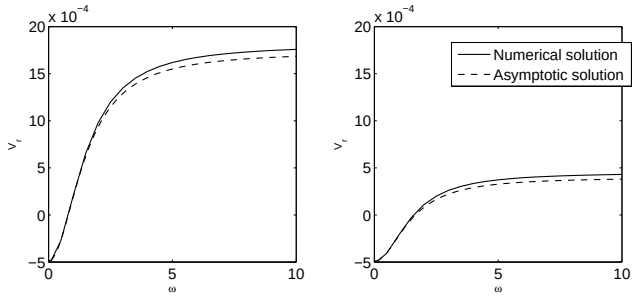


Figure 2.4: Comparison between numerical and asymptotic solutions for the rise velocity of a droplet on an inclined plane against the frequency with $\epsilon = 0.04, \gamma = 25$ and $v'' = 0$ (left), 0.4 (right).

for zero rise velocity,

$$\epsilon = \bar{a}\frac{12(9+4\omega^2)}{\gamma[3+4(1-v'')\omega^2]}. \tag{2.62}$$

These are the two results with which we will compare our solutions. We firstly fix ϵ and γ and examine the rise velocity, V_r and $V_r^{(B)}$, as ω varies. Figure 2.4 shows a comparison between our results and the asymptotic solution for a linear contact line law and a quadratic one with $v'' = 0.4$, which shows good accuracy for small ϵ. The other comparison, a curve showing zero rise velocity, is the left graph given in figure 2.9, which is discussed in the next section. Our next goal will be to include contact angle hysteresis in the model and to examine how and why this affects the rise velocity. Before we do this we take (33) and (35) from [2] and write the first order correction for the radius of the droplet as a function of polar angle ϕ, in a stationary frame of reference as

$$R^{(1)}(\phi,t) = \epsilon\left[\frac{\gamma}{12}\frac{3\sin\omega t - 2\omega\cos\omega t}{9+4\omega^2} + \frac{1}{\omega}\cos\omega t\cos\phi\right],$$

where $\phi = 0$ is the positive $x-$axis. This is the leading order motion of the droplet and it consists of a term with ϕ dependance - the swaying mode - and a term without - the spreading mode. Although these two modes are independent of each other at leading order and individually give no net motion, the non-linear interaction between the two causes the droplet to climb or slide, [2][3]. If we write this in terms of a phase shift we obtain

$$R^{(1)}(\phi,t) = \epsilon\left\{\frac{\gamma}{3}\frac{\cos\left[\omega t - \tan^{-1}(2\omega/3) - \pi/2\right]}{\sqrt{9+4\omega^2}} + \frac{\cos\omega t}{\omega}\cos\phi\right\}, \tag{2.63}$$

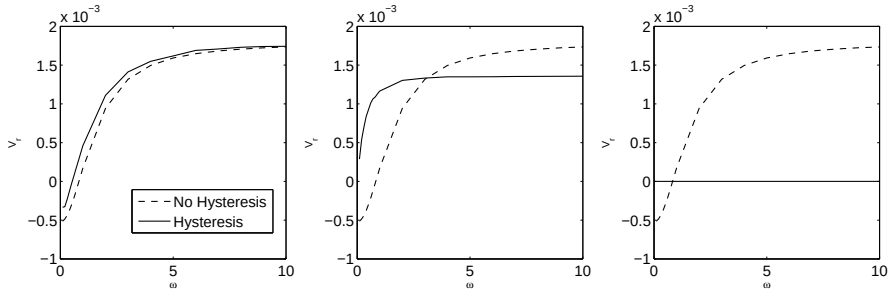


Figure 2.5: Rise velocity of a droplet against the frequency where $\epsilon = 0.04, \gamma = 25$, a linear contact line law and hysteresis intervals of 0.02, 0.2 and 0.4 respectively. The dashed line represents the rise velocity of the droplet for the same parameter values but no contact angle hysteresis present.

and we can see that the phase difference between the two modes varies monotonically with ω from $\pi/2$ out of phase, when $\omega = 0$, to fully in phase, as $\omega \to \infty$. What we can conclude from [2] is that for a linear contact line law ($v'' = 0$) the largest rise velocity occurs when the spreading and swaying modes are in phase, in qualitative agreement with [3]. We will use this result to help understand how the addition of contact angle hysteresis to the model changes the rise velocity.

2.3.2 The effect of hysteresis

Now that we have some confidence in our numerical solution method, we include contact angle hysteresis in the model, so that $\theta_A > \theta_R$. When ϵ is sufficiently small, this pins the whole contact line, so that the droplet cannot move. We will begin our investigation by considering the case $\epsilon = 0.04$, $\gamma = 25$ and $v'' = 0$, which we studied in the previous section. With the inclusion of hysteresis in the problem we can no longer define θ_0 as the angle at which the contact line is stationary and so we will redefine it as

$$\theta_0 = \frac{h_0}{R_0}, \tag{2.64}$$

where h_0 is the height of the unperturbed droplet. We will scale both θ_A and θ_R with respect to the redefined θ_0 and define the hysteresis interval as the difference between the advancing and receding angles. Figure 2.5 shows the rise velocity of the droplet for increasing hysteresis intervals with $\epsilon = 0.04, \gamma = 5$ and a linear contact line law. Firstly, these graphs show that a small hysteresis interval does not cause much of a change in the overall motion of the droplet.

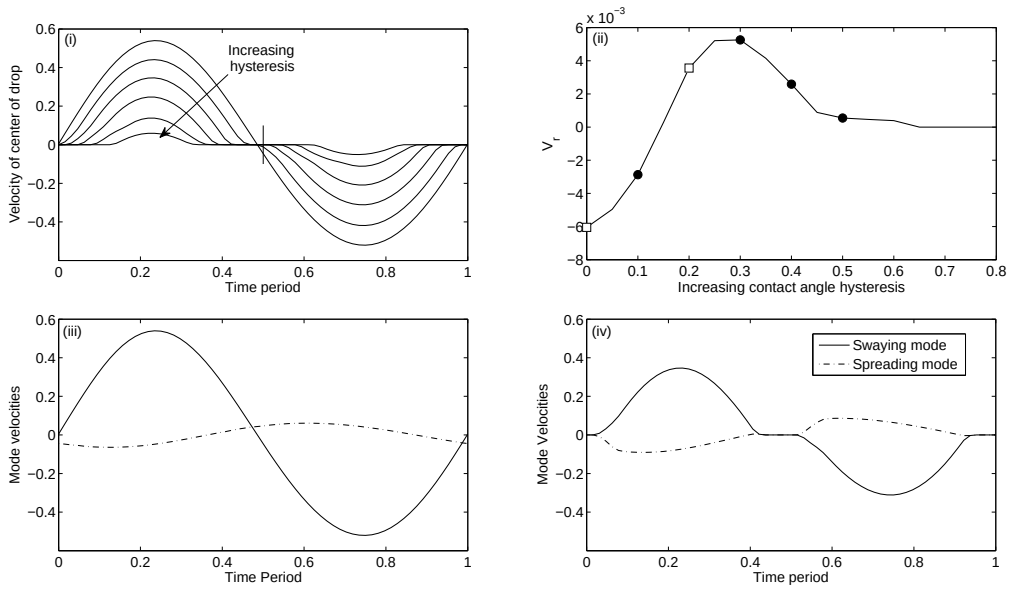


Figure 2.6: (i) The velocity of the centre of the droplet (taken along the $x-$axis) over one period of oscillation for increasing contact angle hysteresis. (ii) The rise velocity of the droplet for increasing contact angle hysteresis. (iii) and (iv) The velocity of the centre of the droplet and the contact line over one period of oscillation for no hysteresis and a hysteresis interval of 0.2 respectively. Each of the markers on (ii) coincide with the velocity profiles on (i) with the white squares also matching the results shown in (iii) and (iv). The parameters are $\epsilon = 0.53, \gamma = 1, \omega = 1.5, \bar{a} = 1/25$ and $v'' = 0$.

They also show that when a large enough hysteresis interval is present, for $\omega = O(1)$, the droplet will climb uphill instead of sliding down and also that the rise velocity is not as large for large enough ω. Finally figure 2.5 also shows that for the given parameters, the hysteresis interval can become large enough that the droplet continues to move but the contact line is fully pinned.

In order to understand how contact angle hysteresis changes the motion of the droplet we will now look at the velocity of the centre of the droplet (taken along the $x-$axis) over one period of oscillation, for different parameters. As already stated the leading order motion of a droplet on an inclined plane with small amplitude oscillations can be written as the combination of two independent modes, a spreading one and a swaying one. We can also see from (2.63) that the spreading mode scales linearly with γ and so we will examine how the size of this affects the interaction between the modes when contact angle hysteresis is included.

For our solution, where ϵ is not necessarily small, we will define the swaying mode as the difference between the position of the leading edge and the trailing

edge and the spreading mode as the mean of the two. We will begin with the case $\gamma = 1$ which produces a spreading mode that is numerically smaller than the swaying mode. We can see in figure 2.6.i that increasing the size of the hysteresis interval reduces the magnitude of the velocity of the droplets centre proportionally. This is because the leading order motion is dominated by the swaying mode (figure 2.6.iii) and so as the velocity of the contact line is restricted from the inclusion of hysteresis, the actual shape of the droplet remains unchanged. If we look at the velocity profile, with no hysteresis, carefully we can see that first of all the droplet spends more time sliding than it does climbing but also that the magnitude of the peak is slightly larger than that of the trough (these points are better illustrated in figure 2.7.i). If we now take the area of the climbing section of the graph and compare it to the sliding section, we will see that when no hysteresis is included the net motion of the droplet is down the substrate. As larger hysteresis intervals are included into the problem, both the peak and the trough are being 'reduced' at the same rate, and so what is effectively happening is a larger proportion of sliding distance is being removed compared to the climbing distance. Due to this what eventually occurs (figure 2.6.ii) is that the net motion of the droplet becomes positive. This continues up to a peak rise velocity where eventually the contact angle hysteresis starts to become too large, until eventually the droplet becomes pinned giving zero net motion.

Now we will look at an example of when $\gamma = 25$, so that the magnitude of the spreading mode velocity is of a similar order to that of the swaying mode velocity. We have also changed the value of $\bar{a}$ from $1/25$ to $1/5$, in order to better emphasize the different durations of the droplets climbing and sliding periods, as well as reducing ϵ, in order to stop the receding contact angle from reaching zero. Now we are dealing with a γ large enough that both modes are of similar magnitude (figure 2.7.iii), we will also need to consider the phase difference between them that is controlled by ω. This phase difference ranges from $\pi/2$ to 0 as ω varies between 0 and ∞ and depending on how large the phase difference is changes how the inclusion of hysteresis affects the velocity profile. We will begin with $\omega = 1.5$ as shown in figure 2.7 which approximately gives a phase difference of $\pi/4$. As we can see initially the droplet is sliding down the substrate, but when hysteresis in included in this problem the velocities of both the spreading mode and the swaying modes are forced to be zero at the same time (figure 2.7.iv). This causes the two modes to

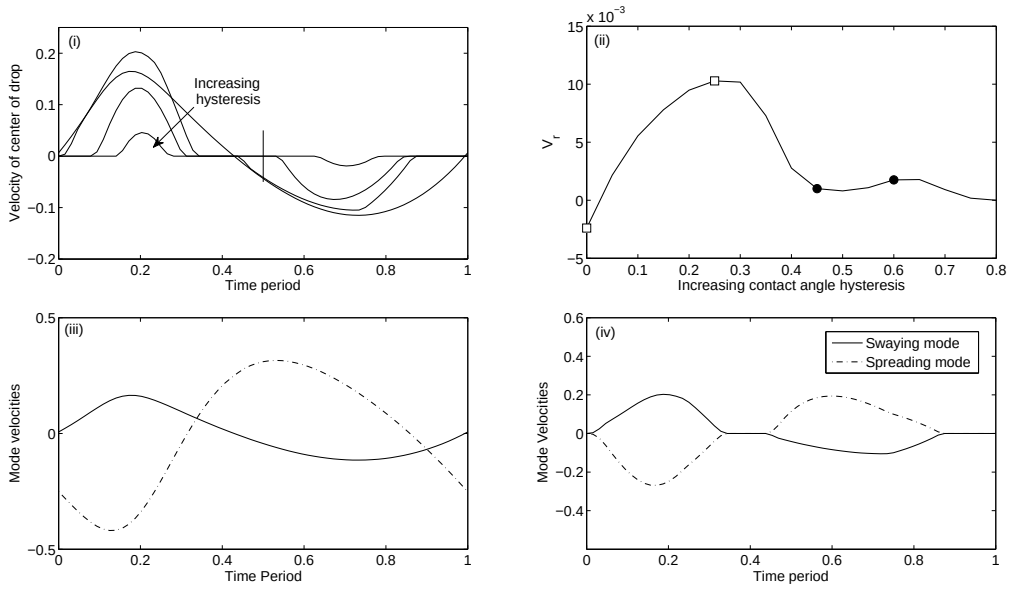


Figure 2.7: (i) The velocity of the centre of the droplet (taken along the $x-$axis) over one period of oscillation for increasing contact angle hysteresis. (ii) The rise velocity of the droplet for increasing contact angle hysteresis. (iii) and (iv) The velocity of the centre of the droplet and the contact line over one period of oscillation for no hysteresis and a hysteresis interval of 0.2 respectively. Each of the markers on (ii) coincide with the velocity profiles on (i) with the white squares also matching the results shown in (iii) and (iv). The parameters are $\epsilon = 0.125, \gamma = 25, \omega = 1.5, \bar{a} = 1/5$ and $v'' = 0$.

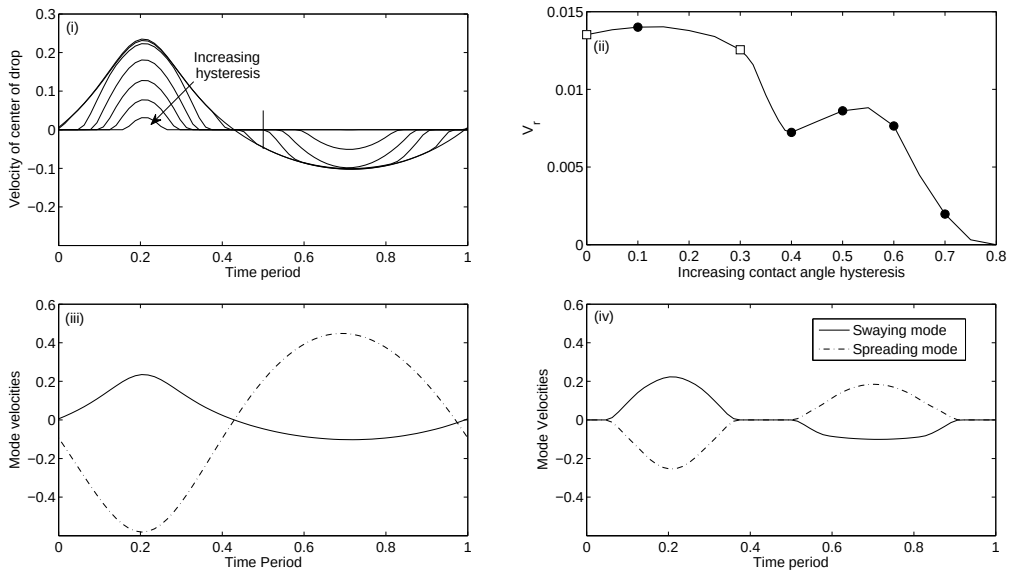


Figure 2.8: (i) The velocity of the centre of the droplet (taken along the $x-$axis) over one period of oscillation for increasing contact angle hysteresis. (ii) The rise velocity of the droplet for increasing contact angle hysteresis. (iii) and (iv) The velocity of the centre of the droplet and the contact line over one period of oscillation for no hysteresis and a hysteresis interval of 0.2 respectively. Each of the markers on (ii) coincide with the velocity profiles on (i) with the white squares also matching the results shown in (iii) and (iv). The parameters are $\epsilon = 0.125, \gamma = 25, \omega = 20, \bar{a} = 1/5$ and $v'' = 0$.

be in phase meaning that the droplet experiences a more positive rise velocity, which is the reason why the sliding droplet begins to climb in figure 2.5. As the hysteresis interval is increased the velocity becomes restricted enough for the rise velocity to begin to decrease, up to the point where the contact line is once again pinned.

For the final example, shown in figure 2.8, we will look at the same parameters as before only now with $\omega = 20$ so that the modes are approximately in phase before hysteresis is included. Due to this fact the inclusion of hysteresis does not cause a dramatic increase in the rise velocity like figure 2.7 (it does produce a small increase since the two modes were only approximately in phase prior), and instead the velocity profile begins to decrease near the edges of the curve whilst remaining the same at the peak/trough. The point at which the entire velocity profile begins to decrease, similar to figure 2.6, begins at the hysteresis interval 0.4 and is the reason why a slight increase in the rise velocity can be seen at this point. This example helps to explain why the rise velocity of the droplet is smaller for large enough ω in figure 2.5.

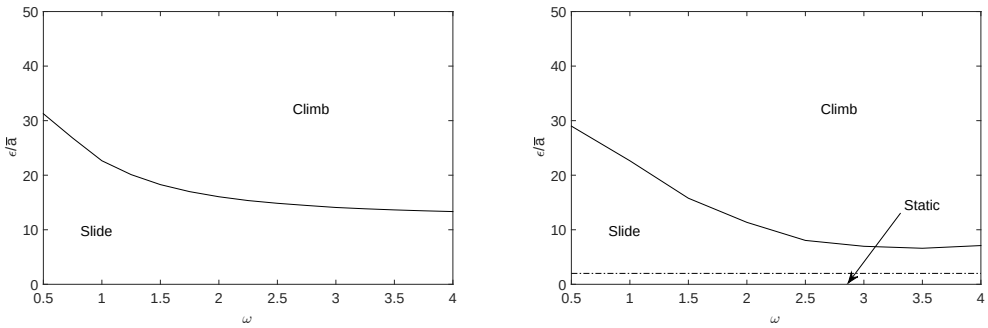


Figure 2.9: A slide-climb phase diagram for the droplet to compare between no hysteresis (left) and hysteresis (right) for $\gamma = 1$. The contact line law is given by $V(\theta) = \theta - 1$ for no hysteresis and $V(\theta) = \theta - 1.1$ for $(\theta > 1.1), \theta - 0.9$ for $(\theta < 0.9)$ and 0 in between, otherwise.

Now we will look at phase diagrams for when the droplet is either sliding or climbing for a given frequency and amplitude. This is shown in figure 2.9 and some observations can be made from these graphs: (i) the graph on the left is very similar to figure 4 in [2] (with differences coming from the fact that $\epsilon \approx 0.56 - 1.24$). (ii) The main difference between these phase diagrams is that when hysteresis is included a smaller value of ϵ is required to make the droplet climb and also a static region appears for very small ϵ. (iii) There is no transition between the sliding and climbing sections, on the hysteresis phase diagram, where the droplet remains static. This means that it is difficult to compare this graph to the one produced by [8]. Unfortunately we are unable to conclude why this static section does not appear.

In this section we have examined how adding contact angle hysteresis into the model changes the rise velocity of the droplet and why it can cause a sliding droplet to climb by including it. We began by recognising that since the motion can be separated into two modes, that hysteresis may affect both of the modes differently and so we would have to vary γ in order to cover all possibilities. For the case $\gamma = 1$ we found that the motion is dominated by the swaying mode alone and so this is all we needed to focus on. Over a single oscillation a droplet will tend to slide for a longer period than it is climbing, due to the added effect of gravity, and due to this the inclusion of hysteresis favours the uphill motion instead which can often cause a previously sliding droplet to climb. We then moved onto the case where the spreading mode was of similar size to the swaying mode and found that depending on the frequency of the oscillations the two modes have a phase difference between them. When

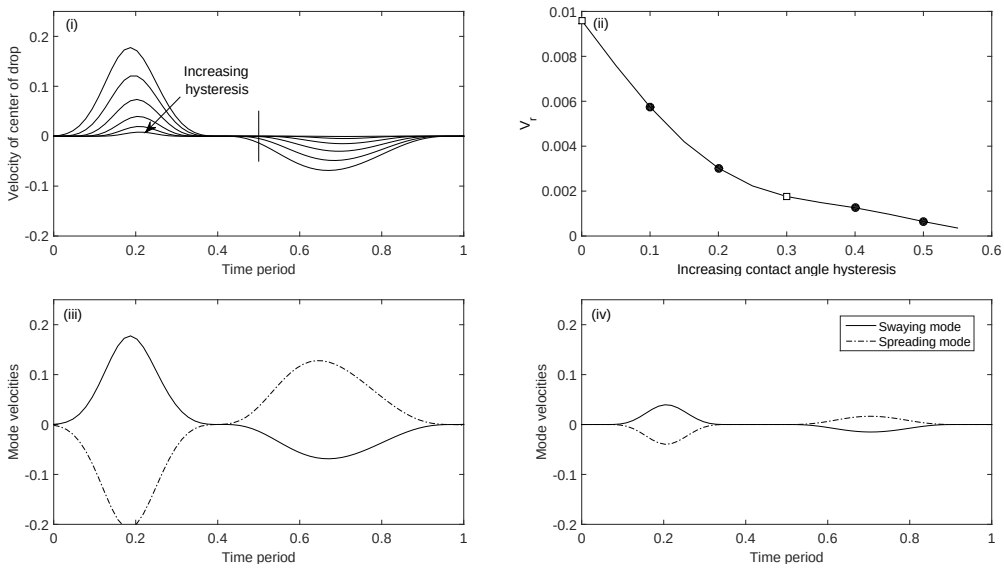


Figure 2.10: (i) The velocity of the centre of the droplet (taken along the $x-$axis) over one period of oscillation for increasing contact angle hysteresis. (ii) The rise velocity of the droplet for increasing contact angle hysteresis. (iii) and (iv) The velocity of the centre of the droplet and the contact line over one period of oscillation for no hysteresis and a hysteresis interval of 0.2 respectively. Each of the markers on (ii) coincide with the velocity profiles on (i) with the white squares also matching the results shown in (iii) and (iv). The parameters are $\epsilon = 0.125, \gamma = 25, \omega = 1.5, \bar{a} = 1/5$ and a cubic contact line law.

hysteresis is included the two modes are forced into phase which causes the rise velocity to increase. If ω is large enough for the two modes to already be in anti-phase, the inclusion of hysteresis just causes the magnitude of the rise velocity to decrease. All three of these situations will eventually reach a point where the contact line remains pinned for a large enough hysteresis interval.

2.3.3 Alternative contact line law

So far we have considered the contact line law to be a linear function of the contact angle. Therefore in this section we will examine the effects of a cubic contact line law on the mechanics of the problem. For this we will use

$$\hat{v}(\hat{\theta}) = \begin{cases} v_A|\hat{\theta} - \hat{\theta}_A|^3 & \text{for } \hat{\theta} \geq \hat{\theta}_A, \\ 0 & \text{for } \hat{\theta}_A > \hat{\theta} > \hat{\theta}_R, \\ -v_R|\hat{\theta} - \hat{\theta}_R|^3 & \text{for } \hat{\theta}_R \geq \hat{\theta}, \end{cases} \tag{2.65}$$

in dimensionless form where $v_{A,R}$ are dimensionless velocities. This equation has been shown to match the behaviour of the contact line velocity [33] with more accuracy than the linear law used previously. In this section we compare this law to our previous one, as well as attempting to make a qualitative comparison to the actual experiment. For simplicity we will set $v_{A,R} = 1$ for the remainder of this chapter.

The magnitude of the contact angle is proportional to ϵ and from examination of both of the contact line laws we know that the magnitude of the velocity in the original model is proportional to ϵ also, but the new law is proportional to ϵ^3. This means that for small ϵ the rise velocity is larger for the linear contact line law however as ϵ reaches $O(1)$ the cubic law overtakes it. Also due to the non-linearity of the cubic contact line law, the mode velocities are in phase for small ω and so the inclusion of hysteresis causes the rise velocity to decrease, whereas it would increase for a linear contact line law with the other parameters equal. The latter can be seen more clearly in figure 2.11 which has parameter values identical to the results shown in figure 2.7 only using the cubic contact line law instead. For the case where there is no hysteresis the shape of the velocity profile of the swaying mode is very similar for both of these figures, with the main difference being the rise velocity of the droplet approaches the solid line in figure 2.11 cubically whereas it approaches the line in figure 2.7 linearly (as expected). When hysteresis is included the rise velocity of the droplet decreases, since the modes are already in phase, and the velocity profile changes similar to figure 2.6. This again supports our explanation that the increasing rise velocity is due to the phase difference of the modes being forced to zero, as well as showing the main difference changing the contact line law makes to the velocity of the droplet.

Now we will look at a slide-climb phase diagram similar to figure 2.9 only now with the contact line law being cubic. The main thing we can observe in these graphs is how little the added hysteresis affects the line where the droplet begins to climb. This is due to the fact that the modes are already in phase without including hysteresis and so the addition of a hysteresis interval of only 0.1 will change the magnitude of the rise velocity but does little to change where it becomes positive. Also it seems as if these results are independent of ω but this is again due to how little changing ω affects the phase difference between the modes. It should be noted that a similar result can occur for our original contact line law [equation (2.62) with $v'' = 2/3$]. Unfortunately these

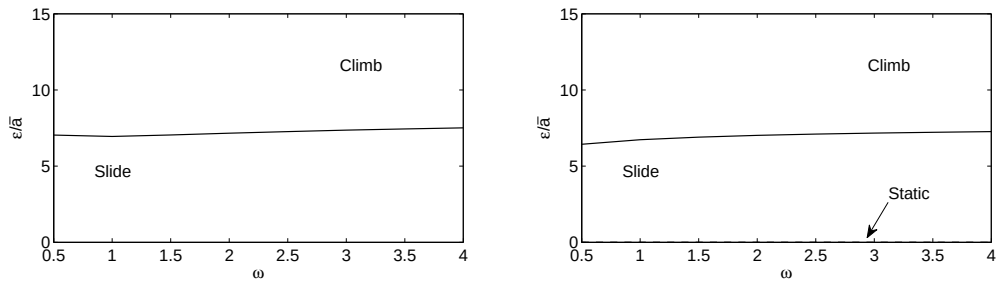


Figure 2.11: A slide-climb phase diagram for the droplet to compare between no hysteresis (left) and hysteresis (right) for $\gamma = 1$. The contact line law is given by $V(\theta) = (\theta - 1)^3$ for no hysteresis and $V(\theta) = (\theta - 1.1)^3$ for $(\theta > 1.1), (\theta - 0.9)^3$ for $(\theta < 0.9)$ and 0 in between, otherwise.

results do not show much similarity to [8] meaning we cannot use this as a qualitative comparison to actual experiments.

2.3.4 Droplet footprints

Finally, we will briefly study how the shape of the footprint of the droplet changes as it moves across the substrate. We will look at how it differs with or without hysteresis and also how changing the contact line law affects it.

As well as looking at how the droplet evolves as the substrate oscillates we can first examine the footprint for the simplified case of a stationary substrate, where the droplet slides down the plane. If there is no hysteresis, or if $(\theta_A + \theta_R)/2 = 1$, so that the hysteresis interval is symmetric, the footprint remains close to circular as it slides. The shape is more interesting for an asymmetric hysteresis interval and a small receding contact angle. In this case, the droplet deforms in three stages (figure 2.12). The first stage of the motion is for the lower half to slide down the plane with the top half moving more slowly. The lower half also thins in the lateral direction whereas the upper half spreads out slightly. We will see similar behaviour when the plane is oscillating (figure 2.14). However, unlike the unsteady flow, the droplet continues to move in the same direction and in the second stage of the initial motion the receding contact line begins to catch up with the advancing contact line. The bottom of the droplet is noticeably thinner than the top.

As the droplet continues to slide, the top of the droplet also thins laterally, until a steady state is reached in which the lateral thickness of the droplet has reached an equilibrium value somewhat smaller than the initial width. It has

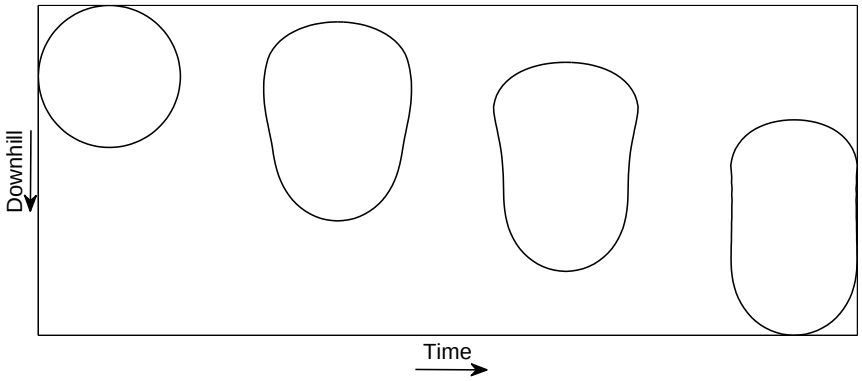


Figure 2.12: The four stages a sliding droplet undergoes on a stationary substrate ranging from an unperturbed shape to its steady state (from left to right respectively) for $\epsilon = 0.4, \gamma = 5, \omega = 0$, a linear contact line law, $\theta_A = 1.1$ and $\theta_R = 0.4$. Constant time increments have been taken in between each stage.

been shown [16] that, for a model with prescribed values for the advancing and receding contact angles, the round rectangle shape (the final stage given in figure 2.12) is in fact the only shape that is allowed in order to avoid singularities. If we instead look at a plot of the full surface of the sliding droplet for these same time increments (figure 2.13) we can see that the rounded rectangle shape is the result of the trailing end of the droplet thinning out whereas the leading end remains almost unchanged.

When the plate is oscillating, for a linear contact line law with no hysteresis, or if the hysteresis interval is symmetric, as for the steady flow, the footprint remains circular. For asymmetric hysteresis intervals, we observe almost circular footprints with the base of the droplet expanding slightly for $(\theta_A + \theta_R)/2 < 1$ or contracting slightly for $(\theta_A + \theta_R)/2 > 1$. Although these are not significant, changing the contact line law can make a big difference.

Now we will return to the cubic contact line law with $\theta_R = 0.5$ and $\theta_A = 1.1$ in order to see the effect of a small receding contact angle. Figure 2.14 shows what the footprint looks like for these parameters and the result is a sliding droplet where the lower part of the contact line moves a lot more than the higher part. The droplet deforms mainly in the downhill direction. This is the most interesting result produced in terms of footprint shapes as it very closely resembles results shown in figure 4 of [8] which shows that our model can produce results comparable to the actual experiment despite its simplified assumptions.

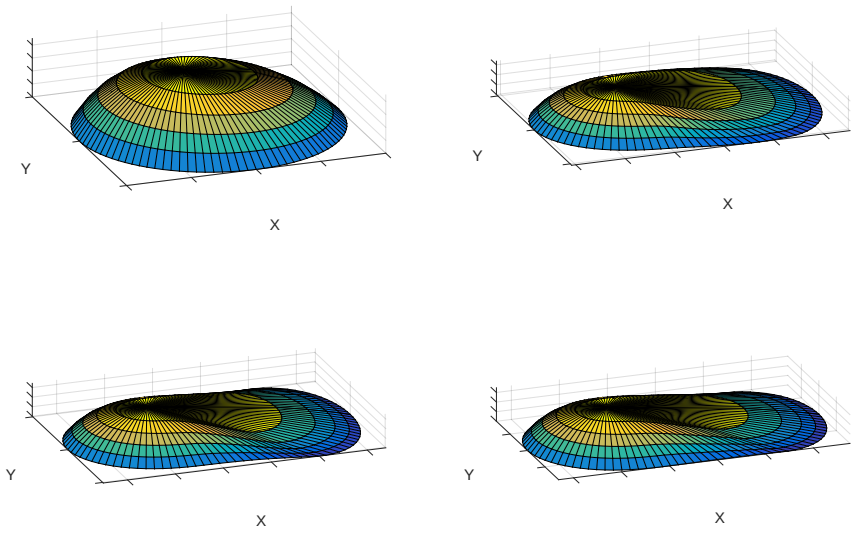


Figure 2.13: 3D plots of the four stages a sliding droplet undergoes on a stationary substrate ranging from an unperturbed shape to its steady state for $\epsilon = 0.4, \gamma = 5, \omega = 0$, a linear contact line law, $\theta_A = 1.1$ and $\theta_R = 0.4$. Constant time increments have been taken in between each stage.

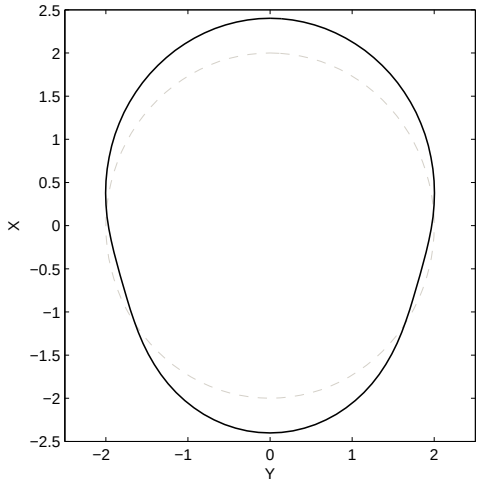


Figure 2.14: Example footprint of a sliding droplet, for $\epsilon = 0.44, \gamma = 4.5, \omega = 5$, a cubic contact line law, $\theta_A = 1.1$ and $\theta_R = 0.5$.

The final result we will show for Model 1 is a three-dimensional plot of a droplet as it oscillates over one time period (figure 2.15).

2.4 Discussion

In this chapter we have considered the motion of surface tension dominated, oscillating droplets, and neglected the effects that inertia and viscosity have on the fluid. We also assumed that the slope of the free surface is small. If the magnitude of the forcing is sufficiently small we found that a droplets motion can be separated into two modes and the non-linear interaction between these modes is what causes the droplet to slide or climb. The droplet can climb uphill for most parameter values as long as ω is large enough with the rise velocity reaching its maximum when the two modes are in phase. Adding hysteresis can cause an otherwise sliding droplet to climb by forcing the two modes into phase producing a larger rise velocity. Although we could not compare this model directly to the experimental results in [8] it is possible to obtain footprints similar to those observed in the actual experiment. We also looked at how a small receding contact angle leads to non-circular contact lines. In spite of the strong simplifications that we have used, we have been able to examine the effect of contact angle hysteresis on the rise or fall of strongly driven droplets.

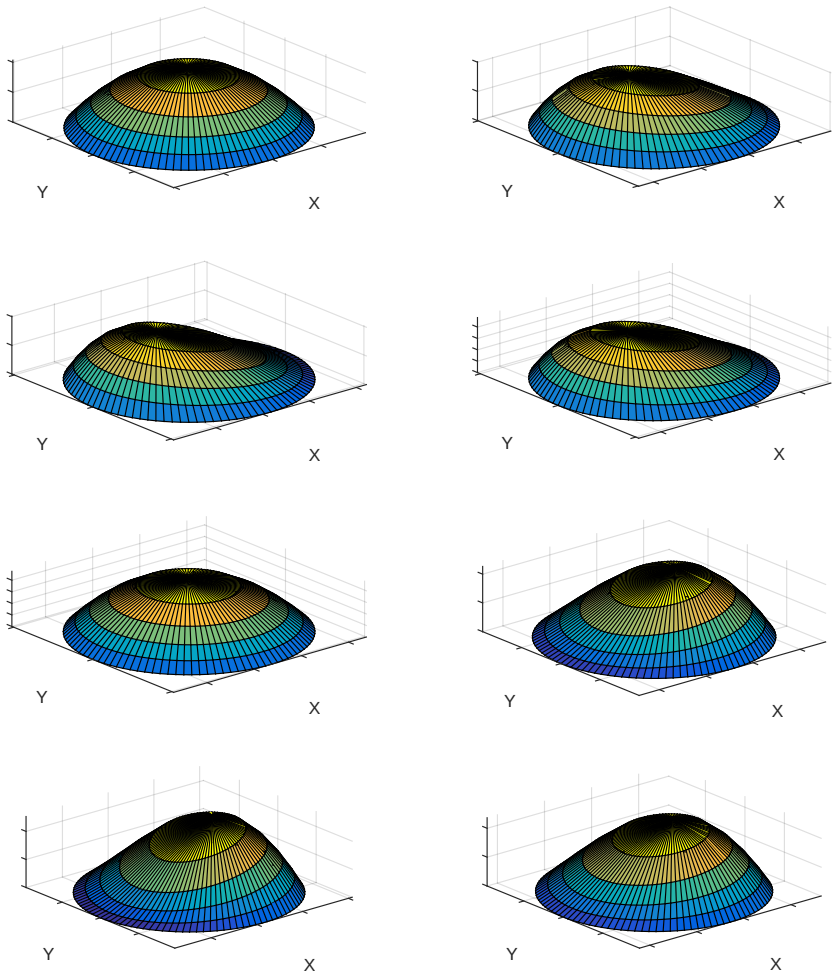


Figure 2.15: 3D plots of the motion undergone by a droplet over the course of one time period for $\epsilon = 0.8, \gamma = 1, \omega = 1$, a linear contact line law, $\theta_A = 1.1$ and $\theta_R = 0.9$. Constant time increments have been taken in between each stage.

Chapter 3

Model 2: The inviscid, two-dimensional droplet

In this chapter we will look at a two-dimensional, inviscid droplet. The benefits of this model compared to Model 1 are that we will not neglect inertia and that we can vary the thickness of the droplet. The advantage of these changes are that the inclusion of inertial forces will much better describe the motion of the fluid and $O(1)$ contact angles mean the results are much closer to the experiment [8]. The downside of this model compared to Model 1 is that we are looking at a two-dimensional 'ridge' instead of three-dimensional droplet. Since the flow is initially irrotational we know that it will remain this way, since we have assumed it to be inviscid, and so we can simplify the flow velocity $\mathbf{u}$ as the gradient of the velocity potential ϕ. These simplifications will mean we just need to solve Laplace's equation throughout the fluid and Bernoulli's equation and the kinematic condition on the surface, along with the boundary conditions at the contact points.

3.1 The model

3.1.1 Two-dimensional Euler equations

Consider an incompressible fluid of density ρ and surface tension σ, on a substrate inclined at angle α to the horizontal that is oscillating sinusoidally, with amplitude a_0 and frequency ω, parallel to gravity. The frame of reference is aligned with the $x-$axis such that these oscillations act at an angle $\pi/2-\alpha$ to the substrate. We will assume that the viscous forces are weak in comparison

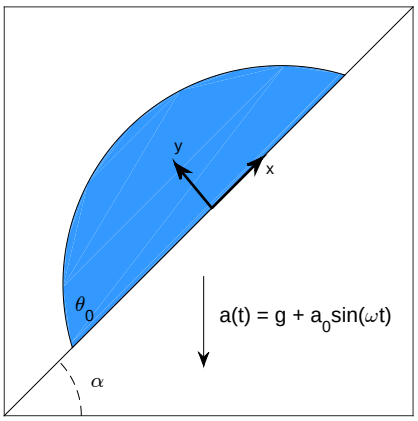


Figure 3.1: Setup for the droplet including coordinate system.

to the surface tension and inertia in order to use the equations

$$\boldsymbol{\nabla} \cdot \mathbf{u} = 0, \tag{3.1}$$

$$\frac{d\mathbf{u}}{dt} = -\frac{1}{\rho}\boldsymbol{\nabla} p - a(t)\boldsymbol{\nabla}(x \sin\alpha + y\cos\alpha), \tag{3.2}$$

where $\mathbf{u}$ is the flow velocity, p is the pressure and $a(t) = g + a_0 \sin(\omega t)$ is the combined acceleration of gravity and the oscillating plate. We will use (3.2) only on the surface of droplet so that the pressure will be given by the curvature κ, i.e. $p = -\sigma\kappa$. The next step will be to use the assumption that the flow is irrotational to let $\mathbf{u} = \boldsymbol{\nabla}\phi$ so that we can rewrite (3.1) as

$$\nabla^2\phi = 0, \tag{3.3}$$

throughout all of the droplet. Now we are using the velocity potential we will rewrite (3.2) as

$$\frac{\partial\phi}{\partial t} + \frac{1}{2}|\boldsymbol{\nabla}\phi|^2 - \frac{\sigma\kappa}{\rho} + a\,(X\sin\alpha + Y\cos\alpha) = 0, \quad \text{on } \mathbf{x} = \mathbf{X}(s,t), \tag{3.4}$$

as well as now having the kinematic condition

$$\mathbf{n} \cdot \frac{d\mathbf{X}}{dt} = \frac{\partial\phi}{\partial n}, \quad \text{on } \mathbf{x} = \mathbf{X}(s,t), \tag{3.5}$$

where $\mathbf{X}(s,t)$ is the free surface of the droplet and $s \in [0, L(t)]$ is the arc length. The other boundary condition that is present is the impermeability condition

$$v = 0, \quad \text{on } y = 0,$$

which we will satisfy implicitly with our choice of ϕ within our solution method.

The contact line model

For our model we have assumed our fluid is two-dimensional meaning that we can reduce our contact line down to two contact 'points', where the free surface is in contact with the substrate. We can write this as

$$X = x_-, \quad Y = 0, \quad \text{at } s = 0, \tag{3.6}$$

$$X = x_+, \quad Y = 0, \quad \text{at } s = L, \tag{3.7}$$

where $x_\pm$ are the x value of the contact points. Now the velocity at these points is given by

$$\frac{\partial \phi}{\partial s} = \frac{dx_-}{dt}\cos\theta_-, \quad \frac{dx_-}{dt} = v(\theta_-), \quad \text{at } s = 0, \tag{3.8}$$

$$\frac{\partial \phi}{\partial s} = \frac{dx_+}{dt}\cos\theta_+, \quad \frac{dx_+}{dt} = v(\theta_+), \quad \text{at } s = L, \tag{3.9}$$

where $v(\theta_\pm)$ is the contact line law given by (1.4) and

$$\tan\theta_- = \left.\frac{\partial Y/\partial s}{\partial X/\partial s}\right|_{s=0}, \quad \tan\theta_+ = -\left.\frac{\partial Y/\partial s}{\partial X/\partial s}\right|_{s=L}.$$

Initially we will examine when the force per unit length applied by the oscillating plate is small, in comparison to the droplet's surface tension, and there is no contact angle hysteresis; meaning that we can approximate the contact line law using a Taylor expansion for contact angles close to the equilibrium angle. Later we will examine larger amplitude oscillations, as well as more realistic contact line laws and the inclusion of contact angle hysteresis.

3.1.2 Moving reference frame

We will now go through a couple of steps that will make solving (3.3)-(3.9) a little easier. The first will be to use a moving reference frame in order to keep

the droplet centered at the origin. This will make using a polar coordinate system a lot simpler and make the solution time periodic. To do this we will define the velocity of the frame as

$$V_s(t) = \frac{1}{2}\left(\frac{dx_+}{dt} + \frac{dx_-}{dt}\right),$$

so that the droplet in this new frame will still move, but the contact points will always be an equal distance from the origin. This means that the variables in the new frame (denoted with a subscript n) need to be redefined using

$$x = x_n + \frac{1}{2}(x_+ + x_-), \quad \phi = \phi_n + V_s x_n, \quad D(t) = \frac{1}{2}(x_+ - x_-),$$

and so instead of finding the leading and trailing ends of the droplet (x_+ and x_- respectively) we will now solve for D, the half-width of the droplet, and V_s, the velocity of the droplet's centre. Applying these redefinitions to (3.3)-(3.9) and omitting subscripts gives

$$\nabla^2\phi = 0, \tag{3.10}$$

where

$$\frac{\partial\phi}{\partial t} + \frac{1}{2}|\boldsymbol{\nabla}\phi|^2 + \frac{dV_s}{dt}x - \frac{\sigma\kappa}{\rho} + a\left(X\sin\alpha + Y\cos\alpha\right) = 0, \quad \text{on } \mathbf{x} = \mathbf{X}(s,t), \tag{3.11}$$

$$\mathbf{n}\cdot\frac{d\mathbf{x}}{dt} = \frac{\partial\phi}{\partial n}, \quad \text{on } \mathbf{x} = \mathbf{X}(s,t), \tag{3.12}$$

and

$$\frac{dD}{dt} = v(\theta_-) + V_s, \quad y = 0, \quad \frac{\partial\phi}{\partial s} = -\frac{dD}{dt}\cos\theta_-, \quad \text{at } s = 0, \tag{3.13}$$

$$\frac{dD}{dt} = v(\theta_+) - V_s, \quad y = 0, \quad \frac{\partial\phi}{\partial s} = \frac{dD}{dt}\cos\theta_+, \quad \text{at } s = L. \tag{3.14}$$

3.1.3 Dimensionless variables

The next step we will carry out is non-dimensionalising our variables so that we can generalise our results by only having to vary specific dimensionless parameters. We will define our scales in order to write (3.10)-(3.14) in a dimensionless form that is comparable to [3] whilst keeping (3.10) unchanged.

These scales are

$$\begin{aligned} x = D_0\hat{x}, \quad y = D_0\hat{y}, \quad \phi = \frac{D_0^2}{T}\hat{\phi}, \quad t = T\hat{t} \quad V = \frac{D_0}{T}\hat{V}, \\ a = a_0\hat{a}, \quad \kappa = \frac{1}{D_0}\hat{\kappa}, \quad D = D_0\hat{D}, \quad s = D_0\hat{s}, \quad L = D_0\hat{L}, \end{aligned} \tag{3.15}$$

where D_0 is the radius of an unperturbed droplet and θ_0 is the magnitude of the contact angle. We will also define the time scale as

$$T = \sqrt{\frac{\rho D_0^3}{\sigma\theta_0}},$$

in order to balance the surface tension with the material derivative. These scalings give rise to some new dimensionless parameters

$$\epsilon = \frac{\rho a_0 D_0^2 \sin\alpha}{\sigma\theta_0}, \quad \gamma = \frac{\theta_0}{\tan\alpha}, \tag{3.16}$$

which characterise the strength of the effective gravitational force relative to surface tension and inertia and the ratio between the slope of the droplets surface and the slope of the substrate respectively. As well as these, the other dimensionless parameters are given by

$$\hat{\omega} = 2\pi T f, \quad \hat{g} = \frac{g}{\epsilon a_0}, \tag{3.17}$$

which are the dimensionless frequency of the oscillations and the gravitational acceleration respectively. The final parameter that will appear in the governing equations is θ_0. Now we have our set of parameters we should check their typical sizes, using Table 1.1. Due to the definitions used in Model 1 we calculated the diameter of the droplet using the mass scaling but since Model 2 is two-dimensional this cannot be done. Instead we will extrapolate from [8] that a droplet with a volume of 5 μl will have a radius of approximately 1 mm. Now using typical values we know that parameter values which match those used in [8] are given by

$$\epsilon \approx 2.05, \quad \gamma \approx 1.08, \quad \hat{\omega} \approx 1.30, \quad \hat{g} \approx 2.75 \times 10^{-2}, \quad \theta_0 \approx 1.08. \tag{3.18}$$

As well as this we also need to justify our assumption that the flow is inviscid, i.e. that the Reynolds number is large. Since our velocity is scaled using the

length over the time scale then the Reynolds number is given by

$$Re = \frac{D_0^2}{T\nu} \approx 7.89.$$

3.1.4 Governing equations

Now we have examined our dimensional scalings and justified our choices used to balance them we will use them to rewrite (3.10)-(3.14) as

$$\nabla^2\phi = 0, \tag{3.19}$$

with

$$\frac{\partial\phi}{\partial t} + \frac{1}{2}|\boldsymbol{\nabla}\phi|^2 + \frac{dV_s}{dt}x - \frac{1}{\theta_0}\kappa + \epsilon a\left(X + \frac{\gamma}{\theta_0}Y\right) = 0, \quad \text{on } \mathbf{x} = \mathbf{X}(s,t), \tag{3.20}$$

$$\mathbf{n}\cdot\frac{d\mathbf{x}}{dt} = \frac{\partial\phi}{\partial n}, \quad \text{on } \mathbf{x} = \mathbf{X}(s,t), \tag{3.21}$$

and

$$\frac{dD}{dt} = v(\theta_-) + V_s, \quad y = 0, \quad \frac{\partial\phi}{\partial s} = -\frac{dD}{dt}\cos\theta_-, \quad \text{at } s = 0, \tag{3.22}$$

$$\frac{dD}{dt} = v(\theta_+) - V_s, \quad y = 0, \quad \frac{\partial\phi}{\partial s} = \frac{dD}{dt}\cos\theta_+, \quad \text{at } s = L, \tag{3.23}$$

where hats have now been omitted for simplicity. These are the governing equations that we will solve both asymptotically and numerically, the methods for which are contained in sections 3.2 and 3.3 respectively.

3.2 Small amplitude asymptotic solution

3.2.1 Polar coordinates

Now we will solve the (3.19)-(3.23) asymptotically for small ϵ. This corresponds to the forcing being small in comparison to the droplet's surface tension and inertia. In this section we are looking at a linear expansion of (3.19) - (3.23) and so we will only examine the case where $\theta_A = \theta_R \equiv \theta_0$, i.e. there is no contact angle hysteresis present. Since ϵ is small the shape of the droplet will only ever be slightly perturbed from the initial state and so the contact angles will always remain near equilibrium. This means that we can replace

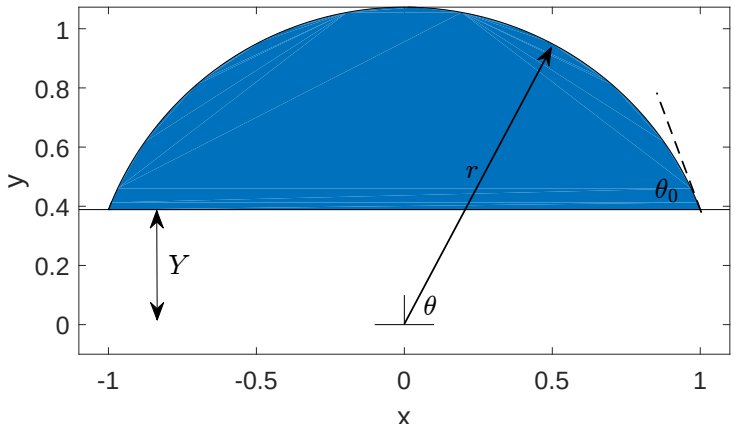


Figure 3.2: Setup of the model in polar coordinates. Y is the distance of the substrate above the origin, θ_0 is the magnitude of the contact angles and (r, θ) is the coordinate system.

the contact line law with a Taylor series expansion for $\theta_\pm \approx \theta_0$, giving

$$v(\theta_\pm) = v'\left(\frac{\theta_\pm}{\theta_0} - 1\right) + \frac{1}{2}v''\left(\frac{\theta_\pm}{\theta_0} - 1\right)^2 + ..., \tag{3.24}$$

where v', v'' are the dimensionless derivatives of the contact velocity at equilibrium. To make our expansion easier we will begin by converting to a polar coordinate system and also have the moving frame of reference sit at a height $Y = \cot\theta_0$ above the horizontal axis (see figure 3.2). Applying all of these to the system gives

$$\nabla^2\phi = 0, \tag{3.25}$$

where

$$\begin{aligned}\frac{\partial\phi}{\partial t} + \frac{1}{2}|\boldsymbol{\nabla}\phi|^2 + \frac{dV_s}{dt}R\cos\theta + \frac{\kappa}{\theta_0} &= \epsilon\frac{a\gamma}{\theta_0}Y \\ - \epsilon aR\left(\cos\theta + \frac{\gamma}{\theta_0}\sin\theta\right), &\quad \text{on } r = R(\theta, t),\end{aligned} \tag{3.26}$$

$$\frac{\partial R}{\partial t} = \frac{\partial\phi}{\partial r} - \frac{1}{R^2}\frac{\partial R}{\partial\theta}\frac{\partial\phi}{\partial\theta}, \qquad r = R(\theta, t), \tag{3.27}$$

where $R(\theta, t)$ is the free surface. At the contact points we know that

$$\begin{aligned}R = \sqrt{Y^2 + D^2}, \quad v(\theta_\pm) - \frac{dD}{dt} = \pm V_s, \quad \frac{\partial\phi}{\partial\theta} = \mp Y\frac{dD}{dt}, \\ \text{at } \theta = \frac{\pi}{2} \mp \tan^{-1}\left(\frac{D}{Y}\right),\end{aligned} \tag{3.28}$$

where the contact angles are now given by

$$\tan\theta_{\pm} = \frac{DR \pm YR'}{YR \mp DR'}. \tag{3.29}$$

On the substrate the impermeability boundary condition becomes

$$\frac{\partial\phi}{\partial r} + \cot\theta \frac{1}{r}\frac{\partial\phi}{\partial\theta} = 0, \qquad r = \frac{\cot\theta_0}{\sin\theta}. \tag{3.30}$$

Now we have the equations in a form that we can expand more easily, we will assume $\epsilon \ll 1$ and look for an asymptotic solution to these equations. The leading order solution, which represents a droplet with no external forces acting upon it, is

$$\phi_0 = -\frac{\sin\theta_0}{\theta_0}t, \quad R_0 = \frac{1}{\sin\theta_0}, \quad V_0 = 0, \tag{3.31}$$

and the unperturbed half-width of the droplet has been scaled to equal 1. We can see from (3.31) that the leading order solution, or the exact solution when there is no external force applied, is a stationary segment of a circle where the size (and positioning above the $x-$axis) are both determined by the equilibrium angle θ_0. The area of this segment is given by

$$A_0 = \frac{2\theta_0 - \sin(2\theta_0)}{1 - \cos(2\theta_0)}. \tag{3.32}$$

Now we have obtained the leading order solution we will look at the first order expansion of (3.25) - (3.28), which will give us the leading order deformation of the droplet over the period of an oscillation, and the second order expansion, which will give us the leading order mean velocity of the droplet.

3.2.2 Asymptotic expansion

We will obtain the first and second order asymptotic equations for small amplitude oscillations one equation at a time, expanding terms within the equations separately if deemed necessary. The asymptotic expansions are

$$\phi(r,\theta,t) = \phi_0(t) + \epsilon\phi_1(r,\theta,t) + \epsilon^2\phi_2(r,\theta,t) + ...,$$
$$R(\theta,t) = R_0 + \epsilon R_1(\theta,t) + \epsilon^2 R_2(\theta,t) + ...,$$
$$V(t) = \epsilon V_1(t) + \epsilon^2 V_2(t) + ..., \quad D(t) = 1 + \epsilon D_1(t) + \epsilon^2 D_2(t) + ...$$

We will begin with (3.25) which is very simple to expand and separate since the Laplace operator is linear giving

$$\nabla^2\phi_1 = 0, \tag{3.33}$$

$$\nabla^2\phi_2 = 0. \tag{3.34}$$

The next step is to expand (3.26). To do this we will split the equations and expand each term separately. The partial derivative of the velocity potential with respect to time becomes

$$\left.\frac{\partial\phi}{\partial t}\right|_{r=R} = \frac{\partial\phi_0}{\partial t} + \epsilon\frac{\partial\phi_1}{\partial t} + \epsilon^2\frac{\partial\phi_2}{\partial t} + \epsilon^2 R_1\frac{\partial^2\phi_1}{\partial t\partial r} + ..., \quad \text{on } r = R_0, \tag{3.35}$$

whereas the modulus of the velocity squared is

$$|\boldsymbol{\nabla}\phi|^2 = \epsilon^2|\boldsymbol{\nabla}\phi_1|^2 + ..., \quad \text{on } r = R_0. \tag{3.36}$$

The most complicated term to expand in (3.26) is the curvature, which in polar coordinates is given by

$$\kappa = \frac{R^2 + (R')^2 - RR''}{(R^2 + (R')^2)^{3/2}},$$

and so we will expand this into powers of ϵ to give

$$\kappa = \frac{1}{R_0} - \epsilon\frac{R_1'' + R_1}{R_0^2} - \epsilon^2\left(\frac{R_2' + R_2}{R_0^2} - \frac{R_1^2 + (R_1')^2/2 + 2R_1R_1''}{R_0^3}\right) + ... \tag{3.37}$$

Inserting (3.35)-(3.37) back into (3.26), expanding the rest of the terms into powers of ϵ and then separating the powers gives the first and second order equations as

$$\frac{\partial\phi_1}{\partial t} + \frac{dV_1}{dt}R_0\cos\theta - \frac{R_1'' + R_1}{\theta_0 R_0^2} = -\sin(\omega t)R_0\left(\cos\theta + \frac{\gamma}{\theta_0}\sin\theta\right), \quad \text{on } r = R_0, \tag{3.38}$$

and

$$\frac{\partial \phi_2}{\partial t} + \frac{dV_2}{dt} R_0 \cos\theta - \frac{R_2'' + R_2}{\theta_0 R_0^2} = -[gR_0 + \sin(\omega t) R_1] \left(\cos\theta + \frac{\gamma}{\theta_0} \sin\theta \right) - R_1 \frac{\partial^2 \phi_1}{\partial t \partial r} - \frac{dV_1}{dt} R_1 \cos\theta - \frac{1}{2} |\boldsymbol{\nabla} \phi_1|^2 - \frac{R_1^2 + (R_1')^2/2 + 2R_1 R_1''}{\theta_0 R_0^3}, \text{ on } r = R_0, \tag{3.39}$$

respectively. Next (3.27) can be separated into powers of ϵ to give

$$\frac{\partial R_1}{\partial t} = \frac{\partial \phi_1}{\partial r}, \quad \text{on } r = R_0, \tag{3.40}$$

$$\frac{\partial R_2}{\partial t} = \frac{\partial \phi_2}{\partial r} + R_1 \frac{\partial^2 \phi_1}{\partial r^2} - \frac{1}{R_0^2} \frac{\partial R_1}{\partial \theta} \frac{\partial \phi_1}{\partial \theta}, \quad \text{on } r = R_0. \tag{3.41}$$

We will now expand each of the boundary conditions in (3.28). To do this we first must expand

$$\theta = \frac{\pi}{2} \mp \tan^{-1}\left(D \tan\theta_0\right),$$

which becomes

$$\theta = \frac{\pi}{2} \mp \theta_0 \mp \epsilon D_1 \sin\theta_0 \cos\theta_0 \mp \epsilon^2 \left(D_2 - D_1 \sin^2\theta_0\right) \sin\theta_0 \cos\theta_0 + ..., \tag{3.42}$$

at the boundary points. In addition to this we need to separate (3.29) into powers of ϵ which gives

$$\tan\theta_\pm = \tan\theta_0 + \epsilon \tan\theta_0 \left(D_1 \pm \sec\theta_0 R_1'\right) + \epsilon^2 \tan\theta_0 \left[D_2 + R_1 R_1'' + \tan^2\theta_0 \left(R_1'\right)^2 \pm \left(\sec\theta_0 R_2' + \tan\theta_0 R_1 R_1'\right)\right] + ...,$$

and so by writing $\theta_\pm = \theta_0 + \epsilon\theta_{\pm 1} + \epsilon^2 \theta_{\pm 2} + ...$ we get

$$\theta_{\pm 1} = \sin\theta_0 \cos\theta_0 D_1 \pm \sin\theta_0 R_1', \tag{3.43}$$

$$\theta_{\pm 2} = \sin\theta_0 \cos\theta_0 [D_2 - R_1(R_1'' + R_1)] \pm \sin\theta_0 (R_2' - \sin\theta_0 R_1 R_1'). \tag{3.44}$$

Inserting (3.42) into the first boundary condition in (3.28) and expanding in powers of ϵ gives

$$R_1 = D_1 \sin\theta_0, \quad \text{at } \theta = \frac{\pi}{2} \mp \theta_0, \tag{3.45}$$

$$R_2 = D_2 \sin\theta_0 + D_1 \sin\theta_0 \cos\theta_0 \left(\frac{1}{2} D_1 \cos\theta_0 \pm \frac{\partial R_1}{\partial \theta}\right), \quad \text{at } \theta = \frac{\pi}{2} \mp \theta_0. \tag{3.46}$$

The second boundary condition of (3.28) is expanded to give

$$\frac{dD_1}{dt} \pm V_1 = v' \frac{\theta_{\pm 1}}{\theta_0}, \quad \frac{dD_2}{dt} \pm V_2 = v' \frac{\theta_{\pm 2}}{\theta_0} + \frac{1}{2} v'' \frac{\theta_{\pm 1}^2}{\theta_0^2}, \quad \text{at } \theta = \frac{\pi}{2} \mp \theta_0, \tag{3.47}$$

and inserting (3.43)-(3.44) gives

$$\frac{dD_1}{dt} \pm V_1 = v' \frac{\sin\theta_0}{\theta_0} \left(\cos\theta_0 D_1 \pm \frac{\partial R_1}{\partial \theta} \right), \quad \text{at } \theta = \frac{\pi}{2} \mp \theta_0, \tag{3.48}$$

$$\begin{aligned} \frac{dD_2}{dt} \pm V_2 = v' \frac{\sin\theta_0}{\theta_0} \left[\cos\theta_0 \left(D_2 - R_1^2 - R_1 \frac{\partial^2 R_1}{\partial \theta^2} \right) \pm \frac{\partial R_2}{\partial \theta} \mp \sin\theta_0 R_1 \frac{\partial R_1}{\partial \theta} \right] \\ + \frac{1}{2} v'' \frac{\sin^2\theta_0}{\theta_0^2} \left[\cos\theta_0 D_1 \pm \frac{\partial R_1}{\partial \theta} \right]^2, \quad \text{at } \theta = \frac{\pi}{2} \mp \theta_0. \end{aligned} \tag{3.49}$$

The final boundary condition in (3.28) is expanded as

$$\epsilon \frac{\partial \phi_1}{\partial \theta} + \epsilon^2 \left(\frac{\partial \phi_2}{\partial \theta} \mp \hat{\theta}_1 \frac{\partial^2 \phi_1}{\partial \theta^2} \right) = \mp \epsilon \cot\theta_0 \frac{dD_1}{dt} \mp \epsilon^2 \cot\theta \frac{dD_2}{dt} + \ldots, \quad \text{at } \theta = \frac{\pi}{2} \mp \theta_0,$$

which can be separated to give

$$\frac{\partial \phi_1}{\partial \theta} = \mp \cot\theta_0 \frac{dD_1}{dt}, \quad \text{at } \theta = \frac{\pi}{2} \mp \theta_0, \tag{3.50}$$

$$\frac{\partial \phi_2}{\partial \theta} = \mp \left(\cot\theta_0 \frac{dD_2}{dt} - \hat{\theta}_1 \frac{\partial^2 \phi_1}{\partial \theta^2} \right), \quad \text{at } \theta = \frac{\pi}{2} \mp \theta_0. \tag{3.51}$$

Now we have expanded our equations and separated them for powers of ϵ, we will now look at each system of equations independently and solve them to find an asymptotic expansion for the rise velocity.

3.2.3 First order terms

In this section we will look at the first order asymptotic expansion of (3.19)-(3.23). We will begin by removing the time dependence from the equations and then look at the shallow water limit which will be our first comparison to [3]. After this we will separate the odd terms from the even ones in order to examine the problem in terms of two independent modes. A summary of the first order equations, taken from section 3.2.2, are

$$\nabla^2 \phi_1 = 0, \tag{3.52}$$

where

$$\frac{\partial \phi_1}{\partial t} + \frac{dV_1}{dt}\frac{\cos\theta}{\sin\theta_0} = \frac{\sin^2\theta_0}{\theta_0}\left(\frac{\partial^2 R_1}{\partial\theta^2} + R_1\right) - \frac{\sin(\omega t)}{\sin\theta_0}\left[\cos\theta + \frac{\gamma}{\theta_0}(\sin\theta - \cos\theta_0)\right], \quad \text{on } r = R_0, \tag{3.53}$$

$$\frac{\partial R_1}{\partial t} = \frac{\partial \phi_1}{\partial r}, \quad \text{on } r = R_0, \tag{3.54}$$

and

$$R_1 = D_1 \sin\theta_0, \quad \frac{\partial \phi_1}{\partial \theta} = \mp \cot\theta_0 \frac{dD_1}{dt}, \qquad \text{at } \theta = \frac{\pi}{2} \mp \theta_0, \tag{3.55}$$

$$v' \frac{\sin\theta_0}{\theta_0}\frac{\partial R_1}{\partial \theta} - V_1 \pm \left(v' \frac{\sin\theta_0}{\theta_0}\cos\theta_0 D_1 - \frac{dD_1}{dt}\right) = 0, \quad \text{at } \theta = \frac{\pi}{2} \mp \theta_0. \tag{3.56}$$

In order to simplify these equations we will extract the time dependence since it only appears explicitly as $\sin(\omega t)$. We will do this by defining

$$\phi_1 = \Re\left\{\tilde{\phi} e^{i\omega t}\right\}, \quad V_1 = \Re\left\{\tilde{V} e^{i\omega t}\right\}, \quad R_1 = \Im\left\{\tilde{R} e^{i\omega t}\right\}, \quad D_1 = \Im\left\{\tilde{D} e^{i\omega t}\right\}, \tag{3.57}$$

and so if we insert these into (3.52) - (3.56) and cancel the exponential terms we get

$$\nabla^2 \tilde{\phi} = 0, \tag{3.58}$$

where

$$\omega\tilde{\phi} + \omega\tilde{V}\frac{\cos\theta}{\sin\theta_0} + \frac{\sin^2\theta_0}{\theta_0}\left(\frac{\partial^2 \tilde{R}}{\partial\theta^2} + \tilde{R}\right) = \frac{1}{\sin\theta_0}\left[\cos\theta + \frac{\gamma}{\theta_0}(\sin\theta - \cos\theta_0)\right], \quad \text{on } r = R_0, \tag{3.59}$$

$$\omega\tilde{R} = \frac{\partial\tilde{\phi}}{\partial r}, \quad \text{on } r = R_0, \tag{3.60}$$

and

$$\tilde{R} = \sin\theta_0 \tilde{D}, \quad \frac{\partial\tilde{\phi}}{\partial\theta} = \mp\cot\theta_0 \omega\tilde{D}, \qquad \text{at } \theta = \frac{\pi}{2} \mp \theta_0, \tag{3.61}$$

$$v' \frac{\sin\theta_0}{\theta_0}\frac{\partial\tilde{R}}{\partial\theta} - i\tilde{V} \pm \left(v' \frac{\sin\theta_0}{\theta_0}\cos\theta_0 - i\omega\right)\tilde{D} = 0, \quad \text{at } \theta = \frac{\pi}{2} \mp \theta_0. \tag{3.62}$$

We now have a linear system of equations and by replacing (3.58) with a boundary integral equation we can solve them simultaneously to get $\tilde{R}, \tilde{\phi}, \tilde{V}$ and $\tilde{D}$. Now we have the first order time independent equations we will look into some methods for simplifying these equations further. First off all we will decouple $\tilde{V}$ and $\tilde{D}$ using symmetry arguments and then we will look at both the thin droplet and low frequency asymptotic limits of the equations. After this we will use a conformal map to produce an alternate method for solving. The numerical solution method for (3.58)-(3.62) can be found in section 3.3.2.

Odd and even modes

From observation of (3.58)-(3.62) we can see that the forcing terms are either even or odd about $\theta = \pi/2$ and so, since all the equations are linear, we are able to separate both $\tilde{\phi}$ and $\tilde{R}$ into an even function and an odd one with respect to $\theta = \pi/2$. The benefit of this is that it decouples $\tilde{V}$ and $\tilde{D}$ from each other, meaning that the leading order motion of the droplet is actually a combination of two independent motions, one which is symmetric about the centre and one that is antisymmetric. And so if we write

$$\tilde{\phi}(r,\theta) = \phi_E(r,\theta) + \phi_O(r,\theta), \qquad \tilde{R}(\theta) = R_E(\theta) + R_O(\theta), \tag{3.63}$$

where the subscript E is even and O is odd about $\theta = \pi/2$. Now if we insert these into (3.58)-(3.62) we can write the even mode equations as

$$\nabla^2 \phi_E = 0, \tag{3.64}$$

where

$$\omega\phi_E + \frac{\sin^2\theta_0}{\theta_0}\left(\frac{\partial^2 R_E}{\partial\theta^2} + R_E\right) = \frac{\gamma(\sin\theta - \cos\theta_0)}{\theta_0 \sin\theta_0}, \quad \text{on } r = R_0, \tag{3.65}$$

$$\omega R_E = \frac{\partial\phi_E}{\partial r}, \quad \text{on } r = R_0, \tag{3.66}$$

and

$$R_E = \sin\theta_0 \tilde{D}, \quad \frac{\partial\phi_E}{\partial\theta} = -\cot\theta_0 \omega\tilde{D}, \qquad \text{at } \theta = \frac{\pi}{2} - \theta_0, \tag{3.67}$$

$$\frac{\partial R_E}{\partial\theta} = -\left(\cos\theta_0 - \frac{i\omega\theta_0}{v'\sin\theta_0}\right)\tilde{D}, \quad \text{at } \theta = \frac{\pi}{2} - \theta_0, \tag{3.68}$$

$$\frac{\partial R_E}{\partial \theta} = 0, \quad \frac{\partial \phi_E}{\partial \theta} = 0, \qquad \text{at } \theta = \frac{\pi}{2}. \tag{3.69}$$

This system of equations describe how the droplet 'spreads' over the substrate. One thing to notice from these equations is that γ can be scaled out of the equations by redefining each of the unknowns to scale linearly with γ. Now we will look at the other set of equations given by

$$\nabla^2 \phi_O = 0, \tag{3.70}$$

where

$$\omega \phi_O + \frac{\sin^2 \theta_0}{\theta_0} \left(\frac{\partial^2 R_O}{\partial \theta^2} + R_O \right) = \frac{\cos \theta}{\sin \theta_0} \left(1 - \omega \tilde{V} \right), \quad \text{on } r = R_0, \tag{3.71}$$

$$\omega R_O = \frac{\partial \phi_O}{\partial r}, \quad \text{on } r = R_0, \tag{3.72}$$

and

$$R_O = 0, \quad \frac{\partial \phi_O}{\partial \theta} = 0, \quad v' \frac{\sin \theta_0}{\theta_0} \frac{\partial R_O}{\partial \theta} = i\tilde{V}, \qquad \text{at } \theta = \frac{\pi}{2} - \theta_0, \tag{3.73}$$

$$R_O = 0, \quad \phi_O = 0, \qquad \text{at } \theta = \frac{\pi}{2}. \tag{3.74}$$

This is the other system of equations and it describes how the droplet 'sways' along the substrate. What these sets of equations show is that $\tilde{V}$ is only associated with the swaying mode whereas $\tilde{D}$ with the spreading mode. Later we will see the interaction between these produces a net velocity of the droplet.

Thin droplet asymptotic limit

In this section we will cover a method we will use to check our first order, time independent equations (3.58)-(3.62). What we will do is take the limit as $\theta_0 \to 0$ to find the shallow water limit of our equations in order to compare our model to [3]. We begin by scaling θ_0 out of our variables so that the domain remains bounded in this limit. We will start with

$$\theta = \frac{\pi}{2} - \theta_0 x, \tag{3.75}$$

which gives the limits $x \in [-1, 1]$. This means the derivatives become

$$\frac{\partial}{\partial \theta} = -\frac{1}{\theta_0}\frac{\partial}{\partial x}, \qquad \frac{\partial^2}{\partial \theta^2} = \frac{1}{\theta_0^2}\frac{\partial^2}{\partial x^2}.$$

Our other variable is redefined as

$$r = \frac{1}{\sin\theta_0} - \theta_0 y, \tag{3.76}$$

since this counteracts both the distance between the droplet and the horizontal axis tending to infinity and the thickness of the droplet tending to zero as $\theta_0 \to 0$. Similar to above the derivatives are given by

$$\frac{\partial}{\partial r} = -\frac{1}{\theta_0}\frac{\partial}{\partial y}, \qquad \frac{\partial^2}{\partial r^2} = \frac{1}{\theta_0^2}\frac{\partial^2}{\partial y^2},$$

however the limits are slightly more complicated. The free surface is given by the limit $y = 0$ whereas the other other limit is given by

$$\frac{\cot\theta_0}{\cos(\theta_0 x)} = \frac{1}{\sin\theta_0} - \theta_0 y,$$

which can be rearranged to

$$y = \frac{\cos(\theta_0 x) - \cos\theta_0}{\theta_0 \sin\theta_0 \cos(\theta_0 x)}.$$

As $\theta_0 \to 0$ the other boundary becomes

$$y = \frac{1 - x^2}{2} + O(\theta_0^2).$$

Now that we redefined our variables we will insert them into each of (3.58)-(3.62) and look at the small θ_0 limit. Starting with (3.58) we get

$$\frac{1}{\theta_0^2}\frac{\partial^2\tilde{\phi}}{\partial y^2} - \frac{\sin\theta_0}{\theta_0(1 - \theta_0\sin\theta_0 y)}\frac{\partial\tilde{\phi}}{\partial y} + \frac{\sin^2\theta_0}{\theta_0^2(1 - \theta_0\sin\theta_0 y)^2}\frac{\partial^2\tilde{\phi}}{\partial x^2} = 0,$$

which can be rearranged to give

$$\frac{\partial^2\tilde{\phi}}{\partial y^2} = \theta_0^2\left(\frac{\partial\tilde{\phi}}{\partial y} - \frac{\partial^2\tilde{\phi}}{\partial x^2}\right) + O(\theta_0^4). \tag{3.77}$$

From (3.77) we can expand $\tilde{\phi}$ asymptotically for small θ_0 as

$$\tilde{\phi}(x,y) = \phi_a(x,y) + \theta_0^2\phi_b(x,y) + ..., \tag{3.78}$$

and so inserting this into (3.77) we get

$$\frac{\partial^2\phi_a}{\partial y^2} = 0, \qquad \frac{\partial^2\phi_b}{\partial y^2} = \frac{\partial\phi_a}{\partial y} - \frac{\partial^2\phi_a}{\partial x^2}.$$

These can both be solved easily to give

$$\phi_a(x,y) = A(x)y + B(x), \tag{3.79}$$

$$\phi_b(x,y) = -\frac{1}{6}A''(x)y^3 + \frac{1}{2}\left(A(x) - B''(x)\right)y^2 + C(x)y + D(x). \tag{3.80}$$

Now we will apply the impermeability boundary condition in order to eliminate some of these unknowns. So if we take the first order, time independent version of (3.30), i.e.

$$\frac{\partial\tilde{\phi}}{\partial r} + \cot\theta\frac{1}{r}\frac{\partial\tilde{\phi}}{\partial\theta} = 0, \qquad \text{on } r = \frac{\cot\theta_0}{\sin\theta},$$

and replace the polar coordinates with our new variables we get

$$\frac{\partial\tilde{\phi}}{\partial y} + \frac{\sin\theta_0\tan(\theta_0 x)}{1 - \theta_0\sin\theta_0 y}\frac{\partial\tilde{\phi}}{\partial x} = 0, \qquad \text{on } y = \frac{1-x^2}{2} + O(\theta_0^2).$$

Again, by letting $\theta_0 \to 0$ this reduces to

$$\frac{\partial\tilde{\phi}}{\partial y} = -\theta_0^2 x\frac{\partial\tilde{\phi}}{\partial x} + O(\theta_0^4), \qquad \text{on } y = \frac{1-x^2}{2} + O(\theta_0^2),$$

and so by expanding $\tilde{\phi}$ the same way as before we get,

$$\frac{\partial\phi_a}{\partial y} = 0, \qquad \frac{\partial\phi_b}{\partial y} = -x\frac{\partial\phi_a}{\partial x}, \qquad \text{on } y = \frac{1-x^2}{2}. \tag{3.81}$$

Now if we insert (3.79)-(3.80) into (3.81) we get

$$A(x) = 0, \qquad C(x) = \left(\frac{1-x^2}{2}B'(x)\right)',$$

or

$$\phi_a = B(x), \quad \phi_b = -\frac{1}{2}B''(x)y^2 + \left(\frac{1-x^2}{2}B'(x)\right)' y + D(x). \tag{3.82}$$

Our next step now is to insert ϕ_a and ϕ_b into the free surface and the contact point boundary conditions in order to obtain the shallow water equations we want. So if we take (3.60) and replace the variables and $\tilde{\phi}$ we get

$$\omega\tilde{R}(x) = -\theta_0\left(\frac{1-x^2}{2}B'(x)\right)' + O(\theta_0^3).$$

From observation of this equation we know that we can use the expansion $\tilde{R}(x) = \theta_0 h(x) + O(\theta_0^3)$ and also if we replace $B'(x)$ with $u(x)$ we get

$$\omega h + \frac{\partial}{\partial x}\left(\frac{1-x^2}{2}u\right) = 0. \tag{3.83}$$

If we do the same for (3.59) we get

$$\begin{aligned}\omega\phi_a + \theta_0^2\omega\phi_b + \omega\tilde{V}\frac{\sin(\theta_0 x)}{\sin\theta_0} + \frac{\sin^2\theta_0}{\theta_0^2}\left(\frac{\partial^2 h}{\partial x^2} + \theta_0^2 h\right) \\ = \frac{1}{\sin\theta_0}\left(\sin(\theta_0 x) + \frac{\gamma}{\theta_0}(\cos(\theta_0 x) - \cos\theta_0)\right) + O(\theta_0^4), \quad \text{on } y = 0,\end{aligned}$$

and by letting $\theta_0 \to 0$ this becomes

$$\omega B(x) + \omega x\tilde{V} + \frac{\partial^2 h}{\partial x^2} = x + \gamma\frac{1-x^2}{2}.$$

If we differentiate this with respect to x it becomes

$$\omega u + \omega\tilde{V} + \frac{\partial^3 h}{\partial x^3} = 1 - \gamma x. \tag{3.84}$$

Finally we need to do the same thing for the boundary conditions at the contact points and so (3.61)-(3.62) become

$$h = \tilde{D}, \quad u = \pm\omega\tilde{D}, \quad \frac{\partial h}{\partial x} = \frac{1}{iv'}\tilde{V} \pm \left(\frac{\omega}{iv'} + 1\right)\tilde{D}, \qquad \text{at } x = \pm 1. \tag{3.85}$$

By taking (3.83),(3.84) and (3.85) and separating u and h into odd and even functions about $x = 0$ gives (3.26)-(3.31) in [3]. We can conclude from this section that our first order, time independent equations are accurate in the

limit of $\theta_0 \to 0$.

Low frequency asymptotic limit

We have a set of equations for both the spreading and swaying modes and now we will look at the case where $\omega \ll 1$. In order to do this we start with the swaying mode, equations (3.70)-(3.74), and expand our variables as

$$\phi_O(r,\theta) = \omega\phi_\beta(r,\theta) + ..., \quad R_O(\theta) = R_\alpha(\theta) + \omega R_\beta(\theta) + ..., \quad \tilde{V} = V_\alpha + \omega V_\beta + ..., \tag{3.86}$$

where we know $\boldsymbol{\nabla}\phi_O$ will equal zero up to order ω, and any constants will have to be zero since ϕ_O also needs to be odd. Inserting these expansions into (3.71)-(3.74) and taking the leading order terms gives

$$\frac{\partial^2 R_\alpha}{\partial\theta^2} + R_\alpha = \frac{\theta_0}{\sin^3\theta_0}\cos\theta, \tag{3.87}$$

where

$$R_\alpha = 0, \quad \text{at } \theta = \frac{\pi}{2}, \tag{3.88}$$

$$R_\alpha = 0, \quad \frac{\partial R_\alpha}{\partial\theta} = \frac{i\theta_0 V_\alpha}{v'\sin\theta_0}, \quad \text{at } \theta = \frac{\pi}{2} - \theta_0. \tag{3.89}$$

We will now solve these equations to find R and $\tilde{V}$ for the case where $\omega = 0$. Solving (3.87) and inserting the boundary conditions gives

$$R_\alpha = \frac{\theta_0}{2\sin^3\theta_0}\left[\theta_0\cot\theta_0\cos\theta - \left(\frac{\pi}{2} - \theta\right)\sin\theta\right],$$

$$V_\alpha = \frac{iv'}{2\sin\theta_0}A_0, \qquad A_0 = \frac{2\theta_0 - \sin(2\theta_0)}{1-\cos(2\theta_0)}.$$

Now we have the leading order solution we will solve the order ω terms, given by

$$\frac{\partial^2 R_\beta}{\partial\theta^2} + R_\beta = -\frac{\theta_0 V_\alpha}{\sin^3\theta_0}\cos\theta, \tag{3.90}$$

$$R_\beta = 0, \qquad \theta = \frac{\pi}{2}, \tag{3.91}$$

$$R_\beta = 0, \quad \frac{\partial R_\beta}{\partial\theta} = \frac{i\theta_0 V_\beta}{v'\sin\theta_0}, \qquad \theta = \frac{\pi}{2} - \theta_0. \tag{3.92}$$

These equations are solved almost identically to (3.87)-(3.89), giving

$$R_\beta = -\frac{\theta_0 V_\alpha}{2\sin^3\theta_0}\left[\theta_0\cot\theta_0\cos\theta - \left(\frac{\pi}{2}-\theta\right)\sin\theta\right],$$

$$V_\beta = -\frac{iv'}{2\sin\theta_0}V_\alpha A_0 = -V_\alpha^2.$$

We can now combine these back together and write

$$R_O = \frac{\theta_0}{2\sin^3\theta_0}\left(1-i\omega\tilde{V}_\alpha\right)\left[\theta_0\cot\theta_0\cos\theta - \left(\frac{\pi}{2}-\theta\right)\sin\theta\right] + ..., \tag{3.93}$$

$$\tilde{V} = \tilde{V}_\alpha\left(i+\omega\tilde{V}_\alpha\right) + ..., \qquad V_\alpha = i\tilde{V}_\alpha. \tag{3.94}$$

Since R_O is an odd function with respect to $\theta = \pi/2$ then we already know that mass is conserved. Now we have solved the odd mode in order to find $\tilde{V}$, we will also solve the even mode.

The even mode is more complicated to solve asymptotically compared to the odd mode since ϕ_E can be constant at leading order, and in fact will be needed in order to satisfy mass conservation. This means that for the even modes the variables will be expanded as

$$\begin{aligned}\phi_E(r,\theta) &= \frac{1}{\omega}\phi_{-1} + \phi_a + \omega\phi_b(r,\theta) + ..., \\ R_E(\theta) = R_a(\theta) + \omega R_b(\theta) + ..., \quad \tilde{D} &= D_a + \omega D_b + ...,\end{aligned} \tag{3.95}$$

where the ϕ_{-1} term is included to balance (3.65). Now inserting these into (3.65)-(3.69) and expanding gives the order 1 terms as

$$\frac{\partial^2 R_a}{\partial\theta^2} + R_a = \frac{\gamma}{\sin^3\theta_0}\left[\sin\theta - \left(\cos\theta_0 + \frac{\theta_0\sin\theta_0}{\gamma}\phi_{-1}\right)\right], \tag{3.96}$$

$$\frac{\partial R_a}{\partial\theta} = 0, \quad \text{at } \theta = \frac{\pi}{2}, \tag{3.97}$$

$$R_a = D_a\sin\theta_0, \quad \frac{\partial R_a}{\partial\theta} = -D_a\cos\theta_0, \quad \text{at } \theta = \frac{\pi}{2}-\theta_0. \tag{3.98}$$

Now, in order to solve for ϕ_{-1} we also need the equation

$$\int_{\pi/2-\theta_0}^{\pi/2+\theta_0} R_a(\theta)\mathrm{d}\theta = 0. \tag{3.99}$$

Solving (3.96) gives

$$R_a = \frac{\gamma}{2\sin^3\theta_0}\left[\left(\frac{\pi}{2}-\theta\right)\cos\theta + B\sin\theta - 2\left(\cos\theta_0 + \frac{\theta_0\sin\theta_0}{\gamma}\phi_{-1}\right)\right],$$

where B is a constant of integration. Inserting the boundary conditions at $\theta = \pi/2 - \theta_0$ gives

$$D_a\sin\theta_0 = \frac{\gamma}{2\sin^3\theta_0}\left[\left(1-\frac{2}{\gamma}\phi_{-1}\right)\theta_0\sin\theta_0 + (B-2)\cos\theta_0\right],$$

$$-D_a\cos\theta_0 = \frac{\gamma}{2\sin^3\theta_0}\left[(B-1)\sin\theta_0 - \theta_0\cos\theta_0\right].$$

Combining these equations gives

$$B = 1 + \cos^2\theta_0 + \frac{2}{\gamma}\phi_{-1}\theta_0\sin\theta_0\cos\theta_0,$$

$$D_a = \frac{\gamma}{2\sin\theta_0}\left[\frac{\theta_0 - \sin\theta_0\cos\theta_0}{\sin^2\theta_0} - \frac{2}{\gamma}\phi_{-1}\theta_0\right].$$

Now we need to apply the last constraint to solve for ϕ_{-1} and give us the spreading mode. Since our function is even about $\theta = \pi/2$ we can reduce the integral to

$$\int_{\pi/2-\theta_0}^{\pi/2} R_a(\theta)\mathrm{d}\theta = 0,$$

where

$$R_a = \frac{\gamma}{2\sin^3\theta_0}\left[\left(\frac{\pi}{2}-\theta\right)\cos\theta + \left(1+\cos^2\theta_0\right)\sin\theta - 2\cos\theta_0 + \frac{2}{\gamma}\phi_{-1}\theta_0\sin\theta_0\left(\cos\theta_0\sin\theta - 1\right)\right].$$

Looking at each part of this integral separately we get

$$\begin{aligned}\int_{\pi/2-\theta_0}^{\pi/2}\left(\frac{\pi}{2}-\theta\right)\cos\theta\mathrm{d}\theta &= \left[\left(\frac{\pi}{2}-\theta\right)\sin\theta\right]_{\pi/2-\theta_0}^{\pi/2} + \int_{\pi/2-\theta_0}^{\pi/2}\sin\theta\mathrm{d}\theta \\ &= \left[\left(\frac{\pi}{2}-\theta\right)\sin\theta - \cos\theta\right]_{\pi/2-\theta_0}^{\pi/2} \\ &= \sin\theta_0 - \theta_0\cos\theta_0,\end{aligned}$$

$$\int_{\pi/2-\theta_0}^{\pi/2}\sin\theta\mathrm{d}\theta = \sin\theta_0, \qquad \int_{\pi/2-\theta_0}^{\pi/2}\mathrm{d}\theta = \theta_0,$$

and so inserting R_a into the mass conservation constraint gives

$$\frac{2}{\gamma}\phi_{-1}\theta_0 = \frac{2+\cos^2\theta_0 - 3\theta_0\cot\theta_0}{\theta_0 - \sin\theta_0\cos\theta_0},$$

and so

$$D_a = \frac{\gamma}{2\sin\theta_0}\left(A_0 - \frac{2+\cos^2\theta_0 - 3\theta_0\cot\theta_0}{\theta_0 - \sin\theta_0\cos\theta_0}\right).$$

Now that we have the leading order solutions we will look at the order ω terms, given by

$$\frac{\partial^2 R_b}{\partial\theta^2} + R_b = -\frac{\theta_0\phi_a}{\sin^2\theta_0}, \tag{3.100}$$

$$\frac{\partial R_b}{\partial\theta} = 0, \quad \text{at } \theta = \frac{\pi}{2}, \tag{3.101}$$

$$R_b = D_b\sin\theta_0, \quad \frac{\partial R_b}{\partial\theta} = \frac{i\theta_0 D_a}{v'\sin\theta_0} - D_b\cos\theta_0, \quad \text{at } \theta = \frac{\pi}{2} - \theta_0. \tag{3.102}$$

Similar to before we will solve (3.100) to give

$$R_b = -\frac{\theta_0\phi_0}{\sin^2\theta_0}\left(1 + A\sin\theta\right),$$

where A is a constant of integration. Before applying the boundary conditions at $\theta = \pi/2 - \theta_0$ we will first apply the mass conservation constraint to give

$$A = -\frac{\theta_0}{\sin\theta_0}.$$

Now we will apply the boundary conditions to give

$$\phi_0 = \frac{iD_a\sin\theta_0}{v'A_0},$$

$$D_b = -\frac{i\theta_0 D_a}{v'}\frac{1-\theta_0\cot\theta_0}{\theta_0 - \sin\theta_0\cos\theta_0}.$$

Now if we combine the terms back together we get

$$\tilde{D} = D_a\left(1 - \omega\frac{i\theta_0}{v'}\frac{1-\theta_0\cot\theta_0}{\theta_0 - \sin\theta_0\cos\theta_0}\right) + ... \tag{3.103}$$

We have now finished our low frequency asymptotic limit of (3.58)-(3.62) and have some more results we can compare to our other solution methods.

Conformal mapping

An alternative way to solving (3.58) - (3.62) is to map the domain from a droplet to the upper half of the imaginary plane, using the transformation

$$w = \left(\frac{1 + z - i \cot \theta_0}{1 - z + i \cot \theta_0} \right)^{\pi/\theta_0}. \tag{3.104}$$

This will map the base of the droplet onto the positive real line and the surface of the droplet onto the negative real line with the point $x = -1$, $y = \cot \theta_0$ becoming the origin. Although this method seems unnecessary and mathematically more complicated, it produces an integral which is numerically simpler to solve and so, from our point of view, worth doing. We will now set up the equations along the line $v = 0$ where first of all the impermeability condition will still hold on the base of the droplet and so

$$\frac{\partial \tilde{\phi}}{\partial n} = \frac{\partial \tilde{\phi}}{\partial v} = 0, \quad \text{for } u > 0, \quad v = 0. \tag{3.105}$$

Next we will transform the kinematic condition on the surface of the droplet, which is

$$\frac{\partial \tilde{\phi}}{\partial r} = \omega \tilde{R}, \quad \text{on } r = \frac{1}{\sin \theta_0}. \tag{3.106}$$

By differentiating (3.104) with respect to z and letting $r = 1/\sin\theta_0$ we get

$$\boldsymbol{\nabla} w = (i, -1) \frac{\pi \sin^2 \theta_0}{\theta_0 (\sin \theta - \cos \theta_0)} \left(\frac{e^{i(\theta_0 - \pi/2)} + e^{i\theta}}{e^{-i(\theta_0 - \pi/2)} - e^{i\theta}} \right)^{\pi/\theta_0}, \tag{3.107}$$

or more simply $\boldsymbol{\nabla} w = (i, -1) b(\theta)$, where $b(\theta)$ is a real function of θ. Now we can convert (3.106) into

$$\frac{\partial \tilde{\phi}}{\partial u} \frac{\partial u}{\partial r} + \frac{\partial \tilde{\phi}}{\partial v} \frac{\partial v}{\partial r} = \omega \tilde{R},$$

and since $\frac{\partial w}{\partial r} = i \frac{\partial v}{\partial r}$ this becomes

$$\frac{\partial \tilde{\phi}}{\partial v} = \frac{\omega \tilde{R}(\theta)}{b(\theta)}, \quad \text{for } u < 0, \quad v = 0. \tag{3.108}$$

Since $\frac{\partial\tilde{\phi}}{\partial v} = 0$ along the positive real line the solution of Laplace's equation can be written as

$$\tilde{\phi}(u,0) - \phi_\infty = \frac{1}{\pi}\int_{-\infty}^{0} \left.\frac{\partial\tilde{\phi}}{\partial v}\right|_{v=0} \ln|u-\xi|\,\mathrm{d}\xi, \tag{3.109}$$

where ϕ_∞ is a constant required so that $\tilde{\phi} - \phi_\infty \to 0$ as $u \to \pm\infty$. Now we can transform (3.109) into polar coordinates to give

$$\tilde{\phi}(1/\sin\theta_0,\theta) = \phi_\infty - \frac{\omega}{\pi\sin\theta_0}\int_{\pi/2-\theta_0}^{\pi/2+\theta_0} \tilde{R}(\hat{\theta})\ln\left|u(\theta)-u(\hat{\theta})\right|\mathrm{d}\hat{\theta}, \tag{3.110}$$

where

$$u(\theta) = \left(\frac{e^{i(\theta_0-\pi/2)}+e^{i\theta}}{e^{-i(\theta_0-\pi/2)}-e^{i\theta}}\right)^{\pi/\theta_0}. \tag{3.111}$$

We can now use (3.110) to eliminate $\tilde{\phi}$ and $\frac{\partial\tilde{\phi}}{\partial r}$ from the problem and so the new system of equations is

$$\begin{aligned}\frac{\sin^3\theta_0}{\theta_0}\left(\frac{\partial^2\tilde{R}}{\partial\theta^2}+\tilde{R}\right) - \frac{\omega^2}{\pi}\int\tilde{R}(\hat{\theta})\ln\left|u(\theta)-u(\hat{\theta})\right|\mathrm{d}\hat{\theta} + \omega\tilde{V}\cos\theta \\ = \cos\theta + \frac{\gamma}{\theta_0}(\sin\theta-\cos\theta_0) - \omega\phi_\infty\sin\theta_0,\end{aligned} \tag{3.112}$$

where

$$\tilde{R} = \tilde{D}\sin\theta_0, \quad \frac{\partial\tilde{R}}{\partial\theta} - \frac{i\theta_0\tilde{V}}{v'\sin\theta_0} \pm \left(\cos\theta_0 - \frac{i\omega\theta_0}{v'\sin\theta_0}\right)\tilde{D} = 0, \quad \text{at } \theta = \frac{\pi}{2}\mp\theta_0. \tag{3.113}$$

Since we now also have a new unknown ϕ_∞ we will apply mass conservation in the form

$$\int_{\pi/2-\theta_0}^{\pi/2+\theta_0}\tilde{R}(\theta)\mathrm{d}\theta = 0. \tag{3.114}$$

Now we have an integral equation to solve for R using the numerical solution method in section 3.3.2.

3.2.4 Second order terms

When deriving the first order asymptotic equations, (3.57) shows that all the terms in the solution are periodic and so the resulting droplet will not have any net motion on the substrate. In order to examine the rise velocity of the

droplet, we need to expand the system of equations further than the first order terms and find the steady part of the second order terms. Since we are looking for the steady terms, ϕ_2 can be uncoupled from the rest of the problem and so we will only look at the second order expansion of (3.20), along with the boundary conditions for R_2. Again we obtain the second order equations from section 3.2.2 giving

$$\begin{aligned}\left.\frac{\partial\phi_2}{\partial t}\right|_{r=R_0} + R_1\left.\frac{\partial^2\phi_1}{\partial t\partial r}\right|_{r=R_0} + \frac{dV_2}{dt}\frac{\cos\theta}{\sin\theta_0} + \frac{dV_1}{dt}R_1\cos\theta + \frac{1}{2}|\boldsymbol{\nabla}\phi_1|^2_{r=R_0} \\ = \frac{\sin^2\theta_0}{\theta_0}\left(\frac{\partial^2 R_2}{\partial\theta^2} + R_2\right) - \frac{\sin^3\theta_0}{\theta_0}\left(R_1^2 + \frac{1}{2}\left(\frac{\partial R_1}{\partial\theta}\right)^2 + 2R_1\frac{\partial^2 R_1}{\partial\theta^2}\right) \\ - \left(\frac{g}{\sin\theta_0} + \sin(\omega t)R_1\right)\left(\cos\theta + \frac{\gamma}{\theta_0}\sin\theta\right),\end{aligned} \tag{3.115}$$

where

$$R_2 = D_2\sin\theta_0 + D_1\sin\theta_0\cos\theta_0\left(\frac{1}{2}D_1\cos\theta_0 \pm \frac{\partial R_1}{\partial\theta}\right), \quad \text{at } \theta = \frac{\pi}{2}\mp\theta_0, \tag{3.116}$$

$$\begin{aligned}\frac{\partial R_2}{\partial\theta} - \frac{\theta_0 V_2}{v'\sin\theta_0} \pm \left(\cos\theta_0 D_2 - \frac{\theta_0}{v'\sin\theta_0}\frac{dD_2}{dt}\right) \\ = \sin\theta_0 R_1\frac{\partial R_1}{\partial\theta} \pm \left(R_1^2 + R_1\frac{\partial^2 R_1}{\partial\theta^2}\right)\cos\theta_0 - \frac{v''\sin\theta_0}{2v'\theta_0}\left\{2\cos\theta_0 D_1\frac{\partial R_1}{\partial\theta}\right. \\ \left. \pm \left[\cos^2\theta_0 D_1^2 + \left(\frac{\partial R_1}{\partial\theta}\right)^2\right]\right\}, \quad \text{at } \theta = \frac{\pi}{2}\mp\theta_0.\end{aligned} \tag{3.117}$$

Now if we extract only the steady parts of these equations, ignoring any periodic terms, we get

$$\begin{aligned}2\left(\frac{\partial^2\bar{R}_2}{\partial\theta^2} + \bar{R}_2\right) = \left(\sin\theta_0 - \frac{\omega\theta_0}{2\sin^2\theta_0}\right)|\tilde{R}|^2 + \frac{\sin\theta_0}{2}\left|\frac{\partial\tilde{R}}{\partial\theta}\right|^2 + \frac{\theta_0}{2}\left|\frac{\partial\tilde{\phi}}{\partial\theta}\right|^2 + \\ \frac{\theta_0 g}{\sin^3\theta_0}\left(\cos\theta + \frac{\gamma\sin\theta}{\theta_0}\right) + \frac{\theta_0}{\sin^2\theta_0}\Re\left\{\left(\cos\theta + \frac{\gamma\sin\theta}{\theta_0}\right)\tilde{R} + \frac{2\sin^3\theta_0}{\theta_0}\tilde{R}\frac{\partial^2\tilde{R}^*}{\partial\theta^2}\right. \\ \left. -\omega\tilde{R}\tilde{V}^*\cos\theta\right\},\end{aligned} \tag{3.118}$$

where

$$\bar{R}_2 - \bar{D}_2 \sin\theta_0 = \frac{1}{2}\sin\theta_0\cos\theta_0\left[\frac{1}{2}\cos\theta_0|\tilde{D}|^2 \pm \Re\left\{\tilde{D}\frac{\partial\tilde{R}^*}{\partial\theta}\right\}\right], \quad \text{at } \theta = \frac{\pi}{2} \mp \theta_0, \tag{3.119}$$

$$\begin{aligned}\frac{\partial\bar{R}_2}{\partial\theta} \pm \bar{D}_2 - \frac{\theta_0}{v'\sin\theta_0}\bar{V}_2 = \frac{\sin\theta_0}{2}\Re\left\{\tilde{R}\frac{\partial\tilde{R}^*}{\partial\theta} + \cot\theta_0\tilde{R}\frac{\partial^2\tilde{R}^*}{\partial\theta^2} - \frac{v''\cos\theta_0}{v'\theta_0}\tilde{D}\frac{\partial\tilde{R}^*}{\partial\theta}\right\} \\ \pm\left[\frac{\cos\theta_0}{2}|\tilde{R}|^2 - \frac{v''\sin\theta_0}{4v'\theta_0}\left(\cos^2\theta_0|\tilde{R}|^2 + \left|\frac{\partial\tilde{R}}{\partial\theta}\right|^2\right)\right], \quad \text{at } \theta = \frac{\pi}{2} \mp \theta_0,\end{aligned} \tag{3.120}$$

We can now use the solution to the first order equations in order to solve this simple second order ordinary differential equation for $\bar{R}_2$, and use the extra boundary conditions to find the constant part of V_2, which we will call V_r. We have two different solutions to the two-dimensional inertia problem; one which solves for the full problem and one which solves the asymptotic solution up to the order ϵ^2. Before comparing the two solutions we will first look at another method for finding the rise velocity.

Force balance

We can calculate the rise velocity of the droplet either by solving for the second order terms in the asymptotic expansion of the equations, or a much easier method is to integrate the momentum equations over the domain, and an oscillation period, to find the average rise velocity. Similar to equations derived previously, the equations for the droplet in a moving reference frame are

$$\frac{d\mathbf{u}}{dt} + \frac{dV_s}{dt}\hat{\mathbf{x}} = \frac{1}{\theta_0}\kappa + \epsilon\mathbf{f}, \tag{3.121}$$

where $\mathbf{f} = -a(1, \gamma/\theta_0)$. Along with the momentum equation we also have

$$\boldsymbol{\nabla}\cdot\mathbf{u} = 0, \tag{3.122}$$

and

$$y = 0, \quad \frac{dx}{dt} = \pm V(\theta_\pm) - V_s, \qquad \text{at } x = \pm D. \tag{3.123}$$

Using Reynold's transport theorem,

$$\frac{d}{dt}\left(\int_{A_0}\mathbf{u}\mathrm{d}A\right)=\int_{A_0}\frac{d\mathbf{u}}{dt}\mathrm{d}A+\int_{A_0}(\boldsymbol{\nabla}\cdot\mathbf{u})\mathbf{u}\mathrm{d}A=\int_{A_0}\frac{d\mathbf{u}}{dt}\mathrm{d}A,$$

the momentum equation can be integrated to become

$$\begin{aligned}\frac{d}{dt}\left(\int_{A_0}\mathbf{u}\mathrm{d}A+V_sA_0\hat{\mathbf{x}}\right)=&\frac{1}{\theta_0}\int_{A_0}\boldsymbol{\nabla}\kappa\mathrm{d}A+\epsilon\mathbf{f}A_0,\\=&\frac{1}{\theta_0}\int_{-D}^{D}\mathbf{n}\kappa\mathrm{d}S+\epsilon\mathbf{f}A_0.\end{aligned}$$

The $x-$component of this equation is given by

$$\frac{d}{dt}\left(\int_{A_0}u\mathrm{d}A+V_sA_0\right)=\frac{1}{\theta_0}\int_{-D}^{D}n_x\kappa\mathrm{d}S-\epsilon aA_0, \tag{3.124}$$

and if we express the surface of the droplet as $y=h(x,t)$ we get

$$n_x=-\frac{\partial h}{\partial x}\left(1+\left(\frac{\partial h}{\partial x}\right)^2\right)^{-1/2},\quad \kappa=\frac{\partial^2 h}{\partial x^2}\left(1+\left(\frac{\partial h}{\partial x}\right)^2\right)^{-3/2},$$

$$\mathrm{d}S=\sqrt{1+\left(\frac{\partial h}{\partial x}\right)^2}\mathrm{d}x.$$

Now if we insert each of the into the curvature integral in (3.124) we get

$$\int_{\partial V_0}n_x\kappa\mathrm{d}S=\left[\left(1+\left(\frac{\partial h}{\partial x}\right)^2\right)^{-1/2}\right]_{-D}^{D}.$$

We also know that

$$\frac{\partial h}{\partial x}=\mp\tan\theta_{\pm},\quad \text{at } x=\pm D,$$

giving

$$\overline{\cos\theta_+-\cos\theta_-}=\theta_0\epsilon\bar{a}A_0. \tag{3.125}$$

By rearranging (3.24), we get

$$\theta_{\pm}=\theta_0\left[1+\frac{V_{\pm}}{v'}-\frac{v''}{2v'}\left(\frac{V_{\pm}}{v'}\right)^2+\ldots\right],$$

and so

$$\overline{\cos\theta_+ - \cos\theta_-} = -\frac{2}{v'}\theta_0 \sin\theta_0 \left[\overline{V_s} - \frac{1}{v'}\left(\frac{v''}{v'} - \theta_0 \cot\theta_0\right)\overline{V_s \frac{dD}{dt}}\right] + ... \quad (3.126)$$

Now if we combine (3.125) and (3.126) and rearrange we get

$$\overline{V_s} = \frac{1}{v'}\left(\frac{v''}{v'} - \theta_0 \cot\theta_0\right)\overline{V_s \frac{dD}{dt}} - \epsilon^2 \frac{gA_0 v'}{2\sin\theta_0}. \quad (3.127)$$

Using (3.32) along with the first order asymptotic solutions for D_1 and V_1 we get the mean velocity as

$$V_r = \epsilon^2 \left[\frac{\omega}{2v'}\left(\frac{v''}{v'} - \theta_0 \cot\theta_0\right)\Re\left(\tilde{V}\tilde{D}^*\right) - \frac{gv'}{2\sin\theta_0}\frac{2\theta_0 - \sin(2\theta_0)}{1-\cos(2\theta_0)}\right]. \quad (3.128)$$

This is the rise velocity of the droplet, when the amplitude is small, and we have obtained vital information about the mechanism of the phenomenon using this equation. First of all we can see that when ϵ is small the rise velocity is proportional to ϵ^2, this again tells us that the leading order motion of the droplet produces zero net motion. We can also see that the rise velocity is made up of two terms which we can write as

$$V_r/\epsilon^2 = V_\omega + V_g. \quad (3.129)$$

The first term, V_ω is the result of the oscillating substrate and so depends on the frequency of the oscillations as well as the real part of $\tilde{V}\tilde{D}^*$. This shows us that it is the interaction between the two modes which allows the droplet to climb uphill. The second term, V_g, depends on the strength of gravity relative to oscillations and for a fixed droplet size, and will apply a negative shift to the value of the rise velocity.

We can now use (3.128) to look at how the rise velocity changes with the magnitude of the contact angles. In the limit of $\theta_0 \to 0$ (3.128) reduces to

$$V_r = \epsilon^2 \left[\frac{\omega}{2v'}\left(\frac{v''}{v'} - 1\right)\Re\left(\tilde{V}\tilde{D}^*\right) - \frac{gv'}{3}\right], \quad (3.130)$$

which is the same as (3.44) from [3] (with a factor of 2/3 difference which needs correcting in [3]). When comparing (3.128) and (3.130) we can see that the only differences between the equations are two separate functions of

θ_0. The first function comes from the more complicated approximation of the curvature for thick droplets whilst the second is the area of the two-dimensional droplet. As the magnitude of the contact angles increases the first of these terms decreases until reaching zero at $\theta_0 = \pi/2$. As the magnitude increases further this term continues to become increasingly negative up to point where it tends to minus infinity as θ_0 tends to π. The area of the droplet grows positively as θ_0 increases and tends to infinity as θ_0 tends to π. The reason for this is that physically the limit of $\theta_0 \to \pi$ represents a completely non-wetting fluid however, due to dimensional scalings, the droplet is always in contact with the substrate in range $x \in [-1, 1]$. Due to this the size of the droplet has to increase substantially to negate the liquid/solid interface and so this is why the area of the droplet increases as such. The rates at which these two functions grow are

$$\theta_0 \cot\theta_0 \propto -\frac{\pi}{\pi - \theta_0}, \qquad \frac{A_0}{\sin\theta_0} \propto \frac{\pi}{(\pi - \theta_0)^3}, \qquad \text{as } \theta_0 \to \infty.$$

What this means is as the droplets become increasingly non-wetting, the rise velocity of the droplet is dominated by the affects of gravity over the oscillations of the substrate.

To summarise, the small amplitude asymptotic approximation has shown that the leading order motion of the droplet (for small ϵ) is a combination of two periodic modes. Although these modes give zero net motion on their own, we can see from (3.128) that the non-linear interaction between them is what causes the droplet to climb up the substrate. We have also shown that the small contact angle limit gives us the shallow water equivalent model as required. We now have the full method, as well as two small amplitude methods, to obtain the rise velocity and so in the next section we will outline the solution methods for (3.19)-(3.23), the first and second order asymptotic equations and the conformal mapping equations.

3.3 Numerical solution method

3.3.1 The full problem

In this section we will cover the solution method that we will use to solve (3.19)-(3.23) numerically, as well as some problems that arise due to this method and

how we will fix them. Apart from (3.19) the rest of our equations are on the surface of the droplet (or the contact points) and so in order to simplify the problem we will use the boundary integral method [31] to replace (3.19) with an integral equation on the boundary. Since we have reduced the solution domain to the surface of the droplet we can discretise this into N straight elements and solve our system at each node. To deal with the time dependency we will use implicit time stepping to find x, y, ϕ and V_s at time t using a previous time $t - \Delta t$. The reasons for using an implicit time step are to deal with the stiffness of the system and, more importantly, the evolution of the contact points. The latter of these is important since the velocity of the nodes at the contact points is a function of the contact angles and so using the droplet's shape at a previous time would not be numerically stable. We will begin by transforming (3.21) into

$$\frac{d\mathbf{x}}{dt} = \frac{\partial \phi}{\partial n}\mathbf{n} + T\mathbf{s},$$

where $\mathbf{n}, \mathbf{s}$ are the normal and tangential vectors at the surface and T at each node will be the spring function (2.52), keeping the grid spacing between each node equal. We can therefore write this in discretised form as

$$\frac{\mathbf{x}_i - \mathbf{x}_i^{t-\Delta t}}{\Delta t} - \left(\frac{\partial \phi}{\partial n}\right)_i \mathbf{n}_i - T_i \mathbf{s}_i = 0, \qquad \text{for } i = 2, ..., N. \tag{3.131}$$

Next we will discretise (3.20) but first we will need to replace the partial derivative with respect to t with a full derivative. To do this we will use

$$\frac{\partial \phi}{\partial t} = \frac{d\phi}{dt} - \frac{d\mathbf{x}}{dt} \cdot \boldsymbol{\nabla}\phi = \frac{d\phi}{dt} - \left(\frac{\partial \phi}{\partial n}\right)^2 - T\frac{\partial \phi}{\partial s},$$

meaning that (3.20) transforms into

$$\begin{aligned} \frac{\phi_i - \phi_i^{t-\Delta t}}{\Delta t} - \frac{1}{2}\left(\frac{\partial \phi}{\partial n}\right)_i^2 + \frac{1}{2}\left(\frac{\partial \phi}{\partial s}\right)_i^2 - T_i\left(\frac{\partial \phi}{\partial s}\right)_i + \frac{V_s - V_s^{t-\Delta t}}{\Delta t} x_i \\ - \frac{1}{\theta_0}\kappa_i + \epsilon a\left(x_i + \frac{\gamma}{\theta_0} y_i\right) = 0, \end{aligned} \tag{3.132}$$

for $i = 2, .., N$. As well as these time dependent equations we will also need to discretise 6 boundary conditions for x, y and ϕ as well as an extra one for

V_s. So by discretising (3.23) we get

$$\frac{x_1 - x_1^{t-\Delta t}}{\Delta t} + V_s + V(\theta_-) = 0, \qquad \frac{x_{N+1} - x_{N+1}^{t-\Delta t}}{\Delta t} + V_s - V(\theta_+) = 0, \tag{3.133}$$

$$y_1 = 0, \qquad y_{N+1} = 0, \tag{3.134}$$

$$\begin{aligned} \frac{\phi_3 - 4\phi_2 + 3\phi_1}{2|\mathbf{x_2} - \mathbf{x_1}|} + \frac{x_1 - x_1^{t-\Delta t}}{\Delta t}\cos\theta_- = 0, \\ \frac{\phi_{N-1} - 4\phi_N + 3\phi_{N+1}}{2|\mathbf{x_{N+1}} - \mathbf{x_N}|} - \frac{x_{N+1} - x_{N+1}^{t-\Delta t}}{\Delta t}\cos\theta_+ = 0, \end{aligned} \tag{3.135}$$

with the extra condition given by

$$x_1 + x_{N+1} = 0. \tag{3.136}$$

Although we have now approximated (3.19)-(3.23) as a set of nodes there are still some terms listed which we have not yet explained how to approximate. The curvature and unit normal on the surface (denoted by κ_i and $\mathbf{n}_i$ respectively), as well as the contact angles $\theta_\pm$, will be approximated using curved arcs across sets of 3 grid points. The tangential derivative of ϕ will be found using a finite difference method whilst the normal derivative we will obtain from the boundary integral equation. These approximation methods are covered in the following sections.

Curved arc approximations

In order to approximate κ and $\mathbf{n}$ at each node, as well as $\theta_\pm$ at the contact points, we will look at sets of three adjacent nodes and join them using a curve. We will then use this curve to find a midpoint $\mathbf{x}_p^{(i)}$, which is an equal distance away from each node, and the radius R_i, which is the length of this distance. So for the points $\mathbf{x}_{i-1}$, $\mathbf{x}_i$ and $\mathbf{x}_{i+1}$ the midpoint is given by

$$\begin{aligned} y_p^{(i)} = \frac{1}{2}\frac{(y_{i+1}^2 - y_i^2)(x_i - x_{i-1}) - (y_i^2 - y_{i-1}^2)(x_{i+1} - x_i)}{(y_{i+1} - y_i)(x_i - x_{i-1}) - (y_i - y_{i-1})(x_{i+1} - x_i)} \\ - \frac{1}{2}\frac{(x_{i+1} - x_i)(x_i - x_{i-1})(x_{i-1} - x_{i+1})}{(y_{i+1} - y_i)(x_i - x_{i-1}) - (y_i - y_{i-1})(x_{i+1} - x_i)}, \end{aligned} \tag{3.137}$$

$$x_p^{(i)} = \frac{1}{2}\left[x_i + x_{i-1} - \frac{(y_i - y_{i-1})(2y_p^{(i)} - y_i - y_{i-1})}{x_i - x_{i-1}}\right], \tag{3.138}$$

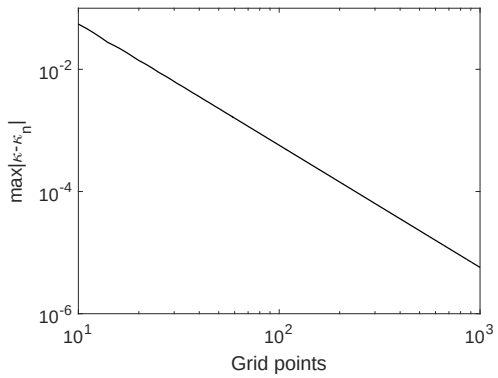


Figure 3.3: The rate of convergence for the maximum difference between the numerical and analytical solutions to the curvature against the amount of grid points. The logarithmic plot has a gradient of -2.

and the radius is

$$R_i = \sqrt{\left(x_i - x_p^{(i)}\right)^2 + \left(y_i - y_p^{(i)}\right)^2}. \tag{3.139}$$

Using these we can calculate the curvature and unit normal for each node on the free surface as

$$\kappa_i = \pm\frac{1}{R_i}, \quad n_x^{(i)} = \pm\frac{x_p^{(i)} - x_i}{R_i}, \quad n_y^{(i)} = \pm\frac{y_p^{(i)} - y_i}{R_i}, \tag{3.140}$$

where the plus or minus are decided by $d_i \gtrless 0$, where

$$d_i = \left(x_i - x_p^{(i)}\right)(y_{i+1} - y_{i-1}) - \left(y_i - y_p^{(i)}\right)(x_{i+1} - x_{i-1}). \tag{3.141}$$

We can also use these arcs to calculate $\theta_\pm$ at the contact points as

$$\theta_- = \frac{\pi}{2} + \tan^{-1}\left(\frac{y_p^{(2)} - y_1}{x_p^{(2)} - x_1}\right), \quad \theta_+ = \frac{\pi}{2} + \tan^{-1}\left(\frac{y_p^{(N)} - y_{N+1}}{x_p^{(N)} - x_{N+1}}\right). \tag{3.142}$$

In order to test these approximations we will compare it to an analytical solution using the simple example

$$h(x) = \left(\frac{1}{2} + x\right)\left(\frac{1}{4} - x^2\right)^2, \quad \text{for } x \in \left[-\frac{1}{2}, \frac{1}{2}\right].$$

We have chosen this since it creates a droplet shape similar to those produced by the model whilst being simple enough to differentiate twice in order to calculate the curvature. The convergence rate for the maximum difference

between the numerical and analytical solutions of the curvature is shown in figure 3.3. The solution is converging with grid spacing squared, as it should, showing our method for calculating $\kappa, \mathbf{n}$ and $\theta_\pm$ is correct.

Laplace's equation

If we look at (3.19)-(3.23) we can see that apart from Laplace's equation, the rest of our system only requires knowledge of the free surface in order to solve the problem. Now if we use the boundary integral method we are able to replace Laplace's equation with

$$\frac{1}{2}f(\mathbf{x_0},t) = \int_{\partial\mathcal{R}(t)} G(\mathbf{x};\mathbf{x_0})\frac{\partial f}{\partial n}(\mathbf{x},t)\mathrm{d}l(\mathbf{x}) - \int_{\partial\mathcal{R}(t)} \frac{\partial G}{\partial n}(\mathbf{x};\mathbf{x_0})f(\mathbf{x},t)\mathrm{d}l(\mathbf{x}), \tag{3.143}$$

where $f(\mathbf{x},t)$ is the function that Laplace's operator was being applied to and $\mathbf{x_0}$ is on the boundary $\partial\mathcal{R}$. This reduces the solution domain to the free surface meaning we no longer need to solve throughout the rest of the fluid. When solving the full system of equations we will use this method to approximate $\partial\phi/\partial n$ at each node given ϕ however, we know from section 3.2.2, when ϵ is small the function ϕ is an order ϵ larger than the normal derivative of ϕ. This can cause the solution to be unstable over a large number of time steps. In order to overcome this we will introduce the stream function ψ that can be defined as

$$\frac{\partial\phi}{\partial s} = -\frac{\partial\psi}{\partial n}, \tag{3.144}$$

$$\frac{\partial\phi}{\partial n} = \frac{\partial\psi}{\partial s}, \tag{3.145}$$

and use (3.143) to instead find ψ given its normal derivative, obtained using (3.144). From here we can then use (3.145) to find $\partial\phi/\partial n$ from ψ. The reason we need to cover whether we are using ϕ or ψ is that it will change the Green's function we need. The boundary we are integrating over is made up of the free surface $\mathbf{X}(s,t)$ as well as the base of the droplet $y=0$. We know that along the base the normal derivative of the velocity potential is zero and the stream function is an arbitrary constant (which we will set to zero). This means that if we use a Green's function of the form

$$G^{\pm}(\mathbf{x};\mathbf{x_0}) = -\frac{1}{2\pi}\left[\ln|\mathbf{x}-\mathbf{x_0}| \pm \ln\sqrt{(x-x_0)^2+(y+y_0)^2}\right], \tag{3.146}$$

where we use plus for solving ϕ and minus for ψ, we can reduce the integral to just the free surface. Now we have our Green's functions we will need to discretise the boundary into N straight elements and integrate across each of them. If we assume that the function f and the normal derivative of f are both constant on these elements, we can reduce (3.143) to

$$\pi f(\mathbf{x_0}, t) = \sum_{i=1}^{N} \left[\beta_i^{\pm}(\mathbf{x_0}, t) f_i(t) - \alpha_i^{\pm}(\mathbf{x_0}, t) g_i(t)\right], \tag{3.147}$$

where g_i is the normal derivative of f on the ith element (E_i),

$$\alpha_i^{\pm}(\mathbf{x_0}, t) = \int_{E_i} \left[\ln|\mathbf{x} - \mathbf{x_0}| \pm \ln\sqrt{(x - x_0)^2 + (y + y_0)^2}\right] \mathrm{d}l(\mathbf{x}),$$

and

$$\beta_i^{\pm}(\mathbf{x_0}, t) = \int_{E_i} \left[\frac{\mathbf{n} \cdot (\mathbf{x} - \mathbf{x_0})}{|\mathbf{x} - \mathbf{x_0}|^2} \pm \frac{n_x(x - x_0) + n_y(y + y_0)}{(x - x_0)^2 + (y + y_0)^2}\right] \mathrm{d}l(\mathbf{x}).$$

Now we need to solve the integral on each element. Unlike in section 2.2 we only need to integrate logarithmic functions which, unlike the Bessel and Modified Bessel functions, we can do analytically. Therefore for this model we will not be using the Gauss-Legendre quadrature to solve our boundary integral equation; unlike Model 1. Since we have approximated each element to be straight, we can write

$$\mathbf{x}^{(i)} = \mathbf{x_i} + \mathbf{x_{21}} u, \quad \text{for } u \in [0, 1],$$

where $\mathbf{x_{21}} = \mathbf{x_{i+1}} - \mathbf{x_i}$, and so on each element

$$\mathrm{d}l = |\mathbf{x_{21}}| \mathrm{d}u, \quad \mathbf{n} = \frac{(-y_{21}, x_{21})}{|\mathbf{x_{21}}|}.$$

If we insert these into $\alpha_i^{\pm}$ and $\beta_i^{\pm}$ we get

$$\alpha_i^{\pm}(\mathbf{x_0}, t) = |\mathbf{x_{21}}| \left[\int_0^1 \ln\sqrt{(x_{10} + x_{21}u)^2 + (y_{10} + y_{21})^2} \mathrm{d}u \right.$$
$$\left. \pm \int_0^1 \ln\sqrt{(x_{10} + x_{21}u)^2 + (\bar{y}_{10} + y_{21}u)^2} \mathrm{d}u\right],$$

and

$$\beta_i^{\pm}(\mathbf{x_0}, t) = \left[\int_0^1 \frac{x_{21}y_{10} - y_{21}x_{10}}{(x_{10} + x_{21}u)^2 + (y_{10} + y_{21}u)^2}\mathrm{d}u \right. \\ \left. \pm \int_0^1 \frac{x_{21}\bar{y}_{10} - y_{21}x_{10}}{(x_{10} + x_{21}u)^2 + (\bar{y}_{10} + y_{21}u)^2}\mathrm{d}u\right],$$

where $\mathbf{x}_{10} = \mathbf{x_i} - \mathbf{x_0}$ and $\bar{y}_{10} = y_i + y_0$. If we compare the two integrals in either $\alpha_i^{\pm}$ or $\beta_i^{\pm}$ we can see that they are the same, only the left integral for each contains y_{10} whilst the right integral contains $\bar{y}_{10}$. This means we only need to solve the two left integrals and just write down the others. We will begin with the first half of $\beta_i^{\pm}$ which can be rearranged to look like

$$I_\beta = \int_0^1 \frac{x_{21}y_{10} - x_{10}y_{21}}{|\mathbf{x_{10}}|^2 + 2(x_{10}x_{21} + y_{10}y_{21})u + |\mathbf{x_{21}}|^2u^2}\mathrm{d}u.$$

To solve this integral we will begin by completing the square on the denominator and then by using the substitution

$$|\mathbf{x_{21}}|^2u + x_{10}x_{21} + y_{10}y_{21} = (x_{21}y_{10} - x_{10}y_{21})\tan v,$$

we get the solution to the integral as

$$I_\beta = \tan^{-1}\left(\frac{b_-}{a_- + m_-^2}\right),$$

or in terms of the full solution

$$\beta_i^{\pm}(\mathbf{x_0}, t) = \tan^{-1}\left(\frac{b_-}{a_- + m_-^2}\right) \pm \tan^{-1}\left(\frac{b_+}{a_+ + m_+^2}\right). \tag{3.148}$$

where

$$a_\pm = x_{10}x_{21} + (y_i \pm y_0)y_{21}, \quad b_\pm = x_{21}(y_i \pm y_0) - x_{10}y_{21}, \quad m_\pm^2 = x_{10}^2 + (y_i \pm y_0)^2.$$

Now we will again do this but for the first part of $\alpha_i^{\pm}$, which expands to gives

$$\begin{aligned}
I_\alpha &= \int_0^1 \ln\sqrt{\left(|\mathbf{x_{21}}|^2 u + \mathbf{x_{10}}\cdot\mathbf{x_{21}}\right)^2 + |\mathbf{x_{10}}|^2|\mathbf{x_{21}}|^2 - (\mathbf{x_{10}}\cdot\mathbf{x_{21}})^2}\mathrm{d}u \\
&\qquad\qquad - \ln|\mathbf{x_{21}}|, \\
&= \frac{b_-}{|\mathbf{x_{21}}|^2}\int_{u=0}^{u=1} \sec^2 v \ln\sqrt{b_-^2\sec^2 v}\mathrm{d}v - \ln|\mathbf{x_{21}}|, \\
&= \frac{b_-}{|\mathbf{x_{21}}|^2}\left[\tan v \ln\sqrt{b_-^2\sec^2 v} - \int_{u=0}^{u=1}\tan^2 v\mathrm{d}v\right]_{u=0}^{u=1} - \ln|\mathbf{x_{21}}|, \\
&= \frac{b_-}{|\mathbf{x_{21}}|^2}\left[\tan v \ln\sqrt{b_-^2\left(1+\tan^2 v\right)} + v - \tan v\right]_{u=0}^{u=1} - \ln|\mathbf{x_{21}}|, \\
&= \frac{1}{|\mathbf{x_{21}}|^2}\left[\left(|\mathbf{x_{21}}|^2 + a_-\right)\ln\sqrt{b_-^2 + \left(|\mathbf{x_{21}}|^2+a_-\right)^2} + b_-\tan^{-1}\left(\frac{|\mathbf{x_{21}}|^2+a_-}{b_-}\right)\right. \\
&\qquad \left. -|\mathbf{x_{21}}|^2 - a_-\ln\sqrt{b_-^2+a_-^2} - b_-\tan^{-1}\left(\frac{a_-}{b_-}\right)\right] - \ln|\mathbf{x_{21}}|, \\
&= \ln\sqrt{m_-^2 + |\mathbf{x_{21}}|^2 + 2a_-} + \frac{a_-}{|\mathbf{x_{21}}|^2}\ln\sqrt{\frac{m_-^2+|\mathbf{x_{21}}|^2+2a_-}{m_-^2}} \\
&\qquad + \frac{b_-}{|\mathbf{x_{21}}|^2}\tan^{-1}\left(\frac{b_-}{m_-^2+a_-}\right) - 1.
\end{aligned}$$

Again if we write out the whole solution we get

$$\begin{aligned}
\alpha_i^{\pm}(\mathbf{x_0}, t) &= |\mathbf{x_{21}}|\left(\ln\sqrt{m_-^2+|\mathbf{x_{21}}|^2+2a_-} - 1\right) + \frac{b_-}{|\mathbf{x_{21}}|}\tan^{-1}\left(\frac{b_-}{m_-^2+a_-}\right) \\
&\quad + \frac{a_-}{|\mathbf{x_{21}}|}\ln\sqrt{1+\frac{|\mathbf{x_{21}}|^2+2a_-}{m_-^2}} \pm \frac{a_+}{|\mathbf{x_{21}}|}\ln\sqrt{1+\frac{|\mathbf{x_{21}}|^2+2a_+}{m_+^2}} \\
&\quad \pm |\mathbf{x_{21}}|\left(\ln\sqrt{m_+^2+|\mathbf{x_{21}}|^2+2a_+} - 1\right) \pm \frac{b_+}{|\mathbf{x_{21}}|}\tan^{-1}\left(\frac{b_+}{m_+^2+a_+}\right).
\end{aligned} \tag{3.149}$$

Now that we can solve the integral analytically for each element on the boundary, we will take $\mathbf{x_0}$ as the midpoint of each element and then we can write (3.147) in matrix form as

$$B_{ji}^{\pm} f_i = A_{ji}^{\pm} g_i, \tag{3.150}$$

where

$$B_{ji}^{\pm} = \beta_i^{\pm}\left(\frac{\mathbf{x}_{j+1}+\mathbf{x}_j}{2}, t\right) - \pi\delta_{ji}, \qquad A_{ji}^{\pm} = \alpha_i^{\pm}\left(\frac{\mathbf{x}_{j+1}+\mathbf{x}_j}{2}, t\right).$$

Before we use this to solve for $\partial\phi/\partial n$ we will cover how $A_{ji}^{\pm}$ and $B_{ji}^{\pm}$ are affected by $j = i$. For simplicity we will start by stating that when $i = j$

$$a_- = -\frac{1}{2}|\mathbf{x_{21}}|^2, \quad b_- = 0, \quad m_-^2 = \frac{1}{4}|\mathbf{x_{21}}|^2,$$

and also

$$a_+ = -\frac{1}{2}|\mathbf{x_{21}}|^2 + y_{21}\bar{y}_{21}, \quad b_+ = x_{21}\bar{y}_{21}, \quad m_+^2 = \frac{1}{4}|\mathbf{x_{21}}|^2 + \bar{y}_{21}(\bar{y}_{21} - y_{21}),$$

where $\bar{y}_{21} = y_{i+1} + y_i$. This means that

$$B_{ii}^{\pm} = \pi \pm \tan^{-1}\left(\frac{x_{21}\bar{y}_{21}}{\bar{y}_{21}^2 - |\mathbf{x_{21}}|^2/4}\right), \tag{3.151}$$

and

$$\begin{aligned} A_{ii}^{\pm} = |\mathbf{x_{21}}|\left(\ln\frac{|\mathbf{x_{21}}|}{2} - 1\right) \pm \Bigg[|\mathbf{x_{21}}|\left(\ln\sqrt{\frac{1}{4}|\mathbf{x_{21}}|^2 + \bar{y}_{21}\left(\bar{y}_{21} + y_{21}\right)} - 1\right) \\ + \left(\frac{\bar{y}_{21}y_{21}}{|\mathbf{x_{21}}|} - \frac{|\mathbf{x_{21}}|}{2}\right)\ln\sqrt{1 + \frac{2\bar{y}_{21}y_{21}}{|\mathbf{x_{21}}|^2/4 + \bar{y}_{21}^2 - \bar{y}_{21}y_{21}}} \\ + \frac{x_{21}\bar{y}_{21}}{|\mathbf{x_{21}}|}\tan^{-1}\left(\frac{x_{21}\bar{y}_{21}}{\bar{y}_{21}^2 - |\mathbf{x_{21}}|^2/4}\right)\Bigg]. \end{aligned} \tag{3.152}$$

We have now covered how we will discretise the boundary integral equation as well as explaining the value of each entry in the resulting matrices. We can now use this to solve for $\partial\phi/\partial n$, either directly from ϕ or via ψ.

If we wish to solve directly from ϕ we we set our matrix equation up as

$$A_{ji}^{+}g_i = B_{ji}^{+}f_i, \tag{3.153}$$

where g_i is the normal derivative of ϕ, approximated at the centre of the element, and $f_i = (\phi_{i+1} + \phi_i)/2$. To solve matrix divide both sides by A_{ji}^{+} in order to give g_i and then we use

$$\left(\frac{\partial\phi}{\partial n}\right)_i = \frac{g_i + g_{i-1}}{2}, \quad \text{for } i = 2, ..., N, \tag{3.154}$$

which will allow us to approximate $\partial\phi/\partial n$ on all of the nodes apart from the

contact points. If we instead use ψ to solve this we instead use the equation

$$B^{-}_{ji} f_i = A^{-}_{ji} g_i, \tag{3.155}$$

where f_i is ψ approximated onto each element and $g_i = (\phi_{i+1} - \phi_i)/|\mathbf{x_{i+1}} - \mathbf{x_i}|$. This time we solve the equation by matrix dividing each side by B^{-}_{ji} and use the fact that $\psi_1 = \psi_{N+1}$ to find ψ at each node. Finally, we then use

$$\left(\frac{\partial \phi}{\partial n}\right)_i = \frac{\psi_{i+1} - \psi_{i-1}}{2|\mathbf{x_{i+1}} - \mathbf{x_i}|}, \quad \text{for } i = 2, ..., N. \tag{3.156}$$

It should be noted that any element length $|\mathbf{x_{i+1}} - \mathbf{x_i}|$ can be used since the spring function (2.52) keeps all the elements evenly spaced. Now that we have our method for approximating $\partial\phi/\partial n$ on the free surface we can use our solution method to solve (3.19)-(3.23). Before we can use this to compute a solution it turns out that over a large amount of time steps the results begin to degrade due to numerical error. What happens is the area of the droplet changes by an insignificant amount at each time step and so by the time the solution converges this change is noticeable. In order to overcome this we will introduce a source function to the droplet in order to maintain a fixed area without affecting the physics of our model.

Conserving mass - numerical accuracy

As the results converge to their periodic solution, the mass of the droplet changes insignificantly each time step due to numerical error within the solution method. Although this does not cause much of a problem at each step, the overall change can be noticeable and so we need to create a method for dealing with this inaccuracy. The method we will use is to introduce an imaginary source into the droplet in order to maintain a constant area [5]. This means that the continuity equation needs to be written as

$$\nabla^2 \phi = -2\pi q \delta(\mathbf{x} - \tilde{\mathbf{x}}), \tag{3.157}$$

where q is the strength of the source and $\tilde{\mathbf{x}}$ is the location of the source and $\delta(\mathbf{x} - \tilde{\mathbf{x}})$ is the two-dimensional delta function. The factor in front of the source term is an arbitrary constant that has been chosen for simplicity. Now when we derive the boundary integral equation, using Poisson's equation above, we

get

$$\int_{\partial\mathcal{R}} G(\mathbf{x};\mathbf{x_0})\frac{\partial\phi}{\partial n}\mathrm{d}l(\mathbf{x}) - \frac{1}{2}\phi(\tilde{\mathbf{x}}) - \int_{\partial\mathcal{R}} \phi(\mathbf{x})\frac{\partial G}{\partial n}\mathrm{d}l(\mathbf{x}) \\ = -2\pi q \int_{\mathcal{R}} G(\mathbf{x};\mathbf{x_0})\delta(\mathbf{x}-\tilde{\mathbf{x}})\mathrm{d}A(\mathbf{x}), \\ = q\ln|\mathbf{x_0}-\tilde{\mathbf{x}}|, \tag{3.158}$$

for $\mathbf{x_0}$ on the boundary $\partial\mathcal{R}$. When solving for ψ instead of ϕ we need to remember that the stream function is the imaginary counterpart to ϕ and so the boundary integral equation will therefore be

$$\int_{\partial\mathcal{R}} G(\mathbf{x};\mathbf{x_0})\frac{\partial\psi}{\partial n}\mathrm{d}l(\mathbf{x}) - \frac{1}{2}\psi(\tilde{\mathbf{x}}) - \int_{\partial\mathcal{R}} \psi(\mathbf{x})\frac{\partial G}{\partial n}\mathrm{d}l(\mathbf{x}) = q\tan^{-1}\left(\frac{y_0-\tilde{y}}{x_0-\tilde{x}}\right). \tag{3.159}$$

We now have an extra unknown q and in order to solve for this at each time step we will add the constraint

$$\frac{dA}{dt} = 0, \tag{3.160}$$

where A is the area of the two-dimensional droplet. We can use the fact that

$$\begin{aligned} A &= \frac{1}{2}\int_A \boldsymbol{\nabla}\cdot\mathbf{r}\mathrm{d}A, \\ &= \frac{1}{2}\int_{\mathbf{X}} \mathbf{n}\cdot\mathbf{r}\mathrm{d}l, \\ &= \frac{1}{2}\sum_{i=1}^{N}\int_{E_i} \mathbf{n}\cdot\mathbf{r}\mathrm{d}l, \\ &= \frac{1}{2}\sum_{i=1}^{N}|\mathbf{x_{i+1}}-\mathbf{x_i}|\int_0^1 \frac{x_{21}(y_i+y_{21}s)-y_{21}(x_i+x_{21}s)}{|\mathbf{x_{i+1}}-\mathbf{x_i}|}\mathrm{d}s, \\ &= \frac{1}{2}\sum_{i=1}^{N}(x_{i+1}y_i - x_iy_{i+1}), \end{aligned}$$

and so inserting this into (3.160) we get

$$\frac{1}{2\Delta t}\sum_{i=1}^{N}\left[x_{i+1}y_i - x_iy_{i+1} - \left(x_{i+1}y_i - x_iy_{i+1}\right)^{t-\Delta t}\right] = 0. \tag{3.161}$$

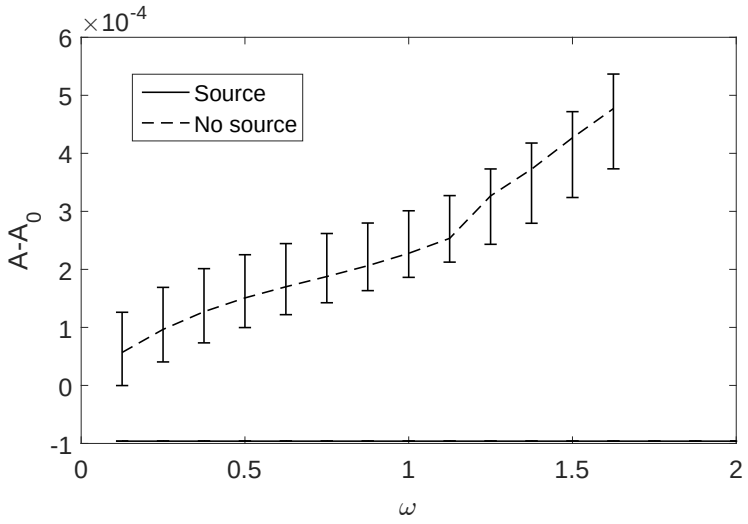


Figure 3.4: The change in area of the droplet between the initial state and the mean area of the periodic solution against the frequency of the oscillations. The solid line is when the source function is included to conserve mass whereas the dashed line has no source function. The error bars represent the maximum/minimum area of the droplet over the period of oscillation. The parameter values are $\epsilon = 0.1, \gamma = 5\theta_0 = 1, v' = 0.5, v'' = 0, g = 0$ and no hysteresis.

In order to see the necessity of this source function figure 3.4 shows the change in the area of the droplet between the initial state and the final periodic solution. If we looked at the difference in the rise velocities for these two methods they are very similar, indicating that the source function is not needed, but the method without the source function could not converge to a solution for $\omega \geq 1.75$. The frequency at which a solution can no longer be found decreases as we increase the amplitude of the oscillations and so the lack of a source function very much limits the numerical method.

Solution convergence

When computing a solution by the full numerical method we need to decide at what point the solution has converged to its periodic state. In order to calculate this we will use a method of comparing the periodic solution over two time periods. Once the change in the mean of the solution is small enough over the two time periods we can deduce that the solution has converged.

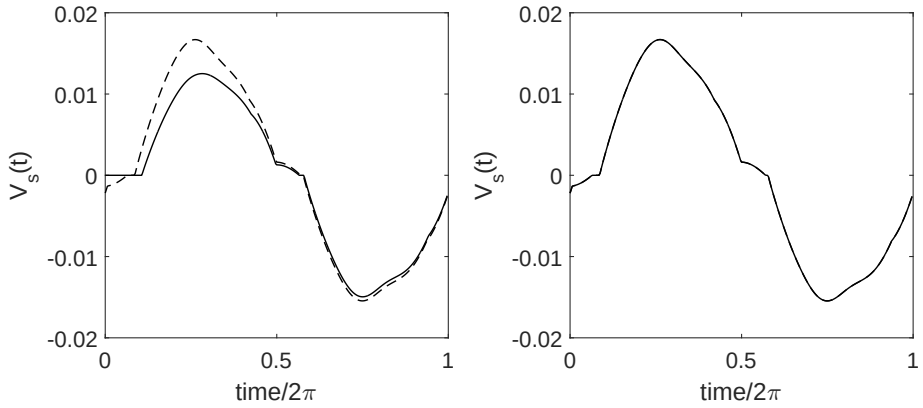


Figure 3.5: The convergence of the solution for an unconverged solution (left) and a converged solution (right). The parameter values used are $\epsilon = 0.1, \gamma = 5, \omega = 1, \theta_0 = 1, v' = 0.5, v'' = 0, g = 0, \theta_A = 1.03$ and $\theta_R = 0.97$.

Mathematically we can write this as

$$\frac{\max|V_s(t) - V_s(t - 2\pi/\omega)|}{\max|V_s(t) + V_s(t - 2\pi/\omega)|} < er, \quad \text{for } t \in [t_0, t_0 + 2\pi/\omega],$$

where V_s is the velocity of the swaying mode, er is the error that we decide to set the accuracy and t_0 is some arbitrary value such that $t \geq t_0$ always satisfies the above condition. As the solution converges we get results such as shown in figure 3.5, where the unconverged solution has an error of 0.1538 and the converged one is 4.8796×10^{-4}. This method is used such that the solution to the swaying mode is accurate to over 99%. With this we can assume the rest of the solution is just as accurate, depending on numerical error.

3.3.2 First order asymptotic, time independent problem

In this section we will cover the solution method we will use to solve (3.58)-(3.62). We will again discretise the free surface into N straight elements and solve for $\tilde{\phi}$ and $\tilde{R}$ at each of them. In order to approximate $\partial\tilde{\phi}/\partial r$ on each inner node we will use (3.153)-(3.154) since the first order problem is time independent. Apart from the boundary integral equation the rest of the system,

with tildes omitted, is given by

$$\begin{aligned}\omega\phi_i + \omega V\frac{\sin\theta_i}{\sin\theta_0} + \frac{N^2\sin^2\theta_0}{4\theta_0^3}\left[R_{i-1} - \left(2 - \frac{4\theta_0^2}{N^2}\right)R_i + R_{i+1}\right] \\ = \frac{1}{\sin\theta_0}\left[\sin\theta_i + \frac{\gamma}{\theta_0}(\cos\theta_i - \cos\theta_0)\right], \quad \text{for } i = 2, ..., N,\end{aligned} \tag{3.162}$$

$$\omega R_i - \left(\frac{\partial\phi}{\partial r}\right)_i = 0, \quad \text{for } i = 2, ..., N, \tag{3.163}$$

where $\theta_i = \theta_0[2(i-1)/N - 1]$. The boundary conditions are now

$$R_1 - \sin\theta_0 D = 0, \quad R_{N+1} - \sin\theta_0 D = 0, \tag{3.164}$$

$$N\frac{3\phi_1 - 4\phi_2 + \phi_3}{4\theta_0} + \omega\cot\theta_0 D = 0, \quad N\frac{3\phi_{N+1} - 4\phi_N + \phi_{N-1}}{4\theta_0} + \omega\cot\theta_0 D = 0, \tag{3.165}$$

$$N\frac{3R_1 - 4R_2 + R_3}{4\theta_0} + \frac{i\theta_0 V}{v'\sin\theta_0} + \left(\cos\theta_0 - \frac{i\omega\theta_0}{v'\sin\theta_0}\right)D = 0, \tag{3.166}$$

$$N\frac{3R_{N+1} - 4R_N + R_{N-1}}{4\theta_0} - \frac{i\theta_0 V}{v'\sin\theta_0} + \left(\cos\theta_0 - \frac{i\omega\theta_0}{v'\sin\theta_0}\right)D = 0. \tag{3.167}$$

This is the system of equations we will use to find the numerical solution to (3.58)-(3.62). If we require only the odd mode we can remove the γ term as well any anything involving D whereas if we want only the even mode we remove the $\sin\theta_i$ term and anything involving V. This is one method for finding the first order, time independent solution to the small amplitude asymptotic, another is described below.

Conformal mapping

Now we will look at the solution method for (3.112)-(3.114). Let us start by looking at the integral

$$I(\theta) = \int_a^b \tilde{R}(\hat{\theta})\ln\left|u(\theta) - u(\hat{\theta})\right|\mathrm{d}\hat{\theta}, \tag{3.168}$$

where

$$a = \frac{\pi}{2} - \theta_0, \quad b = \frac{\pi}{2} + \theta_0, \quad u(\theta) = \left(\frac{e^{-ia} + e^{i\theta}}{e^{ia} - e^{i\theta}}\right)^{\pi/\theta_0}.$$

In order to solve this problem numerically it will be useful to remove the singularities from (3.168) and solve these analytically to smooth out the func-

tions being integrated. As $\hat{\theta}$ tends to a the logarithm within the integral is dominated by

$$-\frac{\pi}{\theta_0}\ln\left|\hat{\theta}-a\right|,$$

and also as $\hat{\theta}$ tends to θ the logarithm is dominated by

$$\ln\left|\theta-\hat{\theta}\right|.$$

We will remove both of these terms from the main integral and solve them separately, giving

$$\begin{aligned} I(\theta) &= \int_a^b \tilde{R}(\hat{\theta})K(\theta,\hat{\theta})\mathrm{d}\hat{\theta} + \int_a^b \tilde{R}(\hat{\theta})\ln\left|\theta-\hat{\theta}\right|\mathrm{d}\hat{\theta} - \frac{\pi}{\theta_0}\int_a^b \tilde{R}(\hat{\theta})\ln\left|\hat{\theta}-a\right|\mathrm{d}\hat{\theta}, \\ &= I_K(\theta) + I_\theta(\theta) - \frac{\pi}{a}I_a, \end{aligned}$$

where

$$K(\theta,\hat{\theta}) = \ln\left|u(\theta)-u(\hat{\theta})\right| - \ln\left|\theta-\hat{\theta}\right| + \frac{\pi}{\theta_0}\ln(\hat{\theta}-a).$$

Now we will look at each integral and see how we will solve them numerically. The first integral I_K now contains a well behaved function across the domain and so can be solved numerically by separating the boundary into N straight elements and using Simpson's rule on each section giving

$$I_K(\theta) = \frac{2\theta_0}{3N}\left\{\sum_{i=1}^{N+1} K(\theta,\theta_i)\tilde{R}_i - \frac{1}{2}\left[K(\theta,\theta_1)\tilde{R}_1 + K(\theta,\theta_{N+1})\tilde{R}_{N+1}\right] + \sum_{i=1}^{N} K\left(\theta,\frac{\theta_i+\theta_{i+1}}{2}\right)(\tilde{R}_i+\tilde{R}_{i+1})\right\}.$$

For the other two integrals, if we again approximate the domain in N straight elements, we can solve them analytically using

$$I_x(x) = \frac{N}{2\theta_0}\sum_{i=1}^{N}\left\{\left[(x-\theta_i)S_i(x) + \frac{1}{2}T_i(x)\right]\tilde{R}_{i+1} + \left[(\theta_{i+1}-x)S_i(x) - \frac{1}{2}T_i(x)\right]\tilde{R}_i\right\},$$

where x can represent either θ or a and

$$S_i(x) = (\theta_{i+1}-x)\left[\ln|\theta_{i+1}-x|-1\right] - (\theta_i-x)\left[\ln|\theta_i-x|-1\right],$$

and

$$T_i(x) = (\theta_{i+1} - x)^2 \left[\ln|\theta_{i+1} - x| - \frac{1}{2}\right] - (\theta_i - x)^2 \left[\ln|\theta_i - x| - \frac{1}{2}\right].$$

Now if we reinsert this back into (3.112) we get

$$\begin{aligned} &\frac{N^2 \sin^3\theta_0}{4\theta_0^3}\left[\tilde{R}_{i-1} - \left(2 - \frac{4\theta_0^2}{N^2}\right)\tilde{R}_i + \tilde{R}_{i+1}\right] - \frac{\omega^2}{\pi} I_{ij}\tilde{R}_j + \omega\tilde{V}\cos\theta_i \\ &\quad = \cos\theta_i + \frac{\gamma}{\theta_0}(\sin\theta_i - \cos\theta_0) - \omega\phi_\infty \sin\theta_0, \quad \text{for } i = 2, ..., N, \end{aligned} \tag{3.169}$$

where I_{ij} is the integral separated into $\tilde{R}_i$ terms. The boundary conditions become

$$\tilde{R}_1 - \tilde{D}\sin\theta_0 = 0, \quad \tilde{R}_{N+1} - \tilde{D}\sin\theta_0 = 0, \tag{3.170}$$

$$N\frac{3\tilde{R}_1 - 4\tilde{R}_2 + \tilde{R}_3}{4\theta_0} - \frac{i\theta_0\tilde{V}}{v'\sin\theta_0} + \left(\cos\theta_0 - \frac{i\omega\theta_0}{v'\sin\theta_0}\right)\tilde{D} = 0, \tag{3.171}$$

$$N\frac{3\tilde{R}_{N+1} - 4\tilde{R}_N + \tilde{R}_{N-1}}{4\theta_0} + \frac{i\theta_0\tilde{V}}{v'\sin\theta_0} + \left(\cos\theta_0 - \frac{i\omega\theta_0}{v'\sin\theta_0}\right)\tilde{D} = 0, \tag{3.172}$$

and the mass conservation constraint becomes

$$\frac{2\theta_0}{3N}\left(\tilde{R}_1 + 3\sum_{i=1}^{N/2}\tilde{R}_{2i} + 2\sum_{i=1}^{N/2-1}\tilde{R}_{2i+1} + \tilde{R}_{N+1}\right) = 0. \tag{3.173}$$

Now we have two different solution methods for the small amplitude asymptotic problem, we will move onto our final solution method

3.3.3 Second order asymptotic, time averaged problem

This is the last solution method we will cover for model 2 and it is also the easiest. In order to make this neater we will write the right hand sides of (3.118)-(3.120) as some functions f_i, g_i and h_i, for $i = 1, ..., N+1$. If we again approximate the boundary as N straight elements and by using a finite difference method we get

$$\frac{N^2}{4\theta_0^2}\left[\bar{R}_{i-1} - \left(2 - \frac{N^2}{4\theta_0^2}\right)\bar{R}_i + \bar{R}_{i+1}\right] = f_i, \quad \text{for } i = 2, ..., N, \tag{3.174}$$

where

$$\bar{R}_1 - \bar{D}\sin\theta_0 = g_1, \quad \bar{R}_{N+1} - \bar{D}\sin\theta_0 = g_{N+1}, \tag{3.175}$$

$$N\frac{3\bar{R}_1 - 4\bar{R}_2 + \bar{R}_3}{4\theta_0} + \bar{D} - \frac{\theta_0 \bar{V}}{v' \sin\theta_0} = h_1, \tag{3.176}$$

$$N\frac{3\bar{R}_{N+1} - 4\bar{R}_N + \bar{R}_{N-1}}{4\theta_0} + \bar{D} + \frac{\theta_0 \bar{V}}{v' \sin\theta_0} = h_{N+1}. \tag{3.177}$$

Now we have covered each solution method we can now move onto the results they produce and start to compare them to each other, as well as [3],[8].

3.3.4 Validation of solution methods

Now we have covered the solution methods for the different ways in which we can solve our governing equations, the next step is to check the convergence rates of each method. Since we have multiple methods for solving the first order asymptotic problem, as well as finding the rise velocity for $\epsilon \ll 1$, we will begin by comparing the methods to each other. Then we will choose which small amplitude approximation method gives the most accurate results and compare that to our low frequency asymptotic results. Finally we will use this to compare to the results for our full solution method to (3.19)-(3.23) in the small amplitude limit, as well as checking the rate of convergence of the full numerical method for both space and time.

Now let us look at the first order equations that use the boundary integral method and compare the results to the conformal mapped integral equation. When looking at the order of magnitude of the error we see that the two very different methods give almost identical results. This would suggest that we have correctly computed two different methods for finding the first order asymptotic solution to the small amplitude problem. In order to decide which of the two methods to use we will compare the convergence rates in space for both the methods. We can see from figure 3.6 that the method where we used conformal mapping produces a solution that converges a lot faster and so this will be what we use for future comparisons.

We will now carry out a similar test for the methods we can use to obtain the rise velocity. We will look at comparing the second order asymptotic equations (solved using a finite difference method) to the force balance, depending on the results from the first order equations. We will keep using the conformal map as our method to solve the first order problem, and then use the results from this to solve both the second order methods. If we look at figure 3.7 we can see that the force balance converges faster than the asymptotic method. This should be obvious because both methods are accurate up to order ϵ^2 but

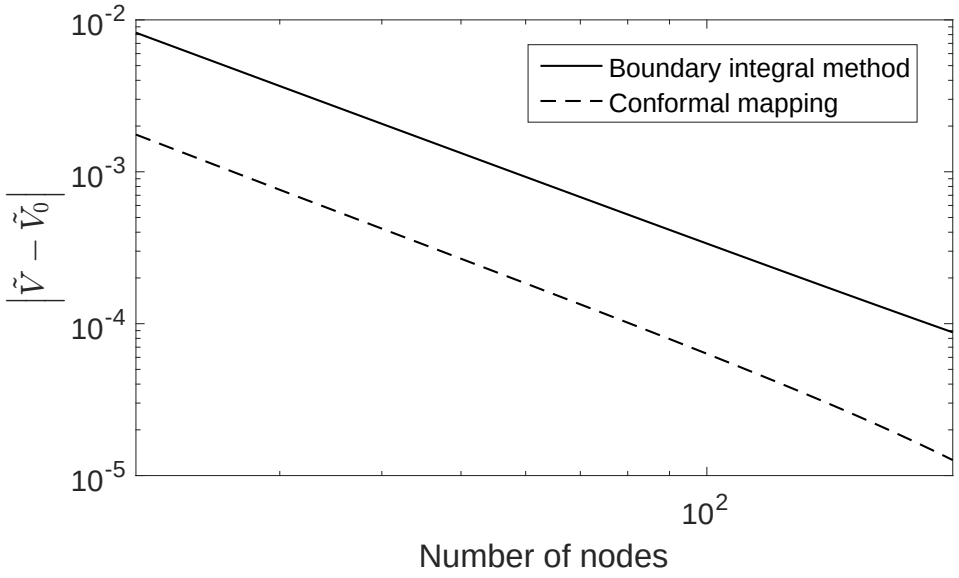


Figure 3.6: Convergence tests for the two different solution methods of the first order asymptotic problem, plotting the maximum error of the modulus of $\tilde{V} - \tilde{V}_0$, across the range $\omega \in (0, 12]$, against the number of grid points (where $\tilde{V}_0$ is the converged first order solution). The parameter values are $\gamma = 5, \theta_0 = 1, v' = 0.5$ and the logarithmic plots have a gradient of -2.

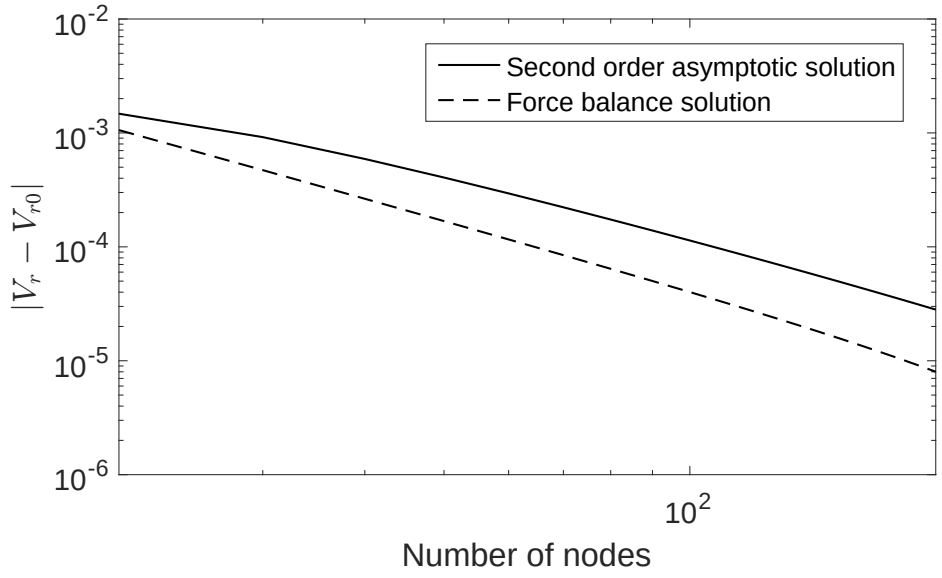


Figure 3.7: Convergence tests for the two different solution methods for the rise velocity of the droplet, plotting the maximum error of the modulus of $V_r - V_{r0}$, across the range $\omega \in (0, 12]$, against the number of grid points (where V_{r0} is the converged rise velocity). The parameter values are $\gamma = 5, \theta_0 = 1, v' = 0.5, v'' = 0, g = 0$ and the logarithmic plot for the dashed line has a gradient of -2.

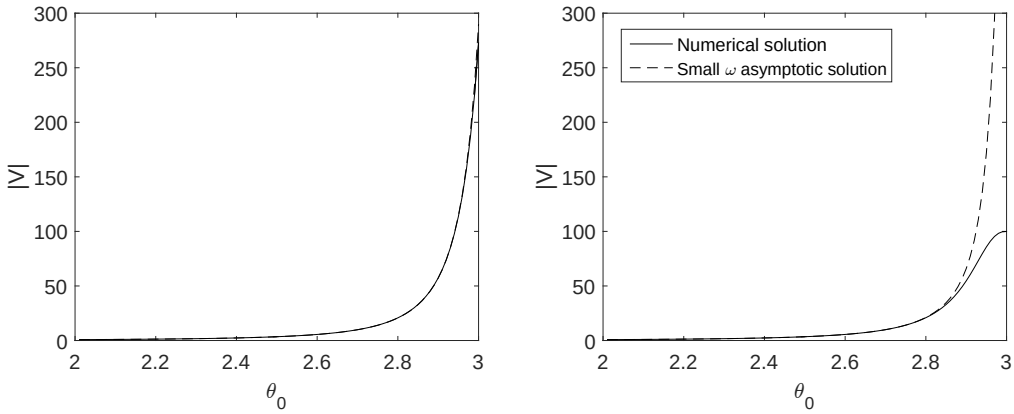


Figure 3.8: The first order, time independent, absolute value of the velocity of the centre of the droplet, V_s, against θ_0 for $\gamma = 1, v(\theta) = (\theta/\theta_0 - 1)/2$, and $\omega = 10^{-3}$ (left) and 10^{-2} (right).

the second order asymptotic equations are a system that we still approximate numerically using a finite difference method; introducing a larger amount of error in comparison to the force balance equation. This error can be seen in the solid line since it is not linear for results with less than 100 nodes. From these two sets of results we can confirm that when we examine the small amplitude limit of our problem we will use the conformal mapped first order solution along with the force balance as our small amplitude method.

Although the agreement between the boundary integral and the conformal mapping methods would suggest that our results are accurate; we will still confirm this using an analytical solution to compare with. Therefore we will now compare the solution for the absolute values of $\tilde{V}$ and $\tilde{D}$ between the conformal mapping method and the low frequency asymptotic method. We will begin with the velocity of the centre of the droplet, $\tilde{V}$, shown in figure 3.8. It is clear from the left graph that for very small ω the two solutions are almost identical however as ω increases there is a higher order term that begins to dominate near $\theta_0 = \pi$. When comparing the first order correction to the half width $\tilde{D}$ (figure 3.9) we see that, for the values of ω chosen, the results stay almost identical. For frequency values larger than shown on these graphs this again is no longer the case, meaning that again a higher order term must dominate for θ_0 close to π. This shows us that the small amplitude solution is correct in the low frequency limit, for contact angles up to 2.8.

We have now shown that the chosen small amplitude asymptotic solution method is accurate and so we will use this to compare to the full solution

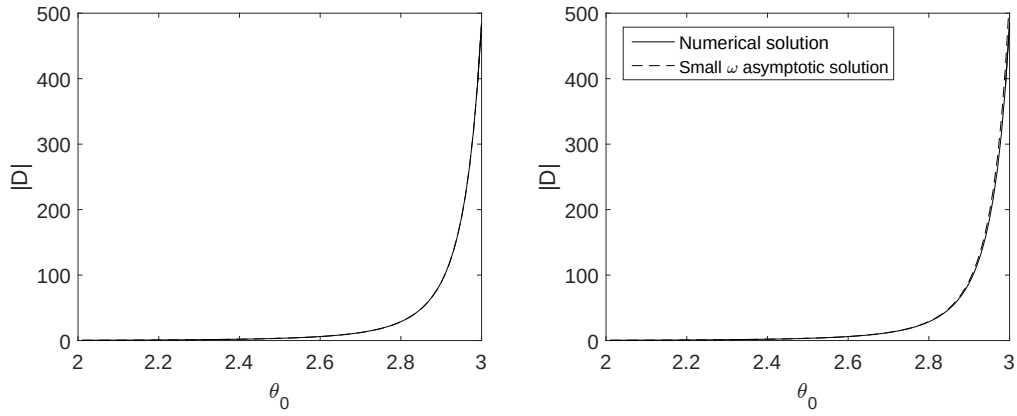


Figure 3.9: The first order, time independent, absolute value of the half width of the droplet D against θ_0 for $\gamma = 1, v(\theta) = (\theta/\theta_0 - 1)/2$, and $\omega = 10^{-3}$ (left) and 10^{-2} (right).

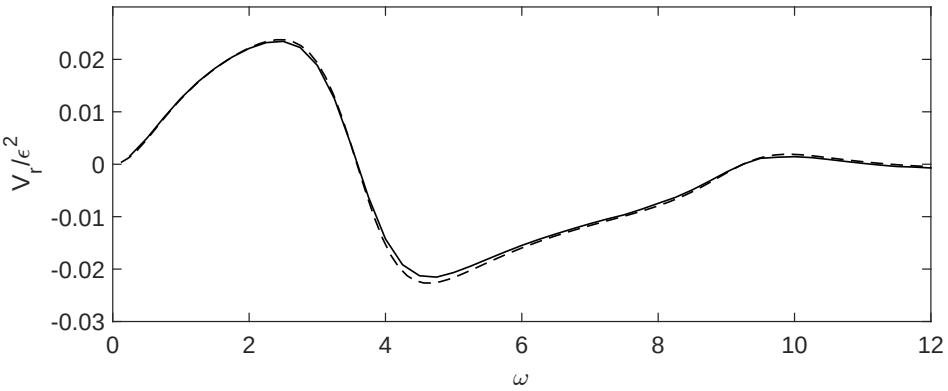


Figure 3.10: Comparison between full numerical solution method and the conformal mapping/force balance solution method for the rise velocity against ω. The parameter values are $\epsilon = 0.1, \gamma = 5, \theta_0 = 0.05, v'' = 0, g = 0$ and $v' = 0.5$.

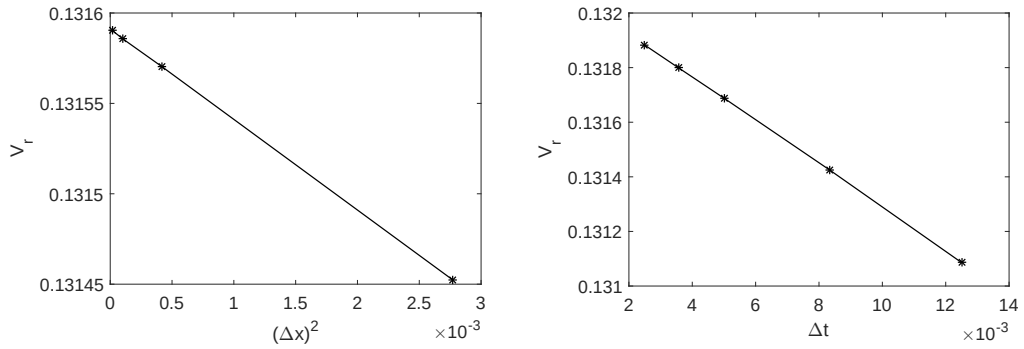


Figure 3.11: The convergence rate of the rise velocity for both space (left) and time (right) for $\epsilon = 0.5, \gamma = 1, \omega = 1, v' = 0.5, v'' = 0, g = 0$ and no hysteresis.

method for $\epsilon \ll 1$. We have done this in figure 3.10 for small θ_0 and considering ϵ is as large as 0.1, in the full solution method, the results are very close. Not only is this a good indication of how accurate the solution methods are in comparison to each other but we can also compare this graph to figure 2 of [3] to verify that the model is correct when compared to the shallow water limit.

The final verification we will use to check our solution method is to check the rate at which the solution converges with respect to space and time. The discretisation of the boundary, along with the integral method used, means that the solution is accurate to the order of grid spacing squared. Also we have used an implicit time step which is accurate to the order of the time step. We can see from figure 3.11 that the solution is converging correctly in both space and time as required. What we have done in this section is verified that both the small amplitude asymptotic solution methods, as well as the full solution method, work and are accurate.

3.3.5 Breaking the droplet

In order to examine more physically realistic parameter values we will need to look at cases where ϵ is too large to be approximated using the small amplitude asymptotic results. What we will find however is that when the forcing becomes too large it can cause the droplet to 'break'. What we mean by the droplet breaking is for one of the next four things to occur.

The first type of break is shown in figure 3.13 and it is when the contact angle at the trailing end of the droplet reaches zero. This is the most common type of break we will encounter as the parameter values required are very close

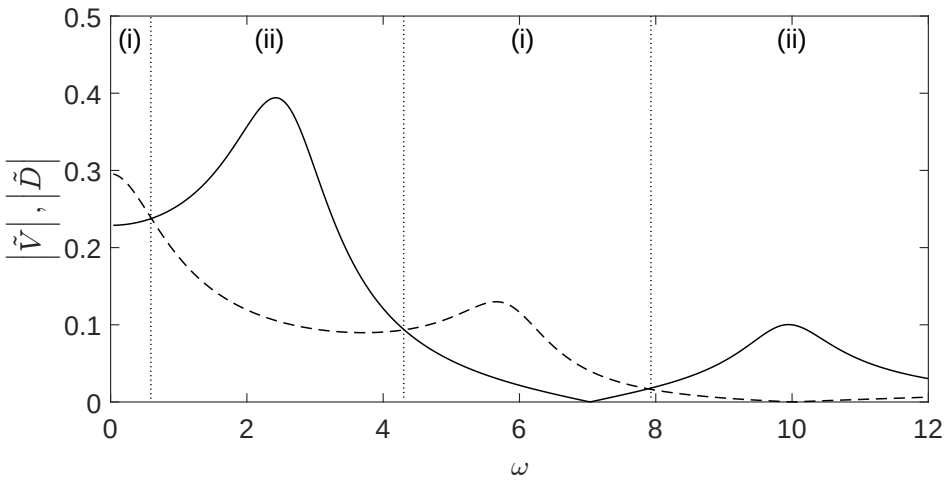


Figure 3.12: The small amplitude asymptotic solution for the magnitude of the velocity of the centre of the droplet (solid) and the change in the half width of the droplet (dashed) against the frequency, for $\gamma = 5, \theta_0 = 1$ and $v' = 0.5$. The dotted lines separate the results into sections where: (i) $\left|\tilde{D}\right| > \left|\tilde{V}\right|$ and (ii) $\left|\tilde{V}\right| > \left|\tilde{D}\right|$.

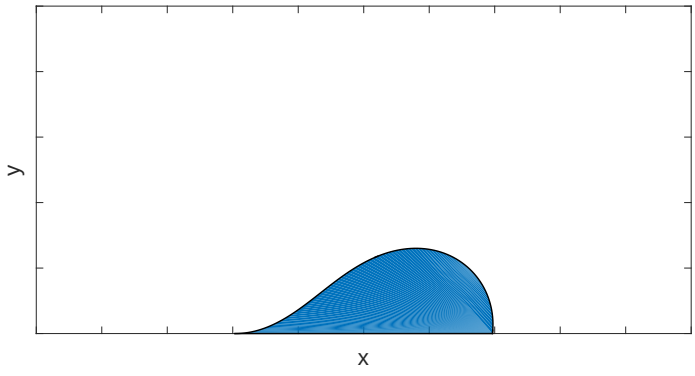


Figure 3.13: Picture of a droplet where the contact angle at the trailing end has reached zero. The parameter values are $\epsilon = 1, \gamma = 1, \omega = 2, \theta_0 = 1, v' = 1, v'' = 0$ and $g = 0$ with no contact angle hysteresis.

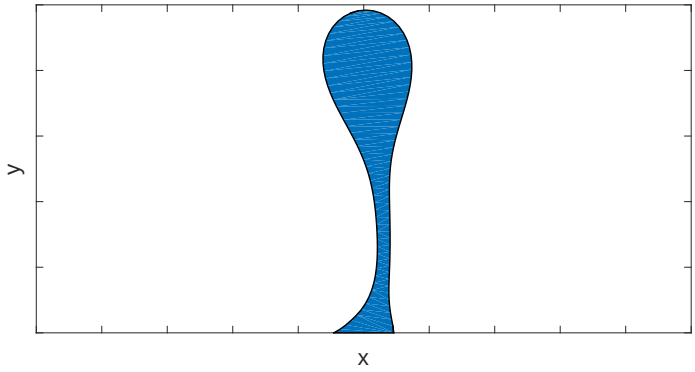


Figure 3.14: Picture of a droplet where part of the fluid almost pinches off from the rest of the droplet. The parameter values are $\epsilon = 0.4, \gamma = 25, \omega = 2, \theta_0 = 1, v' = 2.5, v'' = 0$ and $g = 0$ with no contact angle hysteresis.

to the ones in (3.18), i.e. both γ and θ_0 are approximately 1 and the frequency of the oscillations fall into a range given by (ii) in figure 3.12. What happens is the magnitude of the velocity of the centre of the droplet is much larger than that of the change in the half width of the droplet. As the droplet climbs back uphill the bulk of the fluid, as well as the advancing contact point, travel much faster than the contact line law at the trailing end will allow. This causes the fluid to thin out at the trailing end up to the point where the contact angle reaches negative values.

The second type of break is when part of the droplet almost 'pinches off' as the substrate oscillates. An example of this is shown in figure 3.14 and it occurs when the magnitude of the change in half width is much greater than the velocity of the centre of the droplet. Since $\tilde{D}$ is proportional to γ this result is more likely to occur when γ is large; which physically means the magnitude of the contact angles is larger or the inclination of the substrate is smaller. Again referring to figure 3.12 breakages such as these can occur in sections labelled (i). When the normal component of the acceleration is acting upwards the fluid moves away from the substrate, if the magnitude of the acceleration is large enough this will continue until the fluid closer to the substrate begins to thin. When part of the droplet becomes too thin the numerical method can no longer compute a solution.

The third example is when a part of the free surface touches the substrate (other than at the contact points) and is shown in figure 3.15. Results such as these are obtained very similarly to when the droplet 'pinches off' only now

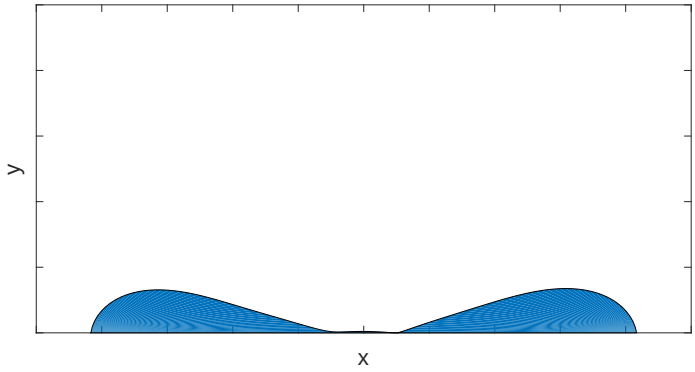


Figure 3.15: Picture of a droplet where the free surface touches the substrate a the midpoint. The parameter values are $\epsilon = 0.4, \gamma = 20, \omega = 2, \theta_0 = 1, v' = 2.5, v'' = 0$ and $g = 0$ with no contact angle hysteresis.

when the acceleration is acting in the opposite direction. The other way for this to occur is if the contact angles are multiplied by a large enough factor in the contact line law (i.e. v' is large enough) in order for the trailing end to keep up with the bulk of the fluid before the contact angle reaches zero. For a large enough ϵ the droplet will spread out enough that the height between the contact points reaches zero causing the free surface to touch.

The final type of break is shown in figure 3.16 and it is when the advancing angle reaches values larger than π. This is very uncommon since it again needs γ to be smaller than 1 but also θ_0 has to be larger than $\pi/2$ (for the current contact line law). What happens is similar to our first example only now the equilibrium contact angle is much larger and so instead of the receding angle not being able to keep up with the velocity of the fluid, the advancing angle cannot keep up and so the bulk of the fluid begins to overlap. Eventually this can get too large and the contact angle at the advancing end goes beyond π.

Depending on what parameter values and contact line law are chosen, many different unusual shapes can occur, e.g. the free surface touching the substrate at multiple points or parts of the droplet pinching off near each contact point, however each example will fall into one of these categories.

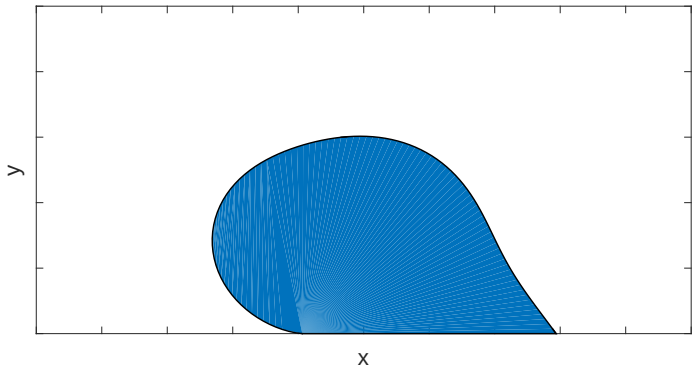


Figure 3.16: Picture of a droplet where the contact angle at the leading end has π. The parameter values are $\epsilon = 5, \gamma = 0.1, \omega = 2, \theta_0 = 2, v' = 1, v'' = 0$ and $g = 0$ with no contact angle hysteresis.

3.4 Results

3.4.1 Linear contact line law

In this section we will examine the motion of the droplet for a linear contact line law. We will initially increase the amplitude of the oscillation in order to diverge away from the asymptotic results, and then we will follow up by varying the other parameters whilst keeping ϵ relatively large. We will use these results to examine how the solution to the model changes as we vary certain parameters, all whilst maintaining a linear contact line law.

Larger amplitude oscillations

The amplitude of the oscillations is the driving force that causes the droplet to climb uphill and so we will examine it for relatively large sizes (ϵ up to order 1) and see how it changes the motion of the droplet compared to the small amplitude asymptotic results. We have already looked at the rise velocity against ω for very small amplitude oscillations (figure 3.10) and so we will extend these results for larger values of ϵ. This analysis is useful to see how large we can make the forcing in order to produce results for parameter values similar to [8]. We can see from figure 3.17 that for small θ_0 the rise velocity is proportional to the amplitude squared. What is interesting about this is how little the proportionality changes as ϵ is increased up to 1, meaning that the small amplitude asymptotic solution is a good approximation for even

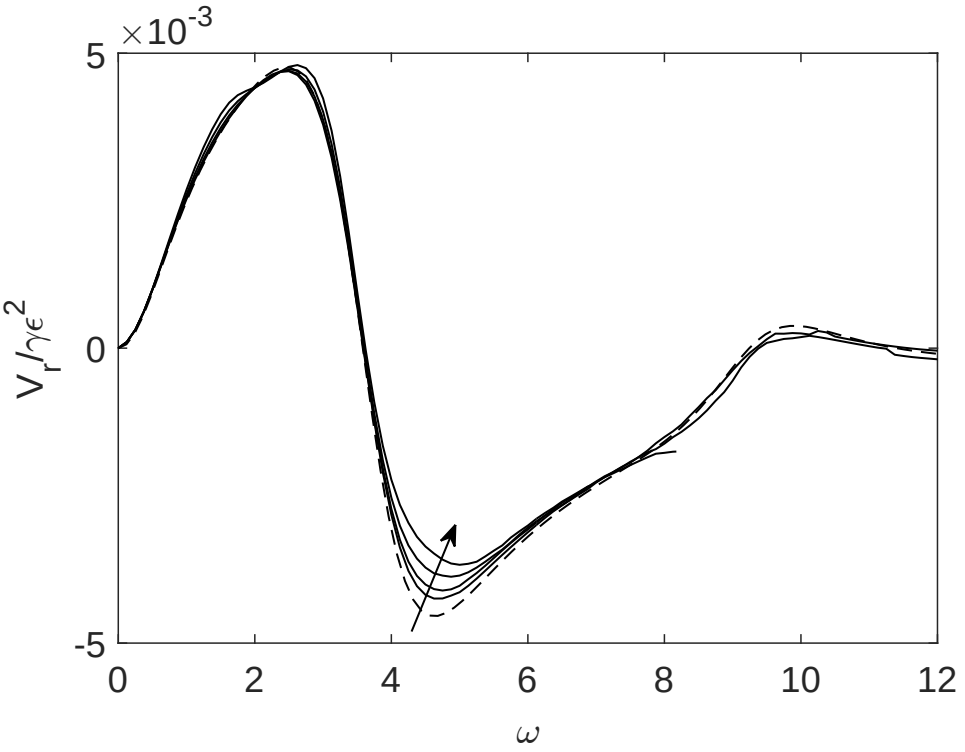


Figure 3.17: The rise velocity of the droplet against ω for $\gamma = 5, \theta_0 = 0.05, v' = 0.5, v'' = 0, g = 0$ and no hysteresis. The dashed line is the small amplitude asymptotic solution whilst the solid lines, following the direction of the arrow, coincide with $\epsilon = 0.25, 0.5, 0.75, 1$ respectively. The results stop at $\omega = 8.225$ for $\epsilon = 0.75$ and 6.975 for $\epsilon = 1$ due to the contact angle at the trailing end reaching zero.

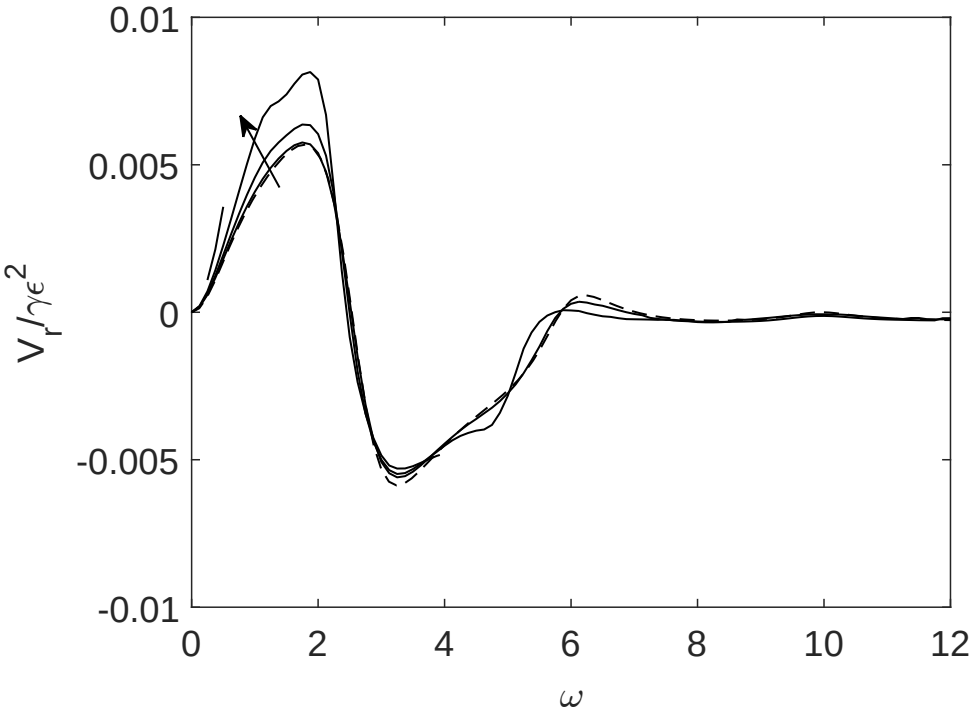


Figure 3.18: The rise velocity of the droplet against ω for $\gamma = 5, \theta_0 = 1, v' = 0.5, v'' = 0, g = 0$ and no hysteresis. The dashed line is the small amplitude asymptotic solution whilst the solid lines, following the direction of the arrow, coincide with $\epsilon = 0.25, 0.5, 0.75, 1$ respectively. The results stop at $\omega = 3.975$ for $\epsilon = 0.75$ and 0.55 for $\epsilon = 1$ due to the contact angle at the trailing end reaching zero. In addition to this the results for $\epsilon = 1$ do not start until $\omega = 0.25$ due to the droplet almost pinching off for frequencies lower that this.

larger amplitude oscillations (also shown in [3]). However when we increase the magnitude of the contact angle so that $\theta_0 = 1$ this is no longer the case. For larger contact angle droplets we see that again the small amplitude asymptotic solution matches well for ϵ up to 0.25 but as we increase this further the rise velocity stops being proportional to ϵ^2, especially at the initial peak. What we can also observe from this graph is that for contact angles with a larger magnitude, the values for ϵ that cause the droplet to 'break', do so at a lower frequency (type of break similar to figure 3.13). In addition to this we can see that for $\epsilon = 1$ the frequencies that produce a result without the droplet breaking do not start until $\omega = 0.25$ because for values lower than this the droplet breaks similar to figure 3.14.

Now let us examine why the droplet breaks for the frequencies that it does. We will only look at the case where $\theta_0 = 1$ as it covers the smaller θ_0 case

also. For the case where the contact angle at the trailing end of the droplet reaching zero we will need to look at the top graph in figure 3.19. We can see from this graph that the small amplitude asymptotic solution contains a peak swaying velocity, where the back-and-forth motion of the droplet will be at a maximum. Since the frequency is low the acceleration of the swaying mode is not too large meaning the droplet has a chance to keep up before the contact angle of the trailing end reaches zero. As we increase the amplitude of the oscillations a second peak begins to form at around $\omega = 1.8$ and a third peak at $\omega = 8.5$. This second peak still causes little problem due to how low the frequency of the oscillation is but at the third peak the droplet again has a large swaying mode velocity, but with a large acceleration now also. This causes the leading end of the droplet to move faster than the trailing end, continuing up to a point where the distance between the two is too large and the contact angle at the trailing end reaches zero. Now for the case where the droplet begins to pinch off we will use the bottom graph in figure 3.19. We can see here that there is a peak in the change of the half width of the droplet at $\omega = 0$. This means that the smaller the frequency the closer the contact points get, during a period of oscillation, and the bulk of the fluid is propelled above the substrate to compensate. As we increase the amplitude of the oscillations this amplifies until most of the fluid is accelerating away from the substrate. When this occurs part of the droplet begins to thin as the fluid moves further away up to the point where the fluid almost pinches off, i.e. the droplet breaks.

What both figures 3.17 and 3.18 show us is that for even a linear contact line law we can produce a droplet that either slides down the substrate or climbs up it depending on the frequency of the oscillations. In addition to this we see that both the rise velocities alternate between negative and positive and the magnitude of the peaks/troughs decrease, as ω increases. The former of these two is due to the inertial forces in the fluid whereas the latter is because the magnitude of the swaying mode is proportional to ω^{-1} and the spreading mode to ω^{-2}. These proportionalities are shown for the shallow water limit in [3] using a high frequency approximation however, due to the presence of the boundary integral equation, we are unable to show this analytically for this model.

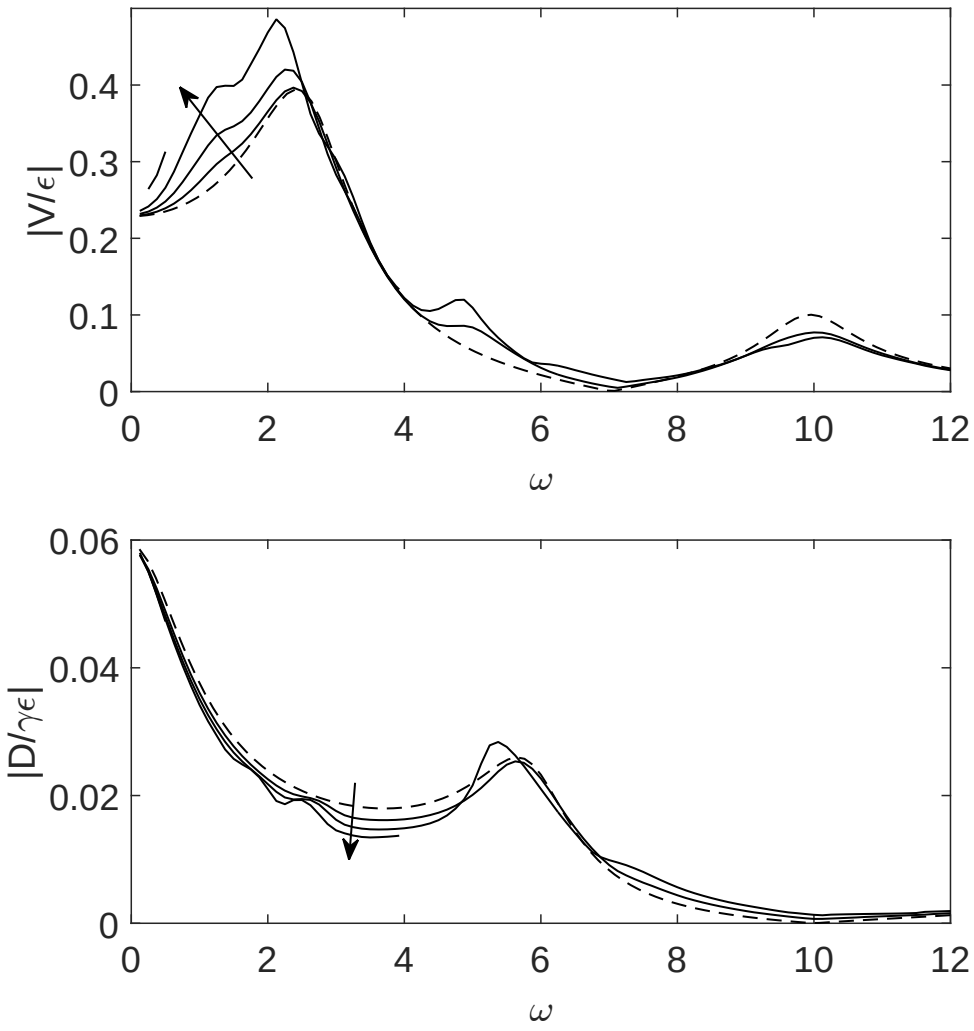


Figure 3.19: The velocity of the centre of the droplet (top) and the change in the half width (bottom) of the droplet against ω for $\gamma = 5, \theta_0 = 1, v' = 0.5, v'' = 0, g = 0$ and no hysteresis. The dashed line is the small amplitude asymptotic solution whilst the solid lines, following the direction of the arrow, coincide with $\epsilon = 0.25, 0.5, 0.75, 1$ respectively. The results stop at $\omega = 3.975$ for $\epsilon = 0.75$ and 0.55 for $\epsilon = 1$ due to the contact angle at the trailing end reaching zero. In addition to this the results for $\epsilon = 1$ do not start until $\omega = 0.25$ due to the droplet almost pinching off for frequencies lower that this.

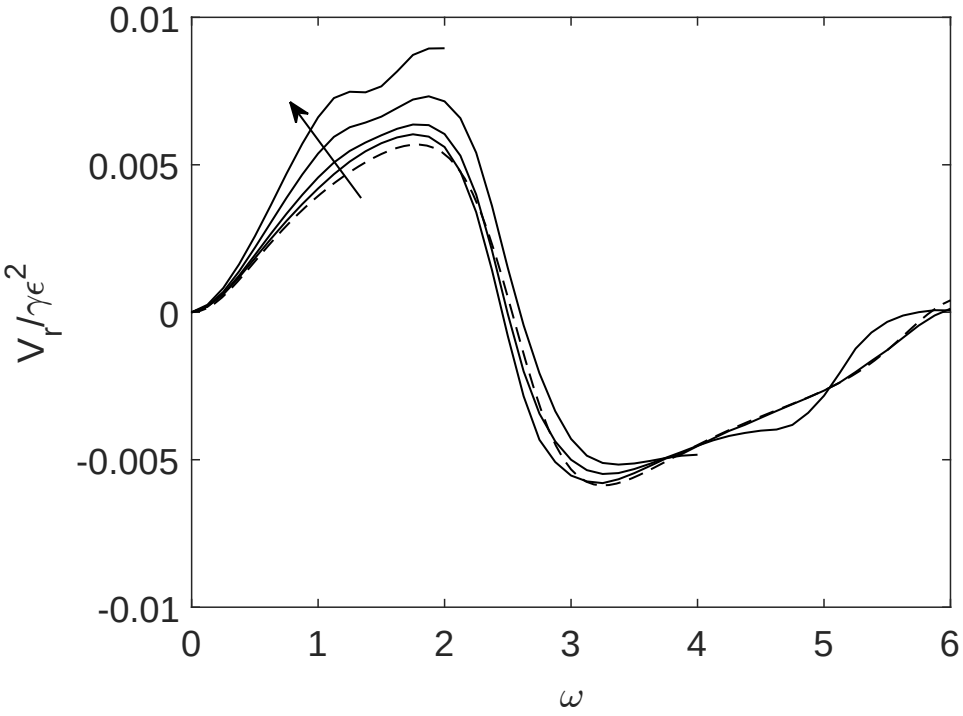


Figure 3.20: The rise velocity of the droplet against ω for $\epsilon = 0.5, \theta_0 = 1, v' = 0.5, v'' = 0, g = 0$ and no hysteresis. The value of γ increases in the direction of the arrow as 1,5,8,10 respectively. The results stop at $\omega = 4.125$ for $\gamma = 8$ and 2.125 for $\gamma = 10$ due to the contact angle at the trailing end reaching zero.

Varying the thickness to inclination ratio

In addition to ϵ the other new dimensionless parameter we obtained from balancing the dimensional scalings in the governing equations was γ, the ratio between the slope of the droplets surface and the slope of the substrate. Now we have looked at what varying the amplitude of the oscillations does to the rise velocity of the droplet we should examine what varying γ does also. We already know from section 3.2.3 that $\tilde{D}$, the first order correction to the half width of the droplet, scales linearly with γ. Applying this knowledge to (3.128) shows that for small amplitude oscillations the rise velocity scales linearly with γ also (when $g = 0$). When we increase the amplitude of the oscillation this is no longer the case, and the increase in γ causes the rise velocity to change in a very similar way to increasing ϵ (but not quite as much, figure 3.20). If we refer back to (3.20) we see that the forcing normal to the substrate is given by $\epsilon\gamma a$ and so this is the reason why increasing one is similar to increasing the other; however the forcing tangential to the substrate is given by ϵa, so this

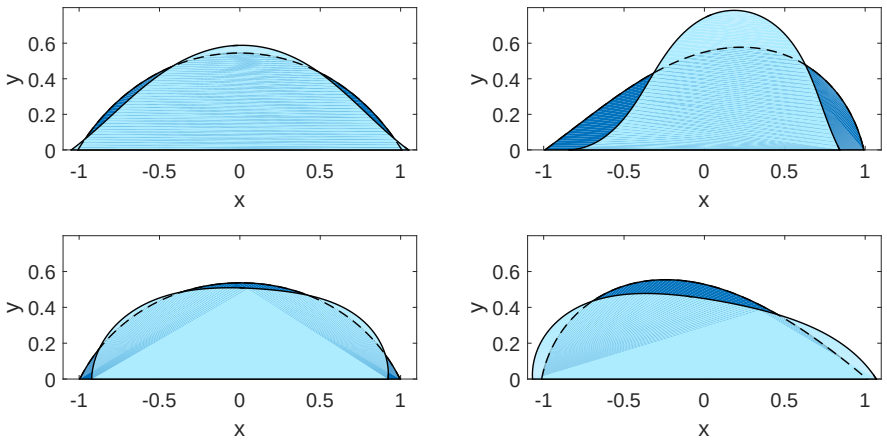


Figure 3.21: Model of the droplet at equal time intervals over one period of oscillation. The parameter values are $\epsilon = 0.5, \theta_0 = 1, \omega = 2, v' = 0.5, v'' = 0, g = 0$, no hysteresis and $\gamma = 1$ for the darker shaded droplet and 10 for the lighter shade.

is why increasing the amplitude of the oscillations has a larger impact on the rise velocity compared to increasing the thickness to inclination ratio by the same factor. We can also see from figure 3.20 that if we make γ too large we can cause the droplet to break again similar to before. Physically a large γ means that the substrate is inclined at a small angle and so we will stick to $\gamma \in (0, 10]$. We will finish examining how varying γ affects the results with a look at the motion of the droplet over a period of oscillation for two different γ values. This can be seen in figure 3.21 at four evenly spaced time increments. It is clear from these graphs that increasing γ has a large affect on the motion of the droplet whereas the darker shaded drop ($\gamma = 1$) changes very little over the period of oscillation.

Varying the magnitude of the linear contact line law

We already know how much contact line laws can dominate fluid dynamics problems, even though we know little behind the mechanics at the actual contact lines. We will now vary the parameter v' to show that even if we keep our contact line law linear, the weighting attached can completely alter the results. What we can see from figure 3.22 is that we increase v' by a factor of 2, the result changes quite significantly. Also by doing this again (figure 3.23) we see a reverse in the direction of the rise velocity, with the frequencies which produced a climbing droplet now slide and vice versa. This result is

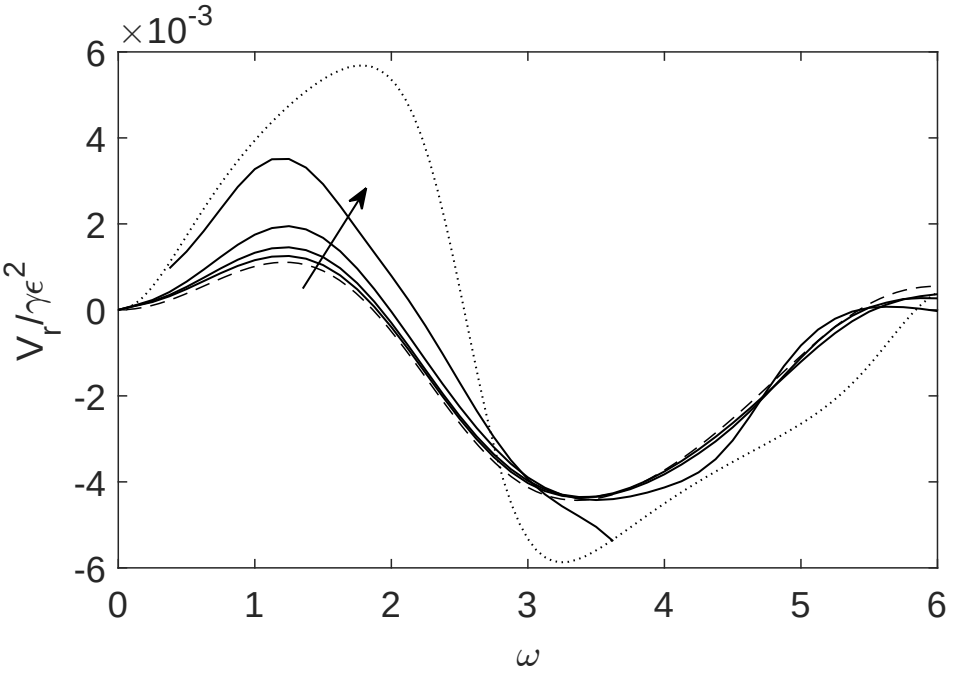


Figure 3.22: The rise velocity of the droplet against ω for $\gamma = 5, \theta_0 = 1, v' = 1, v'' = 0, g = 0$ and no hysteresis. The dashed line is the small amplitude asymptotic solution whilst the solid lines, following the direction of the arrow, coincide with $\epsilon = 0.25, 0.5, 0.75, 1$ respectively. The dotted line represents the small amplitude asymptotic solution when $v' = 0.5$. The results for $\epsilon = 1$ do not start until $\omega = 0.375$ due to the droplet almost pinching off for frequencies lower that this and stop at $\omega = 3.75$ due to the contact angle at the trailing end reaching zero.

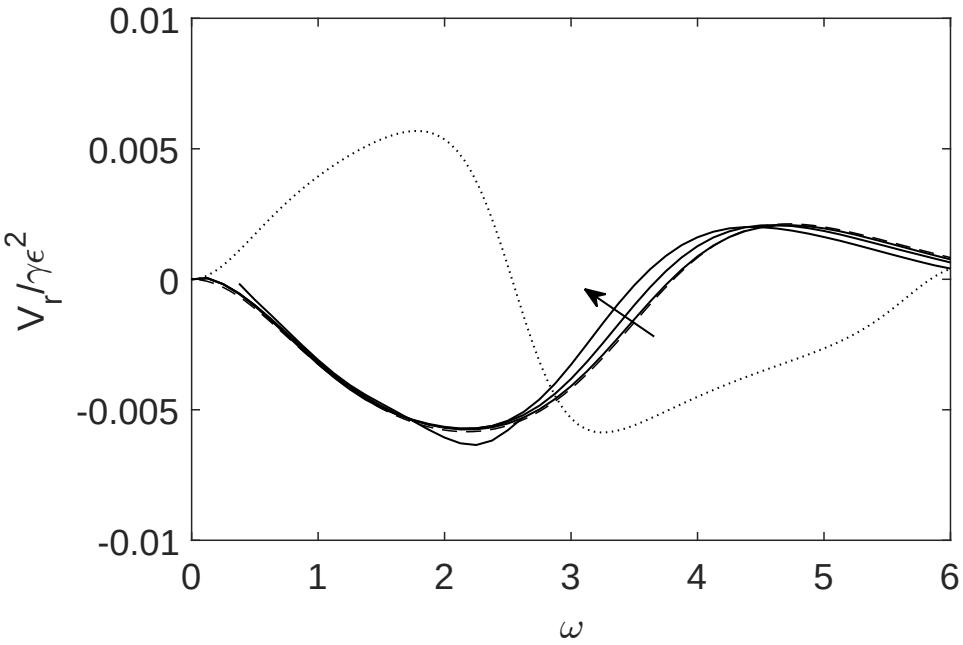


Figure 3.23: The rise velocity of the droplet against ω for $\gamma = 5, \theta_0 = 1, v' = 2, v'' = 0, g = 0$ and no hysteresis. The dashed line is the small amplitude asymptotic solution whilst the solid lines, following the direction of the arrow, coincide with $\epsilon = 0.25, 0.5, 0.75, 1$ respectively. The dotted line represents the small amplitude asymptotic solution when $v' = 0.5$. The results for $\epsilon = 1$ do not start until $\omega = 0.375$ due to the droplet almost pinching off for frequencies lower that this and stop at $\omega = 2.75$ due to the contact angle at the trailing end reaching zero.

very important to show how dominated this problem is by the contact line, again shown in [3] for the shallow water limit, where if we change the constant v' a small amount the solution can change very rapidly. We also see that the droplets still break for $\epsilon = 1$ only now for different values of ω. Now let us consider the limit of $v' \to \infty$ which corresponds to fixed contact angles. From (3.128) we see that in the large v' limit the oscillating term is $O(1/v')$ whereas the gravity term is $O(v')$. What this means is the droplet will always slide down hill regardless of the other parameter values (again covered in [3]). As we decrease the size of v' we get a rise velocity such as the one shown in figure 3.24. We can see from this graph that apart from certain spikes the rise velocity tends to zero for most frequencies. In order to understand what these spikes mean we will need to look at the case where the contact points are pinned (next section).

What this section has shown us is how dominated this problem is by the

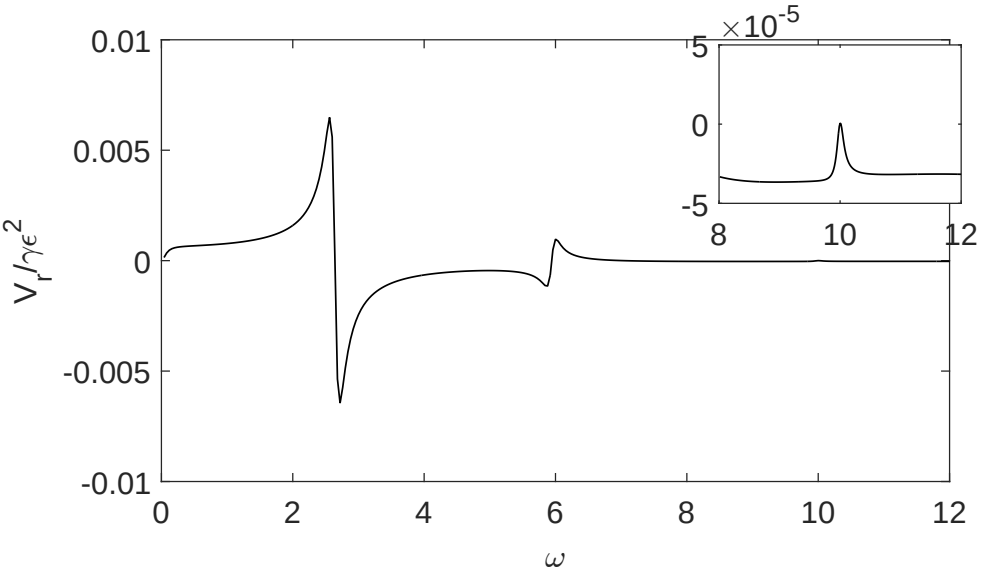


Figure 3.24: The small amplitude asymptotic solution for the rise velocity of the droplet against the frequency for $\gamma = 1, \theta_0 = 1, v' = 0.05, v'' = 0$ and $g = 0$.

contact line law.

Pinned contact points

If we pin the contact points the rest of the droplet will still continue to shake on the spot when an oscillation is applied. Equations (3.58) - (3.62) but with pinned contact points are

$$\nabla^2 \tilde{\phi} = 0, \tag{3.178}$$

where

$$\omega\tilde{\phi} + \frac{\sin^2\theta_0}{\theta_0}\left(\frac{\partial^2\tilde{R}}{\partial\theta^2} + \tilde{R}\right) = \frac{1}{\sin\theta_0}\left(\cos\theta + \frac{\gamma}{\theta_0}(\sin\theta - \cos\theta_0)\right), \qquad r = R_0, \tag{3.179}$$

$$\omega\tilde{R} = \frac{\partial\tilde{\phi}}{\partial r}, \qquad r = R_0, \tag{3.180}$$

and

$$\tilde{R} = 0, \qquad \frac{\partial\tilde{\phi}}{\partial\theta} = 0, \qquad \theta = \frac{\pi}{2} \mp \theta_0. \tag{3.181}$$

If we compare these equations to (3.58) - (3.62) the only difference is that $\tilde{V}$ and $\tilde{D}$ both equal zero and so the boundary conditions for the derivative of $\tilde{R}$ are not required. Instead we will use these derivatives of $\tilde{R}$ to look at the

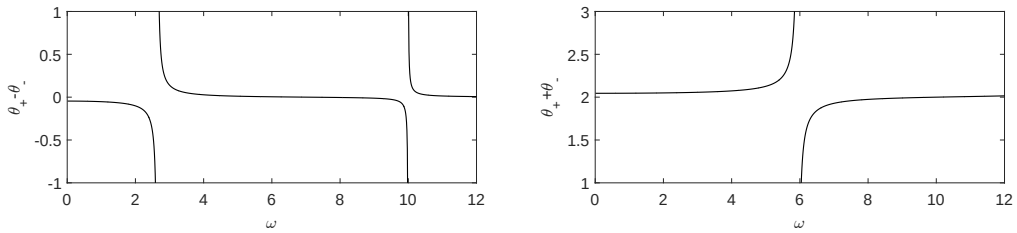


Figure 3.25: The maximum displacements of the contact angles against ω for $\gamma = 5, \theta_0 = 1$ and pinned contact points. The difference between θ_+ and θ_- represents the swaying mode (left) whilst the sum of the two represents the spreading mode (right). The singularities are when the modes vibrate at resonant frequencies.

contact angles, given by

$$\theta_\pm = \theta_0 \pm \epsilon \sin\theta_0 \frac{\partial \tilde{R}}{\partial \theta} + O(\epsilon^2), \quad \text{at } \theta = \frac{\pi}{2} \mp \theta_0, \tag{3.182}$$

and since we want to look at the odd and even modes we can examine the spreading mode using $\theta_+ + \theta_-$ and the swaying mode using $\theta_+ - \theta_-$. If we solve these equations using a similar method as we did for (3.58) - (3.62) we can see that, for the range of ω we are looking at, both modes contain resonant frequencies, as shown in figure 3.25. These resonant frequencies match up with the spikes shown in figure 3.24. We conclude that the reason the rise velocity increases so much at these frequencies is due to the increased motion that occurs on the surface of the droplet when the contact line law is greatly restricted. This effect is also visible when contact angle hysteresis is included in a later section.

The addition of gravity

When thinking about this problem initially the presence of gravity would make you assume that the droplet would roll down the substrate; however in spite of the constant force acting downwards, the droplet can still manage to climb. So far in all of the results for this model we not yet incorporated the constant acceleration due to gravity therefore we must see how the addition of it changes the results. If we refer back to (3.128)-(3.129) we know that for small amplitude oscillations, the effect of gravity on the rise velocity is separate to the oscillating substrate and depends on the magnitude of the contact angles and the contact line law used. In order to see how the rise velocity of the droplet is effected

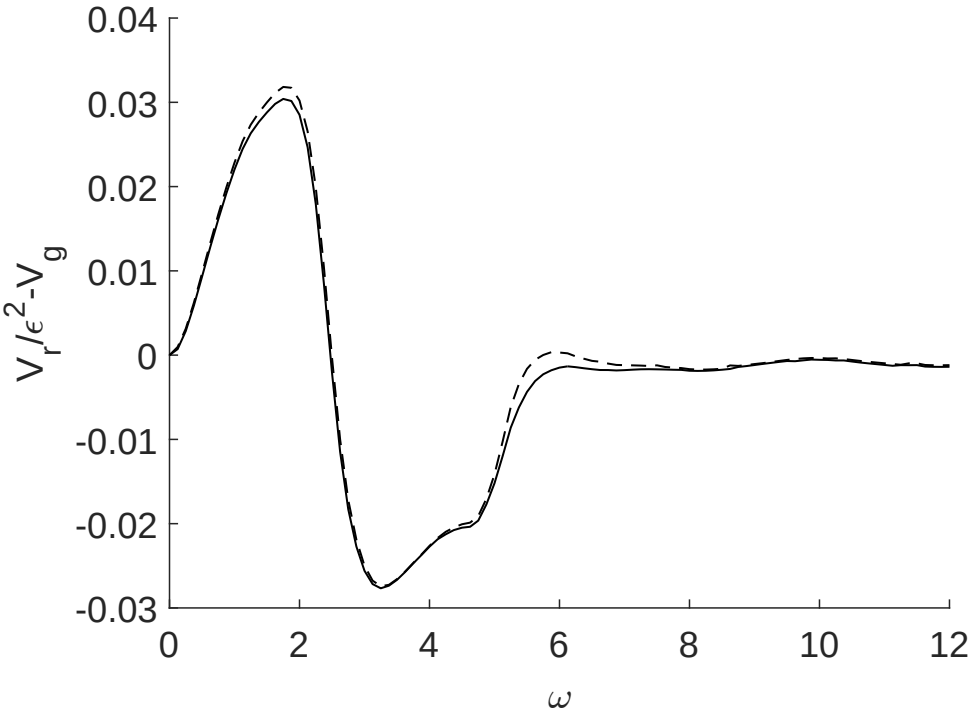


Figure 3.26: The rise velocity of the droplet against the frequency of the oscillations for $\epsilon = 0.5, \gamma = 5, \theta_0 = 1, v' = 0.5$ and $v'' = 0$. The solid line is when there is no gravity included and the dashed line includes gravity with a strength 25 times weaker than the magnitude of the oscillations. The rise velocities have been shifted by an amount proportional to g in order to look how how the curves change when gravity is included, instead of just the negative shift that occurs for all ω.

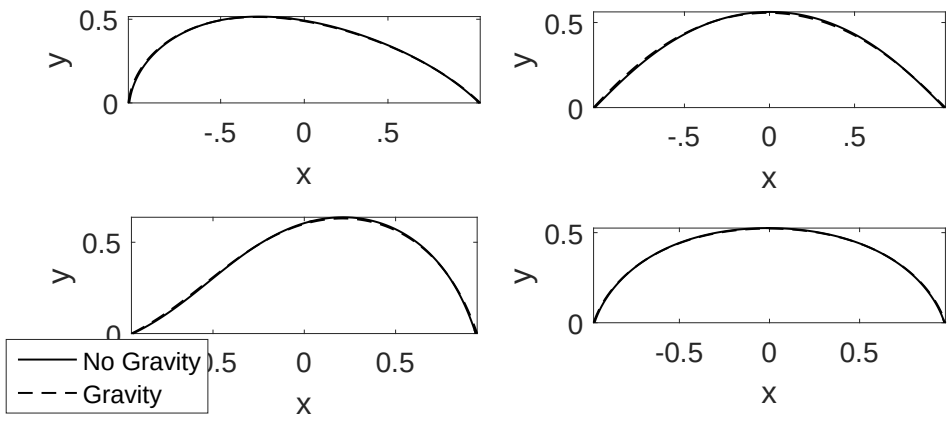


Figure 3.27: The evolution of the droplet over one period of oscillation for $\epsilon = 0.5, \gamma = 5, \omega = 2, \theta_0 = 1, v' = 0.5$ and $v'' = 0$. The solid line is when there is no gravity included and the dashed line includes gravity with a strength 25 times weaker than the magnitude of the oscillations.

by gravity for larger values of ϵ, we will compare the rise velocity for $g = 1/25$ with $g = 0$. In order to examine the shape of the curves we will also subtract off the gravity term from (3.129) so that the rise velocities overlap.

The results for this are shown in figure 3.26 and it is quite clear that for $\epsilon = 0.5$ the effects of gravity are still just a negative shift of V_r. We will also examine the shape of the droplet at four evenly spaced time steps over a period of oscillation to see if the inclusion of gravity does anything to the shape of the droplet. We can see in figure 3.27 that again, the inclusion of gravity does little to the shape of the droplet. Increasing the amplitude of the oscillations further, up to $\epsilon = 1$, still gives results that are very similar with or without gravity and also the droplets break for the same values of ω. What we can conclude from this is that for the values of ϵ we are using, the inclusion of gravity does very little to change to the results and so setting it to zero has done little to impede our understanding of the mechanics behind this problem.

Varying the magnitude of the contact angles

Already we have used our model to look at the case where $\theta_0 \to 0$ in order to compare with [3] and also looked at $\theta_0 \approx 1$ so that the size of the droplets are more physically realistic. We will now look at the difference in the rise velocity as we increase θ_0 and, more specifically, look at what happens to the motion of the droplet as θ_0 tends to π. We will begin by looking at the

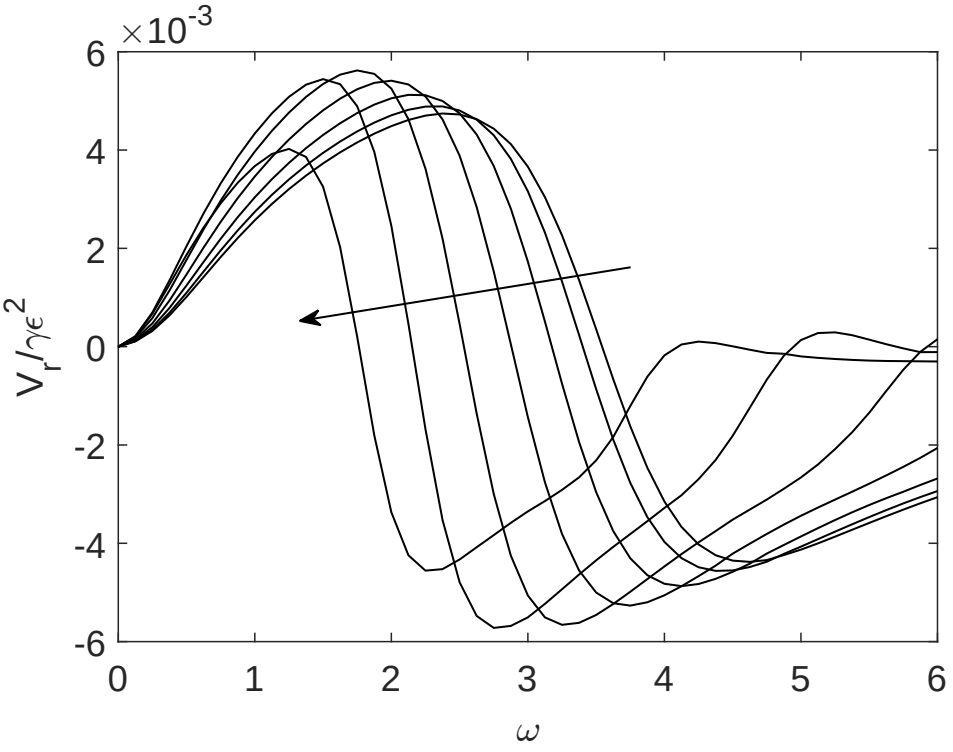


Figure 3.28: The rise velocity of the droplet against the frequency of the oscillations as the magnitude of the contact angles increases. The other parameter values are $\epsilon = 0.1, \gamma = 5, v' = 0.5, v'' = 0, g = 0$, no contact angle hysteresis and θ_0 starting at 0.2 and increasing in multiples of 0.2.

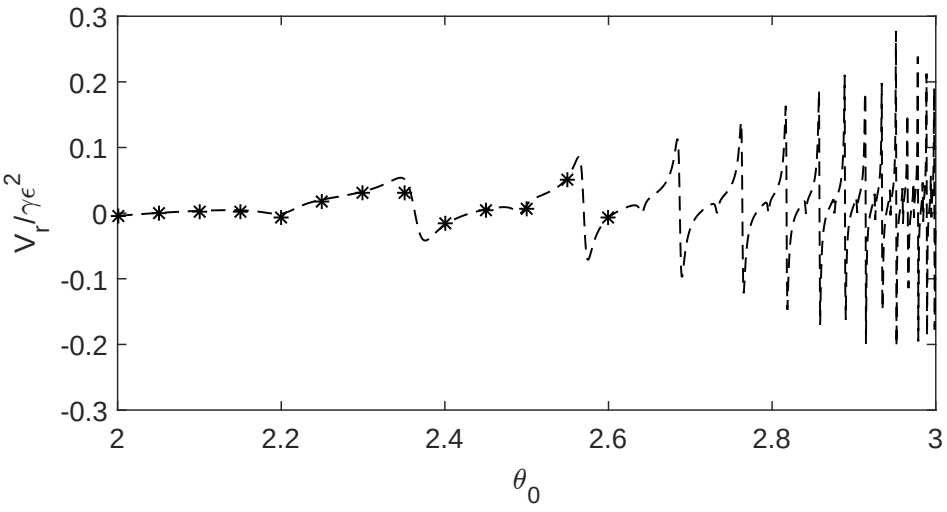


Figure 3.29: The rise velocity of the droplet against the magnitude of the contact angles for $\omega = 2, v' = 0.5, v'' = 0, g = 0$ and no hysteresis. The dashed line is the solution given by the first order asymptotic method, along with the force balance, whilst the markers are results obtained from the full solution method with $\epsilon = 0.1$ and $\gamma = 1$.

rise velocity of the droplet against the frequency, as we slowly increase θ_0 up to 1.4, shown in figure 3.28. We can see the as the magnitude of the contact angles increases up to 1 the peak rise velocity also increases and also the peaks frequency decreases. After this point the frequency continues to decrease but the peak also begins to as well. This continues until $\theta_0 = \pi/2$, where the rise velocity is zero for all frequencies.

As the magnitude of the contact angles surpasses $\pi/2$ the peaks switch signs and begin to increase in size (see figure 3.29 where we have now fixed ω and plotted the rise velocity against θ_0). What is interesting about this graph is when the magnitude of the contact angles surpasses 2.5 the rise velocity begins to vary quite rapidly with θ_0. Looking at the asymptotic result on its own would yield the conclusion that there must be some numerical error encountered within the solution method but if we also include results obtained from the full solution method we observe very good agreement between the two. This leads to the conclusion that the unusual erratic behaviour is actually an interesting result that we need to examine further. The lack of markers shown on figure 3.29 is because of the time taken for the solution method to converge for larger values of θ_0 as well as the fact that, for the current contact line law, the full solution method encountered breakages similar to figure 3.16

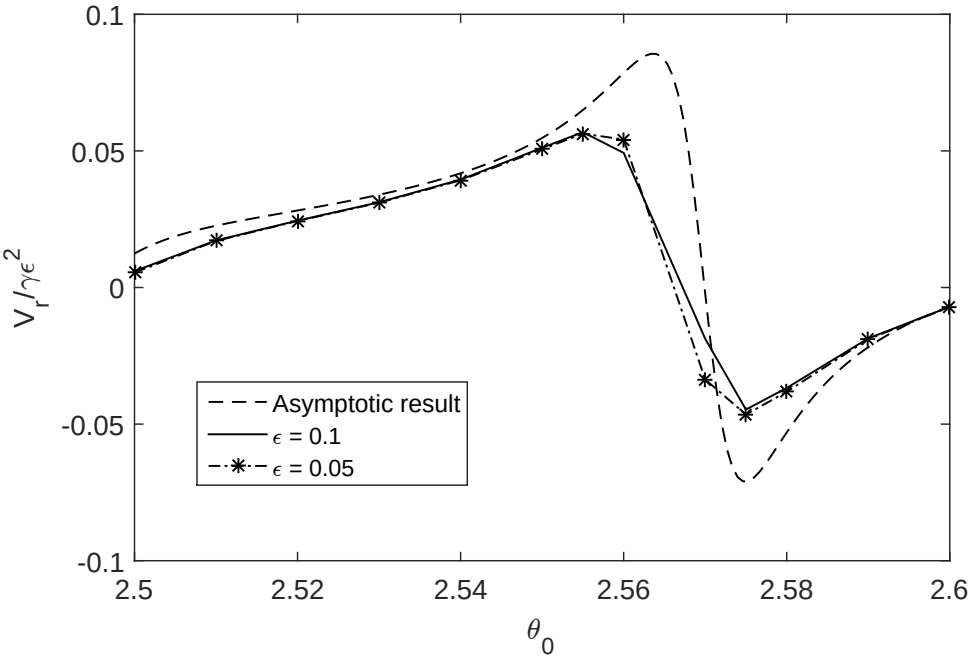


Figure 3.30: Comparison between the asymptotic solution solution and the full solution for the rise velocity of the droplet against the frequency of oscillation with $\gamma = 1, \omega = 2, v' = 0.5, v'' = 0, g = 0$ and no hysteresis.

as θ_0 surpassed 2.7. We have however taken a small section of figure 3.29 and compared the asymptotic result to the solution method more accurately, shown in figure 3.30. We can see from this graph that halving the value of ϵ does little to change the rise velocity of the full solution and so reducing it further will not produce a solution much closer to the asymptotic one. Although the two methods give results that vary slightly at the 'peaks', both rise velocities give the same, unusual behaviour that we want to examine and the similarity between the two means that this is indeed caused by the mechanics of the problem and not an error within the method.

To examine this problem further we will vary ω and fix θ_0 instead, shown in figure 3.31. The first thing we can see is that for large θ_0 the rise velocity also varies rapidly for ω as well. Although it looks like the third graph contains a set of singularities it is actually just rapidly varying similar to figure 3.29. Another thing we can take from these graphs is the change in the order of magnitude of $V_r/\gamma\epsilon^2$ as we increase θ_0. By looking at the $y-$axis we can see that increasing θ_0 by 1 increases the rise velocity by an order of 10. The only other quantity that changes at a similar rate is the area of the droplet given

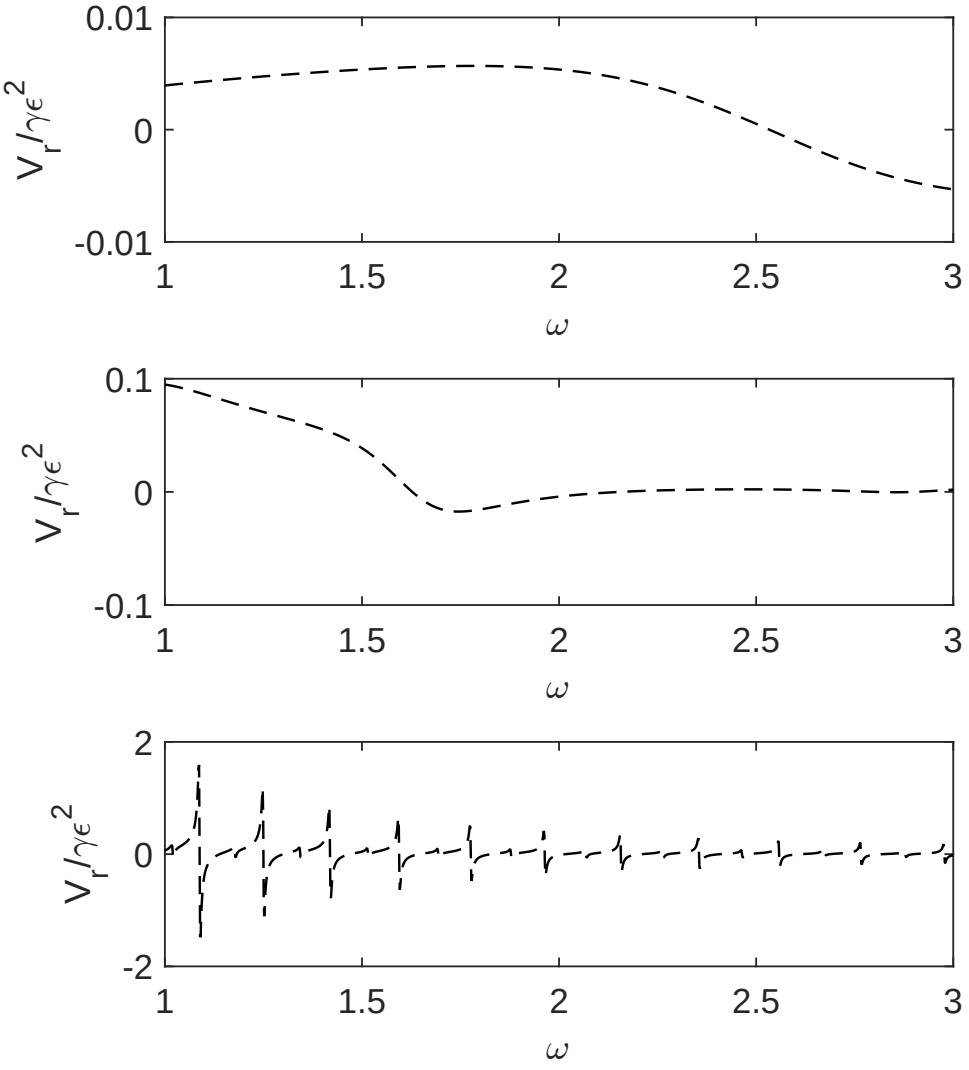


Figure 3.31: The asymptotic solution for the rise velocity of the droplet against ω for $v' = 0.5, v'' = 0, g = 0$ and no hysteresis. The three graphs from top to bottom are for $\theta_0 = 1, 2$ and 3 respectively.

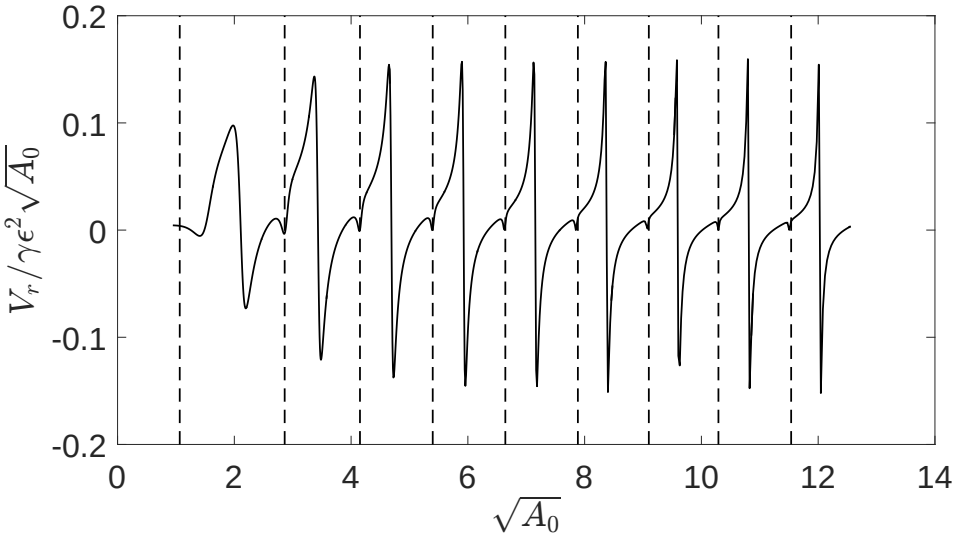


Figure 3.32: The rise velocity of the droplet against the square root of the droplet's area in the range $\theta_0 \in [2, 3]$, for $\omega = 2, v' = 0.5, v'' = 0, g = 0$ and no hysteresis. The dashed lines represent extra modes appearing on the free surface.

by (3.32). If we now look at figure 3.29 again but divide the rise velocity by the square root of the area and plot this against the square root of the area instead of θ_0 we get a result that looks more uniform, shown in figure 3.32. Unfortunately the reason for using the square root of the area as both a scaling on the rise velocity, as well as $x-$axis, is unknown.

Now we will look into what changes between each of these rapidly varying peaks by examining the shape of the droplet for a value of θ_0 between each peak. The results of this are shown in figure 3.33 and it becomes quite clear that each dashed line in figure 3.32 coincides with an extra mode on the surface of the droplet.

To finish this section we will look at the rise velocity of the droplet as we vary both the ω and θ_0 (figure 3.34). This graph clearly shows how must the rise velocity varies with both θ_0 and ω in the limit of $\theta_0 \to 3$. For θ_0 very close to 3 the results have not fully resolved since taking results at too many points makes the graph hard to read.

To summarise, we have looked at the motion of the droplet for a linear contact line law whilst varying all other parameters. We found that in the thin droplet limit the rise velocity remains proportional to ϵ^2 for values of ϵ up to 1 but for more realistic size contact angles this was no longer the case. The

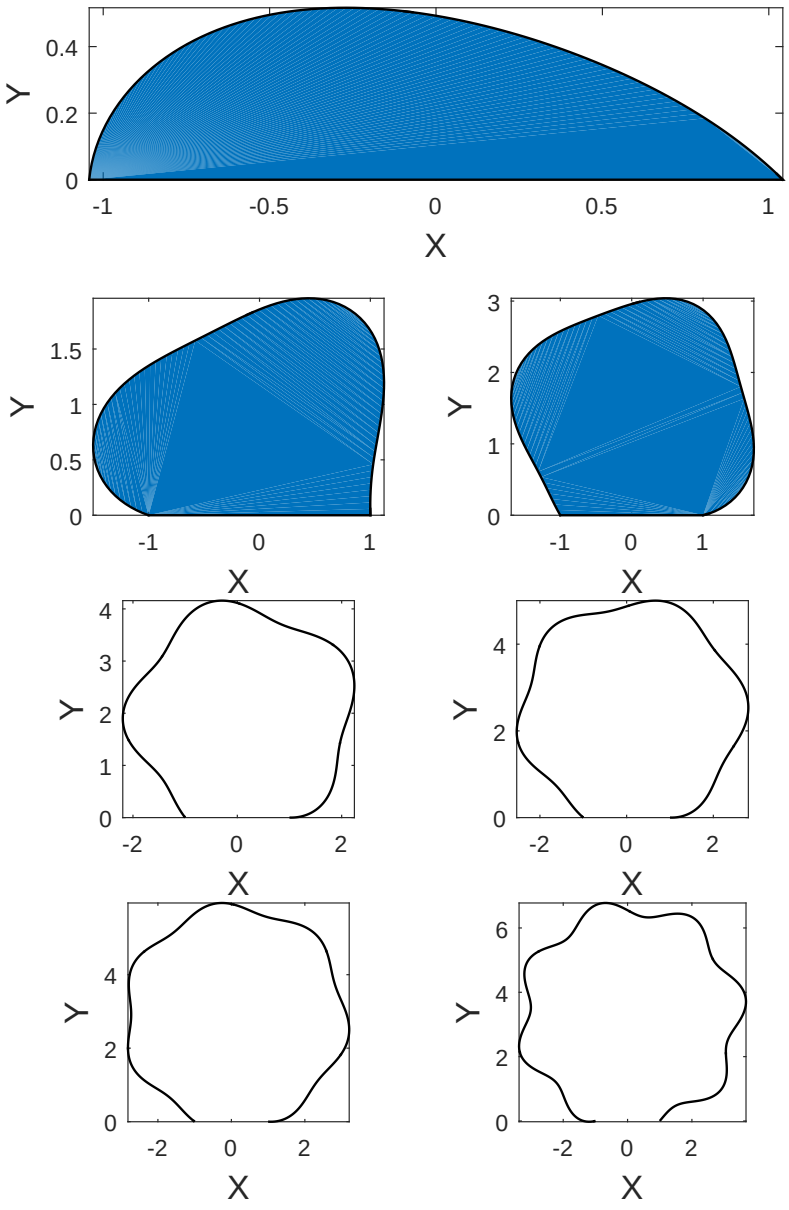


Figure 3.33: The shape of the droplet at for a given time where $\epsilon = 0.5, \gamma = 1, \omega = 2, v' = 0.5, v'' = 0, g = 0$ and no hysteresis. The value of θ_0 for each graph is $1, 2.2, 2.5, 2.65, 2.74, 2.8, 2.84$ respectively and the filled graphs represent the solution to the full numerical method whereas the unfilled graphs are the small amplitude asymptotic solutions.

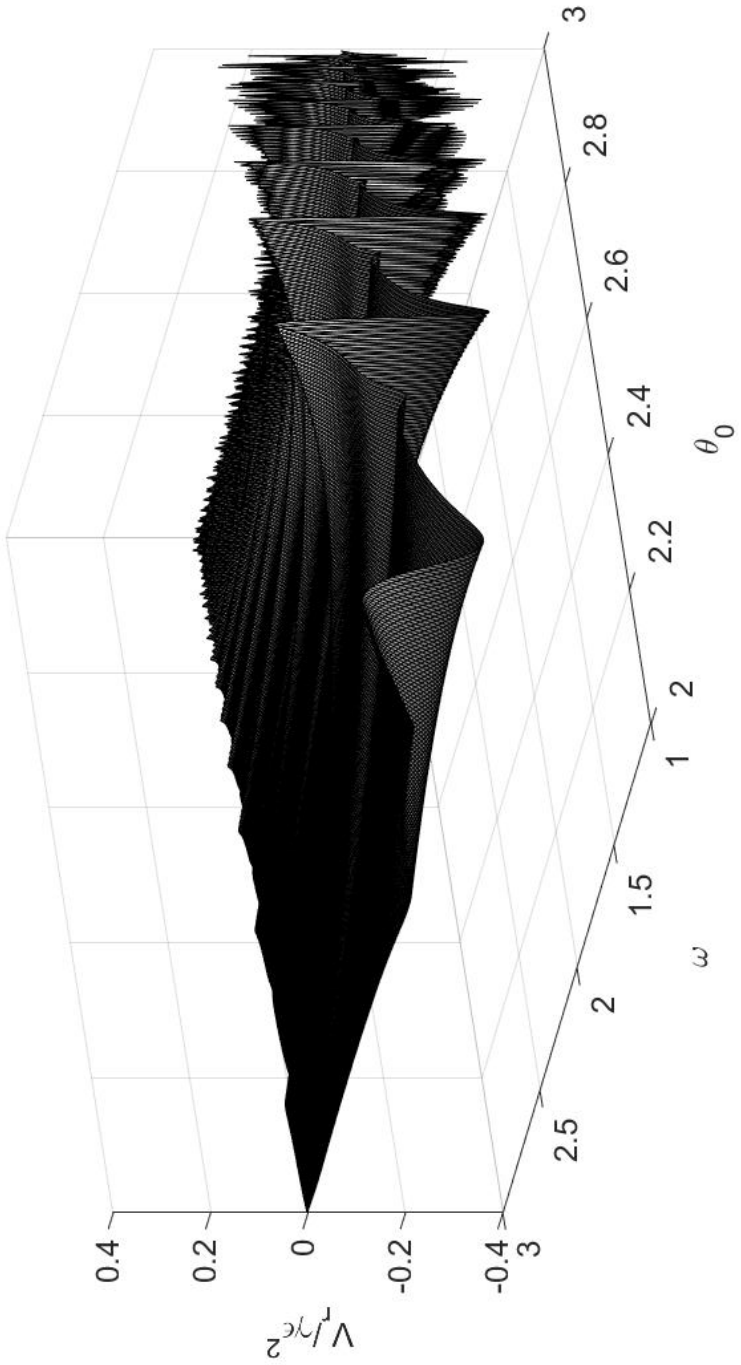


Figure 3.34: A 3-D plot of the rise velocity against the frequency of the oscillations and the magnitude of the contact angles for $\gamma = 1, v' = 0.5, v'' = 0$ and $g = 0$.

larger forcing causes the rise velocity to increase proportionally faster than ϵ^2 in the range $\omega \in [0, 2.5]$ however for frequency values greater than this the rise velocity remains proportional to the amplitude squared as ϵ increases. In addition to this we saw that when the forcing was large enough there is a range of low frequencies where a bulk of the fluid can be made to almost pinch off from the rest of the droplet, a result that was not present in [3].

We examined what happens when we increase γ, which is equivalent to increasing the forcing perpendicular to the substrate. This had a very similar effect on the rise velocity as increasing ϵ but the magnitude of the change is slightly lower due to the forcing parallel to the substrate remaining the same. We have shown how dominant the contact line law is for this problem; by altering the linear law by just a small constant we observed the rise velocity of the droplet change a significant amount. Even more importantly a sliding droplet can been shown to climb and vice versa. This helps to show how little we know about the mechanics of the contact line law and how important it is for unsteady problems involving a contact line. Next we showed that although the gravitational force was important when measuring the rise velocity of the droplet, the inclusion of it does little to change the mechanics of the problem.

Finally we examined how varying the magnitude of the contact angles can alter the problem. We found that for very small θ_0 the solution matched very closely to the shallow water limit [3], and as θ_0 is increased to 1 the magnitude of the initial peak in the rise velocity increased and the frequency of it decreased. Now as θ_0 tends to $\pi/2$, the rise velocity decreases for all frequencies until it reaches zero. After θ_0 surpasses $\pi/2$ the rise velocity begins to increase much quicker than it decreased and as θ_0 nears π the rise velocity changes very rapidly. It turns out that on the free surface of the droplet modes begin to form as θ_0 gets large, and it is these modes that cause the rapid change in the rise velocity.

The main conclusion we make take from this section is that for even the most basic contact line law, without physical effects such as hysteresis, we can create a model of a droplet that can both climb up and slide down the substrate when a sinusoidal oscillation is applied parallel to the acceleration due to gravity.

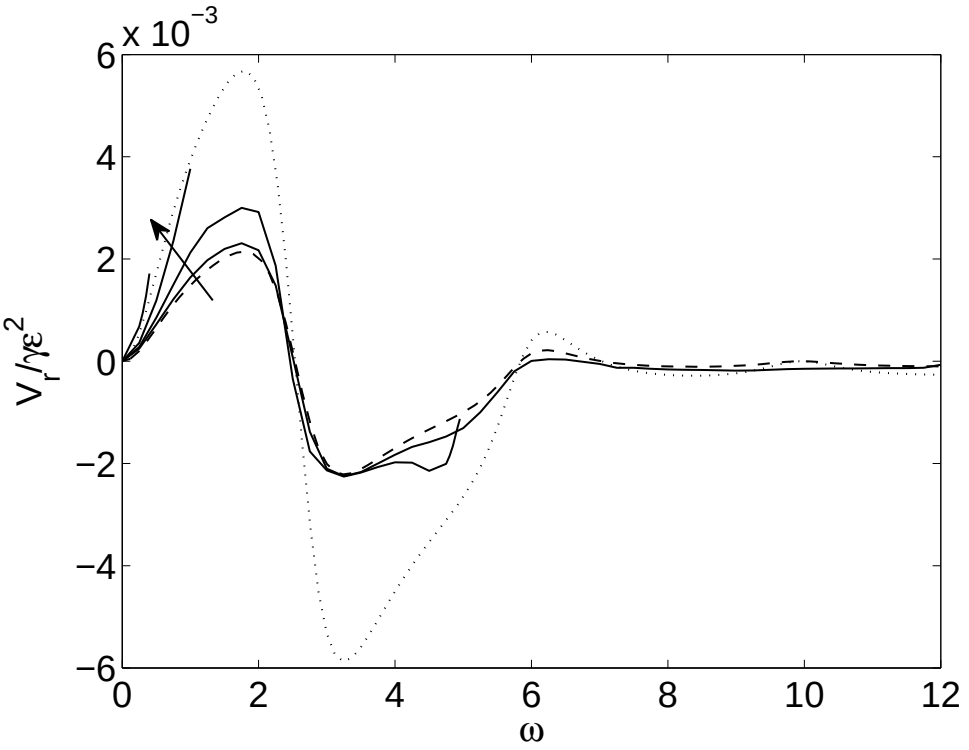


Figure 3.35: The rise velocity of the droplet against ω for $\gamma = 5, \theta_0 = 1, v' = 0.5, v'' = 0.2, g = 0$ and no hysteresis. The dashed line is the small amplitude asymptotic solution whilst the solid lines, following the direction of the arrow, coincide with $\epsilon = 0.25, 0.5, 0.75, 1$ respectively. The dotted line is the small amplitude asymptotic solution for $v'' = 0$. The results stop at $\omega = 5$ for $\epsilon = 0.5$, 1.05 for $\epsilon = 0.75$ and 0.45 for $\epsilon = 1$ due to the contact angle at the trailing end reaching zero.

3.4.2 Non-linear contact line law

As we already know the velocity of the contact line most certainly cannot be modelled as a linear function of the contact angles. In this section we will alter the contact line law in order to see whether we can produce results more qualitatively comparable to [8]. We will begin with the quadratic term already present in the small amplitude asymptotic solution, and then also look at cubic contact line laws [33]. In addition we will include contact angle hysteresis and look at some alternate laws to see how it changes the results.

Quadratic contact line law

When we examined the small amplitude asymptotic approximation we expanded (3.25)-(3.28) up to order ϵ^2. This meant that the Taylor expansion of

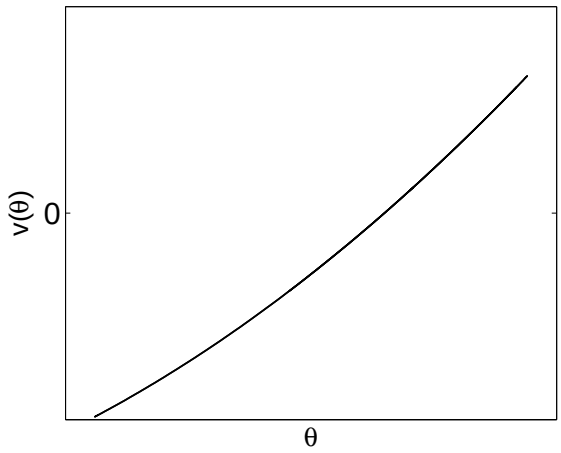


Figure 3.36: The velocity of the contact points as a function of their respective contact angles for a contact line law with both a linear and a quadratic term.

the contact line law contained a quadratic term weighted by v'' and so in this section we will look at some results when $v'' \neq 0$. If we use a fully quadratic contact line law we will result in a local minimum at $\theta = \theta_0$ which is very unrealistic (and unhelpful) therefore we will keep the linear term and set $v'' < v'$. If we now examine the rise velocity produced using this quadratic contact line law (figure 3.35) there are a few points we can discuss. First of we see that the magnitude of the peaks has decreased significantly. The reason for this can be seen in the oscillating term of (3.128) which is weighted by $(v''/v' - \theta_0 \cot \theta_0)$. For the value of θ_0 used the magnitude of this term decreases as the ratio v''/v' increases. We can also see from this graph that the solution breaks for smaller values of ϵ compared to the solely linear case. This is due to the fact that with the additional quadratic term, the speed of the leading contact point has been increased whilst the trailing point has been reduced. The most common cause for the droplet breaking is the trailing end not being able to keep up now, and when using a quadratic contact line law, this occurs for lower values of ϵ.

Although the addition of a quadratic term in the contact line law still produces a droplet that can still either climb up or slide down the substrate when an oscillation is applied, the unusual form of the contact line law (figure 3.36) is unhelpful and so we will not examine it any further.

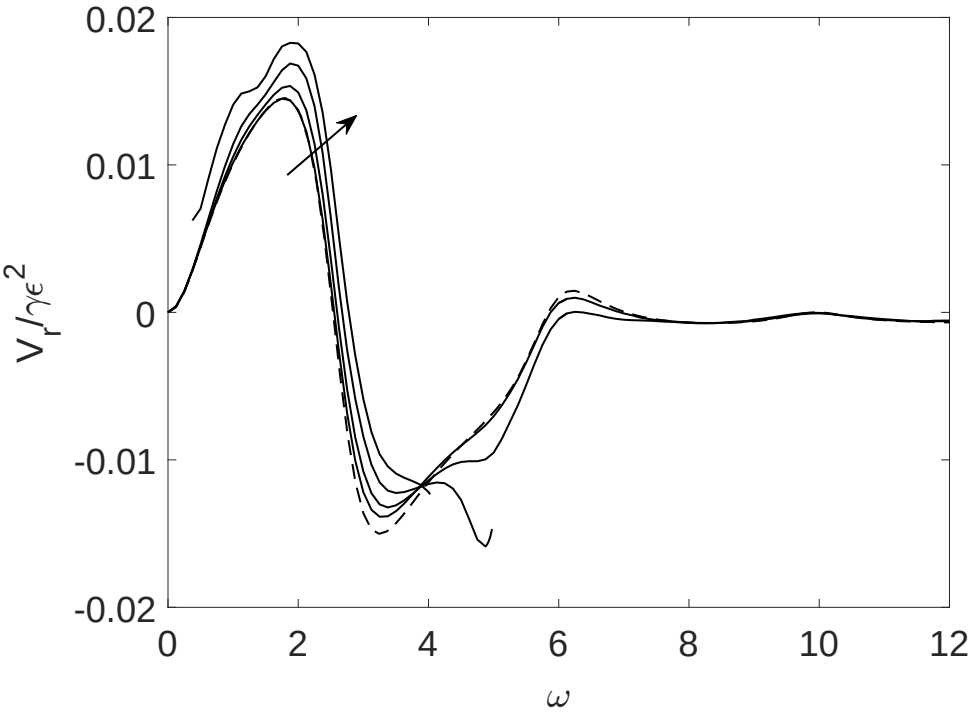


Figure 3.37: The rise velocity of the droplet against ω for $\gamma = 5, \theta_0 = 1, g = 0$ and a contact line law given by $v(\theta) = (\theta - \theta_0)/2\sqrt{\theta_0\theta}$. The dashed line is the small amplitude asymptotic solution whilst the solid lines, following the direction of the arrow, coincide with $\epsilon = 0.25, 0.5, 0.75, 1$ respectively. The results stop at $\omega = 5$ for $\epsilon = 0.75$ and 4.05 for $\epsilon = 1$ due to the contact angle at the trailing end reaching zero. In addition the results for $\epsilon = 1$ do not start until $\omega = 0.375$ due to the bulk of the fluid almost pinching off.

A square root in the contact line law

We will now look at a contact line law that includes the condition $v \to -\infty$ as $\theta \to 0$, in order to examine if we can increase the amplitude of the oscillations compared with the linear contact line law. In order to do this we will model the velocity of the contact line as

$$v(\theta) = \frac{\theta - \theta_0}{2\sqrt{\theta_0 \theta}},$$

where the square root has been chosen in order to fulfill the new condition, as well as agree with (4.9) in [3] as $\theta_0 \to 0$. Although this new law has no physical significance we will use it to look at the mechanics of the problem as ϵ is increased. If we now look at some results produced by this new law (figure 3.37) we can see there are a couple of points worth discussing. The first being that the magnitude of the rise velocity has over doubled that of a fully linear contact line law even for $\epsilon = 0.25$. The reason for this is if we look at the change in the force balance result (A.7) we can see the v''/v' has been replaced with a -1. This means when comparing the results for $v'' = 0$ and $\theta_0 = 1$ we get an increase in the magnitude of the rise velocity by a factor of 2.56. In addition to this we can also see from figure 3.37 that we now need a higher frequency in order for the droplet to break, as expected. What both figures 3.35 and 3.37 show us is that significant changes are seen in the results when we alter the contact line law; again signifying the importance of it in this problem. The final note we will make about this contact line law is that if we set $\theta_0 \ll 1$ we get the same results as figure 5 in [3].

Cubic contact line law

We have looked at some different non-linear contact line laws in order to see how the mechanics of the problem changes but now we will attempt to use something more realistic. To do this we will use results obtained for a steady flow [14][33] and model a contact line law similar. The contact line law will now contain a linear term (weighted by $v' = 1$) and a cubic term, giving

$$v(\theta) = \left(\frac{\theta}{\theta_0} - 1\right) + \left(\frac{\theta}{\theta_0} - 1\right)^3. \tag{3.183}$$

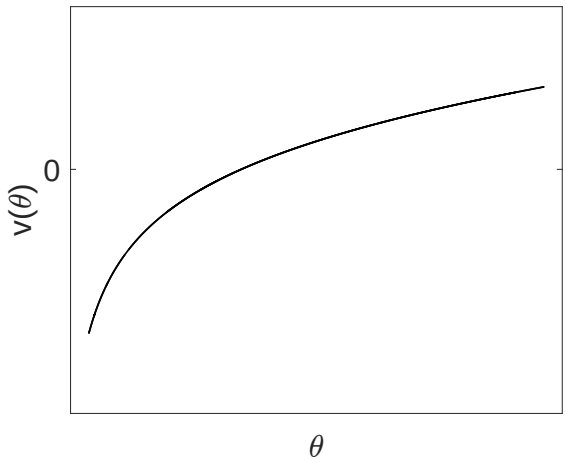


Figure 3.38: The velocity of the contact points as a function of their respective contact angles for a contact line law with a square root.

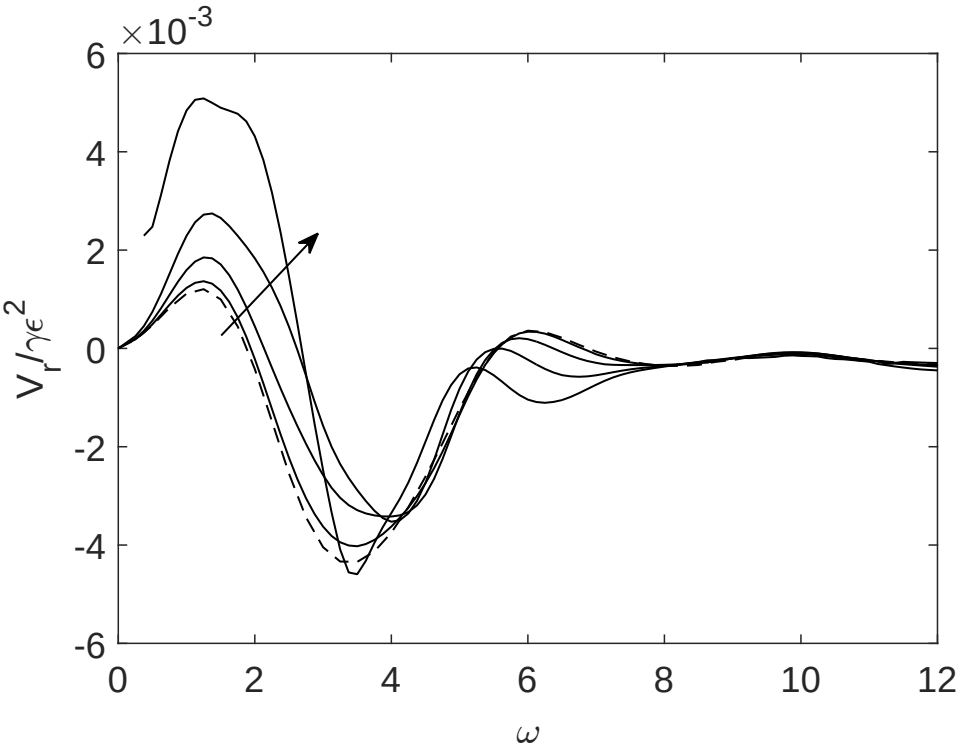


Figure 3.39: The rise velocity of the droplet against ω for $\gamma = 5, \theta_0 = 1, g = 0$ and a contact line law of the form $v(\theta) = (\theta/\theta_0 - 1) + (\theta/\theta_0 - 1)^3$. The dashed line is the solution for a linear contact line law and $\epsilon = 0.1$ and $v' = 1$ whilst the solid lines, following the direction of the arrow, coincide with $\epsilon = 0.25, 0.5, 0.75, 1$ respectively. The results for $\epsilon = 1$ do not start until $\omega = 0.375$ due to the bulk of the fluid almost pinching off.

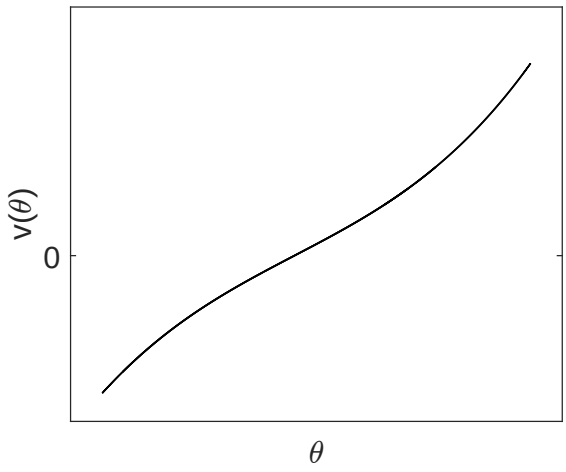


Figure 3.40: The velocity of the contact points as a function of their respective contact angles for a contact line law with both a linear and a cubic term.

Some results given by this new law can be seen in figure 3.39 and, as expected, when the amplitude of the oscillations are small the rise velocity is very similar to the linear contact line law. Again similar to the linear contact line law increasing the amplitude of the oscillations causes the magnitude of the initial peak to increase however unlike the linear law the initial trough becomes increasingly positive also. The rise velocity for $\omega \in [0, 2.5]$ continues to grow faster and faster as ϵ approaches 1, and we can also see that for higher frequencies the droplet does not break due to the increased velocity at the trailing end of the droplet, with the addition of the cubic term. Unfortunately we are still unable to increase ϵ much further without the droplet breaking for all $\omega \in [0, 2]$.

The reason the droplet breaks is due to a bulk of the fluid almost pinching off which is a result of γ being too large. If we look back at (3.18) we see that γ is approximately 1 during the actual experiment and therefore by reducing it for this analysis we can reach the values of ϵ we want (figure 3.41). Unfortunately what the left graph shows us is that as we increase the amplitude of the oscillations whilst using this contact line law, the rise velocity of the droplet decreases. This is the opposite of what we wish to achieve.

Hysteresis

Hysteresis is a very important mechanism in contact line dynamics and plays an important role in the droplet climbing up hill. When talking about hys-

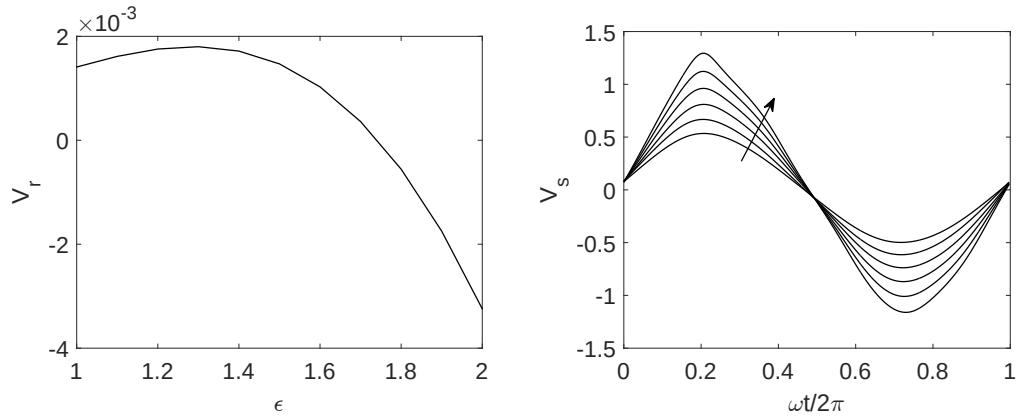


Figure 3.41: The rise velocity of the droplet against ϵ (left) and the velocity of the centre of the droplet over a period of oscillation, for ϵ increasing in the direction of the arrow from 1 to 2 in increments of 0.2 (right). The other parameters are $\gamma = 1, \omega = 1.5, \theta_0 = 1, g = 0$ and a contact line law given by $v(\theta) = (\theta/\theta_0 - 1) + (\theta/\theta_0 - 1)^3$.

teresis we return to a contact line law that includes both θ_A and θ_R, and so we will begin by adding a very small hysteresis interval, θ_I, which will be defined as

$$\theta_I = \theta_A - \theta_R. \tag{3.184}$$

The term hysteresis interval shall only be used for the cases where the average of θ_A and θ_R is θ_0 (as defined) however when we compare this model to [8] we will use the definition

$$\cos\theta_0 = \frac{\cos\theta_A + \cos\theta_R}{2},$$

similar to their method. This means that θ_0 will no longer be the mean (unless $\theta_A = \theta_R = \theta_0$). The first results we will look at is the rise velocity for the same parameters as figure 3.18, only now with the inclusion of hysteresis.

We can see from figure 3.42 that adding hysteresis into the problem (even a small amount) causes a large change in the rise velocity. We will now look at how the rise velocity is affected by examining it in sections. For the initial section when $\omega \in [0, 1]$ we see that adding very small amount of hysteresis to the model causes the rise velocity to increase but as the hysteresis interval is increased the velocity drops again and develops a strange zigzag pattern. We are unsure why this occurs, it is another unusual result of an unsteady flow with a contact line. The next section is $\omega \in [1, 3]$, and the addition of hysteresis causes a large increase in the magnitude of the peak/trough. The reason for

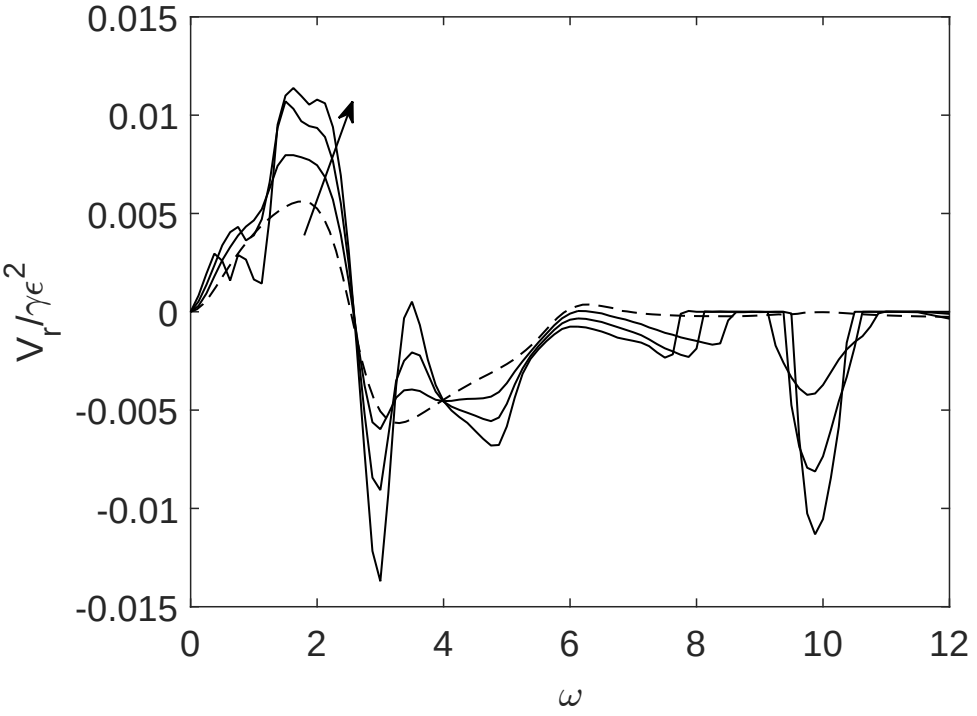


Figure 3.42: Rise velocity of the droplet against ω for $\epsilon = 0.1, \gamma = 5, \theta_0 = 1, v' = 0.5, v'' = 0$ and $g = 0$. The dashed line represents the rise velocity when there is no contact angle hysteresis present whilst the solid lines have a hysteresis interval of 0.02 (1), 0.04 (2) and 0.06 (3) respectively.

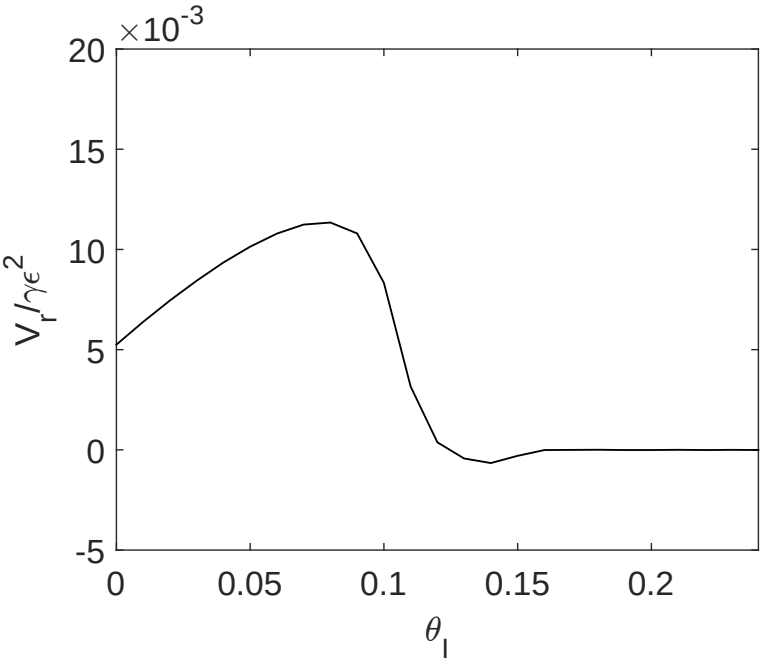


Figure 3.43: The rise velocity of the droplet against the hysteresis interval for $\epsilon = 0.1, \gamma = 5, \theta_0 = 1, \omega = 2, v' = 0.5, v'' = 0$ and $g = 0$.

this is that a resonant frequency of a pinned droplet can be found in this range (figure 3.25) and so as the contact angle hysteresis restricts the motion of the contact line, the droplet in this range shakes quite rapidly causing a net motion to still occur. This range of frequencies is in fact the final section that produces a rise velocity as we increase the hysteresis interval towards the limit of pinned contact lines. The final section we will look at is $\omega \in [9.5, 10.5]$, where the addition of hysteresis has caused a droplet with almost zero net motion to begin to slide very rapidly. This is again due to a resonant frequency for a pinned droplet being at $\omega = 10$. Apart from these sections the effects of hysteresis are either a small change in the rise velocity or, as ω gets larger, the contact points become pinned due to the relative sizes of the contact angles not being able to overcome the hysteresis interval. Another way of examining the effects of hysteresis on the rise velocity is to fix the frequency and increase the hysteresis interval (figure 3.43). We can see that as we increase the θ_I the rise velocity initially increases, as we saw in figure 3.42, however once it reaches its peak ($\theta_I = 0.08$) the hysteresis interval begins to restrict the motion of the contact points instead. This occurs up to a point where V_s is only negative or zero ($\theta_I = 0.14$). After this the more we increase the hysteresis interval the smaller the negative part of the swaying mode velocity becomes until the

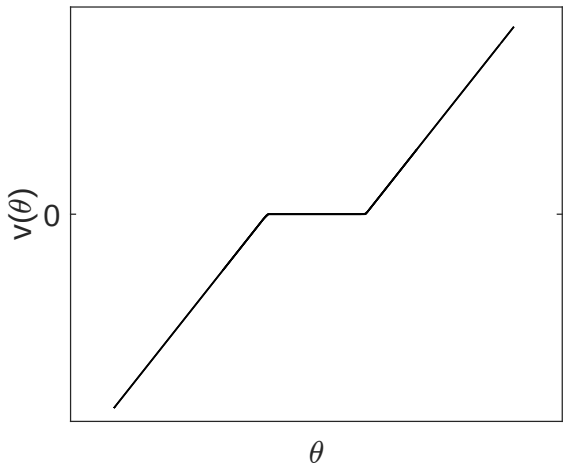


Figure 3.44: The velocity of the contact points as a function of their respective contact angles for a contact line law with contact angle hysteresis.

contact points are completely pinned ($\theta_I = 0.16$). In addition to this we will also examine how the velocity of the contact points look as a function of their respective contact angles (figure 3.44). As expected the velocity increases and decreases linearly when the contact angle is larger than θ_A or smaller than θ_R respectively and is zero otherwise.

Contact line dependence

We observed in section 3.4.1 that varying the weighting parameter of a linear contact line law can cause the rise velocity of the droplet to change dramatically. Now we will look how dominant an effect the contact line law has on the rise velocity when hysteresis is present (figure 3.45). We can see that as the hysteresis interval increases the magnitude of the rise velocity increases (as expected) but what is also clear, and more interesting, is that the three different lines are converging to a similar result. This suggests that although the contact line law is a very important component of this problem, the presence of contact angle hysteresis can be more dominant meaning less emphasis needs to be put on it. The importance of this result is that there is little yet known about modelling an unsteady contact line and so if we can negate the importance of it we will have an easier time understanding the problem.

Now to explain the mechanics behind this result. The effects of adding hysteresis to a contact line law is similar to adding a restriction to it and so adding a hysteresis interval of 1 would be similar to halving v'. This would

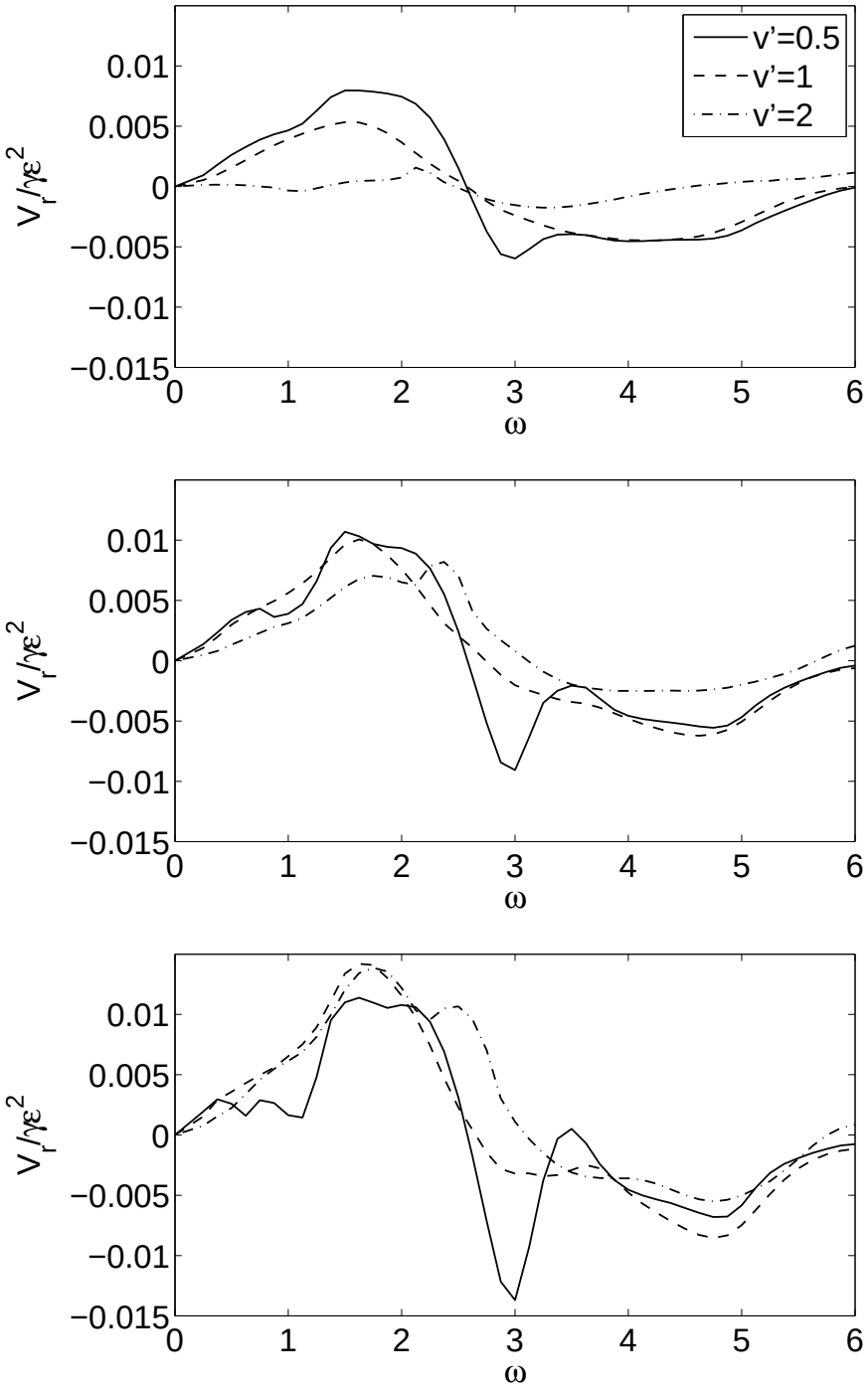


Figure 3.45: The rise velocity of the droplet against ω for $\epsilon = 0.1, \gamma = 5, \theta_0 = 1$, a linear contact line law and no gravity. The different lines on each graph represent different constants within the contact line law whilst the different graphs (top to bottom) represent hysteresis intervals of 0.02, 0.04 and 0.06 respectively.

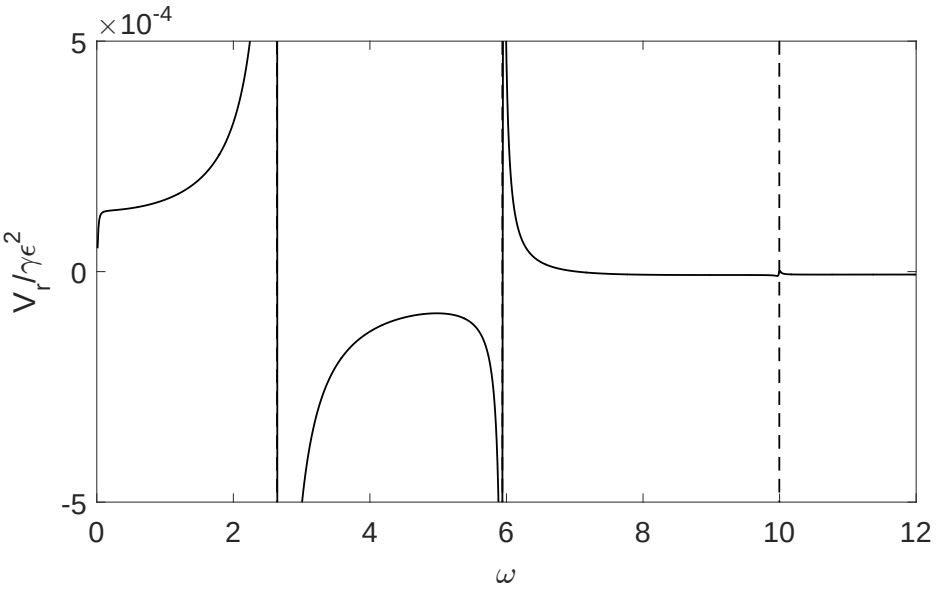


Figure 3.46: The small amplitude asymptotic solution for the rise velocity of the droplet against ω where $\gamma = 5, \theta_0 = 1, v' = 0.01, v'' = 0$ and $g = 0$. The dashed lines (including the two vertical solid lines) represent the droplet's resonant frequencies for the pinned contact point oscillations.

effectively decrease each arbitrary constant meaning the difference between them decreases also. This is the reason the results are getting closer together, and also why the solid line begins to show the resonant point first.

We have looked at how adding hysteresis is similar to decreasing v' and so we will now see how decreasing v' is similar to adding hysteresis. We will do this by examining the small amplitude asymptotic solution for the rise velocity for $v' = 0.01$ (figure 3.46). We can see that the droplet's modes approach resonant points for $\omega \approx 2.7$ and 5.9 however the third resonant point only produces a small peak at $\omega \approx 10$. What can also be seen in this graph is that for the interval between the first two resonant frequencies the rise velocity does not reach zero due to the fact that these modes are close by. This means that the droplet still shakes at quite large amplitudes and so still produces a net motion.

Typical, steady dynamic contact line law

What we discovered using a cubic contact line law is that we can use it to reach parameter values close to that of the actual experiment [8], but when we do the droplet slides. What we have also discovered is that for $\omega \in [1, 2.5]$,

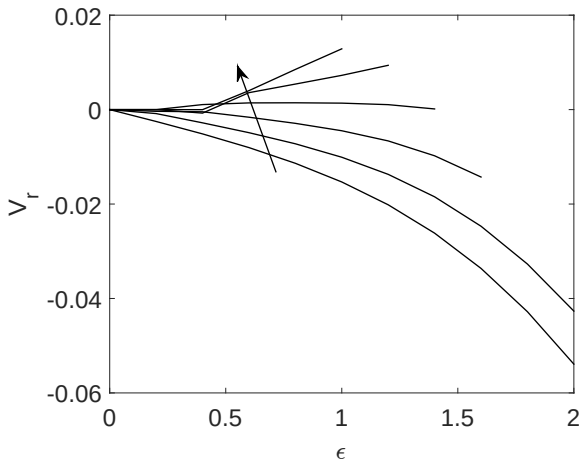


Figure 3.47: The rise velocity of the droplet against ϵ for $\gamma = 1, \theta_0 = 1, \omega = 1.5, g = 0.0275$ and a cubic contact line law. For the contact angle hysteresis, θ_A increases in increments of 0.05 and θ_R decreases in increments of 0.06 in the direction of the arrow, starting at no hysteresis.

the inclusion of contact angle hysteresis can increase the rise velocity. Now by combining these we will see if we can cause a droplet to climb uphill for experimental values. We should note that during the experiment the dimensionless advancing and receding contact angles were observed to be 1.25 and 0.7 respectively, and therefore make an uneven hysteresis interval. What we will examine is how adding increased amount of hysteresis affects the maximum ϵ we can use without the droplet breaking and additionally what effect this has on the rise velocity. The results in figure 3.47 show us that as we increase contact angle hysteresis we are no longer able to produce results for as large an amplitude. The reason for this is that the amplitude of the oscillations will affect the motion of the fluid whereas the hysteresis affects the motion of the contact points. By increasing the hysteresis we restrict the motion of the points whilst the bulk of the fluid is still attempting to travel a similar distance as with the decreased amount of hysteresis. The result of this is the contact angle at the trailing end of the droplet is more likely to reach zero, giving the results shown in figure 3.47. What is more interesting about this graph is the fact that the rise velocity does increase with hysteresis, up to a point where it is positive for the desired values of θ_A and θ_R. An additional way we can use this contact line law to compare to the experiment is by examining the shape of the droplet over one period of oscillation (similar to figure 1.2). We can see from figure 3.48 the shape of the droplet as it climbs up the substrate. This

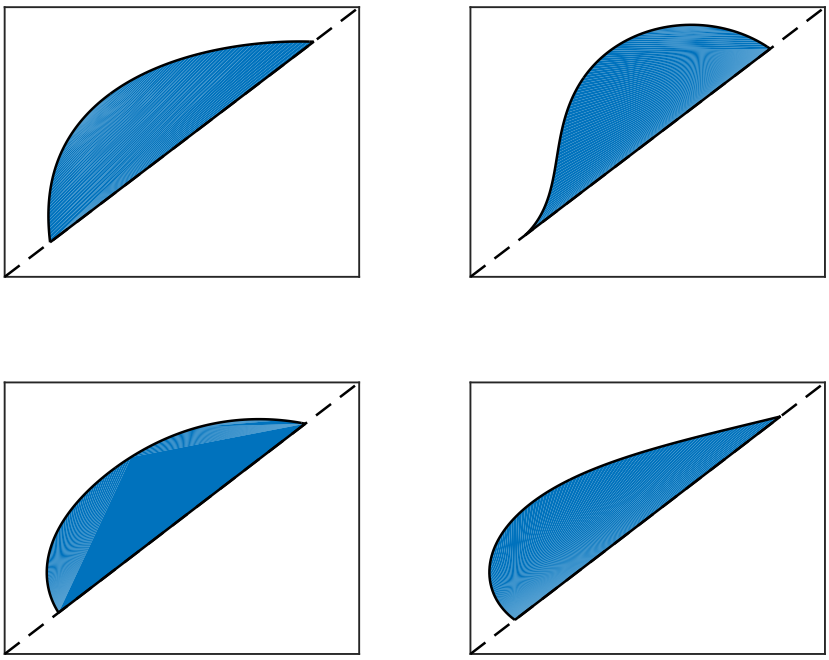


Figure 3.48: Model of the droplet at equal time intervals over one period of oscillation. The parameter values are $\epsilon = 1, \gamma = 1, \theta_0 = 1, \omega = 1.5, g = 0.0275, \theta_A = 1.25, \theta_R = 0.7$ and a cubic contact line law.

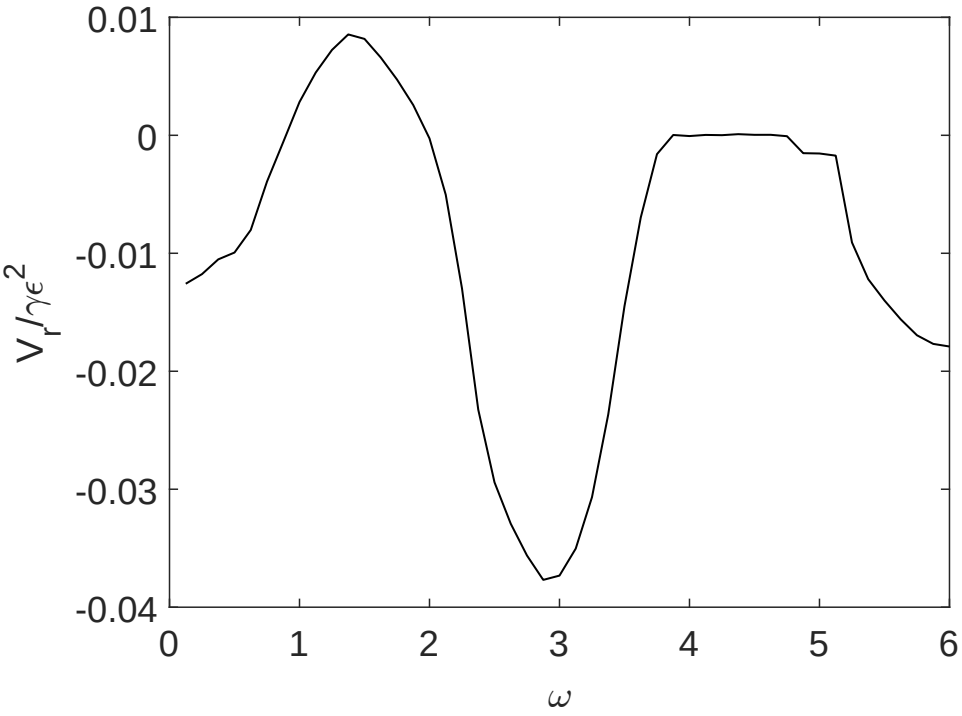


Figure 3.49: The rise velocity of the droplet against the frequency for $\epsilon = 1, \gamma = 1, \theta_0 = 1, g = 0.04, \theta_A = 1.25, \theta_R = 0.7$ and a cubic contact line law.

shows the characteristics of the climbing flow, where the contact angle at the 'bottom' of the droplet varies more than at the 'top', and by taking the average over one period of oscillation for the displacements in the contact points due to the change in angles, we see a net gain up the substrate. Unfortunately apart from that it is difficult to use these graphs as a comparison. We will now look at how the rise velocity changes with the frequency for these parameter values (figure 3.49). We can see from this graph how for these larger values of ϵ and the realistic contact angle hysteresis the droplet is able to climb up the substrate. Unfortunately if we make a direct comparison between figure 3.49 and any horizontal line drawn across figure 2 of [8] we see that the results of this contact line law still do not follow the same pattern of those seen in the experiment. We can however state the rise velocity in both cases tends to zero as the frequency increases. For completeness, we can see in figure 3.50 that the shape of the contact line law is similar to that shown in [14][33] for their analysis of steady moving contact lines.

To summarise, we have examined how the behaviour of the droplet changes when we use a non-linear contact line law. We began by looking at a quadratic

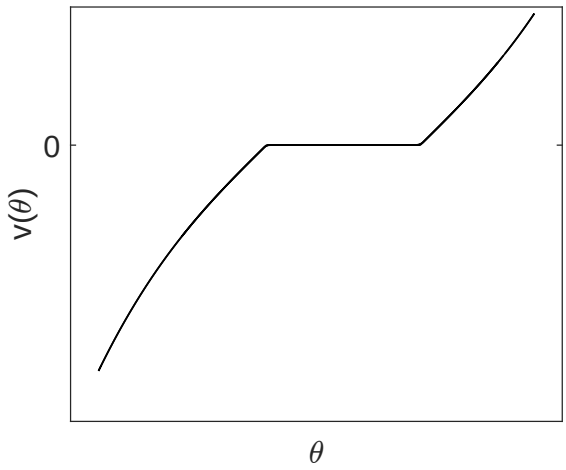


Figure 3.50: The velocity of the contact points as a function of their respective contact angles for a cubic contact line law with contact angle hysteresis.

law which is consistent with the small amplitude asymptotic solution. What we found from this is that, in addition to this law being physically unrealistic, the quadratic term causes the magnitude of the rise velocity peaks to decrease as well as causing the droplet to break for smaller amplitudes compared to the linear law.

We then moved onto a contact line law with a factor of $1/\sqrt{\theta}$ included, to help encourage the contact angle at the trailing end of the droplet to not reach zero. This law did the opposite of the previous one, both increasing the magnitude of the peaks as well as the range of results that could be obtained before the droplet breaks. So far both of these laws have little theoretical justification however and are just included to see how they alter the mechanics of the system.

Next we used a cubic contact line law in order to move towards something more physically realistic. What we found using this law is that the additional term allowed us to reach solutions to even higher amplitude oscillations, even for parameters similar to the experiment, however what we also found was that for these values the droplet slid downhill.

We then added contact angle hysteresis to the linear contact line law and found that it altered the results quite significantly. The magnitude of the rise velocity of the droplet increased quite substantially for frequencies near the pinned contact points resonant frequencies, whereas it tended to zero in other areas. We also discovered that the weighting parameter v' has a decreased

effect on the rise velocity the larger the hysteresis interval.

Finally we combined the last two contact line laws in order to produce a velocity dependence similar to that observed in experiments on steady moving contact lines. What this showed is that we can use parameter values similar to the experiments and produce a droplet that can either climb up or slide down the substrate. This is mainly due to the addition of contact angle hysteresis and how the larger it was, the more the rise velocity increased (even though it caused the maximum allowed amplitude of oscillations to decrease). Overall we have shown how different singled-valued contact line laws can change the mechanics of the problem whilst still all producing droplets that can either move up or down the substrate.

3.4.3 Time dependent contact line law

So far we have only examined results for the case where the velocity of the contact points is a single valued function of the respective contact angle however we know from [34][8] that this is not the case for an unsteady flow. In this section we will add a time dependency to the contact line law of the form

$$\tau \frac{dv}{dt} + v = f(\theta), \quad \text{at } x = \pm D, \tag{3.185}$$

where τ is a constant which we will prescribe and $f(\theta)$ is some function of the contact angle similar to the previous two sections. We currently have no physical justifications for using this law. We are just examining how it changes the mechanics of the problem, and to see if it produces results closer to that of [8]. We will begin by setting $f(\theta) = (\theta/\theta_0 - 1)$ and see how the addition of the time dependency compares to the linear contact line law with $v' = 1$. If we now compare the results for when $\tau = 0$ and 0.1 (figure 3.51) we see that although the rise velocity has changed, it is nothing significant. The reason the difference between $\tau = 0$ and $\tau = 0.1$ increases with ω is due to the $\omega^2\tau^2$ term in (A.11). In addition to this the droplet also does not break in the range of frequencies for $\epsilon = 1$, unlike the purely linear case. What is more interesting is if we now look at the velocity of the contact points as a function of the contact angles. We can see from figure 3.52 that when the contact line law has a time dependency the velocity of the contact points are no longer singled value functions of the contact angles. Due to $f(\theta)$ being linear, and without the presence of contact angle hysteresis, we see that the new relationship between

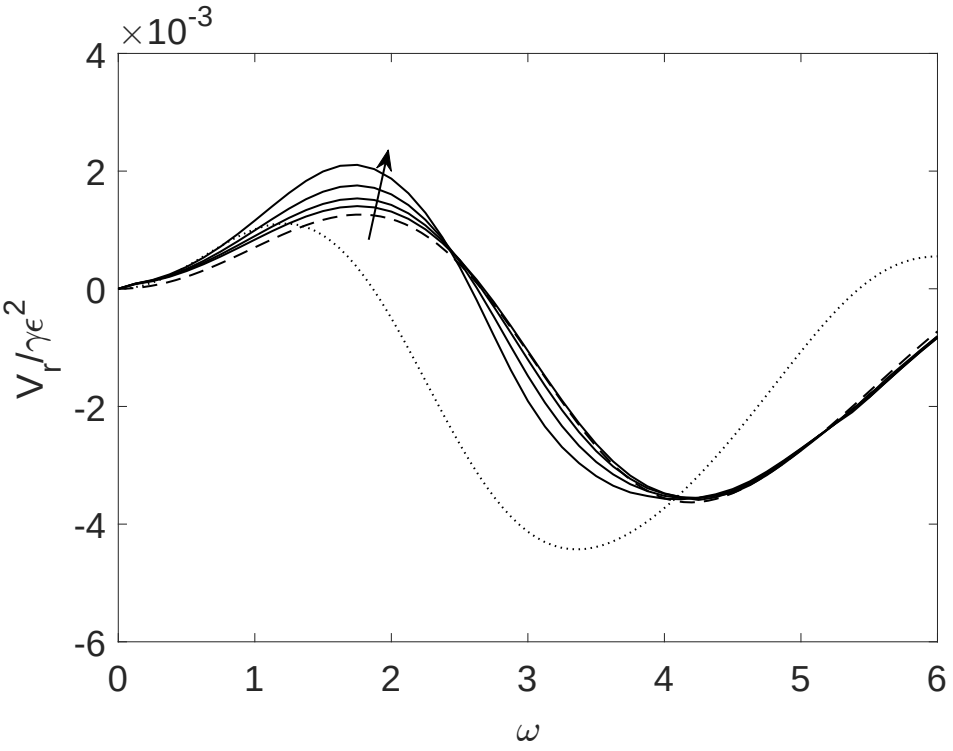


Figure 3.51: The rise velocity of the droplet against ω for $\gamma = 1, \theta_0 = 1, g = 0$ and $f(\theta) = (\theta/\theta_0 - 1)$ within the time dependent contact line law with $\tau = 0.1$. The dashed line is the small amplitude asymptotic solution whilst the solid lines, following the direction of the arrow, coincide with $\epsilon = 0.25, 0.5, 0.75, 1$ respectively. The dotted line is the small amplitude asymptotic solutio for $\tau = 0$.

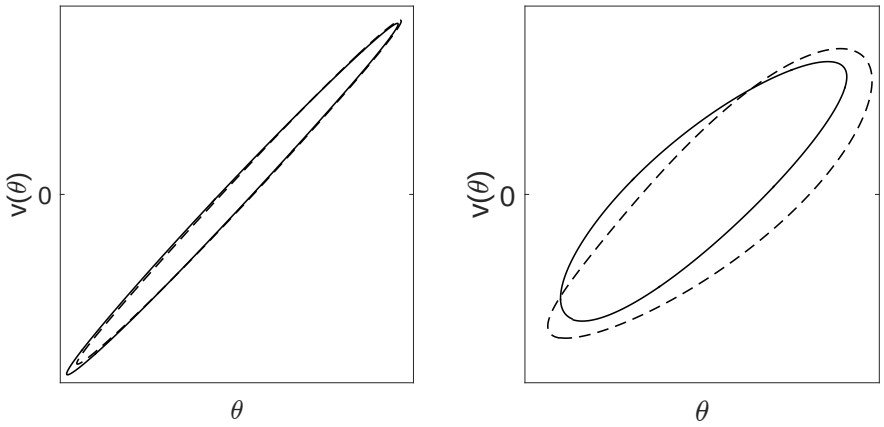


Figure 3.52: The velocity of the contact points as a function of their respective contact angles for a time dependent contact line law with $\tau = 0.1$ and $f(\theta) = (\theta/\theta_0 - 1)$. The left graph is for $\omega = 1$ and the right is for $\omega = 6$. The dashed line is θ_+ and the solid line is θ_-.

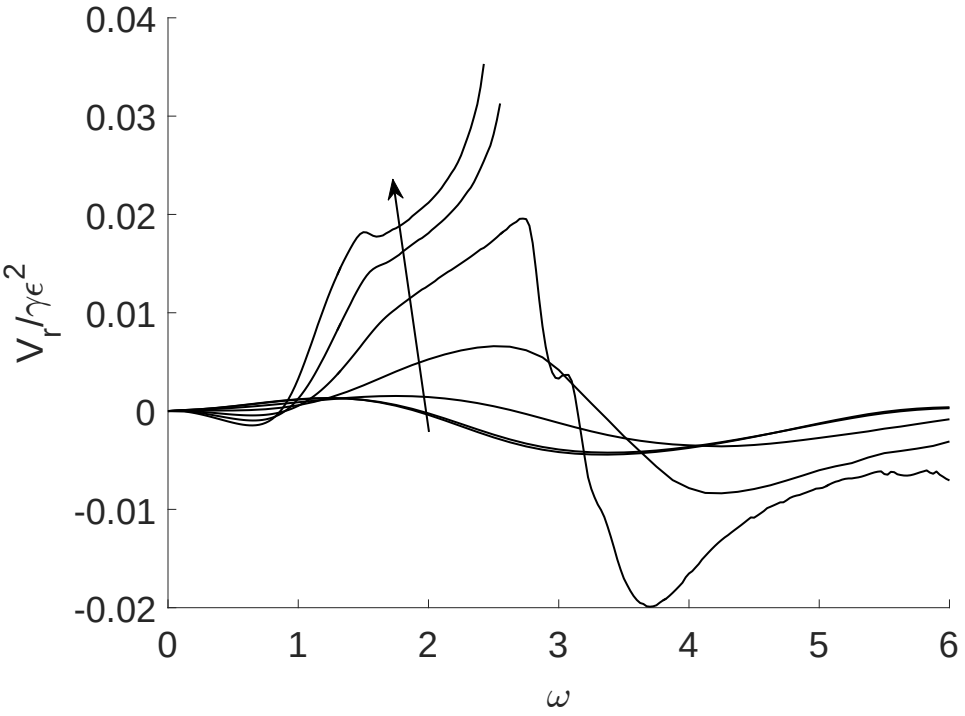


Figure 3.53: The rise velocity of the droplet against the frequency of the oscillations for $\epsilon = 0.5, \gamma = 1, \theta_0 = 1, g = 0$ and $f(\theta) = (\theta/\theta_0 - 1)$ within the time dependent contact line law. The solid lines, following the direction of the arrow, coincide with $\tau = 0, 0.01, 0.1, 0.25, 0.5, 0.75, 1$ respectively. The results stop at $\omega = 2.575$ for $\tau = 0.75$ and 2.45 for $\tau = 1$ due to the contact angle at the trailing end reaching zero.

$v(\theta)$ and θ is that of an ellipse; where the thickness is dependent on the size of ω. This is one step closer to results for an unsteady dynamic contact line.

Increasing τ

Now that we have introduced a new parameter in this section we should vary it to see how it alters the results. We already know that the difference between $\tau = 0$ and 0.1 is quite small for the frequency range we are using but when we start to increase τ further we can see from figure 3.53 that the results start to change significantly. The reason for this again is due to the $\omega^2\tau^2$ term in (A.11) which grows very large for $\tau = 0.75$ and 1, causing the rise velocity to become significantly larger compared to $\tau = 0$ and also causes the droplet to break. If we now look at the contact line law shown in figure 3.54 we can see that increasing τ increases the width of the ellipse. What we can also see from

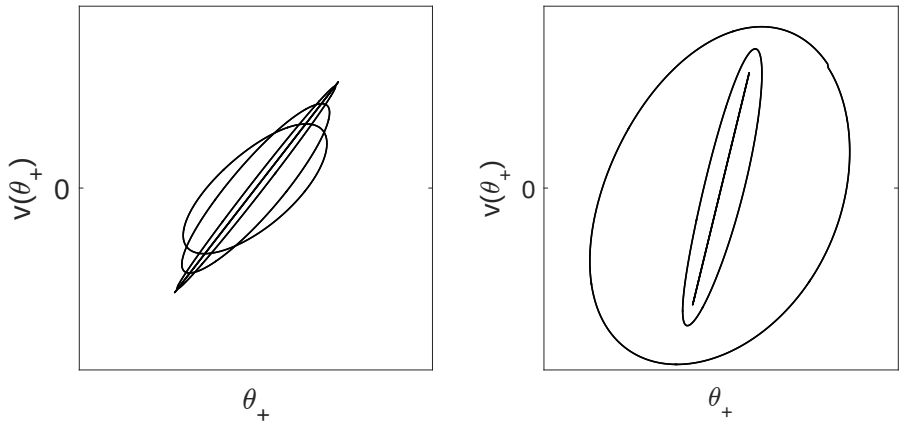


Figure 3.54: The velocity of the positive contact point as a function of θ_+ for a time dependent contact line law with τ increasing as $0, 0.1, 0.5, 1$ and $f(\theta) = (\theta/\theta_0 - 1)$. The left graph is for $\omega = 1$ and the right is for $\omega = 6$. The right graph has no line for $\tau = 1$ as the droplet broke before then.

this though is that for $\omega = 6$ not only does the width of the ellipse increase but so does the whole radius.

The addition of gravity

Similar to before we will again set $g \neq 0$ in order to see if this makes any significant changes to the results, apart from a shift in the rise velocity. If we compare the shape of the rise velocity against the frequency, with and without the acceleration due to gravity (figure 3.55), we see very little change between the two curves for $\omega \in [0, 3]$ and only a slight change for ω larger than 3. This would again suggest that we can set $g = 0$ without much loss of generality for the mechanics of the problem, however if we now look at the velocity of the contact points we see this may not be the case. The contact line law shown in figure 3.56 shows us that when the acceleration due to gravity is present in the problem, there is a shift between the velocity of the contact points as well as the rise velocity. Although this change has little effect on the rest of the solution it does show us that gravity should not be ignored when using a time dependent contact line law.

Additional cubic term

Now that we have established that adding a time dependence to the contact line law is a step closer to a more realistic unsteady flow we will alter the

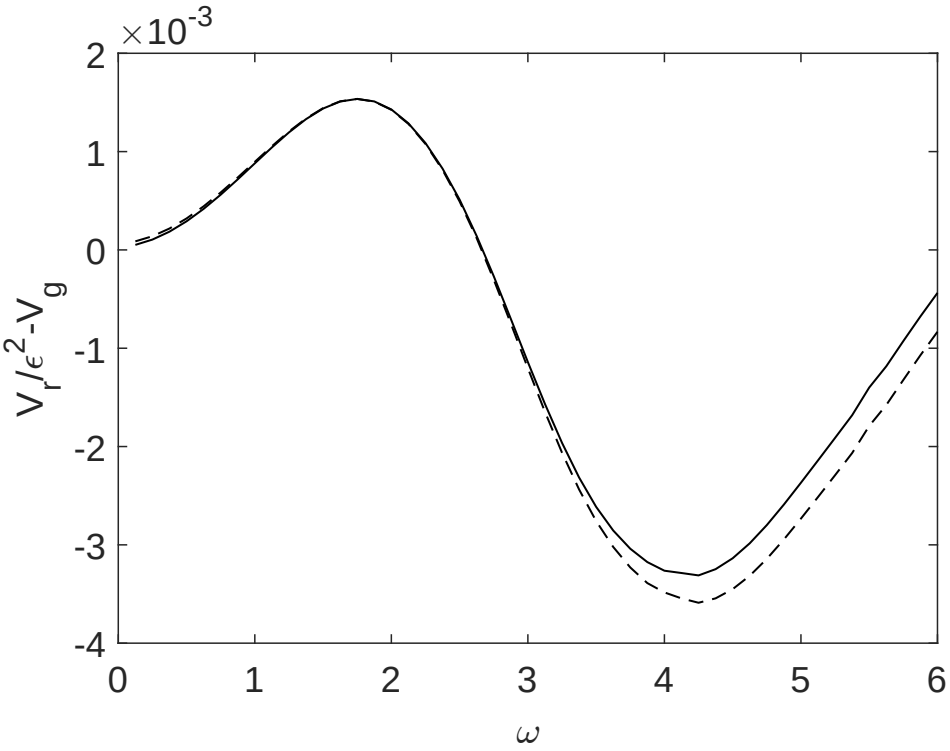


Figure 3.55: The rise velocity of the droplet against the frequency of the oscillations for $\epsilon = 0.5, \gamma = 1, \theta_0 = 1, \tau = 0.1$ and $f(\theta) = (\theta/\theta_0 - 1)$ within the time dependent contact line law. The solid line is when there is no gravity included and the dashed line includes gravity with a strength 25 times weaker than the magnitude of the oscillations. The rise velocities have been shifted by an amount proportional to g in order to look how how the curves change when gravity is included, instead of just the negative shift that occurs for all ω.

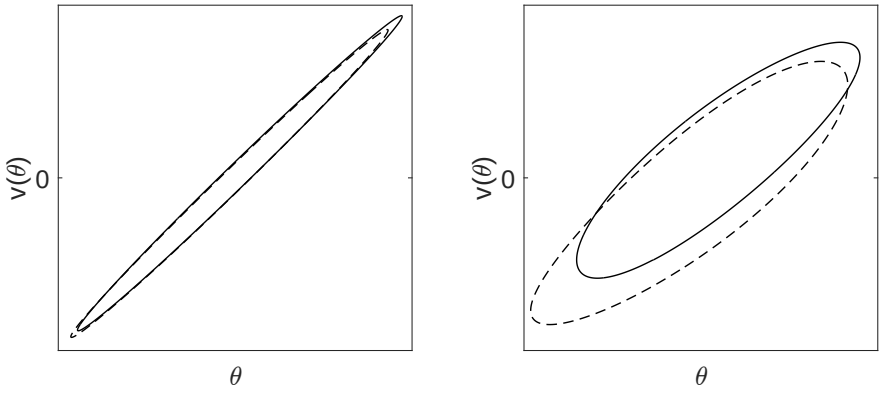


Figure 3.56: The velocity of the contact points as a function of their respective contact angles for a time dependent contact line law with $\tau = 0.1$, $f(\theta) = (\theta/\theta_0 - 1)$ and $g \neq 0$. The dashed line is θ_+ and the solid line is θ_-.

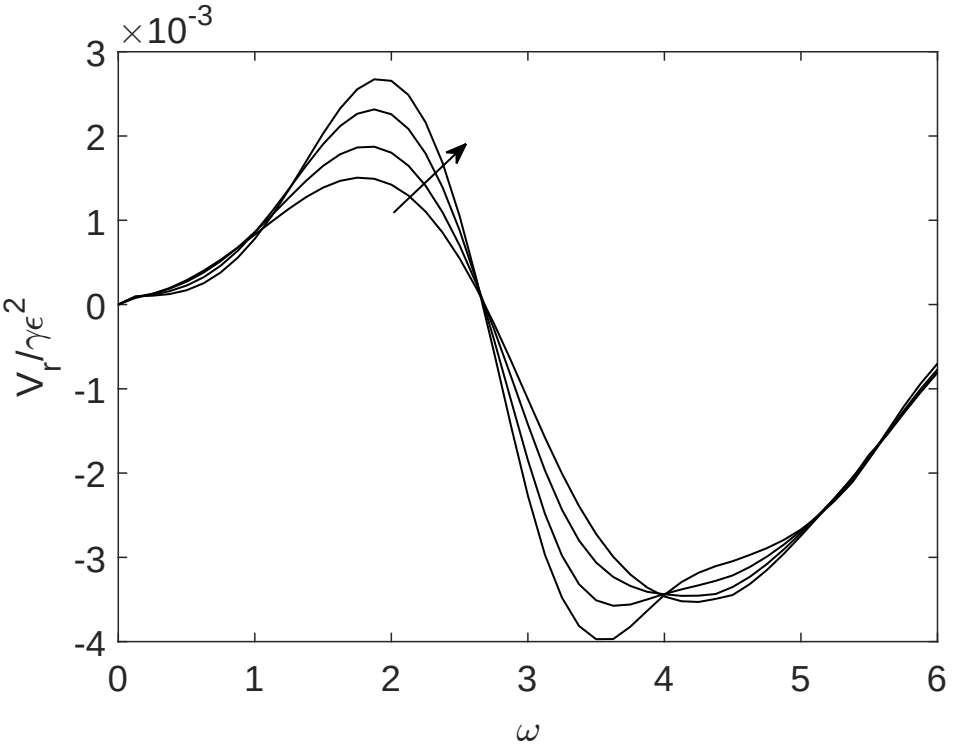


Figure 3.57: The rise velocity of the droplet against ω for $\gamma = 1, \theta_0 = 1, g = 0, \tau = 0.1$ and $f(\theta) = (\theta/\theta_0 - 1) + (\theta/\theta_0 - 1)^3$ within the time dependent contact line law. Following the direction of the arrow coincides with $\epsilon = 0.25, 0.5, 0.75, 1$ respectively.

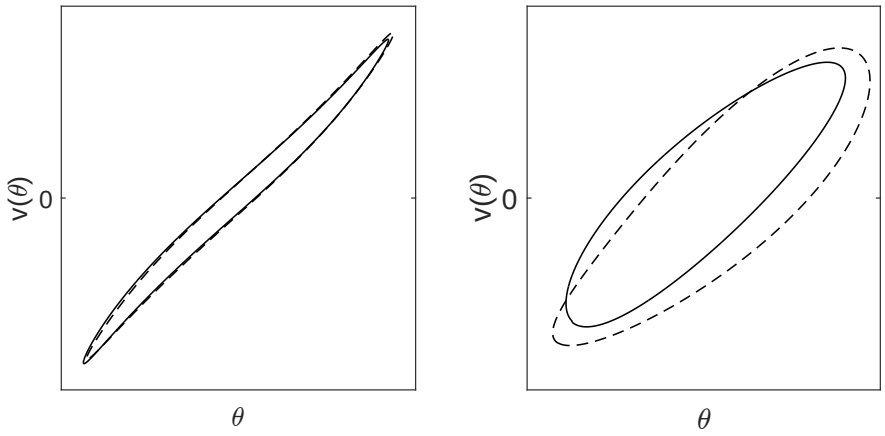


Figure 3.58: The velocity of the contact points as a function of their respective contact angles for a time dependent contact line law with $\tau = 0.1$ and $f(\theta) = (\theta/\theta_0 - 1) + (\theta/\theta_0 - 1)^3$. The left graph is for $\omega = 1$ and the right is for $\omega = 6$. The dashed line is θ_+ and the solid line is θ_-.

function $f(\theta)$ to make it non-linear similar to before. Now we will add a cubic term so that

$$f(\theta) = \frac{\theta}{\theta_0} - 1 + \left(\frac{\theta}{\theta_0} - 1\right)^3,$$

and examine how the solution changes. We can see in figure 3.57 that with the additional term we still get the peak and trough in the range of frequencies used but compared to the solely linear $f(\theta)$, the magnitude of the inflection points has increased. Also as we increase ϵ the magnitudes of the inflection points increase but also we can see that the trough shifts to a lower frequency. What is also possible with this contact line law is we can again insert parameter values similar to the experiment and get results, however they once again show that without hysteresis the droplet will slide. If we now examine the velocity at the contact points (figure 3.58) we see that for $\omega = 6$ we get shapes very similar to when $f(\theta)$ was linear, but for $\omega = 1$ it follows more of a cubic shape but again as a multi valued result.

Hysteresis

For the single valued contact line laws the addition of contact angle hysteresis gave ranges of $\theta_\pm$ where the velocity of the contact points would equal zero. For the time dependent law this is not necessarily the case. We will now look at the change in the rise velocity of the droplet when hysteresis in included.

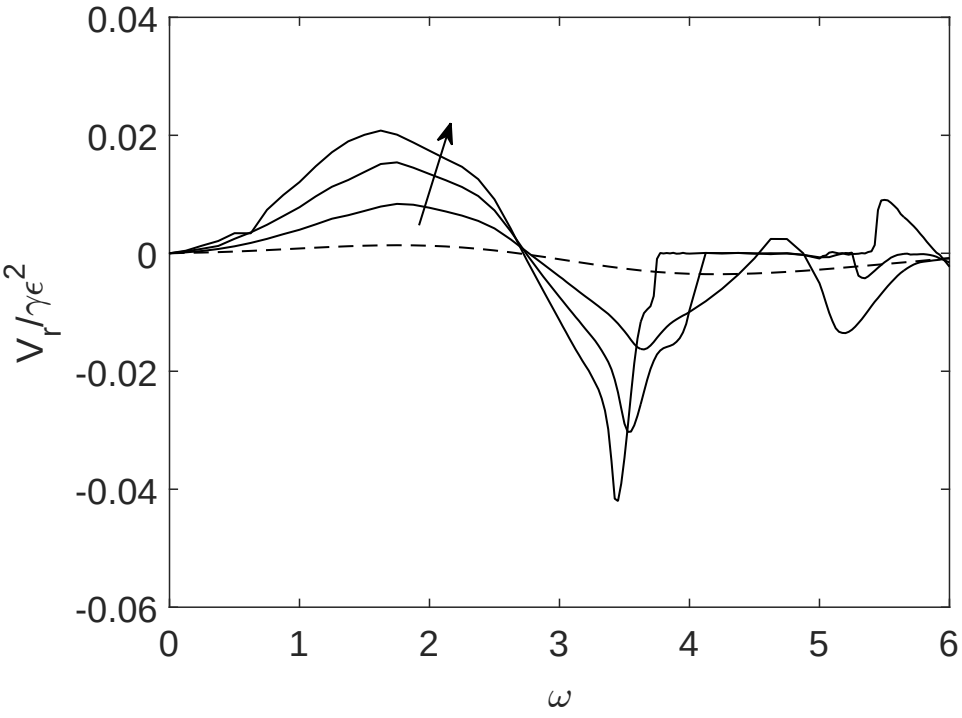


Figure 3.59: The rise velocity of the droplet against ω for $\epsilon = 0.1, \gamma = 1, \theta_0 = 1, g = 0, \tau = 0.1$ and $f(\theta/\theta_0 > \theta_A) = \theta/\theta_0 - \theta_A$, $f(\theta/\theta_0 < \theta_R) = \theta/\theta_0 - \theta_R$ and $f(\theta) = 0$ otherwise. The dashed line represents the rise velocity when there is no contact angle hysteresis present whilst the solid lines, in the direction of the arrow, have a hysteresis interval of 0.02, 0.04 and 0.06 respectively.

The first thing we can see from figure 3.59 is that when even a small amount of contact angle hysteresis is included (the same amount as figure 3.42) the magnitude of the rise velocity increases by over a factor of 5; which is a huge increase compared with the inclusion of hysteresis in section 3.4.2. We can also see that there is a narrow trough forming for $\omega \in [3, 4]$ as θ_I is increased and for $\theta_I = 0.06$ a very rapid increase in the rise velocity occurs for $\omega = [3.5, 3.6]$. This increase is due to the velocity at θ_- reaching zero within this frequency range causing an abrupt stop in the rise velocity. The other thing we will note from figure 3.59 is when $\omega \in [5, 6]$ and the hysteresis interval is very small we get a sliding droplet, but as we increase θ_I the droplet then begins to climb. This is an unusual result since we have observed sliding droplets begin to climb when we go from no hysteresis to some hysteresis, but not when we go from a small amount of hysteresis to a larger amount.

Now we will take the approach of fixing the frequency and look at the

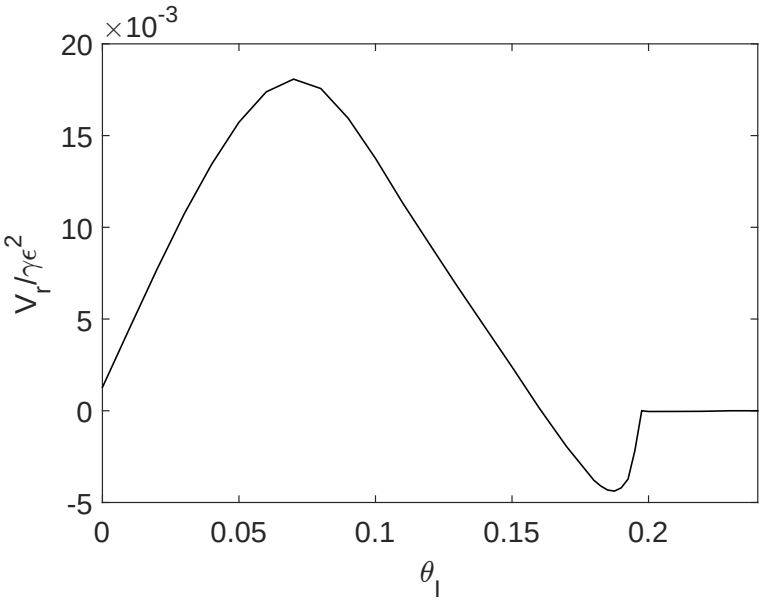


Figure 3.60: The rise velocity of the droplet against the hysteresis interval for $\epsilon = 0.1, \gamma = 1, \theta_0 = 1, \omega = 2$ and $f(\theta/\theta_0 > \theta_A) = \theta/\theta_0 - \theta_A, f(\theta/\theta_0 < \theta_R) = \theta/\theta_0 - \theta_R$ and $f(\theta) = 0$ otherwise.

rise velocity as we increase θ_I. We see in figure 3.60 that the rise velocity of the peak is greater and it takes a larger hysteresis interval to pin the contact points, compared to the similar result shown in section 3.4.2. Both figures 3.59 and 3.60 show us that the inclusion of hysteresis in the model can give a large increase in the rise velocity, which will be useful when increasing the amplitude of the oscillations and the amount of contact angle hysteresis.

The final way we will examine is how increasing the amount of hysteresis effects the mechanics of the problem, is to look at the time dependent contact line directly. We can see in figure 3.61 that as we add a larger amount of hysteresis to the problem the velocity at the contact points slowly develops a range of contact angles where the points are pinned, however unlike the time independent law this is not exactly for the range $\theta_R \leq \theta \leq \theta_A$. We also see as we can increase the amount of hysteresis the contact angles range increases, as we would expect, since the points are moving slower in comparison to the rest of the fluid with increasing θ_I.

Modelling the experiment

Our final analysis for this section will be to use a contact line law to try and find qualitative agreement between this model and the experiment. Due to the

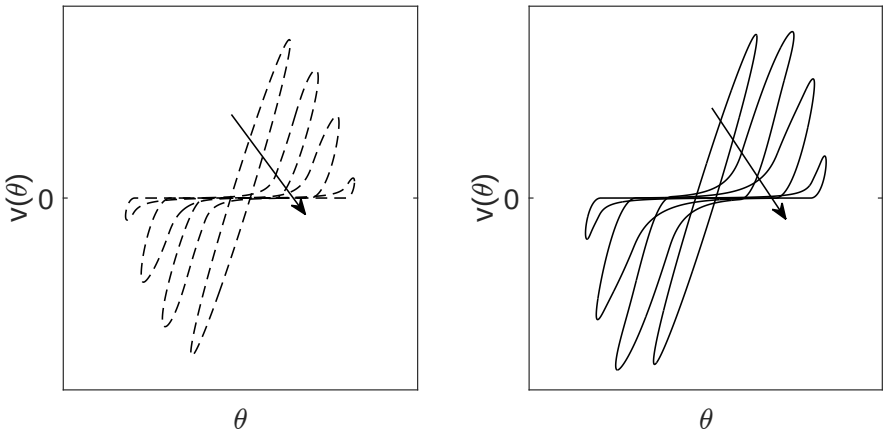


Figure 3.61: The velocity of the contact points as a function of their contact angles for a time dependent contact line law with $\omega = 2, \tau = 0.1$ and $f(\theta/\theta_0 > \theta_A) = \theta/\theta_0 - \theta_A, f(\theta/\theta_0 < \theta_R) = \theta/\theta_0 - \theta_R$ and $f(\theta) = 0$ otherwise. The left graph shows θ_A and the right graph θ_R. The hysteresis interval increases in the direction of the arrow as 0,0.02,0.04,0.06 respectively.

unusual behaviour of unsteady, moving contact lines it is difficult to decide how best to model them and so the approach we will take it to use the cubic contact line law with hysteresis, but with the time dependency included so that $v(\theta)$ is not a single valued function of the contact angle. When including the effects of hysteresis we find that the maximum value of ϵ we can use without the droplet breaking is reduced. For $\omega = 1.5$ we are able to reach $\epsilon = 1$ but for the entire range $\omega \in [0, 6]$ we are only able to reach $\epsilon = 0.8$ due to the droplet breaking for $\omega \in [2.5, 3.5]$. This means that for the rise velocity against the frequency shown in figure 3.62 we have used the latter for a complete curve. This however is not a problem because the results that are possible for $\epsilon = 1$ give a rise velocity very similar to that shown on the graph and so this is the reason why we have not plotted several curves with the 'broken' section missing. We can see in this graph that once again the results are very similar to figure 3.49, with a droplet that can either climb or slide for the desired parameter values. We will now look at the shape of the droplet as it climbs up hill as shown in figure 3.63. What we can see from this (similar to before) is how the bulk of the fluid is responsible for the overall uphill motion however the shape of the surface is still not an informative comparison between this model and the experiment. What we will do for a qualitative comparison between the two is to look at the velocity of the contact points as a function

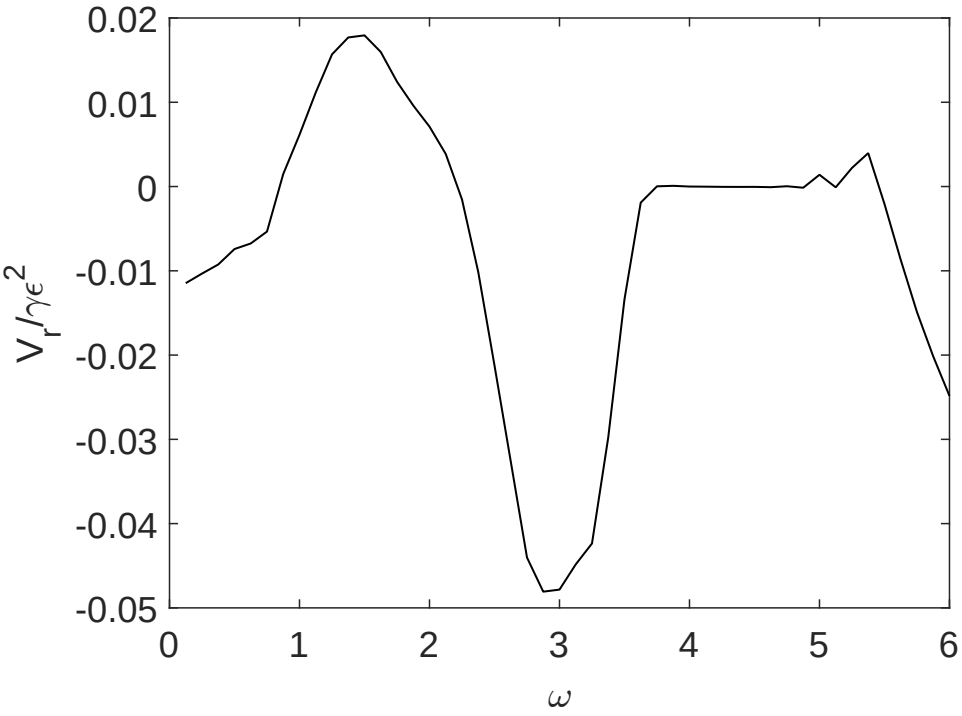


Figure 3.62: The rise velocity of the droplet against the frequency for $\epsilon = 0.8, \gamma = 1, \theta_0 = 1, g = 0.04, \theta_A = 1.25, \theta_R = 0.7$ and a contact line law modelling the experiment.

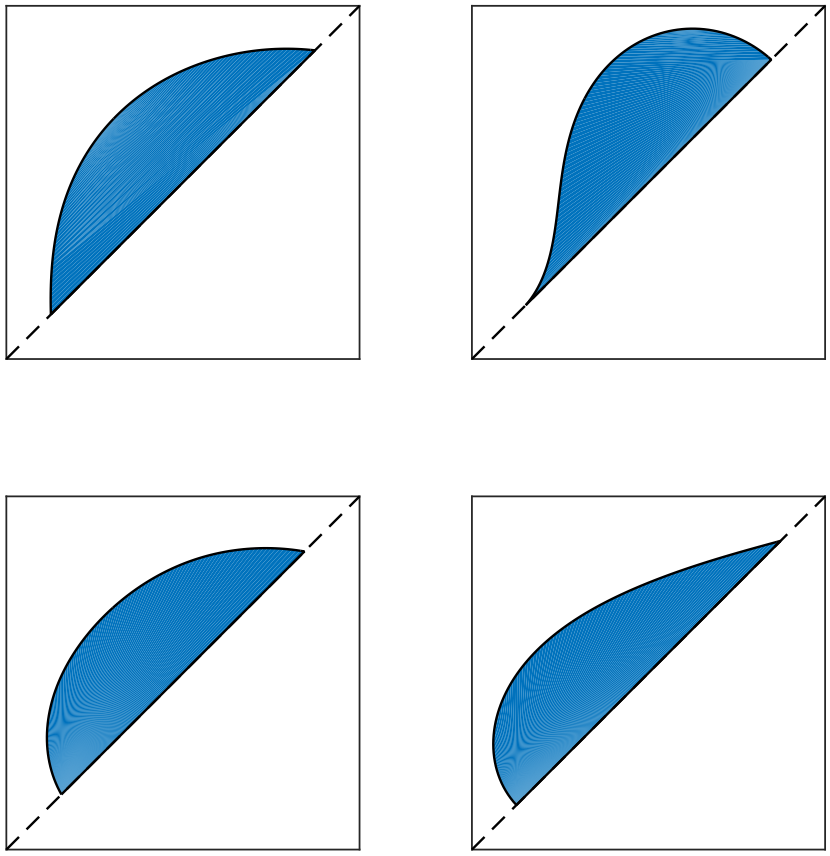


Figure 3.63: Model of the droplet at equal time intervals over one period of oscillation. The parameter values are $\epsilon = 1, \gamma = 1, \theta_0 = 1, \omega = 1.5, g = 0.0275, \theta_A = 1.25, \theta_R = 0.7$ and a contact line law modelling the experiment.

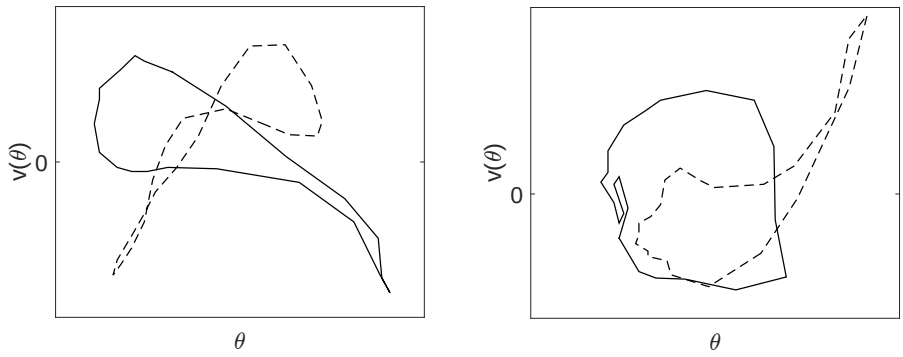


Figure 3.64: The velocity of the contact points as a function of their respective contact angles taken from the experiment. The left graph is for a sliding droplet and the right graph is for a climbing droplet. The dashed lines are θ_+ and the solid lines are θ_-.

of the contact angles.

If we combine the results in figure 6 of [8] we get the results shown in figure 3.64 which show the dimensionless velocity of the contact points as a function of their respective angles, for a sliding and a climbing droplet, from the experiment. We will compare these graphs with those shown in figure 3.65, which are the velocity of the contact points given by the model for parameter values similar to the experiment. Although not shown on the graphs, the dimensionless velocities from both sets of results are of order 10^{-1}. If we start by looking at the velocities of θ_+ (the dashed lines) we see that for all four graphs it is increasing with the contact angle. For the experiment θ_+ has a section for it's sliding droplet where the velocity crosses over itself and then crossing back. This is very unexpected and although we do not know why it occurs we should note that the velocity of the contact point in the model 'loops around' for a similar section of the contact angles. If we now compare the results given by θ_- we can see that, quite simply, the results do not match. For the sliding droplet they show that the velocity of the contact point is negatively affected by increasing the contact angle whereas for the climbing droplet it seems to be circular. Both of these behaviours are very unusual (especially θ_- for a sliding droplet) and have not been explained in any literature covered. This is another prime example of how little we know about unsteady contact lines and although the results give insight into the mechanics of the flow, the model of the dynamic contact line is still incomplete.

To summarise, we have examined the effects of introducing a time deriva-

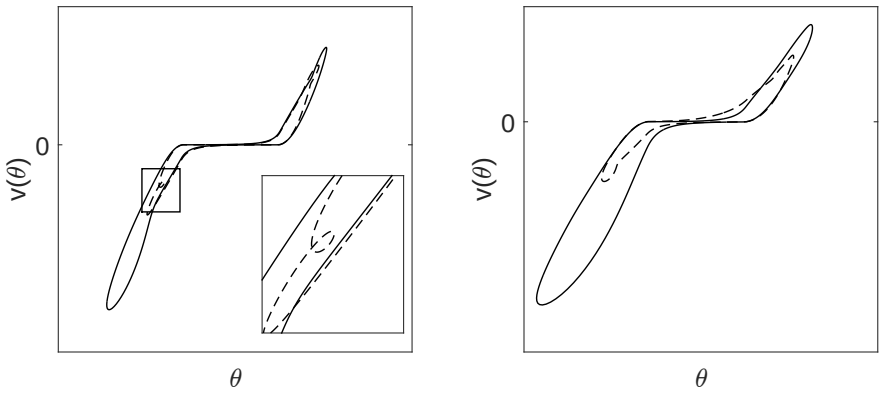


Figure 3.65: The velocity of the contact points as a function of their respective contact angles for a contact line law modelling the experiment. The left graph is for a sliding droplet and the right graph is for a climbing droplet. The dashed lines are θ_+ and the solid lines are θ_-. The box in the left graph is a zoomed in section of the box on the larger graph.

tive to the left hand side of the contact line law and varying the dependency on the contact angle. We began with the law being linearly dependent on the contact angle and examined how the time derivative altered the results compared to section 3.4.1. What this showed is that although the change in the rise velocity did not seem significant, the effect that the new law had on the velocity of the contact points was. The contact point velocity has become a multi-valued function of the respective contact angle, just as experiments on unsteady flows have shown. In addition to this it also tells us that the width of the 'contact velocity ellipses' increase with the frequency of the oscillations. Increasing the size of τ causes the rise velocity of the droplet to increase quite significantly and also increases the width of the ellipse in the contact line law.

The next step was to examine some of the changes we made for single-valued contact line laws to see how they affected the new ones. The addition of gravity caused little change in the mechanics of the problem for $\omega \in [0, 3]$ but for frequencies larger than this the shape of the rise velocity curve begins to diverge from that of no gravity. In addition to this the velocity ellipses of both contact points begin to shift away from each other.

When altering the right hand side of the contact line law to include a cubic term we again see a change in the shape of the rise velocity compared to the time independent law. What is more interesting is the shape of the velocity ellipse. For $\omega > 3$ the shape of the ellipses are almost identical to that of the

solely linear $f(\theta)$ but for lower frequencies we find that the general shape of the middle of the ellipses (measured from the minimum contact angle to the maximum) follows a more cubic shape.

Contact angle hysteresis has some considerable changes on the rise velocity for a time dependent contact line law. First of all the magnitude of the peaks increase a lot more in comparison to single-valued contact line laws with the addition of hysteresis. We also see that a rather significant trough for a small amount of hysteresis can become a rather significant peak when the amount of hysteresis increases. This is very unusual behaviour that has not been seen in any other results.

Combining both hysteresis with the cubic $f(\theta)$ we attempted to create a model contact line law qualitatively comparable to [8]. Using parameter values similar to that of the experiment we found a droplet that can either climb up or slide down the substrate depending on the frequency, however when examining both the shape of the droplet using the model and frames from the actual experiment a comparison could not be made. Finally we took the velocity of the contact points for both a sliding droplet and a climbing one and compared the model to the experiment, and although θ_+ shows similarities between the two, θ_- is completely different.

3.5 Discussion

In this chapter we have considered the motion of a two-dimensional, inviscid droplet travelling along an inclined, oscillating substrate. If the magnitude of the forcing is sufficiently small we found that a droplets motion can be separated into two modes and the non-linear interaction between these modes is what causes the droplet to slide or climb. By making the magnitude of the contact angles sufficiently small we also showed quantitative agreement with the shallow water solution [3]. When examining the rise velocity of the droplet we discovered that it is an oscillatory function of the frequency, due to the inertial forces within the fluid, in addition to being dampened by it. This means that the maximum rise velocity will be given by the size of the initial peak. When examining the rise velocity for a basic linear contact line law we altered its weighting by a constant and found this to have a significant effect on the results, with the droplet sliding for regimes where it was climbing and vice versa. This shows just how dominated this problem is by the contact line

law. When examining pinned contact points we found that the two modes had resonant frequencies causing a large distortion in the shape of the droplet. When increasing the magnitude of the contact angles, causing the droplet to become increasingly more non-wetting, we discovered rapid changes in the rise velocity as well as an increase in the peaks. This unusual behaviour turned out to be a result of modes appearing on the surface on the droplets. Further examination showed that the size of the peaks in rise velocity, as well as the number of modes on the surface, are both proportional to the dimensionless area of the 2-D droplets.

Using non-linear contact line laws caused several changes with the results, some expected but others not. This includes the cubic law allowing us to reach the parameter values of [8] but unfortunately the result of this was a sliding droplet instead of a climbing one. The inclusion of contact angle hysteresis allowed for the peak rise velocity to increase to double that of no hysteresis. A more interesting results is the fact that as we increase the hysteresis further, causing the rise velocity to decline, there is a set of values where the rise velocity becomes negative before reaching the pinned contact points. In addition to the initial peak growing with hysteresis there are also other frequencies, at the points corresponding to the pinned swaying modes resonant frequencies, where the magnitude of the rise velocity increases significantly. This shows us that near these points we are able to increase the hysteresis to values similar to the experiment and still produce a rise velocity. With this additional knowledge the next step was to include the cubic contact line law with experimental parameters and examine the results. With the inclusion of hysteresis we found that the experiments parameters will cause a droplet to climb uphill as required.

The final approach was to consider a time dependent contact line law that causes the velocity of the contact points to no longer be single value functions of their respective contact angles (a result commonly observed for unsteady dynamic contact lines). We found that the additional term in the contact line law caused the rise velocity to change slightly, but what was more important is that fact that the linear relation between the velocity of the contact points and their respective contact angles had become elliptical (with the width of the ellipse increasing with frequency). Altering the right hand side of the contact line law caused changes such as the ellipse curving for a cubic law and a very large increase in the peak rise velocity with the inclusion of hysteresis.

Following a similar method to the previous section we used a time dependent, cubic contact line law with hysteresis and parameter values similar to the experiment to attempt to make qualitative comparisons to [8]. Unfortunately the examination of the contact point velocities shows us a comparison between the two cannot be made. Overall, we have shown that the approximations made are sufficient for a droplet to either climb uphill or slide downhill for parameter values similar to [8]. Due to the ability to vary the magnitude of the contact angles we are able to examine 'thick' droplets that, when moving, have the ability to overhang their contact angles, which is a big improvement when examining the shapes of droplets undergoing large amplitude forcing.

Chapter 4

Model 3: The inviscid, three-dimensional, shallow droplet

In this chapter we will look at the thin, inviscid, three-dimensional droplet. The difference between this model and Model 1 is that we have now included inertia without needing to make other simplifications to compensate. When compared to Model 2 we are now looking at a thin, three-dimensional droplet instead of a thick, two-dimensional one. This adds more accuracy in the geometry of the problem whilst losing the $O(1)$ contact angles which are closer to the experiment [8]. Using these simplifications means we only need to solve the inviscid, two-dimensional shallow water equations, along with the boundary conditions at the contact line.

4.1 The Model

4.1.1 Two-dimensional shallow water equations

Consider a droplet of liquid of density ρ, kinematic viscosity ν and surface tension σ on a solid substrate that is inclined at an angle α to the horizontal and oscillating sinusoidally and vertically. The frame of reference will be fixed so the substrate lies on the plane $z = 0$ with the positive $x-$axis pointing uphill, so gravity and the acceleration due to the substrate can be combined to make an effective gravity acting at an angle $\pi/2-\alpha$ to the $x-$axis. In order to simplify this problem we will make the assumptions that the Reynolds

number is large (so that the viscous forces can be neglected) and that the droplet is very thin. Using these assumptions we can reduce the Navier-Stokes equations to the two-dimensional shallow water equations, i.e.

$$\frac{\partial \mathbf{u}}{\partial t} + (\mathbf{u} \cdot \boldsymbol{\nabla})\mathbf{u} = \frac{\sigma}{\rho}\boldsymbol{\nabla}\nabla^2 h + \mathbf{f}, \tag{4.1}$$

$$\frac{\partial h}{\partial t} + \boldsymbol{\nabla} \cdot (\mathbf{u}h) = 0, \tag{4.2}$$

where $h(\mathbf{x}, t)$ is the thickness of the droplet, $\mathbf{u}(\mathbf{x}, t)$ is the fluid's velocity, $\mathbf{f}$ is the body acceleration per unit mass and $\mathbf{x} = (x, y)$ is a two-dimensional coordinate system. The effective gravity is given by $a(t) = g + a_0 \sin(\omega t)$, where g is the gravitational acceleration and a_0 and ω are the magnitude and frequency of the oscillations of the substrate. We will write the body force as a potential of the form

$$\mathbf{f} = -a\boldsymbol{\nabla}(x \sin\alpha + h\cos\alpha), \tag{4.3}$$

meaning we can write (4.1) as

$$\frac{\partial \mathbf{u}}{\partial t} + (\mathbf{u} \cdot \boldsymbol{\nabla})\mathbf{u} + \boldsymbol{\nabla}\left(ax\sin\alpha + ah\cos\alpha - \frac{\sigma}{\rho}\nabla^2 h\right) = 0. \tag{4.4}$$

Now we need to define some boundary conditions in order to solve (4.2) and (4.4). If we define the contact line as $\mathbf{x} = \mathbf{X}(t)$ then the boundary conditions for the droplet are

$$h = 0, \quad \mathbf{u} \cdot \mathbf{n} = v(\theta) = \mathbf{n} \cdot \frac{d\mathbf{x}}{dt}, \quad \text{on } \mathbf{x} = \mathbf{X}(t), \tag{4.5}$$

where $\mathbf{n}$ is the unit normal on the $xy-$plane pointing away from the droplet. These boundary conditions mean the height of the droplet is always zero at the contact line and the velocity of the contact line is given by (1.4). In addition to this the contact angle will be given by

$$\theta = -\frac{\partial h}{\partial n}, \quad \text{on } \mathbf{x} = \mathbf{X}(t), \tag{4.6}$$

where $\partial/\partial n = \mathbf{n} \cdot \boldsymbol{\nabla}$.

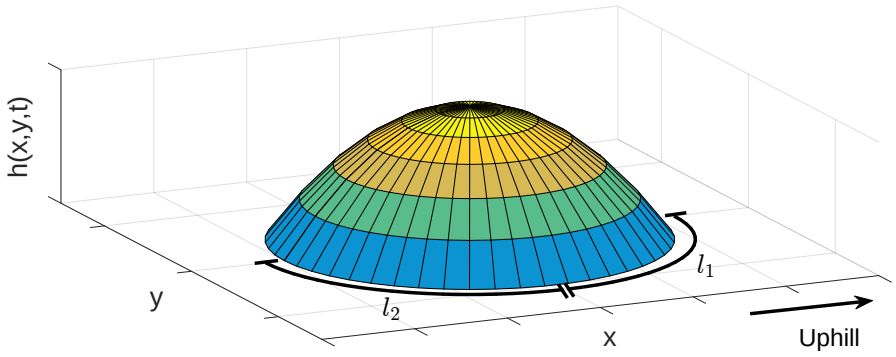


Figure 4.1: Example droplet and x, y coordinate system. The lines l_1 and l_2 represent the sections of the boundary used to keep the area of the footprint equal about the origin.

4.1.2 Moving reference frame

In order to keep the droplet centered around the origin we will now fix the frame of reference to be travelling at some velocity V along the $x-$axis. To do this we will apply the transformation

$$x = \tilde{x} + c(t), \qquad u = \tilde{u} + V, \tag{4.7}$$

where $V(t) = \frac{dc}{dt}$ and $c(t)$ is defined such that the area of the fluid in contact with the substrate is equally spaced about the origin. We therefore need to add an extra constraint given by

$$\int_{l_1} \mathbf{n} \cdot \mathbf{r} \mathrm{d}l = \int_{l_2} \mathbf{n} \cdot \mathbf{r} \mathrm{d}l, \tag{4.8}$$

where l_1 is the edge of the footprint going from the most positive end of the $\tilde{x}-$axis to $\tilde{x} = 0$ and l_2 is the edge of the footprint going from $\tilde{x} = 0$ to the most negative end of the $\tilde{x}-$axis (figure 4.1). Transforming the reference frame this way means that

$$\frac{\partial}{\partial x} = \frac{\partial}{\partial \tilde{x}}, \qquad \left.\frac{\partial}{\partial t}\right|_x = \left.\frac{\partial}{\partial t}\right|_{\tilde{x}} - V\frac{\partial}{\partial \tilde{x}},$$

and the new set of governing equations (with tildes omitted) are

$$\frac{\partial \mathbf{u}}{\partial t} + \frac{dV}{dt}\hat{\mathbf{x}} + (\mathbf{u} \cdot \boldsymbol{\nabla})\mathbf{u} + \boldsymbol{\nabla}\left[ax\sin\alpha - \left(\frac{\sigma}{\rho}\nabla^2 - a\cos\alpha\right)h\right] = 0, \tag{4.9}$$

$$\frac{\partial h}{\partial t} + \boldsymbol{\nabla} \cdot (\mathbf{u}h) = 0, \tag{4.10}$$

$$h = 0, \quad \mathbf{u} \cdot \mathbf{n} = \mathbf{n} \cdot \frac{d\mathbf{x}}{dt} = v(\theta) - V n_x, \quad \text{on } \mathbf{x} = \mathbf{X}(t) - c(t)\hat{x}, \tag{4.11}$$

along with (4.8).

4.1.3 Dimensionless equations

In order to simplify our equations we will introduce a set of scales so we can non-dimensionalise the problem and make Model 3 easier to compare to [3] (or the small θ_0 limit of Model 2). These scaling parameters are

$$\mathbf{x} = L\bar{\mathbf{x}}, \quad h = \theta_0 L\bar{h}, \quad \mathbf{u} = \frac{X}{T}\bar{\mathbf{u}}, \quad v = \frac{X}{T}\bar{v}, \quad a = a_0\bar{a}, \qquad t = T\bar{t}, \tag{4.12}$$

where our time scale will be

$$T = \sqrt{\frac{\rho L^3}{\sigma\theta_0}}, \tag{4.13}$$

in order to balance the surface tension with the material derivative and our mass scale is

$$M = \frac{\pi}{4}\rho\theta_0 L^3, \tag{4.14}$$

in order for the unperturbed, dimensionless droplet to have a unit radius. When using these scalings we will obtain the dimensionless parameters

$$\epsilon = \frac{\rho a_0 L^2 \sin\alpha}{\sigma\theta_0}, \quad \gamma = \frac{\theta_0}{\tan\alpha}, \tag{4.15}$$

which characterise the strength of the effective gravitational force relative to surface tension and the ratio between the slope of the droplet's surface and the slope of the substrate respectively. As well as these, the other dimensionless parameters are given by

$$\bar{\omega} = 2\pi T f, \quad \bar{g} = \frac{g}{\epsilon a_0}, \tag{4.16}$$

which are the dimensionless frequency of the oscillations and the gravitational acceleration respectively. The dimensionless effective gravity is now given by

$$\bar{a}(t) = \sin(\bar{\omega}\bar{t}) + \epsilon\bar{g},$$

so that we can expand $\bar{a}(t)$ in powers of ϵ whilst keeping the dimensionless gravity of $O(1)$ when $\epsilon \ll 1$. Now that we have a set of dimensionless parameters we will check their typical sizes using Table 1.1. Since we are again using a three-dimensional model we can use the mass scaling to calculate that our typical length scale is approximately 1.81 mm. Now if we use the rest of the values in Table 1.1 we know that our dimensionless parameters have the typical values

$$\epsilon \approx 6.73 \quad \gamma \approx 1.08, \quad \bar{\omega} \approx 3.16, \quad \bar{g} \approx 8.38 \times 10^{-3}, \quad \theta_0 \approx 1.08.$$

As we can see from these values, the assumption that the droplet it thin is far from accurate. What we will do with this model is to use the thin droplet approximation and see if our results can compare qualitatively to the actual experiment [8]. The other assumption we have made is that the Reynolds number is large enough for us to ignore the viscosity of the fluid. Again, by using our parameters, we can write the Reynolds number as

$$Re = \frac{L^2}{T\nu} \approx 10.62.$$

4.1.4 Governing equations

Now we have justified our dimensional scalings, we will apply them to (4.9)-(4.11) and rearrange to give (with bars omitted)

$$\frac{\partial \mathbf{u}}{\partial t} + (\mathbf{u} \cdot \boldsymbol{\nabla})\mathbf{u} + \boldsymbol{\nabla}[\epsilon a(x + \gamma h) - \nabla^2 h] = 0, \tag{4.17}$$

$$\frac{\partial h}{\partial t} + \boldsymbol{\nabla} \cdot (\mathbf{u}h) = 0, \tag{4.18}$$

$$h = 0, \quad \mathbf{u} \cdot \mathbf{n} = v(\theta) = \mathbf{n} \cdot \frac{d\mathbf{x}}{dt}, \quad \text{on } \mathbf{x} = \mathbf{X}(t) - c(t)\hat{x}, \tag{4.19}$$

$$\int_{l_1} \mathbf{n} \cdot \mathbf{r} \mathrm{d}l = \int_{l_2} \mathbf{n} \cdot \mathbf{r} \mathrm{d}l. \tag{4.20}$$

These are the governing equations for our model of a three-dimensional, inviscid, thin droplet on an oscillating substrate. Now we will solve these equations in the limit of small amplitude oscillations.

4.2 Small amplitude asymptotic solution

4.2.1 Polar coordinates

Now that we have our governing equations we will solve them for the small amplitude limit. In order to do this we will begin by converting from the Cartesian coordinate system (x, y) to the polar coordinate system (r, ϕ) such that the line $\phi = 0$ is along the positive $x-$axis and the contact line is now given by $r = R(\phi, t)$. Applying this to (4.17) - (4.20) gives

$$\frac{\partial \mathbf{u}}{\partial t} + (\mathbf{u} \cdot \boldsymbol{\nabla})\mathbf{u} + \boldsymbol{\nabla}\left[\left(\epsilon a + \frac{dV}{dt}\right) r\cos\phi - (\nabla^2 - \epsilon a\gamma)h\right] = 0, \tag{4.21}$$

$$\frac{\partial h}{\partial t} + \boldsymbol{\nabla} \cdot (\mathbf{u}h) = 0, \tag{4.22}$$

$$h = 0, \quad \mathbf{u} \cdot \mathbf{n} = \mathbf{n} \cdot \frac{d\mathbf{r}}{dt} = v(\theta) - Vn_x, \quad \text{on } r = R(\phi, t), \tag{4.23}$$

$$\int_0^{\pi/2} \frac{R^2}{\sqrt{1 + \left(\frac{1}{R}\frac{\partial R}{\partial \phi}\right)^2}} \mathrm{d}\phi = \int_{\pi/2}^{\pi} \frac{R^2}{\sqrt{1 + \left(\frac{1}{R}\frac{\partial R}{\partial \phi}\right)^2}} \mathrm{d}\phi. \tag{4.24}$$

In this section we are solving (4.21)-(4.24) for $\epsilon \ll 1$, meaning that the contact angles will only ever differ slightly from the dimensionless equilibrium angle. This means that we are able to approximate the contact line law as a Taylor expansion about the point $\theta = 1$, giving

$$v(\theta) = v'(\theta - 1) + \frac{1}{2}v''(\theta - 1)^2 + ..., \tag{4.25}$$

where v', v'' are the dimensionless parameters for the derivatives of the velocity at the equilibrium angle.

4.2.2 An unperturbed droplet

Before expanding (4.21)-(4.24) asymptotically for small ϵ we will first solve them for the simplified case where $\epsilon = 0$. Since this represents an unperturbed droplet then the velocities $\mathbf{u}$ and V both equal zero and $h_0(r, \phi)$ will be axis-symmetric. The resulting equation is

$$\frac{1}{r}\frac{\partial}{\partial r}\left(r\frac{\partial h_0}{\partial r}\right) = b_1, \tag{4.26}$$

where b_1 is a constant of integration, and the boundary conditions are given by

$$h_0 = 0, \qquad \frac{\partial h_0}{\partial r} = -1, \qquad \text{at } r = 1, \tag{4.27}$$

where the unperturbed droplet radius is a result of the dimensional scalings. The solution to this problem is

$$h_0(r) = \frac{1 - r^2}{2} + b_2 \ln r, \tag{4.28}$$

where the b_2 is another constant of integration which needs to equal zero for the height to remain bounded within the droplet.

4.2.3 Asymptotic expansion

Now that we have the zeroth order solution we will now expand each of the unknown functions, for small amplitude oscillations, as

$$\begin{gathered} h(r,\phi,t) = h_0(r) + \epsilon h_1(r,\phi,t) + \epsilon^2 h_2(r,\phi,t) + ..., \\ \mathbf{u}(r,\phi,t) = \epsilon \mathbf{u}_1(r,\phi,t) + \epsilon^2 \mathbf{u}_2(r,\phi,t) + ..., \\ V(t) = \epsilon V_1(t) + \epsilon^2 V_2(t) + ..., \qquad R(\phi,t) = 1 + \epsilon R_1(\phi,t) + \epsilon^2 R_2(\phi,t) + ..., \end{gathered} \tag{4.29}$$

and use these to expand our equations into orders of ϵ. Now inserting these expansions into (4.21) gives

$$\begin{aligned} \epsilon \frac{\partial \mathbf{u}_1}{\partial t} + \epsilon^2 \frac{\partial \mathbf{u}_2}{\partial t} + \epsilon^2 (\mathbf{u}_1 \cdot \boldsymbol{\nabla}) \mathbf{u}_1 + \boldsymbol{\nabla} \Bigg[\epsilon \left(\sin(\omega t) + \frac{dV_1}{dt} \right) r \cos\phi \\ + \epsilon^2 \left(g + \frac{dV_2}{dt} \right) r \cos\phi - \nabla^2 (h_0 + \epsilon h_1 + \epsilon^2 h_2) + \epsilon \gamma \sin(\omega t) h_0 \\ + \epsilon^2 \gamma (\sin(\omega t) h_1 + g h_0) \Bigg] = O(\epsilon^3), \end{aligned}$$

which can be separated into

$$\frac{\partial \mathbf{u}_1}{\partial t} + \boldsymbol{\nabla} \left[\left(\sin(\omega t) + \frac{dV_1}{dt} \right) r \cos\phi - \nabla^2 h_1 + \gamma \sin(\omega t) \frac{1 - r^2}{2} \right] = 0, \tag{4.30}$$

and

$$\frac{\partial \mathbf{u}_2}{\partial t} + (\mathbf{u}_1 \cdot \boldsymbol{\nabla})\mathbf{u}_1 + \boldsymbol{\nabla}\left[\left(g + \frac{dV_2}{dt}\right) r\cos\phi - \nabla^2 h_2 + \gamma\left(\sin(\omega t)h_1 + g\frac{1-r^2}{2}\right)\right] = 0. \tag{4.31}$$

Similarly if we expand the variables in (4.22) and separate powers of ϵ we get

$$\frac{\partial h_1}{\partial t} + \boldsymbol{\nabla}\cdot\left(\mathbf{u}_1\frac{1-r^2}{2}\right) = 0, \tag{4.32}$$

and

$$\frac{\partial h_2}{\partial t} + \boldsymbol{\nabla}\cdot\left(\mathbf{u}_2\frac{1-r^2}{2}\right) + \boldsymbol{\nabla}\cdot(\mathbf{u}_1 h_1) = 0. \tag{4.33}$$

Now we have the first and second order equations we need to also expand the boundary conditions. The height of the droplet at the boundary can be expanded to give

$$h_0+\epsilon h_1+\epsilon^2 h_2+(\epsilon R_1+\epsilon^2 R_2)\frac{\partial h_0}{\partial r}+\epsilon^2 R_1\frac{\partial h_1}{\partial r}+\frac{1}{2}\epsilon^2 R_1^2\frac{\partial^2 h_0}{\partial r^2} = O(\epsilon^3), \quad \text{on } r=1,$$

which we will separate into

$$h_1 = R_1(\phi,t), \quad \text{on } r=1, \tag{4.34}$$

and

$$h_2 = R_2(\phi,t) - R_1(\phi,t)\frac{\partial h_1}{\partial r} + R_1(\phi,t)^2, \quad \text{on } r=1. \tag{4.35}$$

Before expanding the other boundary conditions we will first express the normal of the droplet's footprint as

$$\mathbf{n} = \frac{\left(1, -\frac{1}{R}\frac{\partial R}{\partial \phi}\right)}{\sqrt{1+\left(\frac{1}{R}\frac{\partial R}{\partial \phi}\right)^2}},$$

meaning the other boundary condition on the contact line can be written as

$$u_r - \frac{u_\phi}{R}\frac{\partial R}{\partial \phi} = \frac{\partial R}{\partial t} = v(\theta)\sqrt{1+\left(\frac{1}{R}\frac{\partial R}{\partial \phi}\right)^2} - V\left(\cos\phi + \frac{\sin\phi}{R}\frac{\partial R}{\partial \phi}\right),$$

which can be transformed into

$$\epsilon u_{r1} + \epsilon^2 \left(u_{r2} + R_1 \frac{\partial u_{r1}}{\partial r} - \frac{u_{\phi 1}}{R_0} \frac{\partial R_1}{\partial \phi} \right) = \epsilon \frac{\partial R_1}{\partial t} + \epsilon^2 \frac{\partial R_2}{\partial t} + O(\epsilon^3) = \epsilon v_1 + \epsilon^2 v_2 - \epsilon V_1 \cos\phi - \epsilon^2 \left(V_2 \cos\phi + V_1 \frac{\sin\phi}{R_0} \frac{\partial R_1}{\partial \phi} \right) + O(\epsilon^3), \quad \text{on } r = 1.$$

This can be separated into

$$u_{r1} = \frac{\partial R_1}{\partial t} = v_1 - V_1 \cos\phi, \quad \text{on } r = 1, \tag{4.36}$$

and

$$u_{r2} + R_1 \frac{\partial u_{r1}}{\partial r} - \frac{u_{\phi 1}}{R_0} \frac{\partial R_1}{\partial \phi} = \frac{\partial R_2}{\partial t} = v_2 - V_2 \cos\phi - V_1 \sin\phi \frac{\partial R_1}{\partial \phi}, \quad \text{on } r = 1, \tag{4.37}$$

where

$$v(\theta) = \epsilon v_1 + \epsilon^2 v_2 + ... = v'(\theta - 1) + \frac{1}{2} v''(\theta - 1)^2 + ... \tag{4.38}$$

Now if we expand (4.6) we get

$$\begin{aligned} \theta =& - \frac{\partial h_0}{\partial n} - \epsilon \frac{\partial h_1}{\partial n} - \epsilon^2 \frac{\partial h_2}{\partial n} - \epsilon (R_1 + \epsilon R_2) \frac{\partial^2 h_0}{\partial n \partial r} - \epsilon^2 R_1 \frac{\partial^2 h_1}{\partial n \partial r} + ..., \\ =& 1 - \frac{1}{2} \epsilon^2 \left(\frac{\partial R_1}{\partial \phi} \right)^2 - \epsilon \frac{\partial h_1}{\partial r} + \epsilon^2 \frac{\partial R_1}{\partial \phi} \frac{\partial h_1}{\partial \phi} - \epsilon^2 \frac{\partial h_2}{\partial r} + \epsilon R_1 + \epsilon^2 R_2 \\ & - \epsilon^2 R_1 \frac{\partial^2 h_1}{\partial r^2} + ..., \quad \text{on } r = 1, \end{aligned} \tag{4.39}$$

giving

$$\begin{aligned} v_1 &= v' \left[R_1 - \frac{\partial h_1}{\partial r} \right], \\ v_2 &= v' \left[R_2 - \frac{\partial h_2}{\partial r} - R_1 \frac{\partial^2 h_1}{\partial r^2} - \frac{1}{2} \left(\frac{\partial R_1}{\partial \phi} \right)^2 \right] + \frac{1}{2} v'' \left[R_1 - \frac{\partial h_1}{\partial r} \right]^2. \end{aligned} \tag{4.40}$$

Finally, (4.24) can be expanded as

$$\int_0^{\pi/2} R_1 \mathrm{d}\phi = \int_{\pi/2}^{\pi} R_1 \mathrm{d}\phi,$$
$$\int_0^{\pi/2} \left[R_2 + \frac{1}{2}R_1^2 - \frac{1}{4}\left(\frac{\partial R_1}{\partial \phi}\right)^2 \right] \mathrm{d}\phi = \int_{\pi/2}^{\pi} \left[R_2 + \frac{1}{2}R_1^2 - \frac{1}{4}\left(\frac{\partial R_1}{\partial \phi}\right)^2 \right] \mathrm{d}\phi. \tag{4.41}$$

4.2.4 First order terms

Now we have expanded all the equations asymptotically for small ϵ, we can group together all the equations of order ϵ in order to solve them. This gives our first order system of equations as

$$\frac{\partial \mathbf{u}_1}{\partial t} + \boldsymbol{\nabla}\left[\left(\sin(\omega t) + \frac{dV_1}{dt}\right) r\cos\phi - \nabla^2 h_1 + \frac{\gamma}{2}\sin(\omega t)(1-r^2)\right] = 0, \tag{4.42}$$

$$\frac{\partial h_1}{\partial t} + \frac{1}{2}\boldsymbol{\nabla}\cdot(\mathbf{u}_1(1-r^2)) = 0, \tag{4.43}$$

where

$$h_1 = R_1, \quad u_{r1} = \frac{\partial R_1}{\partial t} = v'\left[R_1 - \frac{\partial h_1}{\partial r}\right] - V_1\cos\phi, \quad \text{on } r = 1, \tag{4.44}$$

and

$$\int_0^{\pi/2} R_1 \mathrm{d}\phi = \int_{\pi/2}^{\pi} R_1 \mathrm{d}\phi. \tag{4.45}$$

From observation we can see that (4.42)-(4.45) is a linear system of equations where the time dependency only appears explicitly as $\sin(\omega t)$. This means we are able to remove the time dependance using

$$\begin{aligned} \mathbf{u}_1(r,\phi,t) &= \Re[\tilde{\mathbf{u}}(r,\phi)\exp(i\omega t)], \quad V_1(t) = \Re[\tilde{V}\exp(i\omega t)], \\ h_1(r,\phi,t) &= \Im[\tilde{h}(r,\phi)\exp(i\omega t)], \quad R_1(\phi,t) = \Im[\tilde{R}(\phi)\exp(i\omega t)], \end{aligned} \tag{4.46}$$

which will convert (4.42) - (4.45) to

$$\omega\tilde{\mathbf{u}} + \omega\tilde{V}\boldsymbol{\nabla}(r\cos\phi) + \boldsymbol{\nabla}\left(\nabla^2\tilde{h}\right) = \boldsymbol{\nabla}(r\cos\phi) - \gamma r\hat{\mathbf{r}}, \tag{4.47}$$

$$\omega\tilde{h} + \frac{1}{2}\boldsymbol{\nabla}\cdot(\tilde{\mathbf{u}}(1-r^2)) = 0, \tag{4.48}$$

$$\tilde{h} = \tilde{R}, \quad \tilde{u} = \omega\tilde{R}, \quad \text{on } r = 1, \tag{4.49}$$

$$\frac{\partial\tilde{h}}{\partial r} = \frac{1}{iv'}\left(\tilde{V}\cos\phi + \omega\tilde{R}\right) + \tilde{R}, \quad \text{on } r = 1, \tag{4.50}$$

and

$$\int_0^{\pi/2} \tilde{R}\mathrm{d}\phi = \int_{\pi/2}^{\pi} \tilde{R}\mathrm{d}\phi. \tag{4.51}$$

This system of equations is equivalent to (3.21)-(3.23) of [3], only now for a three-dimensional droplet instead of a two-dimensional 'ridge'. Similar to Benilov and Billingham we can separate (4.47)-(4.51) into a spreading and a swaying mode, by looking at the ϕ dependence of each term. This means we can separate each of our unknown functions into

$$\begin{gathered}\tilde{u}(r,\phi) = u_{sw}(r)\cos\phi + u_{sp}(r), \quad \tilde{v}(r,\phi) = v_{sw}(r)\sin\phi, \\ \tilde{h}(r,\phi) = h_{sw}(r)\cos\phi + h_{sp}(r).\end{gathered} \tag{4.52}$$

Since $\tilde{R}(\phi)$ has to either be a constant or a function of $\cos\phi$, we can use (4.51) to verify that it must be a constant, which we will denote as R. By separating the ϕ dependencies we get that the swaying mode is given by

$$\omega u_{sw} + \omega V + \frac{\partial}{\partial r}\left[\nabla^2 - \frac{1}{r^2}\right] h_{sw} = 1, \tag{4.53}$$

$$\omega v_{sw} - \omega V - \frac{1}{r}\left[\nabla^2 - \frac{1}{r^2}\right] h_{sw} = -1, \tag{4.54}$$

$$\omega h_{sw} + \frac{1}{2}\frac{\partial}{\partial r}\left[(1-r^2)u_{sw}\right] + \frac{1-r^2}{2r}(u_{sw} + v_{sw}) = 0, \tag{4.55}$$

$$h_{sw} = 0, \quad u_{sw} = 0, \quad \frac{\partial h_{sw}}{\partial r} = \frac{V}{iv'}, \quad \text{at } r = 1, \tag{4.56}$$

$$h_{sw} = 0, \quad \frac{\partial u_{sw}}{\partial r} = 0, \quad \text{at } r = 0, \tag{4.57}$$

with the tilde neglected. The equations relating to the spreading modes are

$$\omega u_{sp} + \frac{\partial}{\partial r}\left[\nabla^2 h_{sp}\right] = -\gamma r, \tag{4.58}$$

$$\omega h_{sp} + \frac{1}{2r}\frac{\partial}{\partial r}\left[r(1-r^2)u_{sp}\right] = 0, \tag{4.59}$$

$$h_{sp} = R, \quad u_{sp} = \omega R, \quad \frac{\partial h_{sp}}{\partial r} = \left(1 + \frac{\omega}{iv'}\right) R, \quad \text{at } r = 1, \tag{4.60}$$

$$\frac{\partial h_{sp}}{\partial r} = 0, \quad u_{sp} = 0, \quad \text{at } r = 0. \tag{4.61}$$

What we have managed to achieve in this section is to simplify a system of partial differential equations, dependent on (r, ϕ, t), to two set of ordinary differential equations dependent on only r.

4.2.5 The spreading mode

Now we have separated the first order asymptotic equations into two modes we will deal with each separately; first of all the spreading mode. To solve (4.58) - (4.61) numerically we will first have to deal with the singular point present at $r = 1$. To do this we will begin by looking at the equations as $r \to 1$ and then use these, along with the boundary conditions, in order to get an asymptotic, boundary layer solution for $r \in [r_0, 1]$. We can then solve (4.58) - (4.61) numerically up to the point $r = r_0$.

We will start our boundary layer at the point $r = 1 - \delta$ and so within this region the variable will be defined as $r = 1 - \delta x$, where x is our new variable and $|\delta| \ll 1$ is a constant, and the unknown functions will be called h_{sp}^+ and u_{sp}^+. Inserting these into (4.58) and (4.59) and letting $\delta \to 0$ gives

$$\frac{\partial^3 h_{sp}^+}{\partial x^3} = 0, \quad \frac{\partial (x u_{sp}^+)}{\partial x} = \omega h_{sp}^+, \tag{4.62}$$

which solve to give

$$h_{sp}^+(x) = A + \hat{B}x + \hat{C}x^2, \quad u_{sp}^+(x) = \omega A + \frac{1}{2}\omega \hat{B}x + \frac{1}{3}\omega \hat{C}x^2 + \frac{\hat{D}}{x}, \tag{4.63}$$

where $\hat{D}$ will need equal zero. Now if we reinsert r into (4.63) and apply the boundary conditions (4.60) we get

$$\begin{aligned} h_{sp}^+(r) &= R - \left(1 + \frac{\omega}{iv'}\right) R(1-r) + C(1-r)^2, \\ u_{sp}^+(r) &= \omega R - \frac{1}{2}\left(1 + \frac{\omega}{iv'}\right) \omega R(1-r) + \frac{1}{3}\omega C(1-r)^2, \end{aligned} \tag{4.64}$$

where C is now another unknown we need to solve for. We can now use h_{sp}^+ and u_{sp}^+ to create a set of boundary condition at $r = 1 - \delta$ for the full equations giving

$$\omega u_{sp} + \frac{\partial}{\partial r}\left[\nabla^2 h_{sp}\right] = -\gamma r, \tag{4.65}$$

$$\omega h_{sp} + \frac{1}{2r}\frac{\partial}{\partial r}\left[r(1-r^2)u_{sp}\right] = 0, \tag{4.66}$$

$$h_{sp} = R - \delta\left(1+\frac{\omega}{iv'}\right)R + \delta^2 C, \quad \frac{\partial h_{sp}}{\partial r} = \left(1+\frac{\omega}{iv'}\right)R - 2\delta C, \quad \text{at } r = 1-\delta, \tag{4.67}$$

$$u_{sp} = \omega R - \delta\frac{\omega}{2}\left(1+\frac{\omega}{iv'}\right)R + \delta^2\frac{1}{3}C, \tag{4.68}$$

$$\frac{\partial h_{sp}}{\partial r} = 0, \quad u_{sp} = 0, \quad \text{at } r = 0, \tag{4.69}$$

with the extra boundary condition given by

$$\frac{\partial^2 h_{sp}}{\partial r^2} = 2C, \quad \text{at } r = 1-\delta. \tag{4.70}$$

We will solve this system of equations using a finite difference method accurate to the order of grid spacing squared. Now we have a numerical system to solve we will also solve a simpler set of equations analytically in order to compare.

Low frequency approximation of the spreading mode

We will now look at the case where $\omega \ll 1$ representing a very low frequency oscillation. We will do this since mathematically it uncouples h_{sp} and u_{sp} in (4.58)-(4.61), leaving them both relatively simple to solve. For the asymptotic expansion we will refer to the unknown functions as h_a and u_a respectively and expand in orders of ω giving

$$\begin{gathered} h_a = h_0(r) + \omega h_1(r) + O(\omega^2), \quad u_a = \omega u_1(r) + \omega^2 u_2(r) + O(\omega^3), \\ R = R_0 + \omega R_1 + O(\omega^2). \end{gathered} \tag{4.71}$$

Since $\omega = 0$ corresponds to a steady motion of the droplet, u_a will equal zero meaning it begins at order ω. Also we will include u_2 since we will need to go once step further solving for u_a in order to find R_1 (as shown below). The leading order equations are therefore

$$\frac{\partial}{\partial r}\left[\frac{1}{r}\frac{\partial}{\partial r}\left(r\frac{\partial h_0}{\partial r}\right)\right] = -\gamma r, \tag{4.72}$$

$$\frac{\partial h_0}{\partial r} = \frac{\partial^3 h_0}{\partial r^3} = 0, \quad \text{at } r = 0, \tag{4.73}$$

$$h_0 = R_0, \quad \frac{\partial h_0}{\partial r} = R_0, \quad \text{at } r = 1. \tag{4.74}$$

The next set of equations for h_{sp} are

$$\frac{\partial}{\partial r}\left[\frac{1}{r}\frac{\partial}{\partial r}\left(r\frac{\partial h_1}{\partial r}\right)\right] = 0, \tag{4.75}$$

$$\frac{\partial h_1}{\partial r} = \frac{\partial^3 h_1}{\partial r^3} = 0, \quad \text{at } r = 0, \tag{4.76}$$

$$h_1 = R_1, \quad \frac{\partial h_0}{\partial r} = R_1 + \frac{R_0}{iv'}, \quad \text{at } r = 1. \tag{4.77}$$

Solving both of these sets of equations gives

$$h_0 = \frac{1}{2}R_0(1+r^2) - \frac{\gamma}{32}(1-r^2)^2, \quad h_1 = \frac{1}{2}R_1(1+r^2) - \frac{1}{2}\frac{R_0}{iv'}(1-r^2). \tag{4.78}$$

Now we will solve the equations for u_a in order to find out R. The equations for $u_{1/2}$ are therefore

$$\frac{\partial}{\partial r}\left[r(1-r^2)u_{1/2}\right] = -2rh_{0/1}, \tag{4.79}$$

where

$$u_{1/2} = 0, \quad \text{at } r = 0, \qquad u_{1/2} = R_{0/1}, \quad \text{at } r = 1. \tag{4.80}$$

Solving this for u_1 and applying the condition at $r = 0$ gives

$$(1-r)(1+r)u_1 = \frac{\gamma}{32}r\left(1 - r^2 + \frac{1}{3}r^4\right) - \frac{R_0}{4}r\left(2 + r^2\right), \tag{4.81}$$

and in order to examine the behaviour as $r \to 1$ we will set $r = 1 - \eta$ and let $\eta \to 0$. So as $r \to 1$ we get

$$\frac{2+\eta}{1-\eta}\eta R_0 = \frac{\gamma}{96}\left(1 + 2\eta + O(\eta^2)\right) - \frac{R_0}{4}\left(3 - 2\eta + O(\eta^2)\right), \tag{4.82}$$

which can be rearranged to

$$\frac{\gamma}{96} - \frac{3R_0}{4} + \eta\left[\frac{\gamma}{48} + \left(\frac{1}{2} - \frac{2+\eta}{1-\eta}\right)R_0\right] = O(\eta^2), \tag{4.83}$$

which is correct as $\eta \to 0$ as long as

$$R_0 = \frac{\gamma}{72}. \tag{4.84}$$

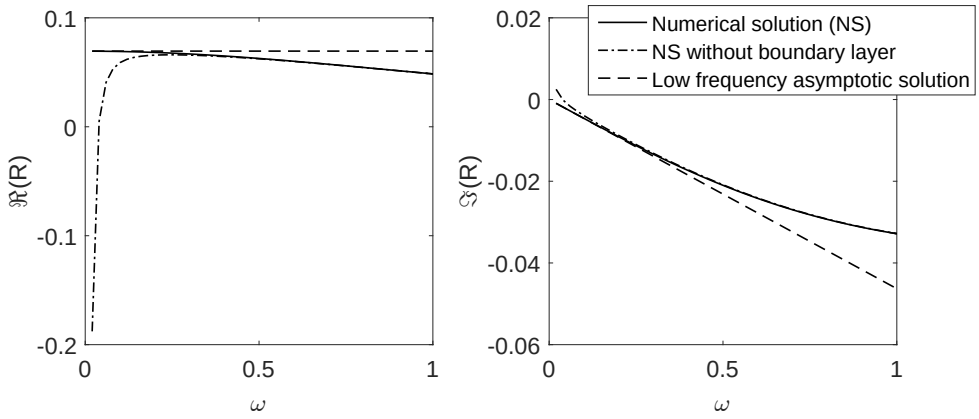


Figure 4.2: Comparison between numerical and asymptotic solution for R with $\gamma = 5, v(\theta) = 0.5(\theta - 1)$ and $\delta = 0.01$. The solid line is the full numerical solution method whereas the dot-dashed line is the solution method without the boundary layer.

Inserting this back into u_1 gives

$$u_1 = \gamma r \frac{7 - 3r^2}{288}. \tag{4.85}$$

Next we will solve for u_2 to find R_1. Similar to before the equation becomes

$$(1 - r^2)u_2 = \frac{r}{4}\left[\frac{R_0}{iv'}(2 - r^2) - R_1(2 + r^2)\right], \tag{4.86}$$

which can only be solved as $r \to 1$ if

$$R_1 = \frac{R_0}{3iv'}. \tag{4.87}$$

To summarise, the low frequency asymptotic solution to (4.58)-(4.61) is

$$h_a = \frac{R_0}{2}(1 + r^2) - \frac{\gamma}{32}(1 - r^2)^2 - \omega\frac{R_0}{3iv'}(1 - 2r^2) + O(\omega^2), \tag{4.88}$$

$$u_a = \omega\gamma r\frac{7 - 3r^2}{288} + O(\omega^2), \qquad R = R_0\left(1 + \omega\frac{1}{3iv'}\right) + O(\omega^2), \tag{4.89}$$

where $R_0 = \gamma/72$. We can see from figure 4.2 that the inclusion of the boundary layer is very important in the solution method, especially for $\omega \ll 1$, and also from figure 4.3 the solution is converging at a rate of grid spacing squared and δ^2, as it should.

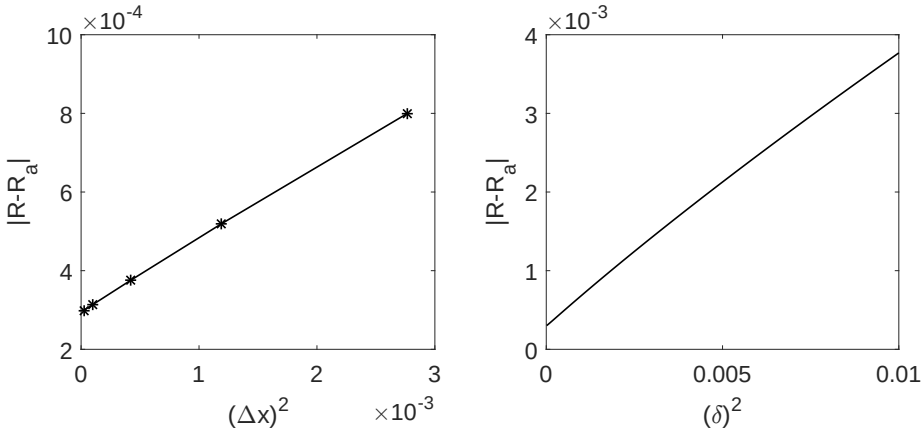


Figure 4.3: The convergence rate of the numerical solution for R, compared to the low frequency analytical solution, for grid spacing with $\delta = 0.001$ (left) and δ with 200 grid points (right). The other parameter values are $\gamma = 5, \omega = 0.1, v(\theta) = 0.5(\theta - 1)$.

4.2.6 The swaying mode

Now we will use a similar method to solve for the swaying mode. By combining (4.53) and (4.54) we get

$$u_{sw} + \frac{\partial}{\partial r}(r v_{sw}) = 0, \tag{4.90}$$

which we will use instead of (4.54). Now if we let $r = 1 - \delta x$ again, call the unknown functions h^+_{sw}, u^+_{sw} and v^+_{sw}, and let $\delta \to 0$ we can replace (4.53),(4.55) and (4.90) with

$$\frac{\partial^3 h^+_{sw}}{\partial x^3} = 0, \quad \frac{\partial (x u^+_{sw})}{\partial x} = \omega h^+_{sw}, \quad \frac{\partial v^+_{sw}}{\partial x} = 0. \tag{4.91}$$

These solve to give

$$h^+_{sw}(x) = A + \hat{B}x + \hat{C}x^2, \quad u^+_{sw}(x) = \omega A + \frac{1}{2}\omega \hat{B}x + \frac{1}{3}\omega \hat{C}x^2 + \frac{\hat{D}}{x}, \quad v^+_{sw} = E, \tag{4.92}$$

where $\hat{D}$ is required to be zero. If we insert the boundary conditions given in (4.60) these become

$$h^+_{sw} = -\frac{V}{iv'}(1-r) + \frac{\hat{V}}{2}(1-r)^2, \quad u^+_{sw} = -\frac{\omega V}{2iv'}(1-r) + \frac{\omega \hat{V}}{6}(1-r)^2, \quad v^+_{sw} = E, \tag{4.93}$$

where

$$\hat{V} = \left[1 + \omega E - \left(\omega + \frac{1}{iv'}\right) V\right].$$

We now have a full set of equations with boundary conditions at $r = 1 - \delta$ given by

$$\frac{\partial}{\partial r}\left[\nabla^2 - \frac{1}{r^2}\right] h_{sw} + \omega u_{sw} + \omega V = 1, \tag{4.94}$$

$$\omega u_{sw} + \frac{\partial}{\partial r}(r v_{sw}) = 0, \tag{4.95}$$

$$\omega h_{sw} + \frac{1}{2r}\frac{\partial}{\partial r}\left[r(1-r^2)u_{sw}\right] + \frac{1-r^2}{2r} v_{sw} = 0, \tag{4.96}$$

$$h_{sw} = -\delta\frac{V}{iv'} + \delta^2\frac{\hat{V}}{2}, \quad u_{sw} = -\delta\frac{\omega V}{2iv'} + \delta^2\frac{\omega\hat{V}}{6}, \quad v_{sw} = E, \quad \text{at } r = 1-\delta, \tag{4.97}$$

$$\frac{\partial h_{sw}}{\partial r} = \frac{V}{iv'} - \delta\hat{V}, \quad \frac{\partial u_{sw}}{\partial r} = \frac{\omega V}{2iv'} - \delta\frac{\omega\hat{V}}{3}, \quad \text{at } r = 1-\delta, \tag{4.98}$$

$$h_{sw} = 0, \quad \frac{\partial u_{sw}}{\partial r} = 0, \quad \text{at } r = 0. \tag{4.99}$$

Similar to the spreading mode, we will use a finite difference method to solve these equations.

Low frequency approximation of the swaying mode

We can look at the case where ω is small which will allow us to uncouple h_{sw} from u_{sw} and v_{sw}. We are only really interested in finding the first order expansion for V which means we can actually just solve (4.53) along with the boundary conditions on h_{sw}. Using the expansions

$$\begin{gathered} h_b(r) = h_0(r) + \omega h_1(r) + O(\omega^2), \quad V = V_0 + \omega V_1 + O(\omega^2), \\ u_{sw} = O(\omega), \quad v_{sw} = O(\omega), \end{gathered} \tag{4.100}$$

where we have labelled the unknown function as h_b, gives (4.53) - (4.57) as

$$\frac{\partial^2}{\partial r^2}\left[\frac{1}{r}\frac{\partial}{\partial r}(h_0 r)\right] = 1, \tag{4.101}$$

$$h_0 = \frac{\partial^2 h_0}{\partial r^2} = 0, \quad \text{at } r = 0, \tag{4.102}$$

$$h_0 = 0, \quad \frac{\partial h_0}{\partial r} = \frac{V_0}{iv'}, \quad \text{at } r = 1, \tag{4.103}$$

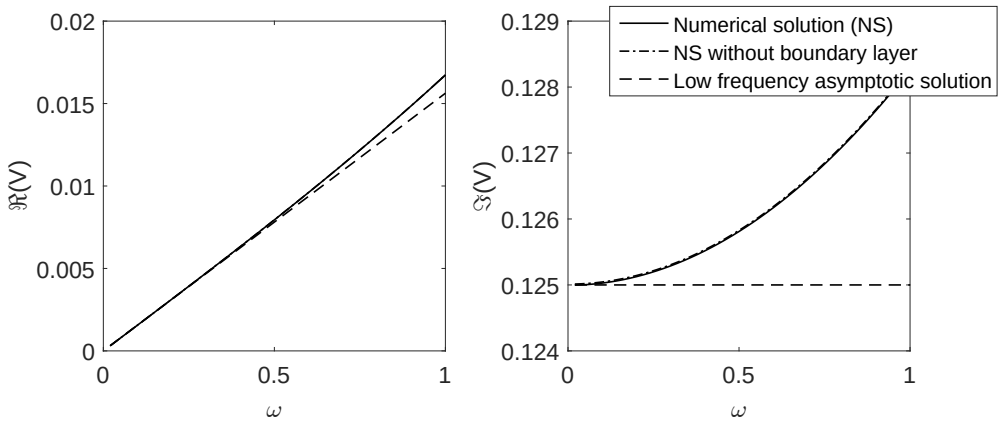


Figure 4.4: Comparison between numerical and asymptotic solution for V with $\gamma = 5, v(\theta) = 0.5(\theta - 1)$ and $\delta = 0.01$. The solid line is the full numerical solution method whereas the dot-dashed line is the solution method without the boundary layer.

and similarly

$$\frac{\partial^2}{\partial r^2}\left[\frac{1}{r}\frac{\partial}{\partial r}(h_1 r)\right] = -V_0, \tag{4.104}$$

$$h_1 = \frac{\partial^2 h_1}{\partial r^2} = 0, \quad \text{at } r = 0, \tag{4.105}$$

$$h_1 = 0, \quad \frac{\partial h_1}{\partial r} = \frac{V_1}{iv'}, \quad \text{at } r = 1. \tag{4.106}$$

Solving both of these sets of equations gives

$$h_b = -\frac{1}{8}r(1 - r^2)\left[1 - \omega\frac{iv'}{4}\right] + O(\omega^2), \tag{4.107}$$

$$V = \frac{iv'}{4} + \omega\frac{(v')^2}{16} + O(\omega^2). \tag{4.108}$$

We can see from figure 4.4 that the inclusion of the boundary layer is not as important for the swaying mode in comparison to the spreading one but we will still keep it to increase accuracy. We also see from figure 4.5 that the solution is converging at a rate of grid spacing squared and δ^2, similar to the spreading mode. Now we have covered the first order solutions for small ϵ we will move onto the second order problem which will allow us to calculate the rise velocity of the droplet.

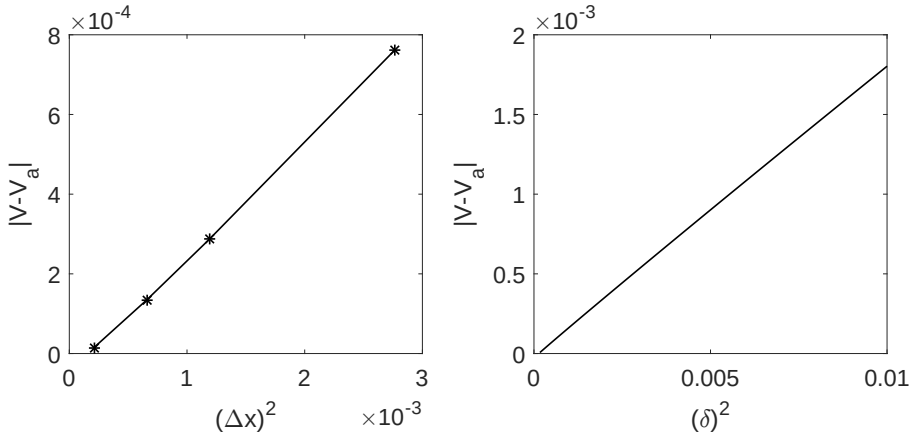


Figure 4.5: The convergence rate of the numerical solution for V, compared to the low frequency analytical solution, for grid spacing with $\delta = 0.001$ (left) and δ with 200 grid points (right). The other parameter values are $\gamma = 5, \omega = 0.1, v(\theta) = 0.5(\theta - 1)$.

4.2.7 Second order terms

Now we will look into finding the rise velocity using the answers obtained from the first order problem. The first method we will look at for doing this is to return to the second order asymptotic problem and solve that to find V_2. Since the rise velocity is the constant part of the second order asymptotic solution of V_2, we will take the time average of the equations obtained in section 4.2.3, which uncouples h_2 and $\mathbf{u}_2$, meaning we only need to look at

$$\frac{\partial \mathbf{u}_2}{\partial t} + (\mathbf{u}_1 \cdot \boldsymbol{\nabla})\mathbf{u}_1 + \boldsymbol{\nabla}\left[\left(g + \frac{dV_2}{dt}\right) r\cos\phi - \nabla^2 h_2 + \gamma\left(\sin(\omega t)h_1 + g\frac{1-r^2}{2}\right)\right] = 0, \tag{4.109}$$

$$h_2 = R_2 - R_1\frac{\partial h_1}{\partial r} + R_1^2, \qquad \frac{\partial R_2}{\partial t} = v_2 - V_2\cos\phi - V_1\sin\phi\frac{\partial R_1}{\partial \phi}, \qquad \text{at } r = 1, \tag{4.110}$$

$$\int_0^{\pi/2}\left[R_2 + \frac{1}{2}R_1^2 - \frac{1}{4}\left(\frac{\partial R_1}{\partial \phi}\right)^2\right]\mathrm{d}\phi = \int_{\pi/2}^{\pi}\left[R_2 + \frac{1}{2}R_1^2 - \frac{1}{4}\left(\frac{\partial R_1}{\partial \phi}\right)^2\right]\mathrm{d}\phi, \tag{4.111}$$

where

$$v_2 = v'\left[R_2 - \frac{\partial h_2}{\partial r} - R_1\frac{\partial^2 h_1}{\partial r^2} - \frac{1}{2}\left(\frac{\partial R_1}{\partial \phi}\right)^2\right] + \frac{1}{2}v''\left[R_1 - \frac{\partial h_1}{\partial r}\right]^2. \tag{4.112}$$

Since we know that R_1 is only a function of time, the time averaged versions of these equations are

$$\overline{(\mathbf{u}_1 \cdot \boldsymbol{\nabla})\mathbf{u}_1} + \boldsymbol{\nabla}\left[gr\cos\phi + \gamma\left(\frac{1}{2}\Re\left\{\tilde{h}\right\} + g\frac{1-r^2}{2}\right) - \nabla^2\bar{h}\right] = 0, \quad (4.113)$$

$$\frac{\partial\overline{h}}{\partial r} = \overline{R} - \overline{R_1\frac{\partial^2 h_1}{\partial r^2}} + \frac{v''}{2v'}\overline{\left[R_1 - \frac{\partial h_1}{\partial r}\right]^2} - \frac{1}{v'}\overline{V}\cos\phi, \quad \text{at } r = 1, \quad (4.114)$$

$$\overline{h} = \overline{R} + \overline{R_1\left(R_1 - \frac{\partial h_1}{\partial r}\right)}, \quad \text{at } r = 1, \quad (4.115)$$

$$\int_0^{\pi/2}\overline{R}\mathrm{d}\phi = \int_{\pi/2}^{\pi}\overline{R}\mathrm{d}\phi. \quad (4.116)$$

Now we need to sort out the time averaged terms included, starting with $(\mathbf{u}_1 \cdot \boldsymbol{\nabla})\mathbf{u}_1$ which we can write as

$$(\mathbf{u}_1 \cdot \boldsymbol{\nabla})\mathbf{u}_1 = \frac{1}{2}\boldsymbol{\nabla}|\mathbf{u}_1|^2 - \mathbf{u}_1 \times (\boldsymbol{\nabla} \times \mathbf{u}_1), \quad (4.117)$$

and from (4.47) we know that $\mathbf{u}_1$ can be written as a potential meaning that

$$\boldsymbol{\nabla} \times \mathbf{u}_1 = 0. \quad (4.118)$$

We can now write our second order equations as

$$\nabla^2\bar{h} = \frac{1}{4}|\tilde{\mathbf{u}}|^2 + gr\cos\phi + \gamma\left(\frac{1}{2}\Re\left\{\tilde{h}\right\} + g\frac{1-r^2}{2}\right) + c, \quad (4.119)$$

$$\overline{h} = \overline{R} + \frac{1}{2v'}\Im\left\{\tilde{R}\tilde{V}^*\right\}\cos\phi, \quad \text{at } r = 1, \quad (4.120)$$

$$\frac{\partial\overline{h}}{\partial r} = \overline{R} - \frac{1}{2}\Re\left\{\tilde{R}\frac{\partial^2\tilde{h}^*}{\partial r^2}\right\} + \frac{v''}{4(v')^3}\left|\omega\tilde{R} + \tilde{V}\cos\phi\right|^2 - \frac{1}{v'}\overline{V}\cos\phi, \quad \text{at } r = 1, \quad (4.121)$$

where c is an arbitrary constant. If we expand out $|\tilde{\mathbf{u}}|^2$ and $|\omega\tilde{R} + \tilde{V}\cos\phi|^2$ we can see that the ϕ dependance in this problem exists in the forms $\cos\phi$ and $\cos(2\phi)$ only. We can therefore separate (4.119)-(4.121) into three sets of equations; one that describes the correction to the spreading mode, one which is the correction to the swaying mode and a new set of equations describing the distortion of the droplet. The rise velocity $\overline{V}$ only appears in the correction to the swaying mode (i.e. a $\cos\phi$ term) and so this is the only set of equations

we will look at. We also know from the extra constraint that $\bar{R}$ contains a constant term and a $\cos(2\phi)$ term meaning we can uncouple this also. The equations we want to look at are

$$\left(\nabla^2 - \frac{1}{r^2}\right)\bar{h}_{\cos} = \frac{1}{2}\Re\left\{u_{sp}u_{sw}^* + \gamma h_{sw}\right\} + gr, \tag{4.122}$$

where

$$\bar{h}_{\cos} = 0, \quad \text{at } r = 0, \qquad \bar{h}_{\cos} = \frac{1}{2v'}\Im\left\{\tilde{R}\tilde{V}^*\right\}, \quad \text{at } r = 1, \tag{4.123}$$

$$\frac{\partial \bar{h}_{\cos}}{\partial r} = \frac{1}{2}\Re\left\{\frac{\omega v''}{(v')^3}\tilde{R}\tilde{V}^* - \tilde{R}\frac{\partial^2 \tilde{h}_{sw}^*}{\partial r^2}\right\} - \frac{1}{v'}\bar{V}, \quad \text{at } r = 1. \tag{4.124}$$

4.2.8 Force Balance

An easier method for finding the rise velocity is to integrate the momentum equations over the volume of the droplet to obtain the force applied to the droplet and then by integrating again, but now over one period of oscillation, we will get the net force applied to the droplet, which should give us the rise velocity. So we will begin with the shallow water equations

$$\frac{\partial \mathbf{u}}{\partial t} + (\mathbf{u}\cdot\boldsymbol{\nabla})\mathbf{u} - \boldsymbol{\nabla}\left(\nabla^2 - \epsilon\gamma a\right)h + \left(\epsilon a + \frac{dV_s}{dt}\right)\hat{\mathbf{x}} = 0, \tag{4.125}$$

$$\frac{\partial h}{\partial t} + \boldsymbol{\nabla}\cdot(h\mathbf{u}) = 0. \tag{4.126}$$

Combining these equations and using suffix notation gives

$$\frac{\partial (hu_i)}{\partial t} + hu_j\frac{\partial u_i}{\partial x_j} + u_i\frac{\partial (hu_j)}{\partial x_j} - h\frac{\partial^3 h}{\partial x_i x_j^2} + \epsilon\gamma a h\frac{\partial h}{\partial x_i} + \left(\epsilon a + \frac{dV_s}{dt}\right)h\delta_{1i} = 0, \tag{4.127}$$

which can be simplified to

$$\begin{aligned}\frac{\partial (hu_i)}{\partial t} + \frac{\partial (hu_j u_i)}{\partial x_j} - \frac{\partial}{\partial x_i}\left(h\frac{\partial^2 h}{\partial x_j^2}\right) + \frac{\partial h}{\partial x_i}\frac{\partial^2 h}{\partial x_j^2} + \frac{1}{2}\epsilon\gamma a\frac{\partial h^2}{\partial x_i} \\ + \left(\epsilon a + \frac{dV_s}{dt}\right)h\delta_{1i} = 0,\end{aligned} \tag{4.128}$$

which we will finally change to

$$\frac{\partial(hu_i)}{\partial t}+\frac{\partial(hu_ju_i)}{\partial x_j}-\frac{\partial}{\partial x_i}\left(h\frac{\partial^2 h}{\partial x_j^2}\right)+\frac{\partial}{\partial x_j}\left(\frac{\partial h}{\partial x_i}\frac{\partial h}{\partial x_j}\right)-\frac{1}{2}\frac{\partial}{\partial x_i}\left(\frac{\partial h}{\partial x_j}\right)^2 + \frac{1}{2}\epsilon\gamma a\frac{\partial h^2}{\partial x_i}+\left(\epsilon a+\frac{dV_s}{dt}\right)h\delta_{1i}=0, \tag{4.129}$$

We will now integrate over the area of the footprint, using the divergence theorem and the fact that

$$\int_{\mathcal{R}} h\mathrm{d}A=\mathcal{V}, \tag{4.130}$$

for volume $\mathcal{V}$, to give

$$\int_{\partial\mathcal{R}}\left[h\mathbf{u}(\mathbf{u}\cdot\mathbf{n})-\mathbf{n}h\nabla^2 h+\boldsymbol{\nabla}h\frac{\partial h}{\partial n}-\frac{1}{2}\mathbf{n}|\boldsymbol{\nabla}h|^2+\frac{1}{2}\epsilon\gamma a\mathbf{n}h^2\right]\mathrm{d}l \int_{\mathcal{R}}\frac{\partial(h\mathbf{u})}{\partial t}\mathrm{d}A+\left(\epsilon a+\frac{dV_s}{dt}\right)\mathcal{V}\hat{\mathbf{x}}=0, \tag{4.131}$$

and now by applying

$$h(\mathbf{x},t)=0 \quad \text{on } \mathbf{x}\in\partial\mathcal{R}, \tag{4.132}$$

gives

$$\int_{\mathcal{R}}\frac{\partial(h\mathbf{u})}{\partial t}\mathrm{d}A+\int_{\partial\mathcal{R}}\left[\boldsymbol{\nabla}h\frac{\partial h}{\partial n}-\frac{1}{2}\mathbf{n}|\boldsymbol{\nabla}h|^2\right]\mathrm{d}l+\left(\epsilon a+\frac{dV_s}{dt}\right)\mathcal{V}\hat{\mathbf{x}}=0. \tag{4.133}$$

Next we will look at the other boundary conditions. We have

$$\frac{\partial h}{\partial n}=\frac{\frac{\partial h}{\partial r}-\frac{1}{R^2}\frac{\partial R}{\partial\phi}\frac{\partial h}{\partial\phi}}{\sqrt{1+\left(\frac{1}{R}\frac{\partial R}{\partial\phi}\right)^2}}=-\theta, \quad \frac{\partial h}{\partial s}=\frac{\frac{1}{R}\frac{\partial h}{\partial r}\frac{\partial R}{\partial\phi}+\frac{1}{R}\frac{\partial h}{\partial\phi}}{\sqrt{1+\left(\frac{1}{R}\frac{\partial R}{\partial\phi}\right)^2}}=0, \quad \text{on } \mathbf{x}\in\partial\mathcal{R}, \tag{4.134}$$

which can be rearranged to give

$$\frac{\partial h}{\partial r}=\frac{-\theta}{\sqrt{1+\left(\frac{1}{R}\frac{\partial R}{\partial\phi}\right)^2}}, \quad \frac{1}{R}\frac{\partial h}{\partial\phi}=\frac{\frac{1}{R}\frac{\partial R}{\partial\phi}\theta}{\sqrt{1+\left(\frac{1}{R}\frac{\partial R}{\partial\phi}\right)^2}}, \quad \text{on } \mathbf{x}\in\partial\mathcal{R}, \tag{4.135}$$

and so

$$\boldsymbol{\nabla}h\frac{\partial h}{\partial n}-\frac{1}{2}\mathbf{n}|\boldsymbol{\nabla}h|^2=\frac{1}{2}\theta^2\frac{\hat{\mathbf{r}}-\frac{1}{R}\frac{\partial R}{\partial\phi}\hat{\phi}}{\sqrt{1+\left(\frac{1}{R}\frac{\partial R}{\partial\phi}\right)^2}}. \tag{4.136}$$

Rearranging (4.25) gives

$$\theta = 1 + \frac{v}{v'} - \frac{v''v^2}{2(v')^2} + ..., \tag{4.137}$$

and so

$$\theta^2 = 1 + \frac{2v}{v'} + \frac{v^2}{(v')^2}\left(1 - \frac{v''}{v'}\right) + ... \tag{4.138}$$

where v is of order ϵ. Substituting (4.138) into (4.136) and integrating around the boundary gives

$$\frac{1}{2}\int_0^{2\pi} R\left[1 + \frac{2v}{v'} + \frac{v^2}{(v')^2}\left(1 - \frac{v''}{v'}\right) + ...\right] \frac{\hat{\mathbf{r}} - \frac{1}{R}\frac{\partial R}{\partial \phi}\hat{\phi}}{\sqrt{1 + \left(\frac{1}{R}\frac{\partial R}{\partial \phi}\right)^2}} \mathrm{d}\phi. \tag{4.139}$$

Next we will write $v = \epsilon\hat{v}$ and expand

$$R(\phi, t) = 1 + \epsilon R_1(t) + \epsilon^2 R_2(\phi, t) + ...,$$

and rewrite (4.139) as

$$\frac{1}{2}\int_0^{2\pi}\left[1 + \epsilon R_1 + \epsilon^2 R_2 + \epsilon\frac{2\hat{v}}{v'} + \epsilon^2\frac{2R_1\hat{v}}{v'} + \epsilon^2\frac{\hat{v}^2}{(v')^2}\left(1 - \frac{v''}{v'}\right) + ...\right]\hat{\mathbf{r}} - \left[\epsilon^2\frac{\partial R_2}{\partial \phi} + ...\right]\hat{\phi}\mathrm{d}\phi,$$

which can be rearranged to

$$\frac{1 + \epsilon R_1}{2}\int_0^{2\pi}\hat{\mathbf{r}}\mathrm{d}\phi + \epsilon\frac{1 + \epsilon R_1}{v'}\int_0^{2\pi}\hat{v}\hat{\mathbf{r}}\mathrm{d}\phi + \epsilon^2\frac{1}{2(v')^2}\left(1 - \frac{v''}{v'}\right)\int_0^{2\pi}\hat{v}^2\hat{\mathbf{r}}\mathrm{d}\phi - \epsilon^2\frac{1}{2}\int_0^{2\pi}\frac{\partial}{\partial\phi}\left(R_2\hat{\phi}\right)\mathrm{d}\phi + ... \tag{4.140}$$

The integrals within this can be solved, leaving

$$\epsilon\frac{\pi}{v'}(1 + \epsilon R_1)(V_1 + \epsilon V_2)\hat{\mathbf{x}} + \epsilon^2\frac{\pi}{(v')^2}\left(1 - \frac{v''}{v'}\right)\frac{\partial R_1}{\partial t}V_1\hat{\mathbf{x}} + ... \tag{4.141}$$

Now if we substitute this into (4.133) we get

$$\int_{\mathcal{R}} \frac{\partial(h\mathbf{u})}{\partial t}\mathrm{d}A + \left[\epsilon\frac{\pi V_1}{v'} + \epsilon^2\frac{\pi}{v'}(R_1V_1 + V_2) + \epsilon^2\frac{\pi}{(v')^2}\left(1 - \frac{v''}{v'}\right)\frac{\partial R_1}{\partial t}V_1 + \epsilon a V_0 + \frac{dV_s}{dt}\mathcal{V}\right]\hat{\mathbf{x}} = 0. \tag{4.142}$$

Next we need to alter the remaining integral in (4.142). By writing it as

$$\int_0^{2\pi}\int_0^{R(\phi,t)} \frac{\partial(h\mathbf{u})}{\partial t} r\mathrm{d}r\mathrm{d}\phi, \tag{4.143}$$

we can use Reynold's transport theorem to change this to

$$\int_0^{2\pi}\left\{\frac{d}{dt}\int_0^R (h\mathbf{u})r\mathrm{d}r - \frac{\partial R}{\partial t}h(R,\phi,t)\mathbf{u}(R,\phi,t)R\right\}\mathrm{d}\phi = \frac{d}{dt}\int_{\mathcal{R}}(h\mathbf{u})\mathrm{d}A, \tag{4.144}$$

and we can use this to take a time average of (4.142) leaving

$$\overline{R_1V_1} + \overline{V_2} + \frac{1}{v'}\left(1 - \frac{v''}{v'}\right)\overline{\frac{dR_1}{dt}V_1} + \frac{gv'}{4} = 0, \tag{4.145}$$

since $\mathcal{V} = \pi/4$. Finally we will time average these terms using R_1 and V_1 from (4.46) and write the rise velocity of the droplet as

$$\overline{V} = \epsilon^2\left[\frac{\omega}{2v'}\left(\frac{v''}{v'} - 1\right)\Re\left\{\tilde{V}\tilde{R}^*\right\} + \frac{1}{2}\Im\left\{\tilde{V}\tilde{R}^*\right\} - \frac{gv'}{4}\right]. \tag{4.146}$$

We now have two separate methods to find the rise velocity of the droplet, and so the first test will be to compare the two solutions. If we attempt to solve the problem for small ω both the second order asymptotic problem for ϵ and the force balance both give

$$\frac{V}{\epsilon^2} = \frac{v'}{4}\left(\frac{\gamma}{144} - g\right) + O(\omega^2), \tag{4.147}$$

which is very encouraging that two completely different methods can give the exact same answer for $\omega = 0$. Unfortunately the correction term is of order ω^2 and so we cannot calculate it without returning to the first order asymptotic problem and expanding that up to order ω^2 also. The comparison between the two solutions, along with the point which they should both tend to as $\omega \to 0$, can be seen in figure 4.6. Since both methods give such similar answers which

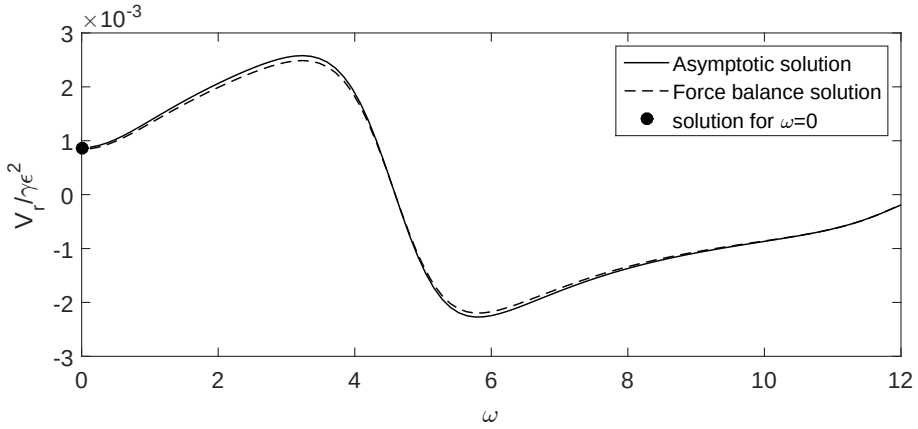


Figure 4.6: The rise velocity of the droplet against the frequency for $\gamma = 5, v(\theta) = 0.5(\theta - 1)$ and $g = 0$. The solid line is given by the second order asymptotic solution, the dashed line is the force balance and the black dot is the solution for $\omega = 0$.

both seem to tend to the correct answer at $\omega = 0$ we can safely say that the numerical method is accurate. The difference between these two curves comes from the numerical error present in the second order asymptotic equations. For convenience we will use the force balance in any further calculations of the rise velocity.

4.2.9 Comparison between model 2 and 3

Although we cannot compare this model directly with [8], due to only being able to examine small amplitude oscillations without the inclusion of contact angle hysteresis, we can compare our three-dimensional, inviscid droplet to the small contact angle limit of Model 2. This is an interesting comparison as it will show how the mechanics of the problem change between using a 'ridge' and a droplet. If we begin this comparison by looking at both (3.130) and (4.146) there is actually only two differences (since $\tilde{R} \equiv \tilde{D}$). The first of these differences is the constant attached to the gravity term, which is the result of the dimensionless scales that were chosen. To compensate for this we will compare solutions when $g = 0$. The second difference is the extra term that is present in (4.146) that does not depend on g or tend to zero with ω. This is interesting since for $g = 0$, the limit of $\omega \to 0$ corresponds to a droplet on a surface with no external forces being applied, and so the resultant droplet should remain fixed. However $\omega \to 0$ is a singular limit in this case, and for Model 3 the rise velocity is not zero but actually (4.147) shows it is a function

of $\gamma v'$.

Now we will compare the solutions of the models (figure 4.7) for the swaying modes velocity, the radial displacement and the rise velocity of the droplet. The first thing we can see from these graphs is that for all three, the lines are very similar. The actual difference between the two solutions is that magnitude of the peaks are smaller and the frequencies are higher for Model 3 compared to 2. What we can conclude from this is that changing between a 2-D and a 3-D model will cause the solution to change but by how much, for larger amplitude oscillations and non-linear contact line laws, is not yet known.

4.3 High frequency, small amplitude limit - WKB

We will now examine a special case of our first order problem, which is the limit as $\omega \to \infty$. To do this we will examine both modes separately and use the standard WKB substitution of an $\exp(\omega^{1/2}\psi)$ in order to solve (4.53)-(4.61) in the large ω limit. We will begin by solving the spreading mode, followed by the swaying one and then finally address the singular point at $r = 1$ for both of the modes by setting up a boundary layer.

4.3.1 High frequency spreading mode

To solve (4.58)-(4.61) we will first combine these equations to eliminate h_{sp} and then we will use a substitution for u_{sp} to solve the remaining equation. As stated, if we combine (4.58) and (4.59) we get

$$\frac{\partial}{\partial r}\left[\frac{1}{r}\frac{\partial}{\partial r}\left(r\frac{\partial}{\partial r}\left\{\frac{1}{r}\frac{\partial}{\partial r}\left[r(1-r^2)u_{sp}\right]\right\}\right)\right] - 2\omega(\omega u_{sp} + \gamma r) = 0, \tag{4.148}$$

$$u_{sp} = 0, \quad \frac{\partial^2 u_{sp}}{\partial r^2} = 0, \quad \text{at } r = 0, \tag{4.149}$$

$$u_{sp} = \omega R, \quad (1-r^2)\frac{\partial u_{sp}}{\partial r} = 0, \quad \text{at } r = 1, \tag{4.150}$$

$$\frac{1-r^2}{2}\frac{\partial^2 u_{sp}}{\partial r^2} - 2\frac{\partial u_{sp}}{\partial r} = \left(1 - \frac{\omega}{iv'}\right)\omega R, \quad \text{at } r = 1. \tag{4.151}$$

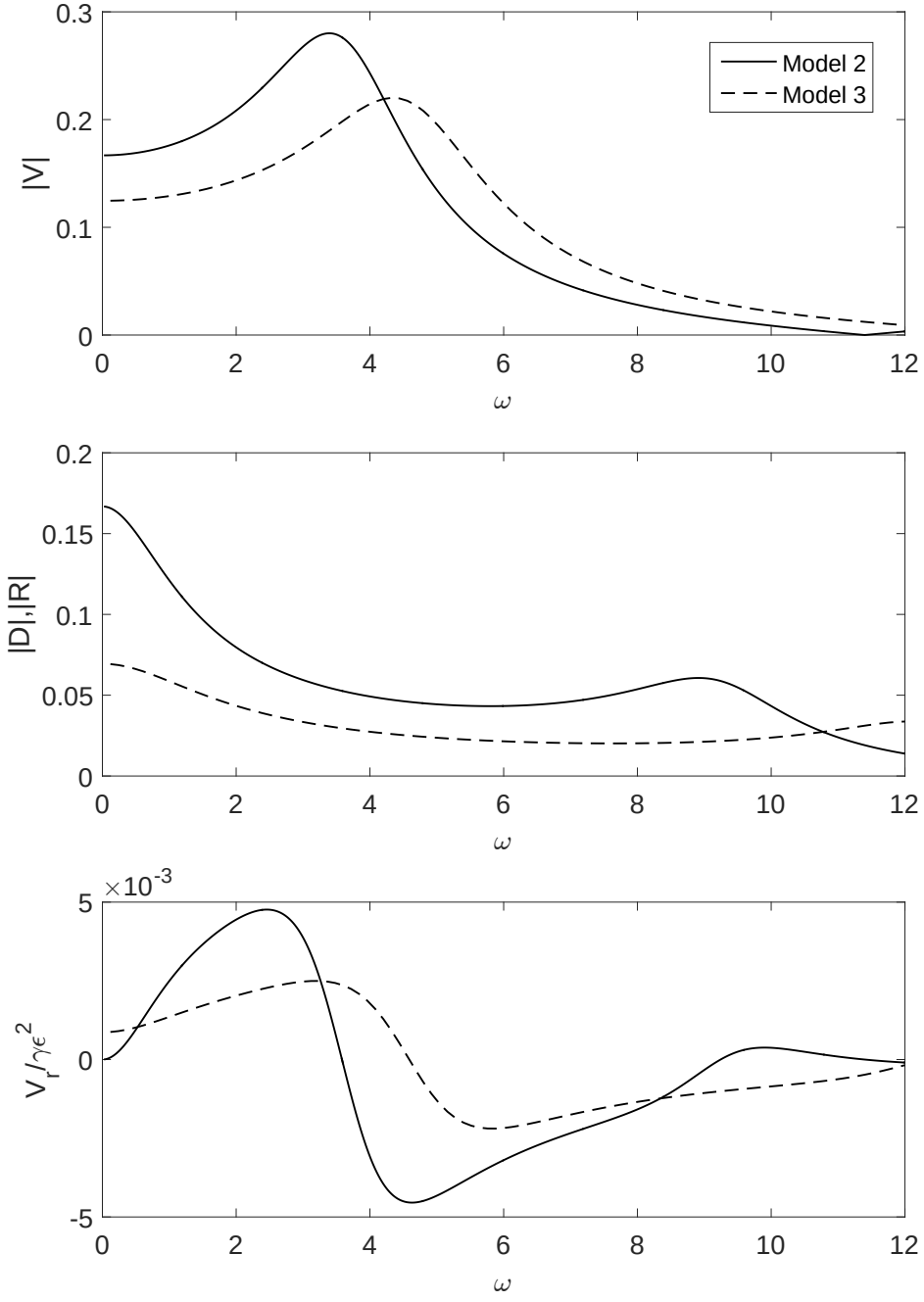


Figure 4.7: A comparison between model 2 (the two-dimensional, inviscid droplet) for $\theta_0 = 0.05$ and model 3 (the three-dimensional, shallow, inviscid droplet). The first graph is of the maximum velocity of the swaying mode over a period of oscillation, the second is the maximum displacement of the spreading mode over a period of oscillation and the third graph is the rise velocity of the droplet. All three graphs are plotted against the frequency of the oscillations for $\gamma = 5, v' = 0.5, v'' = 0$ and $g = 0$.

Next we will simplify this problem by letting $u_{sp} = -\gamma r + \Phi/(1-r^2)$, leaving

$$\frac{\partial}{\partial r}\left[\frac{1}{r}\frac{\partial}{\partial r}\left(r\frac{\partial}{\partial r}\left\{\frac{1}{r}\frac{\partial}{\partial r}\left[r\Phi\right]\right\}\right)\right] - \frac{2\omega^2}{1-r^2}\Phi = 0, \tag{4.152}$$

$$\Phi = 0, \quad \frac{\partial^2\Phi}{\partial r^2} = 0, \quad r = 0, \tag{4.153}$$

where the boundary conditions at $r = 1$ are derived in section 4.3.3. If we expand out the differential equation in (4.152) we get

$$\frac{\partial^4\Phi}{\partial r^4} + \frac{2}{r}\frac{\partial^3\Phi}{\partial r^3} - \frac{3}{r^2}\frac{\partial^2\Phi}{\partial r^2} + \frac{3}{r^3}\frac{\partial\Phi}{\partial r} - \left[\frac{3}{r^4} + \frac{2\omega^2}{1-r^2}\right]\Phi = 0.$$

By letting $\Phi = a_n \exp(\sqrt{\omega}\psi_n(r))$, in the limit of $\omega \to \infty$ this becomes

$$(\psi_n')^4 - \frac{2}{1-r^2} + \frac{2}{\sqrt{\omega}r}\frac{\partial}{\partial r}\left[r(\psi_n')^3\right] = O\left(\omega^{-1}\right). \tag{4.154}$$

Now if we let $\psi_n = \psi_{n0} + \omega^{-1/2}\psi_{n1} + ...$ and separate (4.154) into powers of $\omega^{-1/2}$ we get

$$(\psi_{n0}')^4 = \frac{2}{1-r^2}, \tag{4.155}$$

$$\psi_{n1}' = -\frac{1}{2r(\psi_0')^3}\frac{\partial}{\partial r}\left[r(\psi_{n0}')^3\right] = -\frac{1}{2}\frac{\partial}{\partial r}\left[\ln\left(r(\psi_{n0}')^3\right)\right]. \tag{4.156}$$

solving these gives

$$\psi_{n0} = f(r)\exp(in\pi/2) + A, \quad \psi_{n1} = \ln\left[\frac{(1-r^2)^{3/8}\exp(-3in\pi/4)}{\sqrt{r}}\right] + B, \tag{4.157}$$

where A, B are arbitrary constants of integration and

$$f(r) = 2^{1/4}\int_0^r (1-s^2)^{-1/4}\mathrm{d}s. \tag{4.158}$$

Inserting these back into Φ gives

$$\Phi = \frac{(1-r^2)^{3/8}}{\sqrt{r}}\sum_{n=0}^{3} a_n e^{\sqrt{\omega}f(r)\exp(in\pi/2)} + ..., \tag{4.159}$$

and since we know that $\Phi \to 0$ as $r \to 0$ we can take the solution

$$\Phi(r) = \frac{(1-r^2)^{3/8}}{\sqrt{r}}\left[c_1\sin(\sqrt{\omega}f(r)) + c_2\sinh(\sqrt{\omega}f(r))\right] + ..., \tag{4.160}$$

where c_1 andc_2 need to be determined by the boundary conditions at $r = 1$.

4.3.2 High frequency swaying mode

Unlike the spreading mode, the swaying mode is a little messier to calculate the large ω limit and so we will keep the equations separate instead of solving a single fourth order ODE. We will being by letting $v_{sw} = V - 1/\omega + \exp(\sqrt{\omega}\psi)/(1-r^2)$ in order to transform (4.54) into

$$\frac{1}{r}\left[\nabla^2 - \frac{1}{r^2}\right] h_{sw} = \frac{\omega e^{\sqrt{\omega}\psi}}{1-r^2}, \tag{4.161}$$

and also by combining (4.53) and (4.54) we get

$$u_{sw} = -\frac{\partial}{\partial r}(rv) = -\left(V - \frac{1}{\omega}\right) - \frac{1}{1-r^2}\left[\sqrt{\omega} r \frac{\partial \psi}{\partial r} + \frac{1+r^2}{1-r^2}\right] e^{\sqrt{\omega}\psi}. \tag{4.162}$$

Now if we insert u_{sw} and v_{sw} into (4.55) we get

$$2h_{sw} + \frac{2r}{\omega}\left(V - \frac{1}{\omega}\right) = \chi e^{\sqrt{\omega}\psi}, \tag{4.163}$$

where

$$\chi = r\left(\frac{\partial \psi}{\partial r}\right)^2 + \omega^{-1/2}\left(\frac{3-r^2}{1-r^2}\frac{\partial \psi}{\partial r} + r\frac{\partial^2 \psi}{\partial r^2}\right) + \omega^{-1} 2r \frac{3-r^2}{(1-r^2)^2}. \tag{4.164}$$

Now using (4.163) we get

$$2\left(\frac{\partial^2 h_{sw}}{\partial r^2} + \frac{1}{r}\frac{\partial h_{sw}}{\partial r} - \frac{1}{r^2}h_{sw}\right) = \omega\left[\chi\left(\frac{\partial \psi}{\partial r}\right)^2 + \omega^{-1/2}\left(2\frac{\partial \chi}{\partial r}\frac{\partial \psi}{\partial r} + \chi\frac{\partial^2 \psi}{\partial r^2} + \frac{1}{r}\chi\frac{\partial \psi}{\partial r}\right) + \omega^{-1}\left(\frac{\partial^2 \chi}{\partial r^2} + \frac{1}{r}\frac{\partial \chi}{\partial r} - \frac{1}{r^2}\chi\right)\right] e^{\sqrt{\omega}\psi},$$

and so (4.161) becomes

$$\chi\left(\frac{\partial \psi}{\partial r}\right)^2 + \omega^{-1/2}\left(2\frac{\partial \chi}{\partial r}\frac{\partial \psi}{\partial r} + \chi\frac{\partial^2 \psi}{\partial r^2} + \frac{1}{r}\chi\frac{\partial \psi}{\partial r}\right) = \frac{2r}{1-r^2} + O(\omega^{-1}). \tag{4.165}$$

Now if we let $\psi = \psi_0 + \omega^{-1/2}\psi_1 + ...$, similar to before we get

$$\chi = \chi_0 + \omega^{-1/2}\chi_1 + ... = r\left(\frac{\partial\psi_0}{\partial r}\right)^2 + \omega^{-1/2}\left[2r\frac{\partial\psi_0}{\partial r}\frac{\partial\psi_1}{\partial r} + r\frac{\partial^2\psi_0}{\partial r^2} + \frac{3-r^2}{1-r^2}\frac{\partial\psi_0}{\partial r}\right] + ...,$$

and inserting this into (4.165) gives

$$\left(\frac{\partial\psi_0}{\partial r}\right)^4 + 4\omega^{-1/2}\left(\frac{\partial\psi_0}{\partial r}\right)^3\left[\frac{\partial\psi_1}{\partial r} + \frac{\partial}{\partial r}\left(\frac{3}{2}\ln\left(\frac{\partial\psi_0}{\partial r}\right) + \frac{3}{2}\ln r - \frac{1}{4}\ln(1-r^2)\right)\right] = \frac{2}{1-r^2} + O(\omega^{-1}). \tag{4.166}$$

Separating this for orders of magnitude of $\omega^{-1/2}$ gives

$$\frac{\partial\psi_{n0}}{\partial r} = 2^{1/4}(1-r^2)^{-1/4}e^{in\pi/2}, \quad \text{for } n = 0, 1, 2, 3, \tag{4.167}$$

and

$$\frac{\partial\psi_{n1}}{\partial r} = \frac{\partial}{\partial r}\left[\ln\left(2^{-3/8}e^{-3in\pi/4}r^{-3/2}(1-r^2)^{5/8}\right)\right]. \tag{4.168}$$

If we solve both of these and insert them back into (4.162) we get

$$u_{sw} = \frac{1}{\omega} - V - \frac{(1-r^2)^{3/8}}{\sqrt{r}(1-r^2)}\sum_{n=0}^{3} b_n e^{\sqrt{\omega}f(r)\exp(in\pi/2)} + ..., \tag{4.169}$$

and now if we write $u_{sw} = 1/\omega - V + \Psi/(1-r^2)$ to match the spreading mode, along with the fact that $\partial\Psi/\partial r = 0$, we get

$$\Psi = \frac{(1-r^2)^{3/8}}{\sqrt{r}}c_3\left[\cos(\sqrt{\omega}f(r)) - \cosh(\sqrt{\omega}f(r))\right] + ..., \tag{4.170}$$

where again

$$f(r) = 2^{1/4}\int_0^r (1-s^2)^{-1/4}\mathrm{d}s,$$

but now c_4 appears as an unknown in the boundary conditions at $r = 1$. Both Ψ and Φ are both very similar to Φ_e and Φ_o only with an extra factor of $r^{-1/2}$.

4.3.3 The conditions for the upper boundary

In this section we will use the redefinitions of both u_{sp} and u_{sw} and then use (4.56)-(4.57) and (4.60)-(4.61) in order to find the boundary conditions for Φ and Ψ at $r = 1$. These will then be used to find the unknown constants in the high frequency limit. We will begin by taking (4.59) and inserting the redefinition

$$u_{sp} = \frac{\Phi}{1-r^2} - \delta_f \frac{\gamma}{\omega} r, \tag{4.171}$$

where δ_f is equal to one if we are looking at the forced problem or zero for the unforced problem. We have included this because we will use the high frequency asymptotic results to examine both. It should be noted that from (4.171) we already know that

$$\Phi = (1-r^2)\left(u_{sp} + \delta_f \frac{\gamma}{\omega} r\right),$$

and so $\Phi(r=1) = 0$. Now if we look at (4.59) in terms of Φ we get

$$\frac{\partial \Phi}{\partial r} = -2\omega h_{sp} - \frac{\Phi}{r} - 2\delta_f (2r^2 - 1)\frac{\gamma}{\omega},$$

and by differentiating this with respect to r we also get

$$\frac{\partial^2 \Phi}{\partial r^2} = -2\omega \frac{\partial h_{sp}}{\partial r} - \frac{1}{r}\frac{\partial \Phi}{\partial r} + \frac{\Phi}{r^2} - 8\delta_f \frac{\gamma}{\omega} r.$$

Now if we let $r = 1$ and insert the boundary conditions

$$h_{sp} = R, \quad u_{sp} = \omega R, \quad \frac{\partial h_{sp}}{\partial r} = \left(1 + \frac{\omega}{iv'}\right) R, \quad \text{at } r = 1,$$

we get

$$\Phi = 0, \quad \frac{\partial \Phi}{\partial r} = -2\left(\delta_f \frac{\gamma}{\omega} + \omega R\right), \quad \frac{\partial^2 \Phi}{\partial r^2} = -2\left(\delta_f \frac{3\gamma}{\omega} + \frac{\omega^2 R}{iv'}\right), \quad \text{at } r = 1. \tag{4.172}$$

Now that we have the boundary conditions for the spreading mode, our next step it to define the conditions for the swaying mode. For these conditions we will start with (4.55) and we will insert the redefinition

$$u_{sw} = \frac{\Psi}{1-r^2} + \delta_f \frac{1}{\omega}, \tag{4.173}$$

Again, we can see that from (4.173) that

$$\Psi = (1-r^2)\left(u - \delta_f \frac{1}{\omega}\right),$$

and so $\Psi(r=1) = 0$. Now if we insert Ψ into (4.55) we get

$$\frac{\partial \Psi}{\partial r} = -2\omega h_{sw} - \frac{\Psi}{r} - \frac{1-r^2}{r} v_{sw} + \delta_f \frac{3r^2-1}{\omega r},$$

along with the derivative

$$\frac{\partial^2 \Psi}{\partial r^2} = -2\omega \frac{\partial h_{sw}}{\partial r} - \frac{1}{r}\frac{\partial \Psi}{\partial r} + \frac{\Psi}{r^2} - \frac{1-r^2}{r}\frac{\partial v_{sw}}{\partial r} + \frac{1+r^2}{r^2} v_{sw} + \delta_f \frac{1+3r^2}{\omega r}.$$

Now if we let $r = 1$ and insert the boundary conditions

$$h_{sw} = 0, \quad u_{sw} = 0, \quad v_{sw} = c_4, \quad \frac{\partial h_{sw}}{\partial r} = \frac{V}{iv'}, \quad \text{at } r = 1,$$

we get

$$\Psi = 0, \quad \frac{\partial \Psi}{\partial r} = 2\delta_f \frac{1}{\omega}, \quad \frac{\partial^2 \Psi}{\partial r^2} = 2\left(\delta_f \frac{1}{\omega} + c_4 - \frac{\omega V}{iv'}\right), \quad \text{at } r = 1, \tag{4.174}$$

where c_4 is an arbitrary unknown we must discover.

4.3.4 Boundary Layer

We will now find the unknowns $c_{1,2,3,4}$ in the functions Φ and Ψ by using a boundary layer near $r = 1$ as well as the boundary conditions derived in section 4.3.3. To do this we will have to solve the equation

$$\frac{\partial^4 F}{\partial X^4} - \frac{F}{X} = 0, \tag{4.175}$$

where F can be replaced by Φ or Ψ. Instead of solving this problem exactly we will look at the limits of X tending to 0 and ∞ in order to solve for the unknowns. First of all we know that four linear solutions to (4.175) can be defined as

$$F_1 \sim 1, \quad F_2 \sim X, \quad F_3 \sim X^2, \quad F_4 \sim X^3, \quad \text{as } X \to 0, \tag{4.176}$$

and since we know that at the boundary

$$F = 0, \quad \frac{\partial F}{\partial X} = 2\omega^{-2/3} a_1, \quad \frac{\partial^2 F}{\partial X^2} = 2\omega^{-4/3} a_2, \quad \text{at } X = 0, \tag{4.177}$$

we can define

$$F = 2\omega^{-2/3} a_1 F_2 + \omega^{-4/3} a_2 F_3 + B F_4, \tag{4.178}$$

where $a_{1,2}$ and B are dependant on if we are solving for Φ or Ψ. Next if we take the outer solutions for Φ and Ψ and look at the limit of $r \to 1$ we know that

$$\begin{aligned} F = 2^{-5/8}\omega^{-1/4} X^{3/8} \Big(& b_1 e^{-4iX^{3/4}/3} + b_2 e^{4iX^{3/4}/3} + b_3 e^{-4X^{3/4}/3} \\ & + b_4 e^{4X^{3/4}/3} \Big), \quad \text{as } X \to \infty, \end{aligned} \tag{4.179}$$

and so $F_{1,2,3,4}$ must be some linear combination of $X^{3/8} e^{\mp 4iX^{3/4}/3}, X^{3/8} e^{\mp 4X^{3/4}/3}$ - i.e.

$$\begin{bmatrix} F_1 \\ F_2 \\ F_3 \\ F_4 \end{bmatrix} = X^{3/8} \begin{bmatrix} A_{11} & A_{12} & A_{13} & A_{14} \\ A_{21} & A_{22} & A_{23} & A_{24} \\ A_{31} & A_{32} & A_{33} & A_{34} \\ A_{41} & A_{42} & A_{43} & A_{44} \end{bmatrix} \begin{bmatrix} e^{-4iX^{3/4}/3} \\ e^{4iX^{3/4}/3} \\ e^{-4X^{3/4}/3} \\ e^{4X^{3/4}/3} \end{bmatrix}, \quad \text{as } X \to \infty. \tag{4.180}$$

Using our current knowledge of F we know that $F_{1,2,3,4}$ are real, and so

$$A_{n2} = A_{n1}^*, \quad \Im(A_{n3}) = \Im(A_{n4}) = 0.$$

Now if we equate (4.178) and (4.179) we get

$$\begin{aligned} 2^{-5/8}\omega^{-1/4} b_1 &= 2\omega^{-2/3} a_1 A_{21} + \omega^{-4/3} a_2 A_{31} + B A_{41}, \\ 2^{-5/8}\omega^{-1/4} b_2 &= 2\omega^{-2/3} a_1 A_{21}^* + \omega^{-4/3} a_2 A_{31}^* + B A_{41}^*, \\ 2^{-5/8}\omega^{-1/4} b_3 &= 2\omega^{-2/3} a_1 A_{23} + \omega^{-4/3} a_2 A_{33} + B A_{43}, \\ 2^{-5/8}\omega^{-1/4} b_4 &= 2\omega^{-2/3} a_1 A_{24} + \omega^{-4/3} a_2 A_{34} + B A_{44}. \end{aligned} \tag{4.181}$$

Now we must look at each problem separately in order to find our solutions. For the spreading mode we have

$$F = \Phi, \quad a_1 = -\left(\delta_f \frac{\gamma}{\omega} + \omega R\right), \quad a_2 = -\left(\delta_f \frac{3\gamma}{\omega} + \frac{\omega^2 R}{iv'}\right),$$

$$b_1 = -ic_1 e^{i\omega^{1/2} f(1)}, \quad b_2 = ic_1 e^{-i\omega^{1/2} f(1)}, \quad b_3 = c_2 e^{\omega^{1/2} f(1)}, \quad b_4 = -c_2 e^{-\omega^{1/2} f(1)},$$

Now inserting these into (4.181) and rearranging we get

$$\begin{aligned}
-i2^{-5/8}\omega^{-1/4} e^{i\zeta} c_1 &= -\frac{\delta_f \gamma}{\omega^{5/3}} \left(2A_{21} + \frac{3A_{31}}{\omega^{2/3}} \right) - \omega^{2/3} R \left(\frac{A_{21}}{\omega^{1/3}} + \frac{A_{31}}{iv'} \right) + BA_{41}, \\
i2^{-5/8}\omega^{-1/4} e^{-i\zeta} c_1 &= -\frac{\delta_f \gamma}{\omega^{5/3}} \left(2A^*_{21} + \frac{3A^*_{31}}{\omega^{2/3}} \right) - \omega^{2/3} R \left(\frac{A^*_{21}}{\omega^{1/3}} + \frac{A^*_{31}}{iv'} \right) + BA^*_{41}, \\
2^{-5/8}\omega^{-1/4} e^{\zeta} c_2 &= -\frac{\delta_f \gamma}{\omega^{5/3}} \left(2A_{23} + \frac{3A_{33}}{\omega^{2/3}} \right) - \omega^{2/3} R \left(\frac{A_{23}}{\omega^{1/3}} + \frac{A_{33}}{iv'} \right) + BA_{43}, \\
-2^{-5/8}\omega^{-1/4} e^{-\zeta} c_2 &= -\frac{\delta_f \gamma}{\omega^{5/3}} \left(2A_{24} + \frac{3A_{34}}{\omega^{2/3}} \right) - \omega^{2/3} R \left(\frac{A_{24}}{\omega^{1/3}} + \frac{A_{34}}{iv'} \right) + BA_{44},
\end{aligned}$$

where $\zeta = \omega^{1/2} f(1)$, and we know that $A_{nm} \to O(1)$ as $\omega \to \infty$ giving the leading order equations as

$$\begin{aligned}
-i2^{-5/8}\omega^{-1/4} e^{i\zeta} c_1 &= -\delta_f \frac{2\gamma}{\omega^{5/3}} A_{21} - \frac{\omega^{2/3} R}{iv'} A_{31} + BA_{41}, \\
i2^{-5/8}\omega^{-1/4} e^{-i\zeta} c_1 &= -\delta_f \frac{2\gamma}{\omega^{5/3}} A^*_{21} - \frac{\omega^{2/3} R}{iv'} A^*_{31} + BA^*_{41}, \\
2^{-5/8}\omega^{-1/4} e^{\zeta} c_2 &= -\delta_f \frac{2\gamma}{\omega^{5/3}} A_{23} - \frac{\omega^{2/3} R}{iv'} A_{33} + BA_{43}, \\
0 &= -\delta_f \frac{2\gamma}{\omega^{5/3}} A_{24} - \frac{\omega^{2/3} R}{iv'} A_{34} + BA_{44}.
\end{aligned} \tag{4.182}$$

Now for the unforced problem we can rearrange the last equation to give

$$B = \frac{\omega^{2/3} R}{iv'} \frac{A_{34}}{A_{44}},$$

which more importantly can be inserted into the others to give

$$-e^{2i\omega^{1/2} f(1)} = \frac{A_{41}A_{34} - A_{31}A_{44}}{A^*_{41}A_{34} - A^*_{31}A_{44}}. \tag{4.183}$$

This is interesting since the right hand side is a complex number with unit modulus, and therefore ω is real at leading order, and

$$2\omega^{1/2} f(1) + \pi \sim 2\Omega_0 f(1) + 2n\pi,$$

or just

$$\omega^{1/2} \sim \Omega_0 + \left(n - \frac{1}{2} \right) \Omega_1, \tag{4.184}$$

where Ω_0 is an undetermined real constant and $\Omega_1 \approx 2.20$. Also we will note that the magnitude of $A_{41}A_{34} - A_{31}A_{44}$ is equal to

$$r = \frac{iv'c_1}{2^{5/8}\omega^{11/12}R}A_{44},$$

for completeness. Now we will move onto the swaying mode which means we now have

$$F = \Psi, \quad a_1 = \frac{\delta_f}{\omega} - V, \quad a_2 = \left[\frac{\delta_f}{\omega} - \left(1 + \frac{\omega}{iv'}\right)V + c_4\right],$$

$$b_1 = c_3 e^{i\omega^{1/2}f(1)}, \quad b_2 = c_3 e^{-i\omega^{1/2}f(1)}, \quad b_3 = -c_3 e^{\omega^{1/2}f(1)}, \quad b_4 = -c_3 e^{-\omega^{1/2}f(1)},$$

and also we will replace B with C to avoid confusion. Now inserting these into (4.181) and rearranging we get

$$\begin{aligned}
2^{-5/8}\omega^{-1/4}e^{i\zeta}c_3 &= \frac{\delta_f}{\omega^{5/3}}\left(2A_{21} + \frac{A_{31}}{\omega^{2/3}}\right) - \frac{V}{\omega^{1/3}}\left(\frac{2A_{21}}{\omega^{1/3}} + \frac{A_{31}}{\omega} + \frac{A_{31}}{iv'}\right) \\
&\qquad + c_4A_{31} + CA_{41}, \\
2^{-5/8}\omega^{-1/4}e^{-i\zeta}c_3 &= \frac{\delta_f}{\omega^{5/3}}\left(2A^*_{21} + \frac{A^*_{31}}{\omega^{2/3}}\right) - \frac{V}{\omega^{1/3}}\left(\frac{2A^*_{21}}{\omega^{1/3}} + \frac{A^*_{31}}{\omega} + \frac{A^*_{31}}{iv'}\right) \\
&\qquad + c_4A^*_{31} + CA^*_{41}, \\
-2^{-5/8}\omega^{-1/4}e^{\zeta}c_3 &= \frac{\delta_f}{\omega^{5/3}}\left(2A_{23} + \frac{A_{33}}{\omega^{2/3}}\right) - \frac{V}{\omega^{1/3}}\left(\frac{2A_{23}}{\omega^{1/3}} + \frac{A_{33}}{\omega} + \frac{A_{33}}{iv'}\right) \\
&\qquad + c_4A_{33} + CA_{43}, \\
-2^{-5/8}\omega^{-1/4}e^{-\zeta}c_3 &= \frac{\delta_f}{\omega^{5/3}}\left(2A_{24} + \frac{A_{34}}{\omega^{2/3}}\right) - \frac{V}{\omega^{1/3}}\left(\frac{2A_{24}}{\omega^{1/3}} + \frac{A_{34}}{\omega} + \frac{A_{34}}{iv'}\right) \\
&\qquad + c_4A_{34} + CA_{44},
\end{aligned}$$

where once again the leading order terms are

$$\begin{aligned}
2^{-5/8}\omega^{-1/4}e^{i\zeta}c_3 &= \delta_f\frac{2}{\omega^{5/3}}A_{21} + \left(c_4 - \frac{V}{iv'\omega^{1/3}}\right)A_{31} + CA_{41}, \\
2^{-5/8}\omega^{-1/4}e^{-i\zeta}c_3 &= \delta_f\frac{2}{\omega^{5/3}}A^*_{21} + \left(c_4 - \frac{V}{iv'\omega^{1/3}}\right)A^*_{31} + CA^*_{41}, \\
-2^{-5/8}\omega^{-1/4}e^{\zeta}c_3 &= \delta_f\frac{2}{\omega^{5/3}}A_{23} + \left(c_4 - \frac{V}{iv'\omega^{1/3}}\right)A_{33} + CA_{43}, \\
0 &= \delta_f\frac{2}{\omega^{5/3}}A_{24} + \left(c_4 - \frac{V}{iv'\omega^{1/3}}\right)A_{34} + CA_{44}.
\end{aligned}$$

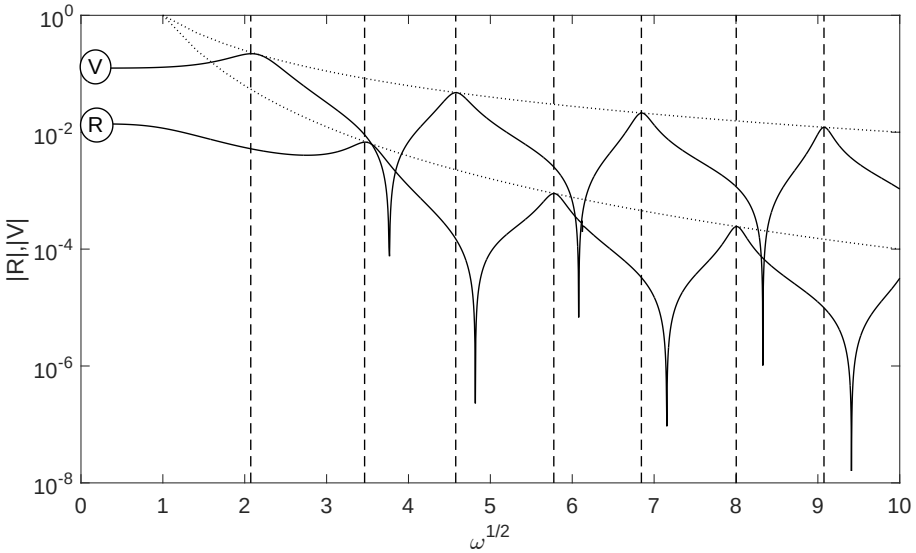


Figure 4.8: The absolute values of V and R against $\omega^{1/2}$ for $\gamma = 1$ and $v' = 0.5$. The vertical dashed lines show the real parts of the natural frequencies of the drop's free oscillations. The dotted lines show the dependencies ω^{-1} and ω^{-2}.

Now we can rearrange the last equations to give

$$C = -\left(c_4 - \frac{V}{iv'\omega^{1/3}}\right)\frac{A_{34}}{A_{44}},$$

which in turn gives

$$e^{2i\omega^{1/2}f(1)} = \frac{A_{41}A_{34} - A_{31}A_{44}}{A_{41}^*A_{34} - A_{31}^*A_{44}}. \tag{4.185}$$

Again the right hand side is a complex number with unit modulus, only now we get

$$\omega^{1/2} \sim \Omega_0 + n\Omega_1, \tag{4.186}$$

meaning that there is a shift in $\omega^{1/2}$ of $\Omega_1/2$ for the two modes. The values for $\omega^{1/2}$ that correspond to the vertical dashed lines in figure 4.8 are

$$2.0736 \quad 3.4641 \quad 4.5771 \quad 5.7749 \quad 6.8447 \quad 8.0031 \quad 9.0747,$$

meaning that the spacing between is

$$1.3905 \quad 1.1130 \quad 1.1978 \quad 1.0698 \quad 1.1584 \quad 1.0716.$$

If we take the average of these (excluding the first value in order to allow the solution to converge) we get an average spacing of 1.12 which is roughly the expected shift in $\omega^{1/2}$.

4.4 Discussion

In this chapter we have considered a three-dimensional, thin droplet, with surface tension and inertia, on an oscillating plate. When small amplitude forcing is applied we found that the motion of the droplet is a combination of two modes, one with no ϕ dependance and one that is proportional to $\cos\phi$. Separately, these two modes give the droplet either an up-and-down the plane swaying motion or a radially in-and-out spreading motion, both of which cause zero net motion. When we examined the non-linear interaction between these two modes we saw that the interaction between them gives the droplet a net motion, either climbing uphill or sliding down. Following this we compared the results of this model with that of Model 2 (in the small contact angle limit). The differences between the two models are only minor, with the absolute values of the swaying modes velocity and the radial displacement both producing similar shaped curves to the 2-D model. For this model however the peaks of these curves are smaller in magnitude and occur at higher frequencies. When comparing the rise velocities we again see a difference in the magnitude and location of the peaks but overall the shape of the curves are relatively similar. This being said, since we made the comparison for $g = 0$ the rise velocity of Model 2 tends to zero with the frequency whereas with this model it reaches a positive value that depends on γ and v'.

We then moved onto the high frequency, small amplitude limit of the model and examined the behaviour of the swaying mode's velocity as well as the spreading mode's radial displacement. We saw that the absolute values of both of these contain natural frequencies that are averagely spaced at $\omega^{1/2} \approx 1.1$. We could also use this to see that the velocity decreased at a rate of $1/\omega$ whereas the radial displacement was at a rate of $1/\omega^2$.

Chapter 5

Conclusion

For this thesis we have considered a variety of different methods for modelling a droplet climbing uphill when placed on an inclined plane and vibrated vertically and sinusoidally [8]. When attempting to model flows that contain a moving contact line two problems arise. The first of these problems is the singularity in the shear stress located at the solid/liquid/fluid interface. Classical continuum mechanics states that a viscous fluid will retain the velocity of any solid it is in contact with along its boundary interface, however this suggests that a droplet on a surface will always remain pinned in one place; a suggestion that we already know to be false. In order to resolve this problem we have assumed that the Reynolds number is large enough for viscosity to be neglected within the models. This allows us to not worry about the 'no-slip' condition, negating the singularity within the stress. The second problem is the method for which we will calculate the velocity of the contact line. In order to resolve this we have used a method similar to [2][3][4][20], which models the contact line velocity as some prescribed function of the respective contact angle. The reason we have chosen this method is that strong correlations between the velocity of the contact line and the size of the contact angles have been observed experimentally [7][23][33], be it for steady flows. Now that we have a description of the general assumptions used throughout the thesis we will cover each model separately explaining advantages, disadvantages and results.

We began with Model 1 which was designed using the quasistatic approximation; which assumes that the surface tension of the droplet, along with the force of the applied accelerations, dominates over the inertial and viscous forces of the fluid. In addition to this we applied the assumption that the slope of the free surface is small. This model was introduced in [2] who went

on to solve the small amplitude forcing problem asymptotically to find the rise velocity of the droplet. If the magnitude of the forcing is sufficiently small we found that a droplet's motion can be separated into two modes, and the non-linear interaction between these modes is what causes the droplet to slide or climb. The droplet can climb uphill for most parameter values as long as ω is large enough, with the rise velocity reaching its maximum when the two modes are in phase. Using a boundary integral method, we have solved the larger amplitude forcing problem numerically which also allowed us to extend the model to include physical effects such as contact angle hysteresis. What we discovered from this is that adding hysteresis can cause an otherwise sliding droplet to climb by forcing the two modes into phase, producing a larger rise velocity. As well as hysteresis we looked at quadratic and cubic contact line laws that, although produced results different to a linear law, did not make a significant change to the mechanics of the problem. Although we could not compare this model directly to the experimental results in [8] it is possible to obtain footprints similar to those observed in the actual experiment. We also looked at how a small receding contact angle leads to non-circular contact lines. In spite of the strong simplifications that we have used, we have been able to examine the effect of contact angle hysteresis on the rise or fall of strongly driven droplets. Further work which could be implemented to improve on this model would be to look at the case where the droplet is no longer assumed thin. This would improve the analysis on the shape of the droplet as it climbs/slides whilst maintaining the quasistatic approximation. A derivation of this, along with the small amplitude asymptotic analysis, has already been carried out [4] and so we would be required to find a numerical solution for larger amplitudes.

We followed this with Model 2, a two-dimensional droplet where we assumed that the Reynolds number is large enough to neglect the fluids viscosity. This model is an extension of [3], allowing the thickness of the droplets to be varied instead of assuming it to be small. In the thin droplet limit this model shows quantitative agreement with [3]. Similar to Model 1 we found that for small amplitude oscillations a droplet's motion can be separated into two modes and the non-linear interaction between these modes is what causes the droplet to slide or climb. Due to the inertial forces present within the fluid the rise velocity of the droplet oscillates between climbing and sliding and the magnitude of the respective peaks decreases with increasing

frequency squared. When non-dimensionalising the small amplitude contact line law a variable parameter was left weighting the linear term. What we discovered was that varying this parameter caused significant change to the solution; with frequencies that once cause the droplet to climb now made them slide and vice versa. This result verified just how dominated the problem is by the presence of the contact line. When extending this further to look at pinned droplets we found that the two modes had resonant frequencies that caused large distortions in the shape of the free surface. When increasing the magnitude of the contact angles we found that in the limit of non-wetting the rise velocity began to oscillate rapidly with increasing magnitude. This behaviour was the result of surface modes appearing for thick droplets, a result not discoverable using a shallow water model.

Again with the use of a boundary integral method, we have solved the larger amplitude forcing problem numerically and looked at alternate contact line laws and contact angle hysteresis. With the use of a cubic law we could reach similar parameter values to that of the experiment, but without the effects of hysteresis the result was a sliding droplet. With the addition of hysteresis we found that the peak rise velocity increases and for frequencies near the pinned resonant frequencies, we found that even for large amounts of hysteresis a rise velocity is still obtainable. When combining both to examine a contact line law similar to [33] we were able to produce a climbing droplet using parameter values similar to the experiment. The shape of the droplet, as well as the velocity of the contact points against the contact angles, were not yet comparable to [8] and so an extra component needed to be added to the contact line law. This came in the form of a time dependent term on the left hand side of the law, weighted by a dimensionless parameter τ. This caused the velocity of the contact points to be multi-valued functions of their contact angles giving results closer to that of experiments involving unsteady, dynamic contact lines. We then examined this new law for many of the same conditions as previous in order to see how the solution would be affected. What we found when attempting to analyse the experiment was again that we could cause a droplet to climb uphill for the parameters that we desired. In addition to this the shape of the droplet was closer to the experiment than before as well as the velocity at the contact points. When directly comparing the results to the experiment however we found that there was still something missing, mainly due to how unusual the contact point velocities look from [8].

Although a quantitative comparison still cannot be made we have found a lot of similarities between this model and the experiment. The inclusion of the time dependency within the contact line law is a large step towards replicating experimental results, however comparisons still are unable to be made. Many experiments/theory for steady moving contact lines have predicted multiple regions where the velocity dependency on the contact angle changes. In order to extend this model further something similar may be required to make it more realistic. Another approach would be to include a boundary layer at the liquid/solid interface that incorporates viscosity; this however would require a slip condition close to the contact points to avoid the shear stress singularity.

We finished with Model 3 which is a three-dimensional, thin droplet where we have ignored the viscosity of the fluid. This again is an extension of [3] only now by examining a droplet instead of a two-dimensional ridge. A familiar result when examining this problem for small amplitude oscillations is the ability to separate the leading order motion of the droplet into two modes, again present in this model. When analysing the non-linear interaction between the two modes there is a term present that is positive when both the acceleration due to gravity and the oscillation of the plate are both set to zero. This is an unusual situation where the droplet has a net motion when no forcing is applied. Examining the high frequency, small amplitude limit of the model we found that the velocity of the swaying mode and the radial displacement both contain natural frequencies that are averagely spaced at $\omega^{1/2} \approx 1.1$. Unfortunately the lack of a numerical solution method means we are unable to solve the larger amplitude problem and hence, compare these results to that of [8]. Due to the nature of this problem a method which can deal with two-dimensional shallow water equations with a contact line will be required. The completion of this would allow us to examine larger amplitude oscillations, as well as incorporate contact angle hysteresis and different contact line laws, within our model.

A direct comparison between Model 1 and either of the other two would not produce any beneficial results due to the significant change the lack of inertia presents. We can however compare Models 2 and 3 and discuss the benefits we they provide. Unfortunately we can only do this for the small amplitude solution since Model 3 is not yet complete. First of all let us note that the difference between these models is that Model 2 has been assumed two-dimensional and with variable thickness whereas Model 3 is three-dimensional

and thin. The advantage of Model 2 therefore is that it allows contact angles of $O(1)$ magnitudes which is very important since the dynamics of the contact line are what we wish to understand. Model 3 on the other hand is geometrically closer to the actual experiment providing a full contact line instead of two contact points. When comparing the two models for small amplitude oscillations and for thin droplets we see that the shape of the results are very similar. We do find that the magnitude of the peaks are larger for Model 2 and they occur at lower frequencies. As already mentioned the rise velocity of a 'Model 2' droplet tends to zero with the frequency whereas a 'Model 3' droplet does not. Without the large amplitude solution to Model 3 a more in depth comparison cannot yet be made. One issue we can discuss regarding Models 2 and 3 is the size of the Reynolds number and how we have used it. When deriving the governing equations we balanced the surface tension with the inertia in both models and the result of this was a Reynolds number of approximately 10. We then went on to argue that this number is large enough for us to neglect viscosity in the problem however some would suggest that this is wrong. In order to solve this problem we have looked at the case where we balance the inertia with the applied acceleration (section B) and have shown that we can achieve a Reynolds number almost 10 times this amount without much change to the governing equations. In fact for the case where $\epsilon = 1$ (the value used when attempting to compare to the experiment in section 3.4) the governing equations are exactly the same. We can conclude from this that the analysis provided for large amplitude oscillations is indeed relevant with the approximations used.

5.1 Future work

Over the course of this work we have discussed three different models that all produce qualitative comparisons to [8] but there are still improvements that can be made. Model 1 uses the quasistatic approximation to look at the uphill motion of the droplet when the frequency of the oscillations are slow and the droplet is thin. The main improvement that could be made to this model is to extend it to include thick droplets. This would in fact be an extension of [4] similar to the way in which Model 1 is an extension of [2].

For Model 2 we looked at a two-dimensional droplet where the viscosity of the fluid is assumed negligible. In order to improve this we could extend

the model to be fully three-dimensional. The benefit of this would be that the rise velocity and the shape of the footprint would be much more comparable to [8] when using a droplet. Compared with thin droplet approximations the change from two- to three-dimensions would greatly change the way in which the vibrations travel across the surface of the droplet (mentioned in [2] for thin droplets).

Model 3 is a thin, three-dimensional droplet where the viscosity of the fluid is assumed negligible. So far only a small amplitude asymptotic solution has been derived and so the next step is to solve the general case for $O(1)$ ϵ. In order to do this a method for solving two-dimensional shallow water equations with a contact line needs to be used.

Now that we have mentioned some ways we can improve each model separately there is some other future work that could be carried out. First of all a justification needs to be made for the time dependent contact line law used in section 3.4.3. Once a physical reason for this has been found, the next step would be to introduce similar laws to Models 1 and 3. Another improvement which could be made is to introduce the effects of viscosity within the models, ideally in a boundary layer close to the substrate. This would mean that a slip condition would also need to be introduced near the contact lines(points).

A much simpler change we could make to all of these models is to alter the way in which the effective gravity is included in the governing equations. By making gravity only act vertically down and having the acceleration due to the oscillations act at an angle, we can use these models to compare with the second experiment in [8]. In addition to this we could also separate the oscillatory acceleration into a horizontal and a vertical component and have them both acting with different amplitudes and a phase difference. This would allow us to use our models to compare with [30].

In addition to improving current models, a new model could be created to simulate the full Navier-Stokes equations for a flow with a contact line. This would be very similar to [35] but would focus on modelling the contact line law in order to quantitatively compare to [8].

Appendix A

Force balance for alternative contact line laws

In this section we will cover the analytical method for finding the rise velocity of the droplet by balancing the forces, as shown in section 3.2.4, but for contact line laws different to (3.24). We will still use the assumption that the contact angles only differ from their initial state by a small amount in order to solve this problem asymptotically for small ϵ. We start with (3.125) only now we will write the contact angles as asymptotic expansions of the form

$$\theta_{\pm} = \theta_0 + \epsilon\theta_{1\pm} + \epsilon^2\theta_{2\pm} + ... \tag{A.1}$$

Now by inserting (A.1) into (3.125) and taking the time average over one period of oscillation we get

$$\overline{\theta}_+ - \overline{\theta}_- = -\frac{1}{4}\left(\left|\tilde{\theta}_+\right|^2 - \left|\tilde{\theta}_-\right|^2\right)\cot\theta_0 - \frac{gA_0\theta_0}{\sin\theta_0} + O(\epsilon), \tag{A.2}$$

where $\overline{\theta}_{\pm}$ is the constant part of $\theta_{2\pm}$ and $\theta_{1\pm} = \Im\left\{\tilde{\theta}_{\pm}\exp(i\omega t)\right\}$. By writing the velocity of the contact points in the form

$$v_{\pm} = \epsilon v_{1\pm} + \epsilon^2 v_{2\pm} + ..., \tag{A.3}$$

and inserting this into the second equation of (3.28) we get

$$\tilde{v}_{\pm} = \omega\tilde{D} \pm \tilde{V}, \quad \overline{v}_{\pm} = \pm\overline{V}, \tag{A.4}$$

where the 'bars' and 'tildes' have the same meaning that they did with $\theta_{\pm}$. The final step to finding the rise velocity is to include a relationship between the velocity of the contact points and the contact angles, i.e. a contact line law. If we used the Taylor expanded law (3.24) at this point we would again obtain (3.128) as expected.

A.1 A square root in the contact line law

The first alternative contact line law we will look at is

$$v_{\pm} = v' \frac{\theta - \theta_0}{\sqrt{\theta_0 \theta}}, \tag{A.5}$$

which is used to make the contact line velocity unbounded as $\theta \to 0$. If we expand both $\theta_{\pm}$ and $v_{\pm}$ and then separate into orders of ϵ we get

$$\theta_{1\pm} = \frac{\theta_0}{v'} v_{1\pm}, \qquad \theta_{2\pm} = \frac{\theta_0}{v'} v_{2\pm} + \frac{\theta_0}{2(v')^2} (v_{1\pm})^2. \tag{A.6}$$

Now if we use the same methods as in section 3.2 to transform these into time-independent equations, and insert them [along with (A.4)] into (A.2) we get

$$\overline{V} = -\frac{\omega}{2v'} \left(1 + \theta_0 \cot \theta_0\right) \Re \left\{ \tilde{V} \tilde{D}^* \right\} - \frac{v' g}{2} \frac{A_0}{\sin \theta_0} + O(\epsilon). \tag{A.7}$$

Comparing this to (3.128), where $V_r = \epsilon^2 \overline{V}$, we see that the only difference is the v''/v' term has been replaced by a -1.

A.2 Time dependent contact line law

The second alternative contact line law we will look at is

$$\tau \frac{dv_{\pm}}{dt} + v_{\pm} = v' \left(\frac{\theta_{\pm}}{\theta_0} - 1 \right) + \frac{1}{2} v'' \left(\frac{\theta_{\pm}}{\theta_0} - 1 \right)^2, \tag{A.8}$$

which causes the velocity of the contact points to become a multi-valued function of the contact angles; closer matching actual results for unsteady flows.

Expanding $\theta_\pm$ and $v_\pm$ the same as before we get

$$\begin{aligned}\theta_{1\pm} &= \frac{v'}{\theta_0}\left(\tau\frac{dv_{1\pm}}{dt} + v_{1\pm}\right), \\ \theta_{2\pm} &= \frac{v'}{\theta_0}\left(\tau\frac{dv_{2\pm}}{dt} + v_{2\pm}\right) - \frac{v''}{v'}\frac{\theta_0}{2(v')^2}\left(\tau\frac{dv_{1\pm}}{dt} + v_{1\pm}\right)^2.\end{aligned} \tag{A.9}$$

This shows that since $\theta_{1\pm}$ has changed compared to using (3.24) we will also need to alter the first order time-independent equations slightly, i.e. replace (3.62) with

$$v'\frac{\sin\theta_0}{\theta_0}\frac{\partial\tilde{R}}{\partial\theta} + (\omega\tau - i)\tilde{V} \pm \left[v'\frac{\sin\theta_0}{\theta_0}\cos\theta_0 + \omega(\omega\tau - i)\right]\tilde{D} = 0, \qquad \text{at } \theta = \frac{\pi}{2} \mp \theta_0. \tag{A.10}$$

Taking the time-independent versions of (A.9) and inserting them [and (A.4)] into (A.2) we get

$$\overline{V} = \frac{\omega}{2v'}\left(\frac{v''}{v'} - \theta_0\cot\theta_0\right)\left(1 + \omega^2\tau^2\right)\Re\left\{\tilde{V}\tilde{D}^*\right\} - \frac{v'g}{2}\frac{A_0}{\sin\theta_0} + O(\epsilon). \tag{A.11}$$

Comparing this to (3.128) we see that the only difference is the term that comes from the oscillating plate is multiplied by a term that depends of ω and τ. This also shows that for $\tau = 0$ we get the original problem back, as we should.

Appendix B

Balancing the inertia with the acceleration of the substrate for Models 2 and 3

When non-dimensionalising the governing equations for both Models 2 and 3 we defined the time scale T in order to balance the typical surface tension force in the droplet with the inertia, i.e.

$$T = \sqrt{\frac{\rho D_0^3}{\sigma \theta_0}}, \tag{B.1}$$

where $D_0 = L$ when switching between Models 2 and 3 (however for the rest of this section we will refer to it as D_0). The reason we chose this balance was to make easier comparison between these models and [3], in addition to having a simple way to examine small amplitude forcing asymptotically. The result of this is a Reynolds number for the model given by

$$Re = \frac{1}{\nu}\sqrt{\frac{\sigma \theta_0 D_0}{\rho}}. \tag{B.2}$$

Now if we insert values from the experiment into (B.2) we will find that the largest possible Reynolds number we can get is 13.67, with a typical value given approximately as 10. During the analysis we concluded this was large enough to neglect the affects of viscosity in the problem. A more appropriate balance may have been to balance the inertia with the applied acceleration

from the oscillating substrate. The result of this is a time scale given by

$$T = \sqrt{\frac{D_0}{a_0 \sin\alpha}}, \tag{B.3}$$

with the respective Reynolds number

$$Re = \frac{\sqrt{a_0 D_0^3 \sin\alpha}}{\nu}. \tag{B.4}$$

Now if we again insert the experimental values into (B.4) we achieve a maximum Reynolds number of 98.71, with a typical value of 32.00. Therefore using this balance provides a much stronger argument for the neglect of viscosity in the models. Now we have explained the argument for a different scaling balance we need to check how it alters the equations. For Model 2 the only equation that is affected is (3.11), which now looks like (with hats omitted)

$$\frac{\partial\phi}{\partial t} + \frac{1}{2}\left|\boldsymbol{\nabla}\phi\right|^2 + \frac{dV_s}{dt}x - \frac{\kappa}{\theta_0\epsilon} + a\left(x + \frac{\gamma}{\theta_0}y\right) = 0, \tag{B.5}$$

where γ and ϵ are the same as before. What we can see from (B.5) is almost unchanged, with ϵ moved from the forcing to under the curvature. Now if we repeat this for Model 3 we only change (4.9) that now looks like

$$\frac{\partial\mathbf{u}}{\partial t} + (\mathbf{u}\cdot\boldsymbol{\nabla})\mathbf{u} + \boldsymbol{\nabla}\left[a(x+\gamma h) - \frac{1}{\epsilon}\nabla^2 h\right] = 0, \tag{B.6}$$

again with ϵ shifting from the forcing to the curvature. What we have shown in this section is that there is a different method for balancing the dimensional scales in both Models 2 and 3 which give a much larger Reynolds number without causing significant change to the governing equations. This does however cause a large change in the small amplitude asymptotic solutions and so should only be used for ϵ of $O(1)$.

Bibliography

[1] E.S. Benilov. Drops climbing uphill on a slowly oscillating substrate. *Phys. Rev. E*, 82:026320, 2010.

[2] E.S. Benilov. Thin three-dimensional drops on a slowly oscillating substrate. *Phys. Rev. E*, 84:066301, 2011.

[3] E.S. Benilov and J. Billingham. Drops climbing uphill on an oscillating substrate. *J. Fluid Mech.*, 674:93–119, 2011.

[4] E.S. Benilov and C.P. Cummins. Thick drops on a slowly oscillating substrate. *Phys. Rev. E*, 88:023013, 2013.

[5] J. Billingham. Nonlinear sloshing in zero gravity. *J. Fluid Mech.*, 464:365–391, 2002.

[6] J. Billingham. On a model for the motion of a contact line on a smooth solid surface. *Eur. J. Appl. Math.*, 17:347–82, 2006.

[7] T.D. Blake and J.M. Haynes. Kinetics of liquid/liquid displacement. *J. Colloid Inteface Sci.*, 30:421–23, 1969.

[8] P. Brunet, J. Eggers, and R.D. Deegan. Vibration-induced climbing of droplets. *Phys. Rev. Lett.*, 99:144501, 2007.

[9] P. Brunet, J. Eggers, and R.D. Deegan. Motion of a drop driven by substrate vibrations. *Eur. Phys. J. Spec. Top.*, 166:11–14, 2009.

[10] J. Crank and P. Nicolson. A practical method for numerical evaluation of solutions of partial differential equations of the heat-conduction type. *Math. Proc. Cambridge*, 43:50–67, 1947.

[11] S.H. Davis. Moving contact lines and rivulet instabilities. part 1. the static rivulet. *J. Fluid mech.*, 98:225–42, 1980.

[12] B. Derby. Inkjet printing of functional and structural materials: Fluid property requirements, feature stability, and resolution. *Annu. Rev. Mater. Res.*, 40:395–414, 2010.

[13] R.H. Dettre and R.E. Johnson. Contact angle hysteresis - study of an idealized rough surface. *Advances in Chemistry*, 43:112–135, 1964.

[14] E.B. Dussan V. On the spreading of liquids on solid surfaces: static and dynamic contact lines. *Ann. Rev. Fluid Mech.*, 11:371–400, 1979.

[15] E.B. Dussan V. and S.H. Davis. On the motion of a fluid-fluid interface along a solid surface. *J. Fluid Mech.*, 65:71–95, 1974.

[16] E.B. Dussan V. and Chow R.T. On the ability of drops or bubbles to stick to non-horizontal surfaces of solids. *J. Fluid Mech.*, 137:1–29, 1983.

[17] J. Eggers and H.A. Stone. Characteristic lengths at moving contact lines for a perfectly wetting fluid: the influence of speed on the dynamic contact angle. *J. Flud Mech.*, 505:309–21, 2004.

[18] R.B. Fair. Digital microfluidics: is a true lab-on-a-chip possible? *Microfluid Nanofluid*, 3:245–81, 2007.

[19] L.M. Hocking. A moving fluid interface on a rough surface. *J. Fluid Mech.*, 76:801–17, 1976.

[20] L.M. Hocking. The damping of capillary-gravity waves at a rigid boundary. *J. Fluid Mech.*, 179:253–66, 1987.

[21] L.M. Hocking. The spreading of drops with intermolecular forces. *Phys. Fluids*, 6:3224–8, 1994.

[22] L.M. Hocking. The wetting of a plane surface by a fluid. *Phys. Fluids*, 7:1214–20, 1995.

[23] R.L. Hoffman. A study of the advancing interface: 1. interface shape in liquid-gas systems. *J. Colloid Interface Sci.*, 50:228–41, 1975.

[24] R.L. Hoffman. A study of the advancing interface: 2. theoretical prediction of the dynamic contact angle in liquid-gas systems. *J. Colloid Interface Sci.*, 94:470–86, 1983.

[25] C. Huh and L.E. Scriven. Hydrodynamic model of steady movement of a solid/liquid/fluid contact line. *J. Colloid Interface Sci.*, 35:85–101, 1971.

[26] K. John and U. Thiele. Self-ratcheting stokes drops driven by oblique vibrations. *Phys. Rev. Lett.*, 104, 2010.

[27] D.V. Lyubimov, T.P. Lyubimova, and S.V. Shklyaev. Behaviour of a drop on an oscillating solid plate. *Phys. Fluids*, 18:012101, 2006.

[28] J.A. Marsh, S. Garoff, and E.B. Dussan V. Dynamic contact angles and hydrodynamics near a moving contact line. *Phys. Rev. Lett.*, 70:2778–82, 1993.

[29] H.K. Moffatt. Viscous and resistive eddies near a sharp corner. *J. Fluid Mech.*, 18:1–18, 1963.

[30] X. Noblin, R. Kofman, and F. Celestini. Ratchetlike motion of a shaken drop. *Phys. Rev. Lett.*, 102:194504, 2009.

[31] C. Pozrikidis. *A practical guide to boundary element methods with the software library BEMLIB*. Chapman and Hall, 2002.

[32] Y.D. Shikhmurzaev. Moving contact lines in liquid/liquid/solid systems. *J. Fluid Mech.*, 334:211–49, 1997.

[33] L.H. Tanner. The spreading of silicone oil drops on horizontal surfaces. *J. Phys. D: Appl. Phys.*, 12:1473–84, 1979.

[34] C-L. Ting and M. Perlin. Boundary conditions in the vicinity of the contact line at a vertyically oscillating upright plate: an experimental investigation. *J. Fluid Mech.*, 295:263–300, 1995.

[35] S.W. Walker. A mixed formulation of a sharp interface model of stokes flow with moving contact lines. *ESAIM Math. Model. Numer. Anal.*, 48:969–1009, 2014.

[36] S.J. Weinstein and K.J. Ruschak. Coating flows. *Annu. Rev. Fluid Mech.*, 36:29–53, 2004.

[37] T. Young. An essay on the cohesion of fluids. *Phil. Trans. R. Soc. Lond.*, 95:65–87, 1805.

[38] W.A. Zisman. Relation of equilibrium contact angle to liquid and solid constitution. *Advances in Chemistry*, 43:1–51, 1964.